Thin Fluid Films Subject to External Airflows

Colin Paterson

Department of Mathematics and Statistics

University of Strathclyde

Glasgow, UK

August 2013

This thesis is submitted to the University of Strathclyde for the degree of Doctor of Philosophy in the Faculty of Science.

This thesis is the result of the author's original research. It has been composed by the author and has not been previously submitted for examination which has led to the award of a degree.

Signed: Date:

Acknowledgements

I wish to thank my supervisors, Prof. Stephen K. Wilson and Dr Brian R. Duffy, for their endless enthusiasm, encouragement and insight during the completion of this thesis.

My thanks also go to my family for their unwavering support and, in particular, to my mum, for everything, and my dad, whose optimism and strength of character in the face of long-term illness is a continual inspiration.

I am grateful for the funding provided by the Department of Mathematics and Statistics at the University of Strathclyde in order to complete this research.

Abstract

We use lubrication theory to analyse the steady flow of thin ridges, rivulets and rings of fluid and, in particular, we study the behaviour when the fluid is in the presence of an external airflow. Firstly, a thin ridge on an inclined planar substrate subject to a spatially varying pressure gradient due to an external airflow is considered. The effect of increasing the strength of the external airflow, and of increasing the inclination of the substrate to the horizontal, on a ridge of prescribed constant volume is investigated, and we identify and quantify the conditions for the ridge to de-pin at one or both of its contact lines. Secondly, we describe the possible pinning and subsequent de-pinning of a thin rivulet with constant non-zero contact angle as well as the possible de-pinning and subsequent re-pinning of a thin rivulet with constant width as they flow with prescribed volume flux in the azimuthal direction from the top to the bottom of a large horizontal cylinder. Thirdly, this problem is extended to include the effects of a prescribed uniform azimuthal surface shear stress arising from an external airflow in the direction opposing gravity. Lastly, we consider a thin ring of fluid with constant width and constant mass that flows in the azimuthal direction all the way round a large horizontal cylinder (a "full ring" of fluid) subject to a prescribed uniform azimuthal surface shear stress due to an external airflow. In particular, there is a maximum mass of fluid above which no full-ring solution exists, and we show that backflow near the cylinder surface is possible.

Contents

Chapter 1

Introduction

1.1 Overview of Thin-Film Flow

Thin-film flow occurs in a wide range of settings in nature, science and industry. In the human body, for example, synovial fluid in the knee joint, peritoneal fluid in the abdomen, and tear films in the eyes all act as lubricant to keep moving parts apart, reduce friction, and protect against wear of joints and organs. On a larger scale, geophysical flows such as lava flowing from a volcano, an avalanche of snow, and water flowing down a mountain are "thin" in the sense that the typical thickness of the flow is much smaller than its typical length. In the motor industry, vehicles use thin fluid films to lubricate many component parts including the engine, brakes and gears, while in the food industry, coatings and glazes are applied to foods to improve appearance, to add nutritional value, to preserve against mould, or simply to improve the taste of a foodstuff (Figure 1.1(a)). In medicine, ointments and moisturisers are applied thinly to the skin to protect it from becoming dry through contact with the air or simply to "lock in" moisture after bathing (Figure 1.1(b)), while steroid creams are used in the treatment of skin complaints such as eczema to reduce itching and inflammation. In many

(a)  (b) 

Figure 1.1: (a) A cake glazed with chocolate sauce. Picture courtesy of su-lin / Foter.com / CC BY-NC-ND. (b) Ointment to be applied as a thin layer to skin. Picture courtesy of shauncampbell / Foter.com / CC BY.

cases, to optimise performance it is important to understand exactly how a film of fluid behaves. For example, when paint is applied to a surface it is preferable that the paint does not sag when drying, so that it coats the surface evenly. In heat exchangers, condensers and evaporators it can be important to have continuous films of fluid with no dry patches to prevent thermal stresses which could have an adverse effect on the performance or lifespan of certain components. In spin-coating processes, excess fluid is applied to a surface which is then rotated at high speed (see, for example, Schwartz and Roy [83]). The rotation results in the fluid spreading along the surface (see, for example, Wilson, Hunt and Duffy [112]) such that an even coating of paint or protective material is obtained. No contact with the surface is required during spin coating which is advantageous when trying to prevent surface heterogeneities.

More specifically, there are many situations in which a thin film or droplet of fluid is subject to an external airflow. When a car is driving quickly enough during rainfall, drops of rainwater can be seen flowing up the windscreen or along the side windows because of the air flowing over and around the vehicle (Figure 1.2(a)). During flight, moisture in the air can accumulate and freeze on the wings of aircraft which can affect the flow of air passing around the aerofoil causing a

(a)  (b) 

Figure 1.2: (a) Rainwater on the windscreen of a moving car. Picture courtesy of Prof. S. K. Wilson. (b) The Erasmus bridge in Rotterdam. Picture courtesy of Wouter van Doorn / Foter.com / CC BY-NC-ND.

loss of lift or control (see, for example, Myers and Charpin [62]).

An intriguing situation in which a thin rivulet of fluid (that is, a narrow stream of fluid) interacts with an external airflow is in so-called Rain–Wind-Induced Vibrations (RWIV) of the cables of cable-stayed bridges (such as, for example, the Erasmus bridge in Rotterdam, shown in Figure 1.2(b)). In specific conditions of moderate wind and rain, the thin rivulets of water that form on the cable surface are seen as crucial to the existence of substantial vibrations observed in the cables. These vibrations can cause damage to the bridge deck and decrease the lifespan of the cables and, although still not fully understood despite considerable research (see, for example, Robertson et al. [78] and Leimatre, de Langre and Hémon [46]), it is thought that the fluid on the cable alters the surrounding airflow, and therefore the forces acting on it, resulting in RWIV.

Another area of industrial interest is that of the removal of droplets of fluid from silicon wafers during certain processes in the production of microchips. To improve resolution during the printing process, immersion technology is used, which means that there is a thin layer of fluid between the wafer and the lens through which ultraviolet light shines to create circuit patterns on the wafer. Some of this fluid is left as droplets on the surface of the wafer because of the high speed at which the lens scans over the wafer, causing imperfections to the final microchip if left

there. One solution is to use a jet of air to remove the droplets from the surface; this was the focus of a workshop that I attended in Leiden, The Netherlands in October 2010 (see van Bokhoven et al. [100]).

Reviews of modelling thin-film flows using the so-called lubrication approximation, or thin-film approximation, and discussion about their applications, are provided by Oron, Davis and Bankoff [71], Myers [61], O'Brien and Schwartz [70] and Craster and Matar [14]. In the next Section we show how the inherent slenderness of a thin film is exploited to simplify greatly the governing mathematical equations describing fluid flow, thus allowing the prospect of at least some analytical progress when studying problems of this type.

1.2 Derivation of the Lubrication Approximation

A Newtonian fluid is one where its stress–rate-of-strain relationship is linear such that (see, for example, Acheson [1])

$$\underline{\underline{\mathbf{T}}} = -p\underline{\underline{\mathbf{I}}} + 2\mu\underline{\underline{\mathbf{e}}}, \tag{1.1}$$

where $\underline{\underline{\mathbf{T}}}$ is the Cauchy stress tensor, p is the fluid pressure, μ is the fluid viscosity and

$$\underline{\underline{\mathbf{e}}} = \frac{1}{2}\left(\nabla\mathbf{u} + (\nabla\mathbf{u})^T\right) \tag{1.2}$$

is the rate-of-strain tensor, where $\mathbf{u}$ is the velocity field in the fluid and ∇ is the usual vector differential operator. The flow of an incompressible, Newtonian fluid (that is, one which satisfies Newton's second law and equation (1.1)) is described by the well-known Navier–Stokes equation

$$\rho\left(\mathbf{u}_t + \mathbf{u}\cdot\nabla\mathbf{u}\right) = -\nabla p + \rho\mathbf{f} + \mu\nabla^2\mathbf{u}, \tag{1.3}$$

where ρ is the constant fluid density, t is time and $\mathbf{f}$ is any body forces acting on the fluid (e.g. gravity), and the mass-conservation equation

$$\nabla\cdot\mathbf{u} = 0, \tag{1.4}$$

which are to be solved for $\mathbf{u}$ and p.

At the boundary between a fluid and a solid, the tangential component of velocity satisfies the no-slip condition

$$\mathbf{u}\cdot\mathbf{t} - \mathbf{U}\cdot\mathbf{t} = 0, \tag{1.5}$$

where $\mathbf{t}$ is a unit vector tangent to the boundary and $\mathbf{U}$ is the velocity of the solid, while the normal component of velocity satisfies the no-penetration condition

$$\mathbf{u}\cdot\mathbf{n} - \mathbf{U}\cdot\mathbf{n} = 0, \tag{1.6}$$

where $\mathbf{n}$ is the unit vector normal to the boundary. Together, (1.5) and (1.6) mean that the velocity of the fluid and the velocity of the solid are equal at the boundary, that is

$$\mathbf{u} = \mathbf{U} \quad \text{on the boundary.} \tag{1.7}$$

Note that it is possible to incorporate slip conditions or flow through a solid boundary (e.g. for a porous material) into the model; however, this is not considered here.

At the boundary between two fluids (denoted by "1" and "2"), the stress-balance equation is given by (see, for example, Acheson [1])

$$\left[\underline{\underline{\mathbf{T}}} \cdot \mathbf{n}\right]_1^2 = \sigma \mathbf{n} \left(\nabla \cdot \mathbf{n}\right) - \nabla \sigma, \tag{1.8}$$

where σ is the surface tension of the boundary and $[\cdot]_1^2$ denotes a change across the boundary. In the special case of constant surface tension, the normal and tangential stress balances are therefore given by

$$\left[\mathbf{n} \cdot \underline{\underline{\mathbf{T}}} \cdot \mathbf{n}\right]_1^2 = \sigma \nabla \cdot \mathbf{n}, \tag{1.9}$$

$$\left[\mathbf{n} \cdot \underline{\underline{\mathbf{T}}} \cdot \mathbf{t}\right]_1^2 = 0, \tag{1.10}$$

respectively.

The equations (1.3) and (1.4) are a pair of nonlinear, coupled partial differential equations which, in general, have to be solved numerically. However, when the flow is slender, these equations may be greatly simplified to permit the possibility of at least some analytical progress. Flows in this geometry are described by so-called lubrication theory. In particular, the flow domain is long and thin if the aspect ratio

$$\epsilon = \frac{H}{L} \ll 1 \tag{1.11}$$

is small, where H and L are typical length scales in the direction transverse and longitudinal to that in which the fluid predominantly flows, respectively. We will

illustrate this simplification by considering the simple problem of gravity-driven two-dimensional film flow on an inclined planar substrate.

Consider a two-dimensional thin film of fluid on a substrate inclined at an angle α to the horizontal, with free surface $h = h(x,t)$, constant density ρ and viscosity μ, where t is time, and refer to Cartesian coordinates Oxy with the x and y directions taken to be the longitudinal (i.e. parallel to the substrate) and transverse (i.e. normal to the substrate) directions, respectively. The velocity and pressure of the fluid are denoted by $\mathbf{u} = (u,v) = (u(x,y,t), v(x,y,t))$ and $p = p(x,y,t)$, respectively. From (1.11) we note that $H = \epsilon L$ and introduce the following non-dimensional variables:

$$\begin{gathered} x = Lx^*, \quad y = \epsilon L y^*, \quad h = \epsilon L h^*, \quad t = \frac{L}{U} t^*, \\ u = Uu^*, \quad v = \epsilon U v^*, \quad p - p_\infty = \frac{\mu U}{\epsilon^2 L} p^*, \quad \underline{\underline{\mathbf{T}}} = \frac{\mu U}{L} \underline{\underline{\mathbf{T}}}^*, \end{gathered} \tag{1.12}$$

where $U = \epsilon^2 \rho g L^2/\mu$ is a characteristic velocity in the longitudinal direction, p_∞ is the ambient pressure and g is the acceleration due to gravity. For clarity, we immediately drop the star subscripts, then (1.3) and (1.4) become

$$\epsilon^2 Re\,(u_t + uu_x + vu_y) = -p_x + \sin\alpha + \epsilon^2 u_{xx} + u_{yy}, \tag{1.13}$$

$$\epsilon^4 Re\,(v_t + uv_x + vv_y) = -p_y - \cos\alpha + \epsilon^2\left(\epsilon^2 v_{xx} + v_{yy}\right), \tag{1.14}$$

$$u_x + v_y = 0, \tag{1.15}$$

where $Re = \rho U L/\mu$ is the well-known Reynolds number. To obtain the governing equations for the two-dimensional thin film we assume that the so-called reduced Reynolds number defined by $Re^* = \epsilon^2 Re \ll 1$ is small so that at leading order (1.13)–(1.15) reduce to

$$0 = -p_x + \sin\alpha + u_{yy}, \quad 0 = -p_y - \cos\alpha, \quad u_x + v_y = 0. \tag{1.16}$$

Note that these equations are often referred to as the lubrication equations. At the stationary boundary $y = 0$ the conditions of no slip and of no penetration given

by (1.5) and (1.6), respectively, are simply

$$u = v = 0. \tag{1.17}$$

At the free surface $y = h(x,t)$ the unit normal vector and unit tangent vector are given by

$$\mathbf{n} = \frac{(-\epsilon h', 1)}{(1+\epsilon^2 h'^2)^{1/2}}, \quad \mathbf{t} = \frac{(1, \epsilon h')}{(1+\epsilon^2 h'^2)^{1/2}}, \tag{1.18}$$

respectively, where a dash denotes differentiation with respect to x, and which gives the quantities

$$\begin{gathered}
\mathbf{n}\cdot\underline{\underline{\mathbf{T}}}\cdot\mathbf{n} = \frac{1}{1+\epsilon^2 h'^2}\left(-\frac{p}{\epsilon^2} + h'^2 p - 2u_y h' + 2v_y + \epsilon^2\left(2u_x h' - 2v_x h'^2\right)\right), \\
\mathbf{n}\cdot\underline{\underline{\mathbf{T}}}\cdot\mathbf{t} = \frac{1}{1+\epsilon^2 h'^2}\left(\frac{u_y}{\epsilon} + \epsilon\left(v_x - 2u_x h' + 2v_x h' - u_y h'^2\right) - \epsilon^3 v_x\right), \\
\nabla\cdot\mathbf{n} = -\frac{\epsilon h''}{\left(1+\epsilon^2 h'^2\right)^{1/2}}.
\end{gathered} \tag{1.19}$$

Hence, from (1.9), (1.10) and (1.19) the normal and tangential stress balances at leading order in the limit $\epsilon \to 0$ are given by

$$[-p]_1^2 = -C^{-1}h'', \tag{1.20}$$

$$u_y = 0, \tag{1.21}$$

respectively, where $C = \mu U/\epsilon^3\sigma$ is the well-known capillary number. We choose $C = O(1)$ (that is, $\epsilon = O(\mu U/\sigma)^{1/3}$) so that the terms balance in (1.20); this is appropriate for the problems we will consider but, of course, need not be the case in all situations.

The so-called kinematic condition is given by $D(h-y)/Dt = 0$, where $D/Dt = \partial/\partial t + \mathbf{u}\cdot\nabla$ is the material derivative, and in the case of unsteady, two-dimensional flow (such that $h = h(x,t)$) this gives

$$h_t + uh_x - v = 0, \tag{1.22}$$

which, using (1.15), may also be written

$$h_t + Q_x = 0, \tag{1.23}$$

where

$$Q = \int_0^h u \, \mathrm{d}y \tag{1.24}$$

is the volume flux per unit width across a station $x =$ constant (nondimensionalised with ϵUL).

1.3 Films, Ridges and Droplets Subject to an External Airflow

In Chapter 2 we will consider the steady flow of a thin ridge (i.e. a thin two-dimensional droplet) of fluid in the presence of an external airflow, and so in Subsection 1.3.1 below we discuss some of the previous work concerning problems of this kind. In particular, we derive a model for the strongly-coupled interaction between a thin ridge and an external airflow. Specifically, as shown in Subsection 1.3.2 this interaction may be modelled by adapting classical thin-aerofoil theory. As an example of a problem in which this approach has been utilised, in Subsection 1.3.3 we re-formulate the analysis of King and Tuck [42], and slightly extend their results.

1.3.1 Literature Review

There have been many studies of a thin film of fluid subject to an external pressure gradient and/or shear stress due to an external airflow. King, Tuck and Vanden-Broeck [43] considered a film on an inclined substrate, and included the effects of both a uniform shear stress and an external pressure gradient from an external flow of air directed up the substrate, as well as surface tension and gravity, and studied the waves that form at the air-fluid interface, and Vanden-Broeck and Miloh [102] considered a moving pressure distribution over two thin films of fluid, with the less dense fluid sitting on top of the other, and found that the lower fluid can dampen the waves obtained at the interface between the air and the upper fluid. Kriegsmann, Miksis and Vanden-Broeck [44] considered a moving pressure distribution over a thin film of fluid on an inclined substrate and found steady solutions where the film thickness upstream and downstream of the disturbance are equal, except for a finite range of parameter values where steady solutions

with different thicknesses upstream and downstream were obtained. Chou and Wu [12] considered a film subject to an applied shear stress flowing over either a solid rectangular hump or a rectangular trough, while Myers and Charpin [62] studied the effect of an applied shear stress over thin layers of water and ice on a planar inclined substrate, a cylindrical substrate, and an aerofoil as a model for ice-accretion on aircraft wings. Shuaib et al. [86] computed numerical solutions for the different types of free surface waves that are obtained when a thin film on an inclined substrate is subject to an applied shear stress either up or down the substrate, and Pascal and D'Alessio [72] studied the waves on the free surface of a non-Newtonian fluid down an inclined substrate and found that an applied upwards shear stress has a stabilising effect (i.e. it reduces the amplitude of the waves). Cuminato et al. [16] studied the steady flow of a thin film on a heated horizontal substrate as a model for dry-out within a steam generating boiler pipe, including a uniform shear stress and an external pressure gradient at the free surface of the film arising from the gas flow, as well as evaporative mass loss from the film, and, in particular, they calculated the location of the dry-out point. Recently, Ueno and Farzaneh [98] considered a thin film of water on top of a layer of ice and subjected to an external airflow. They included the effects of the external pressure gradient, applied shear stress, gravity and surface tension, and predicted that the wavelength of the disturbances at the ice-water interface decreases as the strength of the external airflow is increased.

A ridge or a three-dimensional droplet (hereafter simply referred to as a droplet) of fluid subject to an applied shear stress have also received attention. Li and Pozrikidis [49] computed free surface profiles of a hemispherical droplet with prescribed circular contact line subject to an applied shear stress with constant surface tension, where the viscosity of the droplet and the surrounding fluid were assumed equal because of numerical constraints, and Yon and Pozrikidis [114] extended this

model to include the effects of the droplet and surrounding fluid having different viscosities as well as variable surface tension caused by the presence of surfactant. Dimitrakopoulos and Higdon [19, 20] considered a ridge and a droplet on a horizontal substrate subject to an applied shear stress including the effects of surface tension and gravity, calculating a critical shear rate above which steady solutions do not exist and finding good qualitative agreement in the case of viscous droplets between their numerical computations and the analysis of Dussan [99], who used lubrication theory to study one fluid flowing over the top of a droplet of a second fluid which is attached to a substrate. The spreading of a sessile and of a pendent ridge, and of a sessile and of a pendent droplet, on a horizontal substrate (where "sessile" refers to a ridge or droplet sitting on the substrate and "pendent" refers to a ridge or droplet hanging from the substrate) subject to a jet of air directed either vertically downwards in the sessile case, or vertically upwards in the pendent case, was studied by McKinley, Wilson and Duffy [55], and the stability of these flows was subsequently considered by McKinley and Wilson [53, 54]. Schleizer and Bonnecaze [81] considered shear- or pressure-driven flow between two parallel substrates in the absence of gravity, where a ridge was pinned to one of the substrates. They found that the ridge profile becomes more deformed for a higher ridge viscosity ratio and for a larger ridge volume (or surface area), and that there is a critical viscosity above which no steady solutions exist. Spelt [87] also studied a ridge between parallel substrates in a shear flow, finding a critical shear rate above which steady solutions do not exist and extended the results of Schleizer and Bonnecaze [81] to include inertia after the contact lines have de-pinned. Ding and Spelt [22] studied a droplet on a horizontal substrate subject to an applied shear stress, including the effects of inertia, investigating the critical parameter values for the contact lines to de-pin, while Ding, Gilani and Spelt [21] investigated the motion after de-pinning has occurred and found that the droplet can move steadily

along the substrate, can develop a tail as it slides which may eventually split into smaller drops, or can completely detach from the substrate. Zhang, Miksis and Bankoff [116] studied the shear flow of a ridge attached to a substrate in a channel and found that the ridge can slide steadily along the substrate for low Reynolds and capillary numbers but that fingers of fluid can develop ahead of the ridge for higher parameter values, Dimitrakopoulos [18] considered a droplet in a shear flow sliding along a rough substrate and found that it was equally-favourable for the upstream or downstream contact line to de-pin first, and Sugiyama and Sbragaglia [88] considered the slight deformation of a hemispherical ridge in a shear flow and obtained an exact series solution.

More recently, there have been experimental studies of a droplet attached to a substrate subject to an external airflow. Motivated particularly by the numerical studies of Spelt [87], Ding and Spelt [22] and Ding, Gilani and Spelt [21], Seevaratnam et al. [84] considered a droplet of oil on a substrate in a rectangular channel subject to a pressure-driven flow of water and observed the flow regimes reported by Ding, Gilani and Spelt [21] of steady sliding, crawling whilst developing a tail, or complete detachment from the substrate, for a range of parameter values. Fan, Wilson and Kapur [31] experimentally investigated the motion of a droplet attached to a substrate subject to an airflow and observed the same flow regimes for two fluids with different viscosities, and three substrates with different receding and advancing contact angles, as shown in Figure 1.3. As, for example, Dussan [99] and Blake and Ruschak [9] describe, the receding and advancing contact angles are the smallest and largest values that the contact angle may take before the contact line de-pins and begins to recede or advance, respectively, and in practice their values will depend on the properties of the three phases (air, fluid and substrate) in the vicinity of the contact line. Figure 1.3 shows that the water droplet slides along the substrate retaining its bulk shape whereas the glycerine

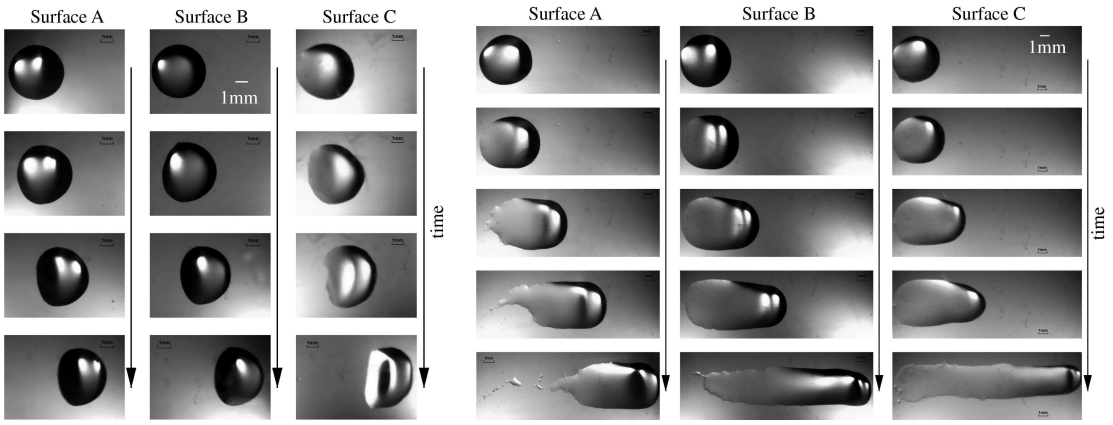

Figure 1.3: Images of droplets subject to an external airflow, observed by Fan, Wilson and Kapur [31]. The fluid in (a) is water, which has a lower viscosity but higher surface tension than glycerine, which is the fluid in (b). Surface A has the highest receding and advancing contact angles while surface C has the lowest. Reprinted from J. Coll. Int. Sci. **356**, J. Fan, M. C. T. Wilson and N. Kapur, Displacement of liquid droplets on a surface by a shearing air flow, 286–292, Copyright 2011, with permission from Elsevier.

droplet develops a large tail and even sheds satellite droplets.

In many real-life situations, the interaction between the flow of a fluid and an external airflow passing over it plays an important role. One way to model this interaction is to adapt classical thin-aerofoil theory to obtain an expression for the pressure gradient in the air (and, in particular, for the pressure gradient on the free surface of the fluid) in terms of the unknown free surface profile of the fluid. This approach was used by both King, Tuck and Vanden-Broeck [43] and Cuminato et al. [16] mentioned above. Previously, Durbin [25, 26] used thin-aerofoil theory to study the steady flow of a thin ridge on a horizontal substrate. He assumed that the external airflow detaches at some point on the free surface of the ridge resulting in an asymmetric ridge profile. In particular, Durbin [26] studied the critical case in which the strength of the external airflow is at the maximum value such that the ridge is deformed but for which the contact lines do not de-pin. Subsequently, King and Tuck [42] also considered a thin ridge of fluid in the presence of an external airflow. Like Durbin [26], they used classical

thin-aerofoil theory to model the external pressure distribution; however, unlike Durbin [26], they included both the effects of a uniform surface shear stress due to the external airflow and the effects of gravity, but neglected surface tension in their numerical calculations. King and Tuck [42] found that, for each value of the angle of inclination of the substrate, there are zero, one or two values of the strength of the external airflow which yield a steady state.

1.3.2 Thin-aerofoil Theory

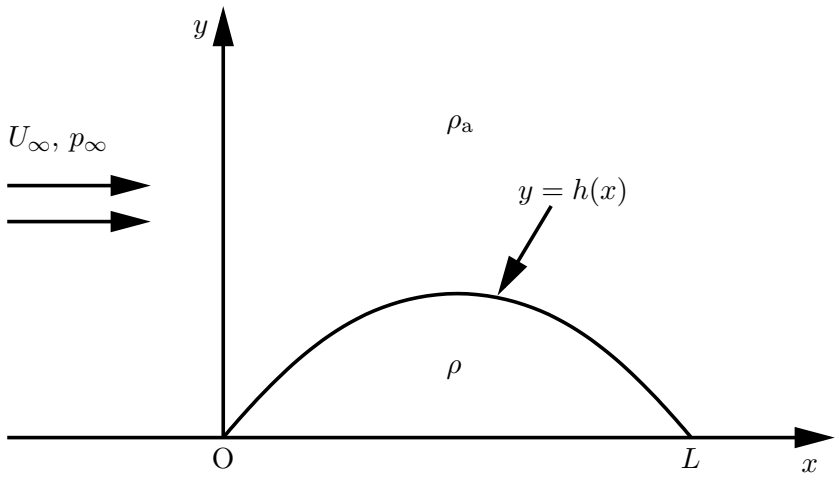

Figure 1.4: Sketch of a thin, steady ridge of fluid on a planar substrate in the presence of an inviscid external airflow.

As mentioned in Subsection 1.3.1, the interaction between the flow of a fluid and an external airflow passing over it can be very significant. In this Subsection, based on the analysis of Van Dyke [101], we derive an expression for the pressure gradient arising from an external airflow passing over a thin ridge of fluid in terms of the shape of the free surface. Of course, in classical thin-aerofoil theory the object over which the air flows is solid (e.g. an aircraft wing), and has a known shape, allowing the pressure to be calculated. However, in the present context of flow over a ridge of fluid we must solve for both the shape of the free surface and

the pressure.

Consider the steady flow of a thin ridge of fluid on a planar substrate, in the presence of a steady external airflow, as sketched in Figure 1.4. We assume that the fluid in the ridge has constant density ρ and coefficient of surface tension σ, and that the external flow of air is inviscid and has constant density $\rho_{\rm a}$, which flows tangentially to the substrate far from the ridge with constant speed U_∞ and ambient pressure p_∞. The airflow is perturbed by the presence of the ridge, resulting in a non-uniform external pressure gradient that depends in a non-trivial way on the unknown free surface profile of the ridge. Referred to Cartesian coordinates Oxy with the x and y directions taken to be parallel and normal to the substrate, respectively, as indicated in Figure 1.4, the ridge has free surface profile $y = h(x)$ for $0 \leq x \leq L$, width L in the transverse (i.e. in the x) direction and volume per unit length in the longitudinal (i.e. in the z) direction V. Note that the transverse and longitudinal coordinates are different from those used for the two-dimensional film in Subsection 1.2. The pressure in both the air and the ridge is denoted by $p = p(x, y)$ and the air velocity is $\mathbf{u}_{\rm a} = (u_{\rm a}, v_{\rm a}) = (u_{\rm a}(x, y), v_{\rm a}(x, y))$. We introduce the following non-dimensionalised and scaled variables:

$$\begin{gathered} x = L_0 x^*, \quad L = L_0 L^*, \quad y = \epsilon L_0 y^*, \quad y = L_0 Y^*, \quad h = \epsilon L_0 h^*, \quad V = \epsilon L_0^2 V^*, \\ p - p_\infty = \frac{\epsilon\sigma}{L_0} p^*, \quad u_{\rm a} = U_\infty u_{\rm a}^*, \quad v_{\rm a} = \epsilon U_\infty v_{\rm a}^*, \quad \phi = L_0 U_\infty \phi^*, \end{gathered} \tag{1.25}$$

where L_0 is the characteristic transverse length scale, $\phi = \phi(x, Y)$ is the velocity potential satisfying $\mathbf{u}_{\rm a} = \nabla\phi$, and $\epsilon \ll 1$ is the (small) aspect ratio of the ridge. Note that in (1.12) we use the governing equations for thin-film flow to determine the pressure scale, but in (1.25) we instead use the normal stress balance at the free surface. Note also that two different non-dimensional y-coordinates, namely y^* and Y^*, are required. Specifically, the re-scaled y-coordinate y^* corresponding to the length scale ϵL_0 ($\ll L_0$) in the y-direction is required to describe the behaviour of

the fluid within the thin ridge, whereas the re-scaled y-coordinate Y^* corresponding to the length scale L_0 in the y-direction (i.e. the same length scale as in the x-direction) is required to describe the behaviour of the air external to the ridge. For clarity, we immediately drop the star superscripts on non-dimensional variables in what follows.

The external airflow satisfies the Laplace equation

$$\phi_{xx} + \phi_{YY} = 0, \tag{1.26}$$

which is to be solved subject to the boundary conditions of a uniform stream far from the ridge

$$\phi_x \to 1, \quad \phi_Y \to 0 \quad \text{as} \quad x^2 + Y^2 \to \infty \tag{1.27}$$

(note that $p \to 0$ far from the ridge as well) and the kinematic free surface condition (1.22), which may be written as

$$\phi_Y = \epsilon h' \phi_x \quad \text{on} \quad Y = \epsilon h. \tag{1.28}$$

We seek a solution ϕ to the problem (1.26) as $\epsilon \to 0$ as a regular asymptotic series in the form

$$\phi(x, Y; \epsilon) = x + \epsilon\phi_1(x, Y) + \epsilon^2\phi_2(x, Y) + O(\epsilon^3), \tag{1.29}$$

while the pressure may then be written in the form

$$p = \epsilon P(x, Y) + O(\epsilon^2), \tag{1.30}$$

where $P = P(x, Y)$ is the pressure due to the external airflow. Note that the $O(1)$ term is zero since the ambient pressure has been scaled out. If we assume that the $\phi_k = \phi_k(x, Y)$, $k = 1, 2, 3, ...$, in (1.29) are twice differentiable at $Y = 0$ then we may use a Taylor expansion about $Y = 0$ to obtain

$$\phi(x, \epsilon h; \epsilon) = x + \epsilon\phi_1(x, 0) + \epsilon^2[\phi_2(x, 0) + h\phi_{1Y}(x, 0)] + O(\epsilon^3), \tag{1.31}$$

from which we deduce that

$$\phi_x = 1 + \epsilon\phi_{1x}(x,0) + \epsilon^2[\phi_{2x}(x,0) + h'\phi_{1Y}(x,0) + h\phi_{1Yx}(x,0)] + O(\epsilon^3), \quad (1.32)$$

$$\phi_Y = \epsilon\phi_{1Y}(x,0) + \epsilon^2[\phi_{2Y}(x,0) + h\phi_{1YY}(x,0)] + O(\epsilon^3). \quad (1.33)$$

At leading order we simply have the uniform stream and at $O(\epsilon)$, equations (1.26)–(1.28) become

$$\phi_{1xx} + \phi_{1YY} = 0, \quad (1.34)$$

$$\phi_{1x} = \phi_{1Y} = 0 \quad \text{as} \quad x^2 + Y^2 \to \infty, \quad (1.35)$$

$$\phi_{1Y} = h' \quad \text{on} \quad Y = 0. \quad (1.36)$$

We may use a distribution of sources and sinks along the x-axis to represent the effect of the ridge on the external airflow (i.e. the perturbation to the uniform stream). A point source of unit strength at the origin is given by (see, for example, Acheson [1])

$$\phi(x,Y) = \frac{1}{2\pi}\ln\sqrt{x^2+Y^2}, \quad (1.37)$$

which gives

$$\phi_x(x,Y) = \frac{1}{2\pi}\frac{x}{x^2+Y^2}. \quad (1.38)$$

Van Dyke [101] states that the local source strength must be twice the aerofoil slope which means that, using the tangency condition (1.36), we get

$$\phi_{1x}(x,Y) = \frac{1}{\pi}\int_0^L \frac{(x-\xi)h'(\xi)}{(x-\xi)^2+Y^2}\,\mathrm{d}\xi. \quad (1.39)$$

Therefore we obtain the appropriate form for the $O(\epsilon)$ term of the velocity potential $\phi_1(x,Y)$ in (1.29) by integrating (1.39) with respect to x to give

$$\phi_1(x,Y) = \frac{1}{2\pi}\int_0^L h'(\xi)\ln\left[(x-\xi)^2+Y^2\right]\,\mathrm{d}\xi. \quad (1.40)$$

From (1.32), (1.33) and (1.40) we get

$$\begin{aligned}|\nabla\phi|^2 &= \phi_x^2 + \phi_Y^2 \\ &= \left(1 + \frac{\epsilon}{\pi}\int_0^L \frac{(x-\xi)h'(\xi)}{(x-\xi)^2+Y^2}\,\mathrm{d}\xi + O(\epsilon^2)\right)^2 \\ &\quad + \left(\frac{\epsilon}{\pi}\int_0^L \frac{Yh'(\xi)}{(x-\xi)^2+Y^2}\,\mathrm{d}\xi + O(\epsilon^2)\right)^2 \\ &= 1 + \frac{2\epsilon}{\pi}\int_0^L \frac{(x-\xi)h'(\xi)}{(x-\xi)^2+Y^2}\,\mathrm{d}\xi + O(\epsilon^2), \end{aligned} \tag{1.41}$$

and then use Bernoulli's equation to calculate the pressure due to the external airflow P in (1.30), namely

$$P(x,Y) = -\Lambda\int_0^L \frac{(x-\xi)h'(\xi)}{(x-\xi)^2+Y^2}\,\mathrm{d}\xi, \tag{1.42}$$

where

$$\Lambda = \frac{\rho_\mathrm{a}U_\infty^2 L_0}{\pi\sigma} \tag{1.43}$$

is a non-dimensional Weber number (i.e. the appropriate measure of the strength of the external airflow, or the ratio of inertia to surface tension). In particular, the pressure due to the external airflow at the free surface and substrate $Y = 0$ is given by

$$P(x,0) = -\Lambda\fint_0^L \frac{h'(\xi)}{x-\xi}\,\mathrm{d}\xi, \tag{1.44}$$

where the integral is of Cauchy principal-value type.

1.3.3 A ridge on an inclined substrate supported against gravity by an external airflow (King and Tuck [42])

In this Subsection, we use the expression obtained for the pressure gradient due to an external airflow in Subsection 1.3.2 to determine the shape of the free surface of a ridge in the specific case studied by King and Tuck [42]. We re-formulate the analysis of King and Tuck [42] to be consistent with the problem that will be considered in Chapter 2, and slightly extend their results.

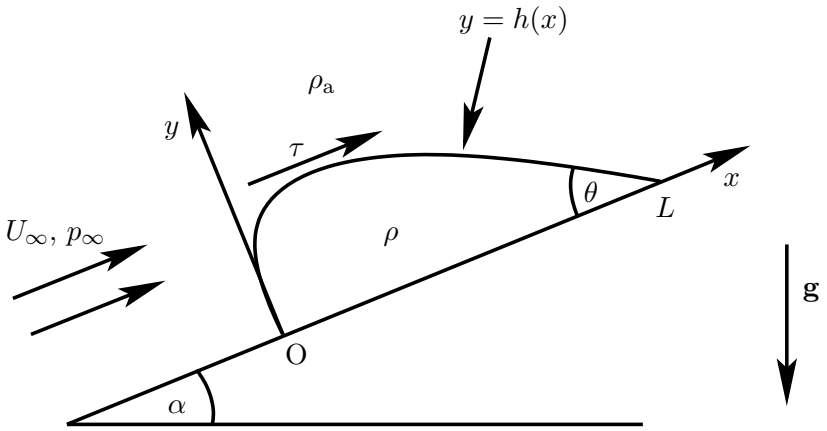

Figure 1.5: Sketch of a thin, steady sessile ridge of fluid on an inclined, planar substrate in the presence of an external airflow, as considered by King and Tuck [42].

Consider the steady flow of a thin, steady sessile ridge of fluid on a planar substrate inclined at an angle α to the horizontal, in the presence of a steady external airflow, as sketched in Figure 1.5.

As in Subsection 1.3.2, the effects of a non-uniform external pressure gradient are included; however, unlike in Subsection 1.3.2, the external airflow now exerts a uniform shear stress τ in the transverse direction on the ridge. Note that $\tau = 0$ corresponds to an inviscid airflow which means the ridge is static. We also denote the downstream contact angle θ, while at the upstream end we will show that the slope is infinite in the case of zero surface tension (this is, the case which will be considered for the numerical computations).

We introduce the following non-dimensionalised and scaled variables:

$$\begin{gathered} x = Lx^*, \quad y = \epsilon L y^*, \quad h = \epsilon L h^*, \quad \theta = \epsilon \theta^*, \\ p - p_\infty = \frac{\epsilon\sigma}{L} p^*, \quad \tau = \frac{\epsilon^2\sigma}{L}\tau^*, \quad u = \frac{\epsilon^3\sigma}{\mu} u^*, \quad Q = \frac{\epsilon^4\sigma L}{\mu} Q^*, \end{gathered} \tag{1.45}$$

where $\epsilon = (3L\tau/2\sigma)^{1/2} \ll 1$ so that $\tau^* = 2/3$ (the factor of $2/3$ will cancel to give unity in the equation for the shape of the free surface h), and Q is the volume flux per unit width given by (1.24). Note that, unlike in (1.25) where an arbitrary length scale L_0 was used, in the present problem the width L is used as the typical

length scale in the transverse direction and therefore the ridge occupies the interval $0 \leq x^* \leq 1$. For clarity, we again immediately drop the star superscripts on non-dimensional variables in what follows. The governing lubrication equations (1.16) now become

$$0 = -p_y - \left(\frac{L}{\ell}\right)^2 \cos\alpha, \quad 0 = -p_x - \left(\frac{L}{\ell}\right)^2 \frac{\sin\alpha}{\epsilon} + u_{yy}, \tag{1.46}$$

where $\ell = (\sigma/\rho g)^{\frac{1}{2}}$ is the capillary length, and the boundary conditions (1.17), (1.20) and (1.21) are now

$$u = 0 \quad \text{on} \quad y = 0 \tag{1.47}$$

and

$$p = P - h'', \quad u_y = \frac{2}{3}\left(\frac{L}{\ell}\right)^2 \quad \text{on} \quad y = h. \tag{1.48}$$

Note that $L = \ell$ in (1.16), that is, the typical length scale in the x direction is equal to the capillary length; however, that is not the case in the present problem, as seen in (1.46).

From (1.46b) we see that we require $\alpha = O(\epsilon)$ for all three terms in the equation to balance; then solving (1.46)–(1.48) for p and u in this case yields

$$p = \left(\frac{L}{\ell}\right)^2 (h - y) + P - h'' \tag{1.49}$$

and

$$u = \frac{y(y-2h)}{2}\left[\left(\frac{L}{\ell}\right)^2 h' + P' - h''' + \left(\frac{L}{\ell}\right)^2 \frac{\alpha}{\epsilon}\right] + \frac{2}{3}\left(\frac{L}{\ell}\right)^2 y. \tag{1.50}$$

The kinematic condition (1.23) implies that $Q = 0$ in the present steady flow problem, and so from (1.24) and (1.50), together with (1.44) to describe the pressure due to the external airflow P via thin-aerofoil theory, we obtain the governing nonlinear singular integro-differential equation for h, namely

$$Sh''' - h' - \hat{\alpha} + \lambda \frac{\mathrm{d}}{\mathrm{d}x} \int_0^1 \frac{h'(\xi)}{x - \xi}\, \mathrm{d}\xi + \frac{1}{h} = 0, \tag{1.51}$$

where

$$S = \left(\frac{\ell}{L}\right)^2 = \frac{\sigma}{\rho g L^2}, \quad \hat{\alpha} = \frac{\alpha}{\epsilon}, \quad \lambda = \frac{\rho_a U_\infty^2 \ell^2}{\pi \sigma L} = \frac{\rho_a U_\infty^2}{\pi \rho g L} \tag{1.52}$$

are dimensionless parameters: S is a Bond number (i.e. a measure of the effect of surface tension), $\hat{\alpha}$ is an appropriately scaled version of the angle of inclination of the substrate to the horizontal, and λ is a measure of the strength of the external airflow. Note that the parameter λ in (1.52) is equal to the parameter Λ from (1.43) in the case when $L_0 = \ell^2/L$.

We assume that the width of the ridge is much greater than the capillary length $L \gg \ell$ which gives $S \ll 1$ in (1.51) (i.e. the case of weak surface tension). Local analysis of (1.51) reveals that near the upstream contact line h behaves according to

$$h \sim (2x)^{\frac{1}{2}} \quad \text{as} \quad x \to 0^+, \tag{1.53}$$

while near the downstream contact line h behaves according to

$$h \sim \lambda^{-\frac{1}{2}}(1-x) \quad \text{as} \quad x \to 1^-. \tag{1.54}$$

This means that the slope is infinite near the upstream contact line, but that the downstream contact angle is $\theta = -h'(1) = \lambda^{-\frac{1}{2}}$.

The behaviour (1.53) describes the free surface all the way to the upstream contact line $x = 0$ only if $S = 0$. For small but non-zero S there is a "boundary layer" near $x = 0$, and we may re-scale (1.51) according to

$$x = S^{\frac{1}{2}}\bar{x}, \quad h = S^{\frac{1}{4}}\bar{h}, \tag{1.55}$$

so that for $x = O(S^{1/2})$ (that is, in the "inner" region near $x = 0$), the leading order free surface shape is given by a balance between surface tension, gravity and shear stress satisfying

$$\bar{h}''' - \bar{h}' + \frac{1}{\bar{h}} = 0, \tag{1.56}$$

subject to the boundary conditions

$$\bar{h} = \bar{h}' = 0 \quad \text{when} \quad \bar{x} = 0 \tag{1.57}$$

and the matching condition to the solution in the "outer" region (given by (1.53))

$$\bar{h} \sim (2\bar{x})^{\frac{1}{2}} \quad \text{as} \quad \bar{x} \to \infty. \tag{1.58}$$

Figure 1.6 shows a plot of the numerically obtained solution of (1.56) subject to (1.57) and (1.58). The inclusion of weak surface tension $S \ll 1$ results in a finite contact angle at $x = 0$, and the solution in the "inner" region near $x = 0$ joins smoothly to the square root behaviour in the "outer" region. Note that, unlike near $x = 0$, the inclusion of weak surface tension does not change the local shape of the free surface near the downstream contact line $x = 1$ since the local behaviour is still given by (1.54) (that is, a balance between the pressure gradient and the shear stress). Given that the inclusion of surface tension does not affect the shape of the ridge when S is small, we can safely set $S = 0$ in (1.51) and solve for h numerically as described below.

Standard numerical methods struggle to cope with the infinite slope of the free surface near $x = 0$ and so, as suggested by Cuminato, Fitt and McKee [15] in their review paper on linear and nonlinear singular integro-differential equations, we use the asymptotic behaviour near $x = 0$ to remove this singularity in the slope from the numerical problem. Following King and Tuck [42], we use (1.53) and (1.54) to write (1.51) in terms of a new variable $G(y)$ by first using the substitution $H(y) = (2x)^{1/2}h(x)$, where $y^2 = x$, to give

$$H(y)\left[\lambda\frac{\mathrm{d}}{\mathrm{d}y}\int_0^1 \frac{H(\zeta)+\zeta H'(\zeta)}{\zeta^2-y^2}\,\mathrm{d}\zeta + H(y) + yH'(y) + \left(\frac{2}{\lambda}\right)^{\frac{1}{2}}\tilde{\alpha}y\right] - 1 = 0, \tag{1.59}$$

where

$$H \to 1 \quad \text{as} \quad y \to 0^+ \quad \text{and} \quad H \sim (2\lambda)^{-\frac{1}{2}}(1-y^2) \quad \text{as} \quad y \to 1^-, \tag{1.60}$$

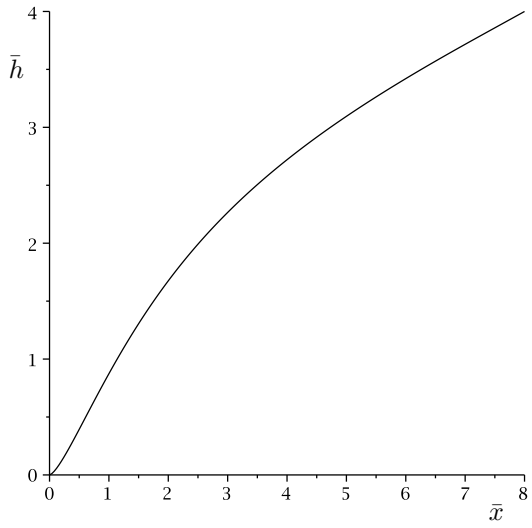

Figure 1.6: Plot of the free surface-shape near the upstream contact line, obtained by solving (1.56) numerically subject to (1.57) and (1.58).

and we then set $G(y) = H(y) + yH'(y)$ to obtain

$$\left[\int_0^y G(\zeta)\,\mathrm{d}\zeta\right]\left[\lambda\frac{\mathrm{d}}{\mathrm{d}y}\int_0^1 \frac{G(\zeta)}{\zeta^2 - y^2}\,\mathrm{d}\zeta + G(y) + \left(\frac{2}{\lambda}\right)^{\frac{1}{2}}\tilde{\alpha}y\right] - y = 0, \tag{1.61}$$

subject to

$$G(0) = 1 \quad \text{and} \quad G(1) = -\left(\frac{2}{\lambda}\right)^{\frac{1}{2}}, \tag{1.62}$$

where $\tilde{\alpha} = \hat{\alpha}/\theta$ is a measure of the ratio of substrate inclination to the downstream contact angle. We solve (1.61) numerically by discretising the interval $[0, 1]$ onto a uniform grid with n subintervals, together with the assumption that $G(y)$ is linear on each subinterval. One of the parameters, λ or $\tilde{\alpha}$, is free to be specified while the other has to be calculated as part of the solution. The resulting set of nonlinear algebraic equations is solved using the mathematical software package MAPLE for a variety of pairs $(\tilde{\alpha}, \lambda)$. Figure 1.7 shows the λ–$\tilde{\alpha}$ parameter plane. In agreement with the results obtained by King and Tuck [42] (who used a Powell method using the routine CO5NBF from the NAG library to solve the set of algebraic equations), we find that there are no solutions when $\tilde{\alpha} > 0.46$, two solutions when $0.08 < \tilde{\alpha} < 0.46$ (an upper and lower branch meeting at the point

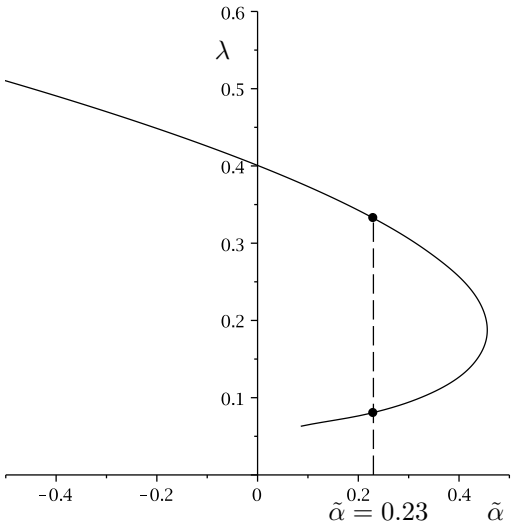

Figure 1.7: The strength of the external airflow λ plotted as a function of the ratio of substrate inclination to downstream contact angle $\tilde{\alpha}$. On the lower branch, the solution could no longer be computed to two-decimal-place accuracy for $\tilde{\alpha} < 0.08$. The dots indicate the two points at which $\tilde{\alpha} = 0.23$, and the free surface profiles at these points are shown in Figure 1.8.

$(\tilde{\alpha}, \lambda) = (0.46, 0.19)$), and one solution when $0 \leq \tilde{\alpha} \leq 0.08$. King and Tuck [42] considered only $\tilde{\alpha} \geq 0$; however, we slightly extend their results to find that the upper branch in Figure 1.7 extends to large, negative values of $\tilde{\alpha}$, with λ increasing monotonically as $\tilde{\alpha}$ becomes increasingly negative. Physically, this corresponds to a negative value of the substrate inclination α such that the airflow is blowing down the substrate in cooperation with gravity (rather than up the substrate against gravity). We measured the accuracy of the numerical results by checking that the boundary condition $h(0) = 0$ was satisfied to within a prescribed tolerance, while King and Tuck [42] performed iterations on an initial guess of a linear function until it converged to within a prescribed tolerance. On the lower branch, like King and Tuck [42], it was found that the boundary condition $h(0) = 0$ condition could no longer be satisfied to at least two-decimal-place accuracy when $\tilde{\alpha} < 0.08$. Figure 1.8 shows the two possible solutions for the free surface profile when $\tilde{\alpha} = 0.23$.

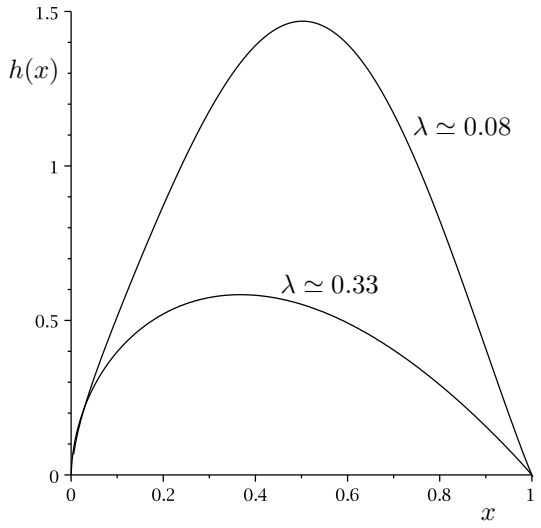

Figure 1.8: Plots of the two possible free surface profiles $h(x)$ when $\tilde{\alpha} = 0.23$, for which $\lambda \simeq 0.08, 0.33$.

1.4 Gravity-Driven Rivulet Flow

In Chapter 3 we will consider the steady, gravity-driven draining of a rivulet with either pinned or de-pinned contact lines. Hence in Subsection 1.4.1 we discuss relevant previous work on gravity-driven rivulet flow, and in Subsection 1.4.2, to introduce key concepts that will be used in Chapter 3, we summarise the main results of Duffy and Moffatt [23] and Wilson and Duffy [107], both of whom considered gravity-driven rivulet flow on a slowly varying substrate. In Subsection 1.4.3 we describe a possible area of application for the types of flow considered in this Section, namely the flow of falling films often observed in horizontal-tube evaporators.

1.4.1 Literature Review

The draining of a gravity-driven rivulet of fluid is a fundamental fluid mechanics problem which has received considerable theoretical and experimental attention. Early work on the subject was undertaken by Towell and Rothfeld [96] who studied

steady, unidirectional flow on an inclined substrate and found good agreement with their own experiments, by Allen and Biggin [4] who used the lubrication approximation to obtain an expression for the velocity profile of the same problem, and by Bentwich et al. [6] who extended this work by relaxing the condition of small contact angles required in lubrication theory.

There are situations in which a continuous film may split into one or more rivulets. A continuous film draining down a vertical substrate was studied by Hartley and Murgatroyd [33] who considered the critical flow rate required to re-wet a dry patch that appears in the film, by Mikielewicz and Moszynski [58] who considered the minimum possible thickness that the film may take before break-up occurs, and by El-Genk and Saber [27] who used a minimum total energy argument to predict when a film will break up, a stable dry patch will form and a dry patch will re-wet, and found good agreement with experiments. Johnson et al. [40] conducted an experiment that showed a film with constant volume flux breaking into a series of rivulets at the leading edge, the exact shape of these rivulets depending on the inclination of the substrate to the horizontal, as shown in Figure 1.9. More recently, Zhang et al. [115] observed complete film flow, the formation of dry patches and the formation of rivulets while studying fluid draining in a falling film microreactor.

There are several different flow regimes for a rivulet draining down an inclined substrate. Schmuki and Laso [82] conducted an experiment in which a jet of fluid drained down an inclined substrate for a range of flow rates, angles of substrate inclination, surface tension and fluid viscosity, and found five regimes of flow, namely film flow, droplet flow, a linear rivulet, a meandering rivulet and an oscillating rivulet, as shown in Figure 1.10. In a similar study, but restricted to a single type of fluid on a single substrate, Nakagwa [65] found droplet flow, a meandering rivulet, an oscillating rivulet and also a braided rivulet, where the latter regime is

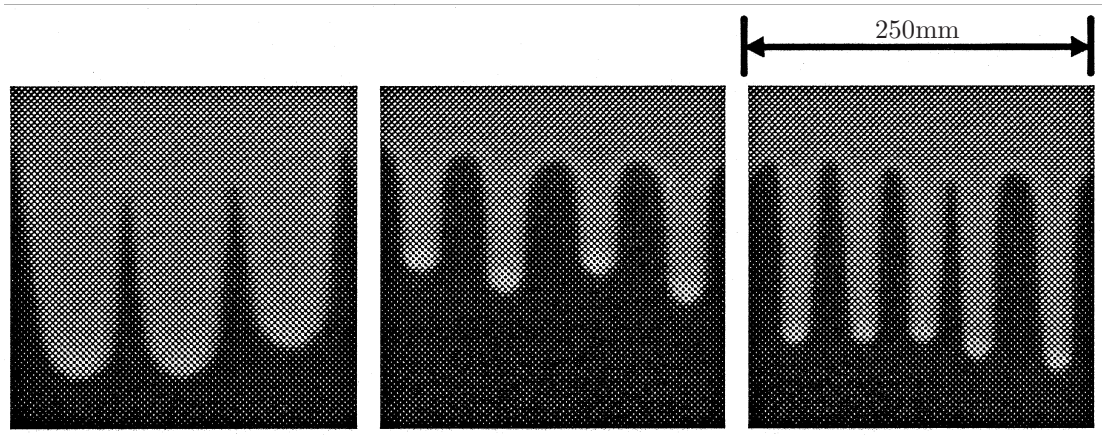

Figure 1.9: Images of a film breaking into a series of rivulets, found by Johnson et al. [40]. The substrate inclination increases from left to right. Reprinted from Johnson et al. [40] with permission of Cambridge University Press.

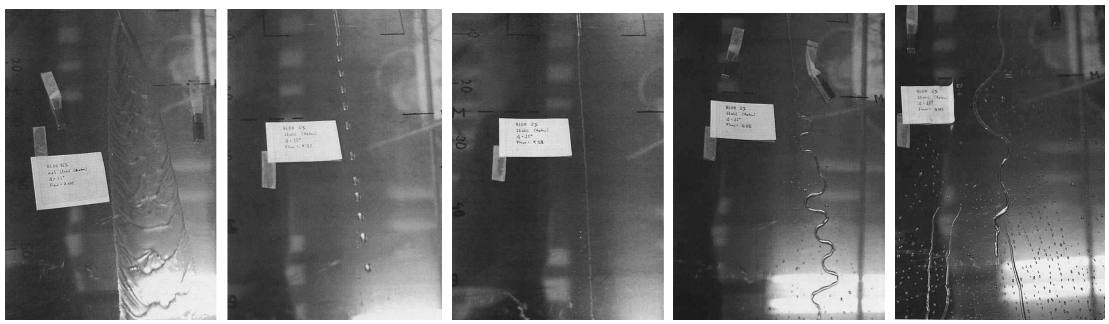

Figure 1.10: Images of the five regimes of flow found by Schmuki and Laso [82], namely, from left to right, film flow, droplet flow, a linear rivulet, a meandering rivulet and an oscillating rivulet. Reprinted from Schmuki and Laso [82] with permission of Cambridge University Press.

characterised by a rivulet whose width periodically increases and decreases. This built on earlier work by Nakagwa and Scott [66], who had observed the meandering and oscillating regimes in their experiments. A model which predicts a braided regime of rivulet flow draining down an inclined substrate when the flow rate is constant was developed by Mertens, Putkaradze and Vorobieff [57] and was also realised in experiments (shown in Figure 1.11), and it is stated that this regime is thought to be a consequence of a combination of surface tension tending to decrease the rivulet width and inertia tending to increase the rivulet width. Birnir

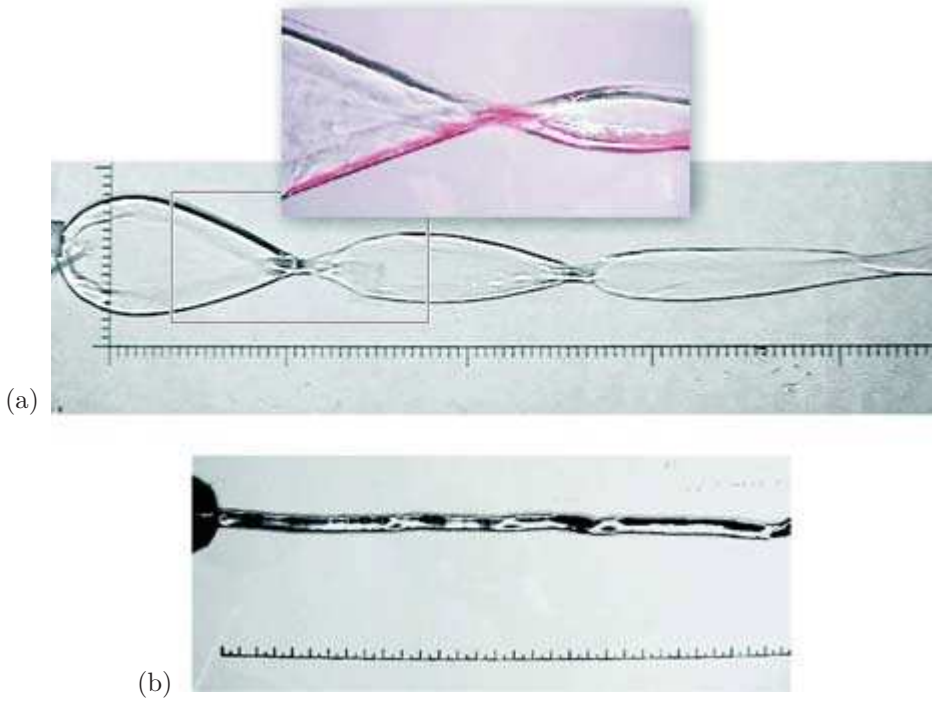

Figure 1.11: Images obtained by Mertens, Putkaradze and Vorobieff [57] of (a) a braided rivulet and (b) a linear rivulet, where the flow is from left to right (as is the downward direction of the substrate), and both the substrate inclination and the flow rate are greater in (a) than in (b). Reprinted from Mertens, Putkaradze and Vorobieff [57] with permission of Cambridge University Press.

et al. [7, 8] subsequently developed a model for a meandering regime of rivulet flow and claimed that the meanders are triggered by small fluctuations in flow rate. The mechanism behind the meandering regime is, however, still not well understood. In their experiments, Le Grand-Piteira, Daerr and Limat [64] observed rivulet meandering with a constant flow rate but reported that the critical flow rate required for the onset of meandering increases as the fluid viscosity increases, while recently, Couvreur and Daerr [13] suggest that the most important factor in the emergence of rivulet meanders is the heterogeneities of the substrate.

In Chapters 3 and 4 we will consider slowly varying rivulets on a slowly varying substrate. Duffy and Moffatt [23], using the solution for the flow of a thin rivulet with constant, non-zero contact angle and prescribed volume flux, but slowly vary-

ing width, down a locally planar, slowly varying substrate, interpreted the solution in terms of the flow in the azimuthal direction from the top to the bottom of a large horizontal cylinder. They found that the rivulet becomes wide and flat near the top of the cylinder but narrow and deep near the bottom of the cylinder. This work has been extended by Wilson and Duffy [105] to consider a rivulet draining down a locally non-planar, slowly varying substrate for a variety of convex and concave transverse substrate profiles, by Holland, Wilson and Duffy [35] to consider a rivulet which is uniformly hotter or uniformly colder than the surrounding atmosphere, by Wilson, Duffy and Ross [111] to consider a viscoplastic fluid, and by Wilson and Duffy [106] to consider a temperature-dependent-viscosity.

All of the studies mentioned above concern a rivulet with non-zero contact angle (that is, a rivulet of partially wetting fluid); however, the flow of a rivulet with zero contact angle (that is, a rivulet of perfectly wetting fluid) has also received attention. Wilson and Duffy [107] considered the unidirectional flow of a thin rivulet with zero contact angle and prescribed volume flux, but slowly varying width, down a slowly varying locally planar or locally non-planar substrate. In the case of a locally planar substrate, again interpreted as the flow from the top to the bottom of a large horizontal cylinder, Wilson and Duffy [107] found that no solution exists on the upper half of the cylinder but that there are infinitely many solutions on the lower half of the cylinder. This work has been extended by Duffy and Wilson [24] to consider a temperature-dependent-viscosity, by Wilson and Duffy [109] to consider when it is energetically favourable for the rivulet to split into two or more sub-rivulets, and by Sullivan, Wilson and Duffy [91] to consider the effects of a uniform longitudinal surface shear stress (which we will discuss in more detail in Subsection 1.5.3). Other studies of rivulets of perfectly wetting fluid have been undertaken by Kuibin [45] and Alekseenko, Geshev and Kuibin [3], who studied the draining of a pendent rivulet on the underside of

an inclined cylinder. The theoretical studies mentioned above concern a rivulet with a constant zero or non-zero contact angle, but variable width; however, in Chapters 3 and 4 we will also consider a rivulet with constant width. Exact solutions of the Navier–Stokes equations were found by Perazzo and Gratton [74] for a sessile rivulet with constant width draining down an inclined, planar substrate and these solutions were found to compare favourably with those obtained from lubrication theory. This work was extended to both sessile and pendent rivulets on an inclined, non-planar substrate by Tanasijczuk, Perazzo and Gratton [92]. Benilov [5] found that a "narrow" sessile or pendent rivulet with constant width draining down an inclined substrate is always stable, but that a "wide" rivulet requires the incline to be sufficiently steep to ensure stability, and Alekseenko et al. [2] experimentally studied the existence of surface waves on a rivulet draining down a vertical substrate.

1.4.2 Rivulet flow on a slowly varying substrate

In this Subsection, to introduce the key concepts that will be used later, we study the gravity-driven draining of a rivulet with constant contact angle down a substrate inclined to the horizontal and, in doing so, we re-visit the analysis of Duffy and Moffatt [23] (who considered a non-zero contact angle) and Wilson and Duffy [107] (who considered a zero contact angle). The results are interpreted as the flow of a rivulet on a slowly varying substrate, specifically the flow in the azimuthal direction from the top to the bottom of a large horizontal cylinder. We note that the analogous two-dimensional case of a thin film draining from the top to the bottom of a cylinder has received much attention from various authors, building on the early work undertaken by Nusselt [68, 69].

Consider the steady three-dimensional gravity-driven draining of a symmetric rivulet with constant volume flux Q on a planar substrate inclined at an angle

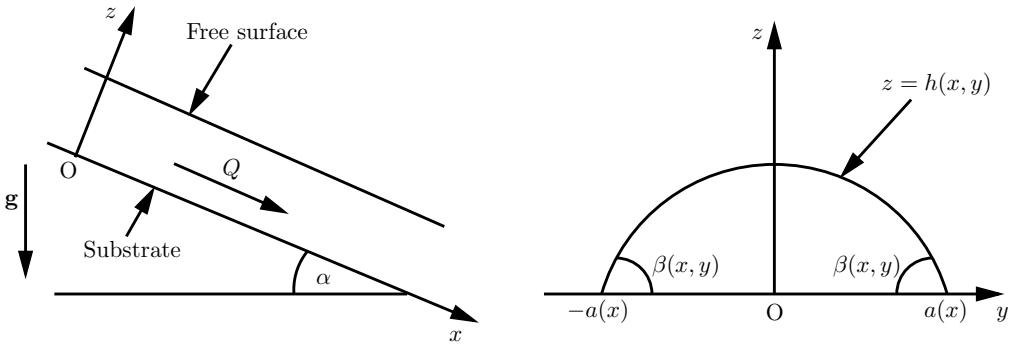

Figure 1.12: Sketch of a thin rivulet draining down a planar substrate inclined at an angle α to the horizontal.

α ($0 \leq \alpha \leq \pi$) to the horizontal, as shown in Figure 1.12. We use Cartesian coordinates $Oxyz$ with the x axis down the line of greatest slope, the y axis horizontal, and the z axis normal to the substrate $z = 0$. The rivulet has velocity $\mathbf{u} = (u, v, w)$ and pressure p. We assume that the fluid is Newtonian with constant viscosity μ, density ρ and coefficient of surface tension σ. The free surface is at $z = h$, where $h = h(x, y)$ is the thickness of the rivulet, the contact angle is denoted by $\beta = \beta(x, y)$, the semi-width by $a = a(x)$ (so that $h = 0$ at the contact lines $y = \pm a$), and the maximum thickness of the rivulet, which always occurs at $y = 0$, by $h_{\mathrm{m}} = h(0)$.

In particular we consider a thin rivulet with $\beta \ll 1$ such that the thickness of the rivulet is much smaller than its width and introduce the following non-dimensionalised and scaled variables:

$$\begin{gathered} x = Lx^*, \quad y = \epsilon L y^*, \quad z = \epsilon\delta L z^*, \quad a = \epsilon L a^*, \quad \beta = \delta\beta^*, \quad h = \epsilon\delta L h^*, \\ u = \frac{\epsilon^2\delta^2\rho g L^2}{\mu}u^*, \quad v = \frac{\epsilon^3\delta^2\rho g L^2}{\mu}v^*, \quad w = \frac{\epsilon^3\delta^3\rho g L^2}{\mu}w^*, \\ p - p_\infty = \epsilon\delta\rho g L p^*, \quad Q = \frac{\epsilon^4\delta^3\rho g L^4}{\mu}Q^*, \end{gathered} \tag{1.63}$$

where p_∞ is the ambient pressure, L is a typical length scale in the longitudinal (i.e. in the x) direction, $\delta \ll 1$ is the transverse aspect ratio and $\epsilon \ll 1$ is the longitudinal aspect ratio. For clarity, we immediately drop the star superscripts on

non-dimensional variables; then the Navier–Stokes and mass-conservation equations (1.3) and (1.4) become

$$\begin{gathered} Re^*\left(uu_x + vu_y + wu_z\right) = -\epsilon\delta p_x + \sin\alpha + \left(\epsilon^2\delta^2 u_{xx} + \delta^2 u_{yy} + u_{zz}\right), \\ \epsilon Re^*\left(uv_x + vv_y + wv_z\right) = -\delta p_y + \epsilon\left(\epsilon^2\delta^2 u_{xx} + \delta^2 u_{yy} + u_{zz}\right), \\ \epsilon\delta Re^*\left(uw_x + vw_y + ww_z\right) = -p_z - \cos\alpha + \epsilon\delta\left(\epsilon^2\delta^2 u_{xx} + \delta^2 u_{yy} + u_{zz}\right), \\ u_x + v_y + w_z = 0, \end{gathered} \tag{1.64}$$

where

$$Re^* = \frac{\epsilon^4\delta^4\rho^2 g L^3}{\mu^2} \tag{1.65}$$

is a suitably defined reduced Reynolds number. Assuming that $Re^* \ll 1$ is sufficiently small then at leading order in δ and ϵ (1.64) reduces to

$$0 = \sin\alpha + u_{zz}, \quad 0 = -\delta p_y + \epsilon v_{zz}, \quad 0 = -p_z - \cos\alpha, \quad u_x + v_y + w_z = 0. \tag{1.66}$$

We consider the particular case $\epsilon \ll \delta \ll 1$, corresponding to locally unidirectional flow on a slowly varying substrate, so that (1.66b) becomes $p_y = 0$. The special case $\epsilon = O(\delta)$ is possible; however, it would require rather specific parameter values and is not considered here.

The governing equations are to be solved subject to conditions of no slip, $u = 0$, at the substrate $z = 0$, and balances of normal and tangential stress, $p = -C^{-1}h''$ (from (1.20)) and $u_z = 0$ (from (1.21)), respectively, at the free surface $z = h$, where $C = \rho g\epsilon^2 L^2/\sigma$ is the dimensionless capillary number. This differs from the capillary number defined in Section 1.2 by a factor of ϵ^3: this is because in (1.12) we use the governing equations for thin-film flow to determine the pressure scale, but in (1.63) we instead use the normal stress balance at the free surface. We define the capillary length $\ell = (\sigma/\rho g)^{1/2}$ and then set $\epsilon = \ell/L$ so that $C = 1$, without loss of generality. At the edges of the rivulet $y = \pm a$ we have conditions of zero thickness $h = 0$ with contact angle $h' = \mp\beta$. Solving (1.66) with $\epsilon \ll \delta$

subject to the boundary conditions for the pressure and the velocity gives

$$p = (h - z)\cos\alpha - h'', \quad u = \frac{\sin\alpha}{2}\left(2hz - z^2\right), \tag{1.67}$$

while the local longitudinal flux $\bar{u} = \bar{u}(y)$ is given by

$$\bar{u} = \int_0^h u \, \mathrm{d}z = \frac{\sin\alpha}{3} h^3, \tag{1.68}$$

and therefore the volume flux Q is given by

$$Q = \int_{-a}^{+a} \bar{u} \, \mathrm{d}y = \frac{\sin\alpha}{3} \int_{-a}^{+a} h^3 \, \mathrm{d}y. \tag{1.69}$$

Also, we use (1.67) together with the fact that $p_y = 0$ to obtain a third-order ordinary differential equation for the free surface profile, namely

$$(h\cos\alpha - h'')' = 0, \tag{1.70}$$

which is to be solved subject to the contact-line conditions. Then for a prescribed constant volume flux $Q = \bar{Q}$, constant angle of inclination α and constant contact angle $\beta = \bar{\beta}$, (1.69) together with the solution of (1.70) provides an implicit equation to be solved for the unknown semi-width a. We use this solution to describe the locally unidirectional flow down a slowly varying substrate, specifically the flow in the azimuthal direction from the top $\alpha = 0$ to the bottom $\alpha = \pi$ of a large horizontal cylinder, of a rivulet with constant contact angle $\beta = \bar{\beta}$ but slowly varying semi-width $a = a(\alpha)$, in both the case $\bar{\beta} = 0$ and the case $\bar{\beta} > 0$.

1.4.2.1 The special case of zero contact angle $\bar{\beta} = 0$ (Wilson and Duffy [107])

In the special case of zero contact angle $\bar{\beta} = 0$ (that is, the fluid wets the substrate perfectly) there are several possible definitions of δ. For example, $\delta = (\mu\bar{Q}/\rho g L^4)^{1/3}$ corresponds to setting $\bar{Q} = 1$; however, to keep the presentation as

general as possible we leave δ unspecified in what follows. We solve (1.69) and (1.70) for a and h subject to the conditions

$$h = 0, \quad h' = 0 \quad \text{at} \quad y = \pm a. \tag{1.71}$$

There are no solutions corresponding to a sessile rivulet or a rivulet on a vertical substrate (i.e. for $0 \leq \alpha \leq \pi/2$) but for pendent rivulets (i.e. for $\pi/2 < \alpha \leq \pi$) we obtain infinitely many solutions, namely

$$a = \frac{n\pi}{m} \quad \text{and} \quad h = \frac{h_{\mathrm{m}}}{2}\left(1 - (-1)^n \cos my\right) \tag{1.72}$$

for $n = 1, 2, 3, ...$, where we have written $m = |\cos\alpha|^{1/2}$. The maximum thickness of the rivulet, $h_{\mathrm{m}} = h(0)$, is given by

$$h_{\mathrm{m}} = 2\left(\frac{3\bar{Q}m}{5n\pi\sin\alpha}\right)^{\frac{1}{3}}. \tag{1.73}$$

Equations (1.72) and (1.73) show that the semi-width a does not depend on the prescribed flux $\bar{Q}$, but that the film thickness behaves according to $h \propto \bar{Q}^{1/3}$. All of these solutions are physically realisable; however, the higher-branch solutions $n = 2, 3, ...$ are simply re-scaled versions of the lowest-branch solution $n = 1$. We therefore choose $n = 1$ without loss of generality in what follows. Figures 1.13(a) and 1.13(b) show the scaled semi-width a/π and the maximum thickness h_{m} as functions of the scaled angle of inclination α/π, and Figure 1.13(c) shows cross-sectional free surface profiles h for various values of α, all when $\bar{Q} = 1$. The rivulet becomes wide and slender near the middle $\alpha = \pi/2$ of the cylinder, while it becomes deep with finite width near the bottom $\alpha = \pi$ of the cylinder.

1.4.2.2 The general case of non-zero contact angle $\bar{\beta} > 0$ (Duffy and Moffatt [23])

In the general case of non-zero contact angle $\bar{\beta} > 0$ (that is, the fluid is non-perfectly wetting) we may choose $\delta = \beta$ in (1.63) so that $\bar{\beta} = 1$ without loss of

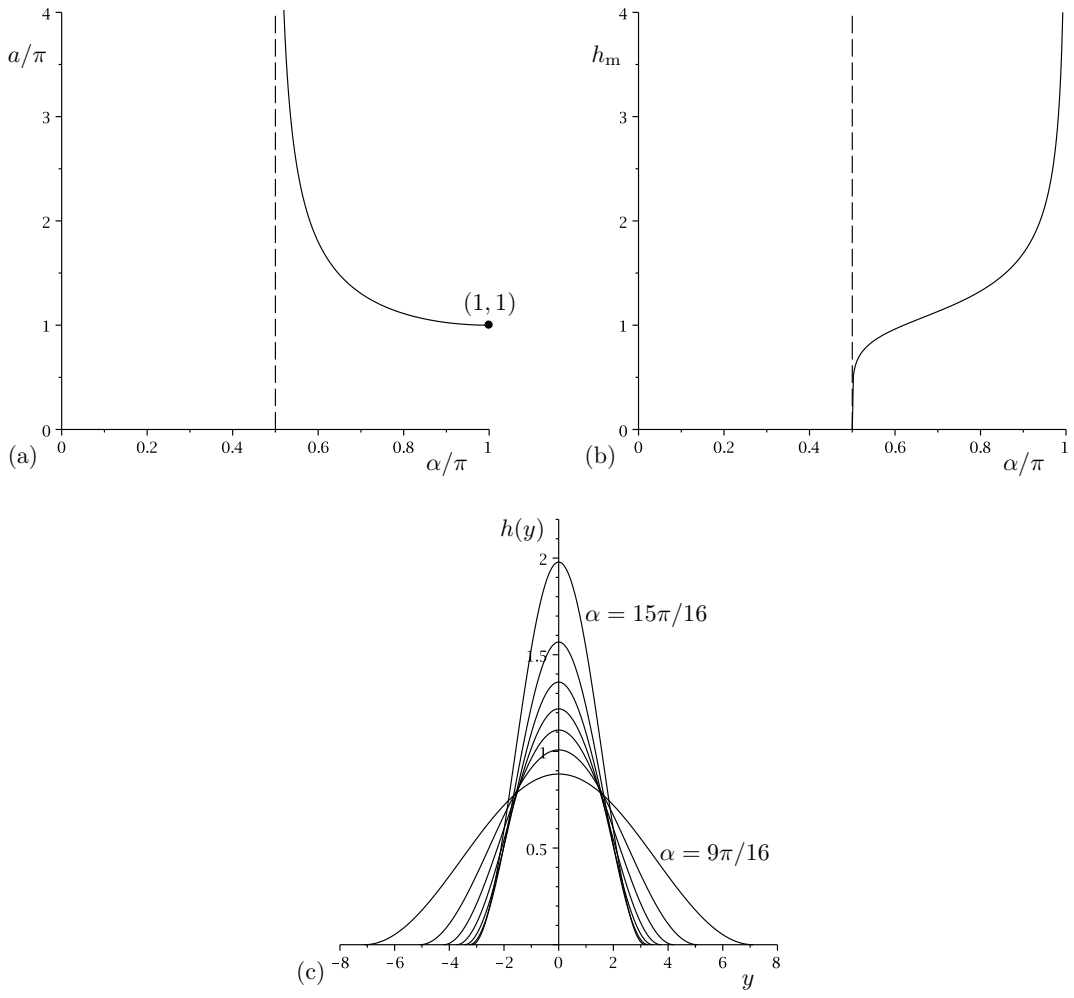

Figure 1.13: Plots of (a) the scaled semi-width $a/\pi = 1/m$ and (b) the maximum thickness $h_{\rm m}$ as functions of α/π, and (c) cross-sectional free surface profiles, $z = h(y)$, at $\alpha = 9\pi/16, 5\pi/8, 11\pi/16, ..., 15\pi/16$, all when $\bar{Q} = 1$, for a rivulet of perfectly wetting fluid.

generality. We solve (1.69) and (1.70) for a and h subject to the conditions

$$h = 0, \quad h' = \mp 1 \quad \text{at} \quad y = \pm a \tag{1.74}$$

to obtain the free surface shape

$$h = \begin{cases} \dfrac{\cosh ma - \cosh my}{m \sinh ma} & \text{for} \quad 0 \le \alpha < \dfrac{\pi}{2}, \\ \dfrac{a^2 - y^2}{2a} & \text{for} \quad \alpha = \dfrac{\pi}{2}, \\ \dfrac{\cos my - \cos ma}{m \sin ma} & \text{for} \quad \dfrac{\pi}{2} < \alpha \le \pi, \end{cases} \tag{1.75}$$

the maximum thickness of the rivulet

$$h_{\mathrm{m}} = \frac{1}{m} \begin{cases} \tanh \dfrac{ma}{2} & \text{for} \quad 0 \le \alpha < \dfrac{\pi}{2}, \\ \dfrac{ma}{2} & \text{for} \quad \alpha = \dfrac{\pi}{2}, \\ \tan \dfrac{ma}{2} & \text{for} \quad \dfrac{\pi}{2} < \alpha \le \pi, \end{cases} \tag{1.76}$$

and the volume flux

$$\bar{Q} = \frac{\sin \alpha}{9m^4} f(ma), \tag{1.77}$$

where the function $f = f(ma)$ appearing in (1.77) is given by

$$f(ma) = \begin{cases} 15ma \coth^3 ma - 15 \coth^2 ma - 9ma \coth ma + 4 & \text{for} \quad 0 \le \alpha < \dfrac{\pi}{2}, \\ \dfrac{12}{35}(ma)^4 & \text{for} \quad \alpha = \dfrac{\pi}{2}, \\ -15ma \cot^3 ma + 15 \cot^2 ma - 9ma \cot ma + 4 & \text{for} \quad \dfrac{\pi}{2} < \alpha \le \pi. \end{cases} \tag{1.78}$$

Note that, unlike in the case when $\bar{\beta} = 0$, solutions for both sessile and pendent rivulets exist (that is, solutions exist for any α, $0 \le \alpha \le \pi$). Figures 1.14(a) and 1.14(b) show the semi-width a and the maximum thickness h_{m} as functions of the scaled angle of inclination α/π for various values of $\bar{Q}$, and Figure 1.14(c) shows cross-sectional free surface profiles h for various values of α when $\bar{Q} = 1$. The rivulet becomes wide with finite thickness near the top $\alpha = 0$ of the cylinder, while it becomes deep with finite width near the bottom $\alpha = \pi$ of the cylinder.

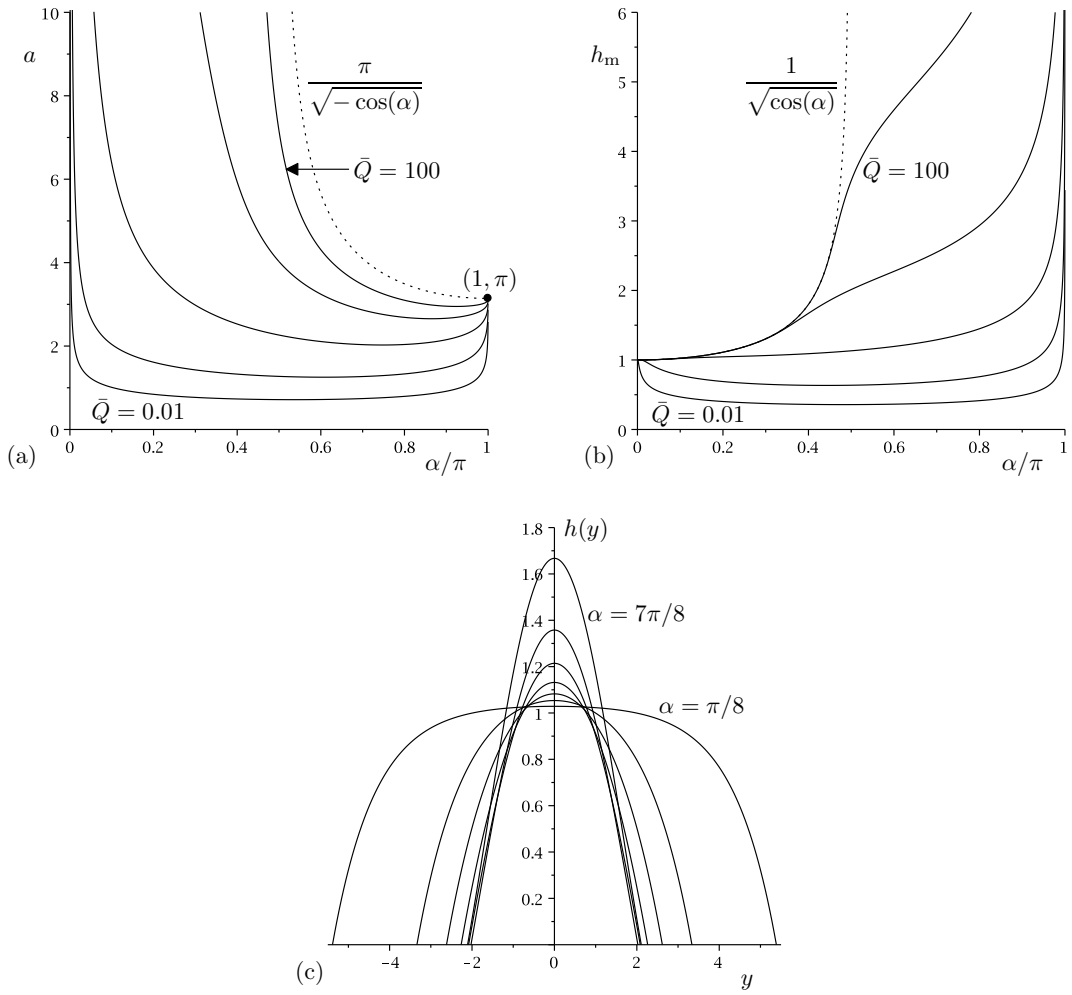

Figure 1.14: Plots of (a) the semi-width a and (b) the maximum thickness h_{m} as functions of α/π for $\bar{Q} = 0.01, 0.1, 1, 10, 100$, and (c) cross-sectional free surface profiles, $z = h(y)$, for $\alpha = \pi/8, \pi/4, 3\pi/8, ..., 7\pi/8$ when $\bar{Q} = 1$, for a non-perfectly wetting rivulet.

1.4.3 Breakup of falling films into rivulets

A practical situation in which a rivulet flowing round the outside of a cylinder may arise is in falling-film horizontal-tube evaporators used in a variety of industries such as refrigeration, desalination and petroleum refining. The review article on falling film evaporation by Ribatski and Jacobi [77] describes how partial film dry-out may occur because of an uneven distribution of fluid on the tubes. This may be caused by a gas flow within the evaporator or uneven draining of fluid from one tube onto the one below in a bundle of horizontal tubes. This regime of partial dry-out causes the breakdown of continuous film flow, and this is where rivulet flow is likely to occur (see, for example, Johnson et al. [40]). The fluid that falls from the bottom of one cylinder onto the top of the one below may take the form of an unbroken sheet, a series of continuous, equally-spaced columns, or drops that detach intermittently. Mitrovic [59] presented experimental results for some of these modes of fluid flow across horizontal cylinders and summarised the predictions available in the literature for the transition from one mode to another in terms of a suitably defined Reynolds number. When the fluid drains from one cylinder onto the one below in a series of equally-spaced columns, each column of fluid may then flow round the cylinder circumference as a single rivulet before draining off the bottom of the tube, again as a column, as shown in Figure 1.15. Fujita and Tsutsui [32] experimentally found that the flow rate of a falling film over a bundle of heated horizontal tubes decreases on the lower tubes leading to dry patches appearing in the film, with the formation of rivulets most likely in regions of severe dry-out, that is, on the lower tubes. In falling-film heat exchangers there is often a flow of gas present, which acts in the direction opposite to that of the fluid flow. The effect this has on the fluid flow may be of importance and was studied experimentally by Ruan, Jacobi and Li [79]. The flow of both a two-dimensional sheet of fluid, and a three-dimensional, single column of fluid, falling onto the top

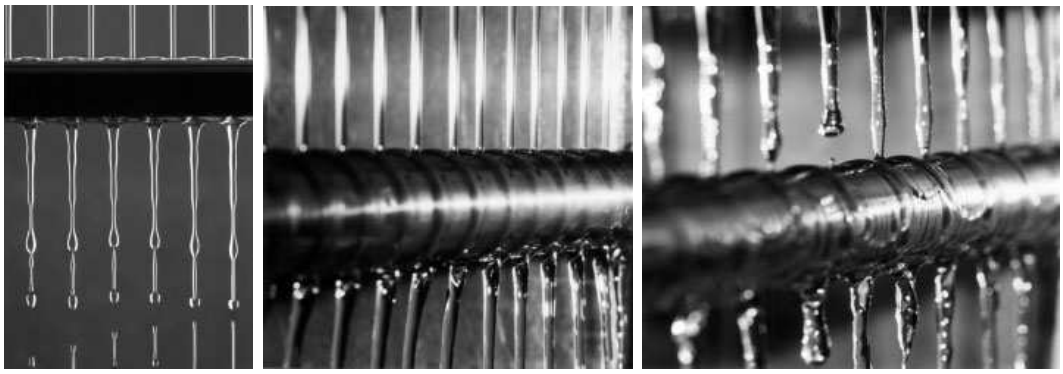

Figure 1.15: Images of columns of fluid falling onto the top of a horizontal cylinder and then draining round the circumference as a series of rivulets, found by Mitrovic [59]. Reprinted from Mitrovic [59] with permission from John Wiley and Sons.

of, and draining round to the bottom of, a horizontal cylinder has been studied numerically by Hunt [37, 38], respectively, and in the three-dimensional case, the fluid on the top of the cylinder spreads along the top to a finite distance away from the column.

1.5 Rivulets Subject to an External Airflow

In Chapter 4 we extend the analysis for a gravity-driven rivulet to include a uniform longitudinal surface shear stress due to an external airflow at the free surface of a rivulet. Hence in Subsection 1.5.1 we discuss some previous work on rivulets subject to an external airflow, and in Subsections 1.5.2 and 1.5.3, to introduce the key concepts that will be used later, we re-visit the analysis of Wilson and Duffy [108] and Sullivan, Wilson and Duffy [91], respectively. In Subsection 1.5.4 we reproduce the results of Sullivan et al. [90] (of which I am an author) in somewhat greater detail. We outline the improved numerical method from that used in Sullivan's [89] thesis to consider the same problem, together with the more accurate numerical results. Specifically, the improved numerical results were calculated using a shooting method rather than the finite differences used by Sullivan [89].

1.5.1 Literature Review

Understanding of the flow of a rivulet in the presence of an external airflow is of importance in many industrial contexts such as distillation, coating processes and heat exchangers. Accordingly, these flows have received attention from a variety of authors. Wilson, Duffy and Hunt [110] used lubrication theory to obtain similarity solutions for a rivulet of non-Newtonian fluid flowing down an inclined substrate subject to a uniform longitudinal shear stress acting down the substrate in both the case of weak surface tension and strong surface tension. Myers, Liang and Wetton [63] also used lubrication theory to study the flow of a rivulet on an inclined substrate subject to a uniform longitudinal shear stress acting up the substrate, obtaining expressions for the pressure, velocity and free surface profile in terms of powers of the (small) aspect ratio. These were then compared to numerical results for any contact angle and good agreement was found between the theoretical and

numerical results for contact angles up to 30 degrees. Wilson and Duffy [108] studied the flow of a rivulet with constant non-zero contact angle on a vertical substrate subject to a uniform longitudinal shear stress acting up or down the substrate and found that the conjecture by Myers, Liang and Wetton [63] that it is never energetically favourable for a purely shear-stress-driven rivulet to split is *not* correct. Wilson and Duffy [108] also found that there are five possible flow patterns that the rivulet may take, and the same five flow patterns were found to be the only possibilities by Sullivan, Wilson and Duffy [91] for a pendent rivulet with zero contact angle on a slowly varying substrate, again subject to a uniform longitudinal shear stress acting up or down the substrate. Sullivan et al. [90] studied both a gravity-driven rivulet on a vertical substrate and a rivulet on a horizontal substrate driven by a longitudinal shear stress, subject to a constant transverse shear stress, and considered the cases when both contact lines are pinned and when one or both contact lines de-pin. Luo et al. [51, 52] conducted experiments of a rivulet flowing down an inclined channel in the presence of an airflow blowing up the channel and found that increasing the flow rate, decreasing the strength of the airflow, or decreasing the inclination of the channel, increases the rivulet width.

The formation of one or more rivulets resulting from the break-up of a thin film that is subject to an external airflow has also received attention. Lopez, Miksis and Bankoff [50] extended lubrication theory to include inertial terms to study a thin film on an inclined substrate driven by a uniform shear stress which breaks up into a series of rivulets with constant width, and found that the predicted wavelength of the instability at the leading edge of the film compared well with experiments, especially in the case of large angles of substrate inclination and low flow rates. Eres, Schwartz and Roy [28] carried out numerical simulations of a thin film driven by shear stress that is perturbed at its leading edge such that rivulets form in the cases of a perfectly wetting and a non-perfectly wetting fluid. In the

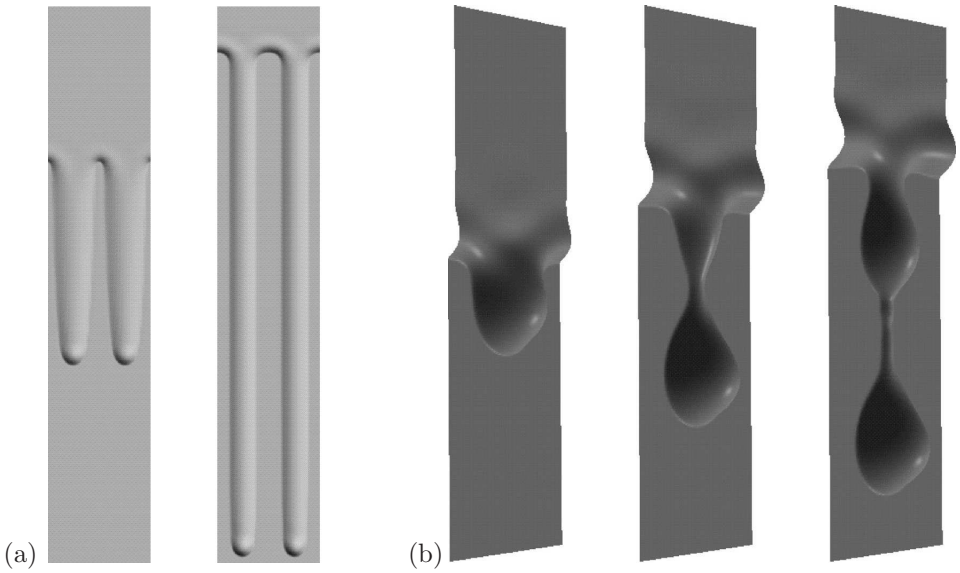

Figure 1.16: Numerical simulations of (a) a film that breaks into steady wedge-shaped rivulets (on the left) and continually-growing constant width rivulets (on the right), and (b) a film that breaks into distinct droplets, computed by Eres, Schwartz and Roy [28]. Reprinted with permission from Eres, Schwartz and Roy [28], copyright 2000, American Institute of Physics.

perfectly wetting case and the case of small, non-zero contact angles, the rivulets are wedge-shaped, for larger contact angles the rivulets have constant width, and for contact angles that are larger still the rivulets break up into distinct droplets, as shown in Figure 1.16. Saber and El-Genk [80] studied a film on an inclined or a vertical substrate subject to gravity and a non-uniform shear stress acting up or down the substrate, and predicted the minimum thickness of the film before break-up occurs. Increasing the strength of a shear stress directed down the substrate decreases the minimum thickness whereas increasing the strength of a shear stress directed up the substrate (while the flow remains downwards everywhere) increases the minimum thickness. Recently, Wilson, Sullivan and Duffy [113] used an energy argument similar to that used by authors such as Mikielewicz and Moszynski [58] and El-Genk and Saber [27] in the case of a purely gravity-driven film to determine when it is favourable for either a film or a rivulet, both flowing on a vertical substrate subject to a uniform longitudinal shear stress acting up or down the

substrate, to break up into a series of rivulets, or into one or more sub-rivulets, respectively. As in the purely gravity-driven case, there is a minimum thickness below which it is energetically favourable for a film to break up, and there is a maximum thickness above which it is energetically favourable for a single rivulet to break up.

1.5.2 A rivulet of non-perfectly wetting fluid on a vertical substrate subject to a uniform longitudinal surface shear stress (Wilson and Duffy [108])

In this Subsection we summarise the results of Wilson and Duffy [108] who studied the flow of a thin symmetric rivulet with constant non-zero contact angle on a vertical substrate subject to a longitudinal surface shear stress τ (nondimensionalised with $\delta\sigma/\ell$), where $\tau > 0$ corresponds to the shear acting down the substrate. This situation is described by (1.66) with $\alpha = \pi/2$ and $\epsilon \ll \delta \ll 1$ subject to no slip at the substrate and the normal stress balance as before, but with the tangential stress balance now given by

$$u_z = \tau \quad \text{at} \quad z = h. \tag{1.79}$$

As in Subsection 1.4.2.2 we set $\delta = \beta$ so that the contact-line conditions are given by (1.74), and we obtain

$$\begin{gathered} p = -h'', \quad u = \frac{(2h - z)z}{2} + \tau z, \quad u_{\text{fs}} = \frac{h^2}{2} + \tau h, \\ h = \frac{a^2 - y^2}{2a}, \quad h_{\text{m}} = \frac{a}{2}, \quad Q = \frac{4a^4}{105} + \frac{2\tau a^3}{15}, \end{gathered} \tag{1.80}$$

where $u_{\text{fs}} = u_{\text{fs}}(y) = u(y, h)$ is the velocity at the free surface. Inspection of (1.80) reveals that for $\tau \geq 0$, the flux Q is an increasing function of the semi-width a but that for $\tau \leq 0$, there exists a minimum value of the flux $Q = Q_{\min}$ at $a = a_{\min}$,

where

$$Q_{\min} = -\frac{3087\tau^4}{5120} < 0 \quad \text{and} \quad a_{\min} = -\frac{21\tau}{8}. \tag{1.81}$$

Also, note that $Q = 0$ when $a = a_0 = -7\tau/2$ (provided that $\tau < 0$).

All of the possible cross-sectional flow patterns that can occur may be categorised into five types which we denote as type I to type V. Figure 1.17 shows sketches of these five different types of flow pattern; regions of downwards flow (that is, regions with $u > 0$) are shaded and regions of upwards flow (that is, regions with $u < 0$) are unshaded. The locations of the maximum and minimum velocities are marked with dots. From (1.80) the free surface velocity at $y = 0$ (i.e. the velocity at $z = h_{\mathrm{m}}$) is given by

$$u_{\mathrm{fs}}(0) = \frac{h_{\mathrm{m}}^2}{2} + \tau h_{\mathrm{m}}. \tag{1.82}$$

When $\tau \geq 0$ the shear stress acts in co-operation with gravity to ensure that the velocity is downwards throughout the rivulet (type-I flow). The maximum velocity $u = u_{\mathrm{fs}}(0)$ occurs on the free surface at $z = h_{\mathrm{m}}$, and the minimum velocity $u = 0$ occurs on the substrate $z = 0$.

When $\tau < 0$ the shear stress acts up the substrate in opposition to the effect of gravity, and the velocity is always upwards near the contact lines. From (1.80) the curve on which the velocity u is zero (other than at the substrate $z = 0$), denoted by $z = H(y)$, is given by

$$H = 2\left(h + \tau\right). \tag{1.83}$$

Since the rivulet occupies $0 \leq z \leq h$, (1.83) yields the condition

$$-\tau \leq h \leq -2\tau \tag{1.84}$$

for upwards flow to occur.

For $h_{\mathrm{m}} > -\tau$ the curve (1.83) meets the substrate $z = 0$ (that is, $H = 0$) when $y = \pm b$, where

$$b = \sqrt{a(a + 2\tau)}, \tag{1.85}$$

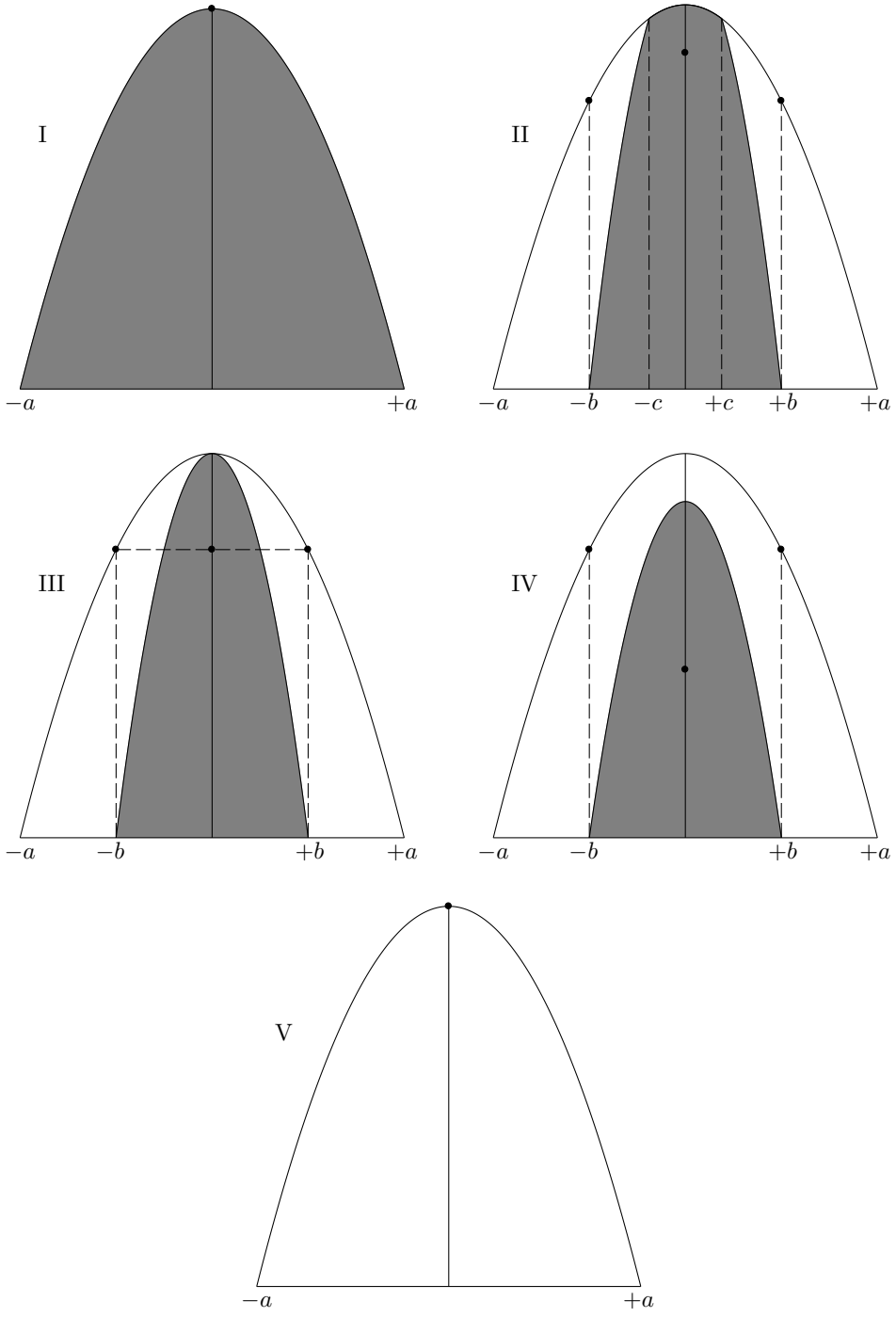

Figure 1.17: Sketches of the five different types of cross-sectional flow pattern, denoted as type I to type V. Regions of downwards flow (that is, regions with $u > 0$) are shaded and regions of upwards flow (that is, regions with $u < 0$) are unshaded. The locations of the maximum and minimum velocities are marked with dots.

and for $h_{\rm m} < -2\tau$ the curve (1.83) meets the free surface $z = h$ (that is, $H = h$) when $y = \pm c$, where

$$c = \sqrt{a(a + 4\tau)}. \tag{1.86}$$

If $H_{\rm m} > h_{\rm m}$ (where $H_{\rm m} = H(0)$) then the flow is type II, if $H_{\rm m} = h_{\rm m}$ then the flow is type III and if $0 < H_{\rm m} < h_{\rm m}$ then the flow is type IV, each of these flow types being a mixture of downwards and upwards flow. If $H_{\rm m} \leq 0$ then the flow is upwards throughout the rivulet (type-V flow). For flow-types II, III and IV the maximum velocity $u = (h_{\rm m} + \tau)^2/2$ occurs within the flow at $y = 0$, $z = H_{\rm m}/2 = h_{\rm m} + \tau$, and the minimum velocity $u = -\tau^2/2$ occurs on the free surface at $y = \pm b$, $z = -\tau$. For flow-type V the maximum velocity $u = 0$ occurs on the substrate $z = 0$, and the minimum velocity $u = u_{\rm fs}(0)$ occurs on the free surface at $y = 0$, $z = h_{\rm m}$.

For a rivulet of prescribed flux $Q = \bar{Q}$, the semi-widths a are given by the positive solutions of the flux equation in (1.80) with $Q = \bar{Q}$ and a prescribed shear stress τ. From (1.85) we deduce that for type-V flow, $a \leq -2\tau$ which gives the critical τ (i.e. at $a = -2\tau$)

$$\tau = \tau_1 = -\left(-\frac{35\bar{Q}}{16}\right)^{\frac{1}{4}}, \tag{1.87}$$

so $\bar{Q} < 0$, while from (1.86) we deduce that for type-III flow, $a = -4\tau$ which gives

$$\tau = \tau_2 = -\left(-\frac{105\bar{Q}}{128}\right)^{\frac{1}{4}}, \tag{1.88}$$

so $\bar{Q} > 0$. When $\bar{Q} < 0$, we see from (1.81) that the maximum possible shear stress $\tau = \tau_{\rm m}$, where

$$\tau_{\rm m} = -\left(-\frac{5120\bar{Q}}{3087}\right)^{\frac{1}{4}}, \tag{1.89}$$

gives $a = a_{\rm min}$. Figure 1.18 is a sketch of the τ–a parameter plane which shows when the different types of flow pattern given in Figure 1.17 occur in each of the cases $\bar{Q} > 0$, $\bar{Q} = 0$ and $\bar{Q} < 0$.

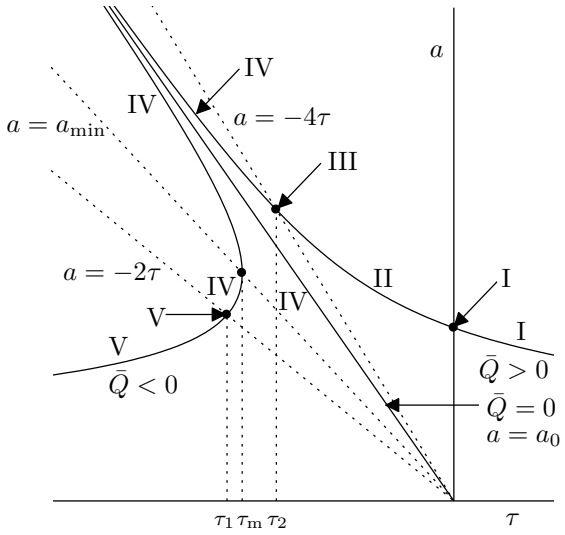

Figure 1.18: Sketch of the a–τ parameter plane showing when the different types of flow pattern given in Figure 1.17 occur in each of the cases $\bar{Q} > 0$, $\bar{Q} = 0$ and $\bar{Q} < 0$.

1.5.3 A rivulet of perfectly wetting fluid subject to a uniform longitudinal surface shear stress (Sullivan, Wilson and Duffy [91])

In this Subsection we summarise some of the results of Sullivan, Wilson and Duffy [91] who studied the flow of a thin rivulet with zero contact angle (in contrast to Subsection 1.5.2 where a non-zero contact angle was considered) on the lower half of a large horizontal cylinder subject to a longitudinal surface shear stress τ (again nondimensionalised with $\delta\sigma/\ell$), where $\tau > 0$ corresponds to the shear acting downwards in the azimuthal direction. This situation is described by (1.66) with $\epsilon \ll \delta \ll 1$ subject to no slip at the substrate and the normal stress balance as before, while the tangential stress balance is given by (1.79) and the contact-line conditions are given by (1.71). Then the pressure p is given by (1.67), the velocity u and free surface velocity $u_{\rm fs} = u_{\rm fs}(y) = u(y,h)$ are given by

$$u = \frac{\sin\alpha}{2}\left(2hz - z^2\right) + \tau z, \quad u_{\rm fs} = \frac{\sin\alpha}{2}h^2 + \tau h, \tag{1.90}$$

the semi-width a and the free surface profile h of the rivulet are given by (1.72) and the volume flux Q is given by

$$Q = \frac{\pi}{24m}\left(5h_{\mathrm{m}}\sin\alpha + 9\tau\right)h_{\mathrm{m}}^2. \tag{1.91}$$

For a prescribed flux $Q = \bar{Q}$, inclination angle α ($\pi/2 < \alpha \leq \pi$) and shear stress τ, we must solve (1.91) for h_{m} then use (1.72) to obtain h.

All of the possible flow patterns in this problem are again those given by Figure 1.17 (except that, of course, the contact angle is zero). From (1.90) the free surface velocity at $y = 0$ is given by

$$u_{\mathrm{fs}}(0) = \frac{h_{\mathrm{m}}^2\sin\alpha}{2} + \tau h_{\mathrm{m}}. \tag{1.92}$$

When $\tau \geq 0$ the flow is type I, the maximum velocity $u = u_{\mathrm{fs}}(0)$ occurs on the free surface at $z = h_{\mathrm{m}}$, and the minimum velocity $u = 0$ occurs on the substrate $z = 0$. When $\tau < 0$ the curve on which the velocity u is zero, again denoted by $z = H(y)$, is given by

$$H = 2\left(h + \frac{\tau}{\sin\alpha}\right) \tag{1.93}$$

and this yields the condition

$$-\frac{\tau}{\sin\alpha} \leq h \leq -\frac{2\tau}{\sin\alpha} \tag{1.94}$$

for upwards flow to occur.

For $h_{\mathrm{m}} > -\tau/\sin\alpha$ the curve (1.93) meets the substrate $z = 0$ when $y = \pm b$, where

$$b = \frac{1}{m}\cos^{-1}\left(-\frac{2\tau}{h_{\mathrm{m}}\sin\alpha} - 1\right), \tag{1.95}$$

and for $h_{\mathrm{m}} < -2\tau/\sin\alpha$ the curve (1.93) meets the free surface $z = h$ when $y = \pm c$, where

$$c = \frac{1}{m}\cos^{-1}\left(-\frac{4\tau}{h_{\mathrm{m}}\sin\alpha} - 1\right). \tag{1.96}$$

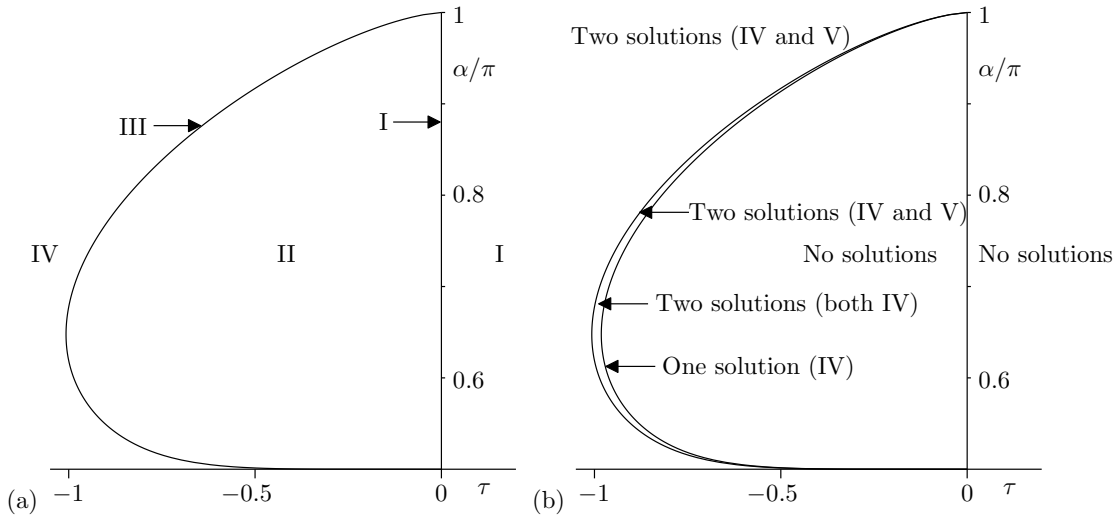

Figure 1.19: Plot of the α/π–τ parameter plane when (a) $\bar{Q} = 1\,(> 0)$ and (b) $\bar{Q} = -1\,(< 0)$. The regions where each type of flow (I–V) occur are indicated.

As in Subsection 1.5.2, if $H_{\rm m} > h_{\rm m}$ (where $H_{\rm m} = H(0)$) then the flow is type II, if $H_{\rm m} = h_{\rm m}$ then the flow is type III, if $0 < H_{\rm m} < h_{\rm m}$ then the flow is type IV and if $H_{\rm m} \leq 0$ then the flow is of type V. For flow-types II, III and IV the maximum velocity $u = u_{\rm fs}(0) + \tau^2/2\sin\alpha$ occurs within the rivulet at $y = 0$, $z = H_{\rm m}/2 = h_{\rm m} + \tau/\sin\alpha$, and the minimum velocity $u = -\tau^2/2\sin\alpha$ occurs on the free surface at $y = \pm b$, $z = -\tau/\sin\alpha$. For flow-type V the maximum velocity $u = 0$ occurs on the substrate $z = 0$, and the minimum velocity $u = u_{\rm fs}(0)$ occurs on the free surface at $y = 0$, $z = h_{\rm m}$.

Figure 1.19 shows plots of the α/π–τ parameter plane when (a) $\bar{Q} = 1\,(> 0)$ and (b) $\bar{Q} = -1\,(< 0)$. The regions where each type of flow (I–V) occur are indicated. Note that when $\bar{Q} > 0$ a single solution always exists (for any τ) but when $\bar{Q} < 0$ either zero, one or two solutions exist and, in particular, there are no solutions for $\tau > 0$.

1.5.4 A rivulet or ridge subject to a uniform transverse shear stress at its free surface (Sullivan et al. [90])

In this Subsection we reproduce the results of Sullivan et al. [90] (of which I am a co-author), outlining the improved numerical method from that used in Sullivan's [89] thesis to consider the same problem, together with the more accurate numerical results.

We analyse three closely related problems involving a thin rivulet or ridge of fluid subject to a prescribed uniform transverse shear stress at its free surface, namely a rivulet draining under gravity down a vertical substrate, a rivulet driven by a longitudinal surface shear stress, and a ridge on a horizontal substrate, and find qualitatively similar behaviour for all three problems.

1.5.4.1 A gravity-driven rivulet

Consider the steady flow of a thin gravity-driven rivulet of fluid on a vertical substrate as in Subsection 1.5.2, but now subject to a prescribed transverse (rather than longitudinal) shear stress τ at its free surface; without loss of generality we take $\tau \geq 0$. Unlike the cases considered up to this point, the rivulet is non-symmetric and so the positions of the contact lines are denoted by $y = a_1$ and $y = a_2$, where $a_1 < a_2$, so that $h(a_1) = h(a_2) = 0$, and the rivulet has contact angles β_1 and β_2 (which are, in general, non-zero) at $y = a_1$ and $y = a_2$, respectively. In the general case of non-zero shear, $\tau > 0$, we have $\beta_1 < \beta_2$, while in the special case of no shear, $\tau = 0$, we have $\beta_1 = \beta_2 = \beta > 0$, say.

We non-dimensionalise according to

$$\begin{gathered} x = Lx^*, \quad y = Ly^*, \quad a_1 = La_1^*, \quad a_2 = La_2^*, \quad z = \delta L z^*, \quad h = \delta L h^*, \\ \beta_1 = \delta\beta_1^*, \quad \beta_2 = \delta\beta_2^*, \quad p - p_\infty = \frac{\delta\sigma}{L}p^*, \quad \tau = \frac{\delta^2\sigma}{L}\tau^*, \\ u = \frac{\delta^3\sigma}{\mu}u^*, \quad v = \frac{\delta^3\sigma}{\mu}v^*, \quad w = \frac{\delta^4\sigma}{\mu}w^*, \end{gathered} \tag{1.97}$$

where L is a typical length scale in the x and y directions, and $\delta = (L/\ell)^2 \ll 1$ is the small transverse aspect ratio. For clarity we immediately drop the star superscripts on non-dimensional variables and, as in Subsection 1.4.2.2, we set $\delta = \beta$.

At leading order in $\beta \ll 1$ the Navier–Stokes and mass-conservation equations are given by (1.66) with $\alpha = \pi/2$ and are to be solved subject to conditions of no slip $u = v = 0$ and no penetration $w = 0$ at the substrate $z = 0$, and balances of normal and tangential stress at the free surface:

$$p = -h'', \quad u_z = 0 \quad \text{and} \quad v_z = \tau \quad \text{on} \quad z = h. \tag{1.98}$$

Solving for p and $\mathbf{u} = (u, v, w)$ yields

$$\begin{gathered} p = -h'', \quad u = \frac{1}{2}(2h - z)z, \quad v = \frac{h'''}{2}(2h - z)z + \tau z, \\ w = -\frac{h''''}{6}(3h - z)z^2 - \frac{h'''h'}{2}z^2. \end{gathered} \tag{1.99}$$

The kinematic free surface condition may be written as

$$\nabla \cdot (\bar{u}, \bar{v}) = 0, \tag{1.100}$$

where $\bar{u}$ and $\bar{v}$ are the local fluxes in the x and y directions, respectively, namely

$$\bar{u} = \int_0^h u \, \mathrm{d}z = \frac{h^3}{3}, \quad \bar{v} = \int_0^h v \, \mathrm{d}z = \frac{h'''h^3}{3} + \frac{\tau h^2}{2}. \tag{1.101}$$

Hence the free surface profile h satisfies the nonlinear ordinary differential equation

$$hh''' + \frac{3\tau}{2} = 0. \tag{1.102}$$

The longitudinal volume flux Q_g through a transverse cross-section of the rivulet $x =$ constant is given by

$$Q_\mathrm{g} = \int_{a_1}^{a_2} \bar{u} \, \mathrm{d}y = \frac{1}{3}\int_{a_1}^{a_2} h^3 \, \mathrm{d}y. \tag{1.103}$$

1.5.4.2 A shear-driven rivulet and a ridge

The analysis in Subsection 1.5.4.1 concerns a gravity-driven rivulet on a vertical substrate, hereafter referred to simply as a "gravity-driven rivulet", but similar analyses apply to two other closely related problems, namely, a rivulet of fluid on a planar substrate driven by a prescribed longitudinal surface shear stress T, hereafter referred to simply as a "shear-driven rivulet", and a ridge of fluid on a horizontal substrate, hereafter referred to simply as a "ridge".

Proceeding as for the gravity-driven rivulet with $\delta = (LT/\sigma)^{1/2}$ for the shear-driven rivulet and δ left general for the ridge, but for simplicity restricting our attention to the case $L \ll l$ so that we may neglect the effect of gravity entirely, p, v and w are again given by (1.99).

For the shear-driven rivulet $u = z$ and so h again satisfies (1.102), while the longitudinal volume flux Q_{s} through a transverse cross-section $x =$ constant is given by

$$Q_{\mathrm{s}} = \int_{a_1}^{a_2} \bar{u}\,\mathrm{d}y = \frac{1}{2}\int_{a_1}^{a_2} h^2\,\mathrm{d}y. \tag{1.104}$$

For the ridge $u = 0$ and so, once again, h satisfies (1.102), while the area A of a transverse cross-section $x =$ constant is given by

$$A = \int_{a_1}^{a_2} h\,\mathrm{d}y. \tag{1.105}$$

As a result of their strong similarities, we shall present results for all three problems in parallel, and, when results apply to all three, we simply refer to the "rivulet/ridge".

1.5.4.3 Equilibrium solutions

All three problems satisfy (1.102) and the boundary conditions

$$h(\pm a) = 0, \quad h'(-a) = \beta_1, \quad h'(+a) = -\beta_2, \tag{1.106}$$

where we have chosen the (arbitrary) location of the origin so that the contact lines are at $y = \pm a$, where a is the semi-width of the rivulet/ridge. Therefore, in this Subsection we describe the basic properties of the solutions of (1.102) subject to (1.106).

Local analysis of (1.102) near the contact lines reveals that when $\beta_1 > 0$ the free surface near the left-hand contact line behaves according to

$$h = \beta_1(a+y) - \frac{3\tau}{4\beta_1}(a+y)^2 \ln(a+y) + O(a+y)^2 \tag{1.107}$$

as $y \to -a^+$, and when $\beta_2 > 0$ the free surface near the right-hand contact line behaves according to

$$h = \beta_2(a-y) + \frac{3\tau}{4\beta_2}(a-y)^2 \ln(a-y) + O(a-y)^2 \tag{1.108}$$

as $y \to +a^-$, showing that h'' is, in general, logarithmically singular at both contact lines. However, when $\beta_1 = 0$ the appropriate local behaviour near the left-hand contact line is

$$h = 2\sqrt{\tau}(a+y)^{\frac{3}{2}} + O(a+y)^{\frac{5+\sqrt{13}}{4}} \tag{1.109}$$

as $y \to -a^+$, in place of (1.107).

An important relationship between the contact angles β_1 and β_2, the rivulet/ridge semi-width a and the shear stress τ is given by

$$\beta_2^2 - \beta_1^2 = 6\tau a. \tag{1.110}$$

Physically (1.110) represents a transverse balance of forces due to capillary and shear-stress effects.

In order to investigate the effect of varying the transverse shear stress τ in a systematic way it is sensible to consider a rivulet/ridge with prescribed flux/area as τ is increased from zero. Physically we may interpret this as the quasi-equilibrium development of a rivulet/ridge with prescribed flux/area as the shear stress is

slowly increased from zero. Prescribing the values of the shear stress τ and the flux/area means that one of the remaining three quantities β_1, β_2 and a must also be prescribed. The most physically sensible way to do this is firstly to prescribe the semi-width a (corresponding to a rivulet/ridge with two pinned contact lines and with the unknown contact angles β_1 and β_2 determined as part of the solution), then to prescribe β_1 or β_2 (corresponding to a rivulet/ridge with one pinned and one de-pinned contact line and with the unknown semi-width a and the other contact angle determined as part of the solution), and finally to prescribe β_1 and β_2 (corresponding to the critical "yield" condition beyond which no equilibrium solutions are possible).

In the special case of no transverse shear stress, $\tau = 0$, the rivulet/ridge has the familiar parabolic free surface profile $h = H(y)$ given by

$$H = \frac{a^2 - y^2}{2a} \tag{1.111}$$

with maximum thickness $h_{\mathrm{m}} = a/2$ at $y = 0$ and equal contact angles $\beta_1 = \beta_2 = 1$, and (1.103)–(1.105) yield

$$Q_{\mathrm{g}} = \frac{4a^4}{105}, \quad Q_{\mathrm{s}} = \frac{2a^3}{15}, \quad A = \frac{2a^2}{3}, \tag{1.112}$$

respectively. For simplicity of presentation in what follows we choose (without loss of generality) the prescribed flux/area values to be

$$Q_{\mathrm{g}} = \frac{4}{105}, \quad Q_{\mathrm{s}} = \frac{2}{15}, \quad A = \frac{2}{3}, \tag{1.113}$$

corresponding to setting $a = 1$ in the appropriate expressions in the case $\tau = 0$ given by (1.112). Note, however, that prescribing Q_{g}, Q_{s} and A according to (1.113) does not guarantee that $a = 1$ for all $\tau > 0$; indeed determining when and how a varies as τ is varied is one of the key issues discussed in Subsections 1.5.4.4 and 1.5.4.5.

1.5.4.4 Pinned solutions with prescribed semi-width

In this Subsection we describe the development of the equilibrium rivulet/ridge solutions with prescribed semi-width $a = 1$ but varying β_1 and β_2 as τ is increased from zero. Physically we can interpret these solutions as a rivulet/ridge with pinned (i.e. fixed) contact lines but varying contact angles as τ varies.

In the general case of non-zero transverse shear stress, $\tau > 0$, the rivulet/ridge is non-symmetric with $0 < \beta_1 < \beta_2$ and the free surface profile is obtained by solving (1.102) numerically subject to (1.106) and the prescribed flux/area condition. This was done by converting the problem into an initial value problem by using the local behaviour of h near either $y = -a$ given by (1.107) or near $y = a$ given by (1.108) to generate approximate initial conditions which were imposed close to (but not at) the appropriate contact line. For example, using (1.107) yields the approximate initial conditions

$$h(-a+\delta) = \beta_1\delta - \frac{3\tau}{4\beta_1}\delta^2\ln\delta + k\delta^2, \tag{1.114}$$

$$h'(-a+\delta) = \beta_1 - \frac{3\tau}{4\beta_1}(2\delta\log\delta + \delta) + 2k\delta, \tag{1.115}$$

$$h''(-a+\delta) = -\frac{3\tau}{4\beta_1}(2\log\delta + 3) + 2k, \tag{1.116}$$

where $\delta \ll 1$ was chosen to be sufficiently small (typically $\delta = 10^{-6}$) and k is a free parameter. Solutions were then obtained by iterating τ and k for a given value of β_1 until the conditions of zero thickness at the other contact line, $h(a) = 0$, and of prescribed flux/area were satisfied to within an appropriate tolerance (typically 10^{-6}). The consistency of the numerical results obtained were checked by substituting the values of β_1, β_2, τ and a into the transverse balance of forces (1.110).

Figure 1.20 shows numerically calculated free surface profiles of a gravity-driven rivulet with $a = 1$ for various values of τ, illustrating how the profile becomes increasingly skewed to the right as τ is increased from zero. The corresponding

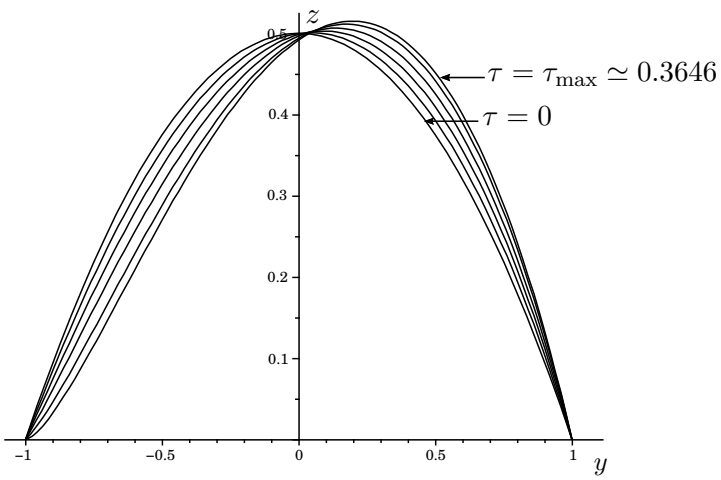

Figure 1.20: Free surface profiles $z = h(y)$ of a gravity-driven rivulet for $\tau = 0$, 0.08, 0.16, 0.24, 0.32 and $\tau_{\max} \simeq 0.3646$. The corresponding profiles for a shear-driven rivulet and for a ridge are qualitatively similar.

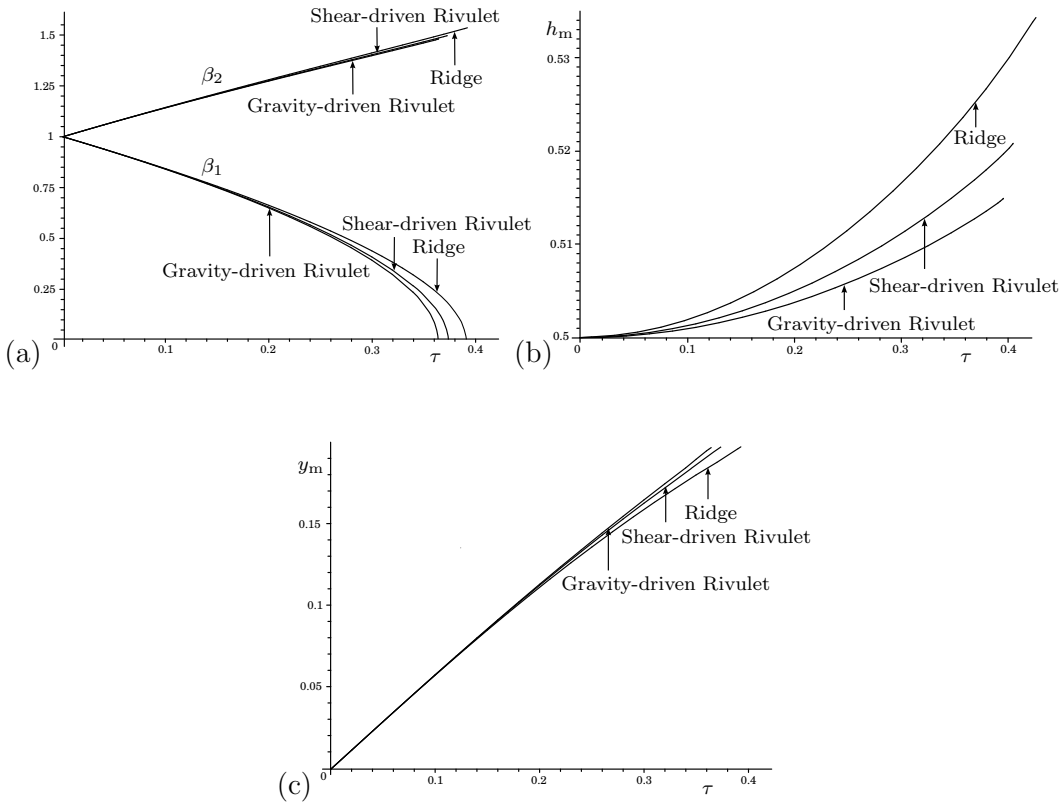

Figure 1.21: Plot of (a) the contact angles β_1 and β_2, (b) the maximum thickness of the rivulet/ridge $h_{\rm m}$, and (c) the location of the maximum thickness of the rivulet/ridge $y_{\rm m}$, as functions of τ for each of the three problems.

	Gravity-driven Rivulet	Shear-driven Rivulet	Ridge
$\tau_{\max}$	0.3646	0.3730	0.3924
$\beta_{\max}$	1.4791	1.4959	1.5344
h_{m}	0.5149	0.5208	0.5342
y_{m}	0.1962	0.1962	0.1962

Table 1.1: Values of $\tau_{\max}$ and the corresponding maximum values of $\beta_2 = \beta_{\max}$, h_{m} and y_{m} when $\tau = \tau_{\max}$ for each of the three problems.

profiles for a shear-driven rivulet and for a ridge are qualitatively similar and hence are omitted for brevity. Figure 1.21 shows how the contact angles β_1 and β_2, the maximum thickness h_{m}, and the location of the maximum thickness y_{m}, vary with τ. In particular, Figure 1.21 shows that for all three problems $\beta_2\,(>1)$, $h_{\mathrm{m}}\,(>1/2)$ and $y_{\mathrm{m}}\,(>0)$ increase monotonically while $\beta_1\,(<1)$ decreases monotonically (with, of course, $a = 1$) as τ is increased from zero. Figure 1.21 also shows that there is a maximum value of τ, denoted by $\tau_{\max}$, at which $\beta_1 = 0$, and hence from (1.110) at which $\beta_2 = \beta_{\max} = (6\tau_{\max})^{1/2}$, beyond which no equilibrium solution with prescribed semi-width $a = 1$ is possible. Table 1.1 gives the values of $\tau_{\max}$ and the corresponding maximum values of $\beta_2 = \beta_{\max}$, h_{m} and y_{m} when $\tau = \tau_{\max}$ for each of the three problems.

1.5.4.5 De-pinned solutions with variable semi-width

To illustrate a rivulet/ridge that de-pins only at the advancing (i.e. right-hand) contact line we choose $\beta_{\mathrm{A}} = 1.3$ and $\beta_{\mathrm{R}} = 0$, but note that any other value of β_{A} satisfying $1 < \beta_{\mathrm{A}} < \beta_{\max}$ will give qualitatively similar results. Table 1.2 gives the values of τ_{depin} and the corresponding values of β_1, h_{m} and y_{m} when $\tau = \tau_{\mathrm{depin}}$ for each of the three problems in the case $\beta_{\mathrm{A}} = 1.3$. Figure 1.22 shows the free surface profiles $z = h(y)$ of a gravity-driven rivulet for various values of

	Gravity-driven Rivulet	Shear-driven Rivulet	Ridge
$\tau_{\rm depin}$	0.2208	0.2187	0.2149
β_1	0.6041	0.6145	0.6330
$h_{\rm m}$	0.5054	0.5070	0.5099
$y_{\rm m}$	0.1236	0.1217	0.1183

Table 1.2: Values of $\tau_{\rm depin}$ and the corresponding values of β_1, $h_{\rm m}$ and $y_{\rm m}$ when $\tau = \tau_{\rm depin}$ for each of the three problems in the case $\beta_{\rm A} = 1.3$.

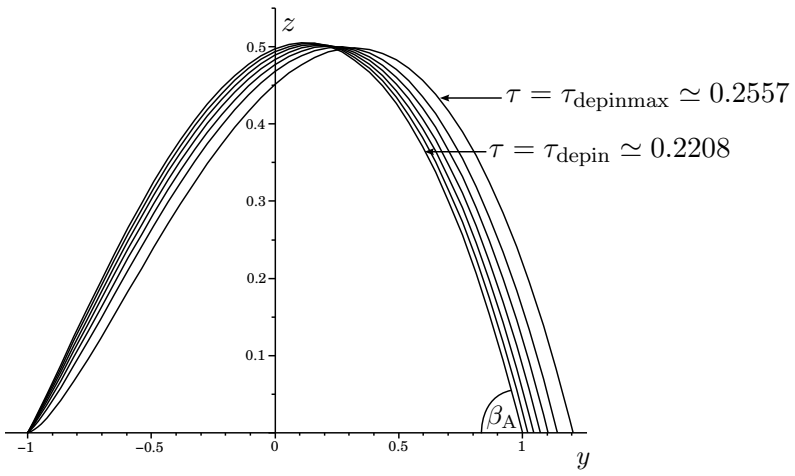

Figure 1.22: Free surface profiles $z = h(y)$ of a gravity-driven rivulet with advancing contact angle $\beta_2 = \beta_{\rm A} = 1.3$ for $\tau = \tau_{\rm depin} \simeq 0.2208$, 0.2266, 0.2324, 0.2382, 0.2440, 0.2498 and $\tau_{\rm depinmax} \simeq 0.2557$. The corresponding profiles for a shear-driven rivulet and for a ridge are qualitatively similar.

$\tau \geq \tau_{\rm depin} \simeq 0.2208$ illustrating how the profile is further skewed to the right, and is flattened and widened as τ is increased from $\tau_{\rm depin}$. The corresponding profiles for a shear-driven rivulet and for a ridge are qualitatively similar and hence are omitted for brevity.

There is a maximum value of τ, denoted now by $\tau_{\rm depinmax}$, at which $\beta_1 = 0$, and hence from (1.110) at which $a = a_{\rm max} = \beta_{\rm A}^2/(6\tau_{\rm depinmax})$, beyond which no equilibrium solutions with prescribed advancing contact angle $\beta_2 = \beta_{\rm A}$ is possible. Table 1.3 gives the values of $\tau_{\rm depinmax}$ and the corresponding values of $a = a_{\rm max}$,

	Gravity-driven Rivulet	Shear-driven Rivulet	Ridge
τ_{depinmax}	0.2557	0.2565	0.2593
$a_{\max}$	1.1016	1.0981	1.0864
h_{m}	0.4986	0.4970	0.4917
y_{m}	0.3178	0.3136	0.2996

Table 1.3: Values of τ_{depinmax} and the corresponding values of $a = a_{\max}$, h_{m} and y_{m} when $\tau = \tau_{\text{depinmax}}$ for each of the three problems in the case $\beta_{\text{A}} = 1.3$.

	Gravity-driven Rivulet	Shear-driven Rivulet	Ridge
τ_{depin}	0.2635	0.2674	0.2756
β_2	1.3532	1.3617	1.3797
h_{m}	0.5076	0.5104	0.5163
y_{m}	0.1457	0.1462	0.1472

Table 1.4: Values of τ_{depin} and the corresponding values of β_2, h_{m} and y_{m} when $\tau = \tau_{\text{depin}}$ for each of the three problems in the case $\beta_{\text{R}} = 0.5$.

h_{m} and y_{m} when $\tau = \tau_{\text{depinmax}}$ for each of the three problems in the case $\beta_{\text{A}} = 1.3$.

To illustrate a rivulet/ridge that de-pins only at the receding (i.e. left-hand) contact line we choose $\beta_{\text{R}} = 0.5$ and $\beta_{\text{A}} = \infty$, but note that any other value of β_{R} satisfying $0 < \beta_{\text{R}} < 1$ will give qualitatively similar results. Table 1.4 gives the values of τ_{depin} and the corresponding values of β_2, h_{m} and y_{m} when $\tau = \tau_{\text{depin}}$ for each of the three problems in the case $\beta_{\text{R}} = 0.5$. Figure 1.23 shows the free surface profiles $z = h(y)$ of a gravity-driven rivulet for various values of $\tau \geq \tau_{\text{depin}} \simeq 0.2635$ illustrating how the profile is again further skewed to the right but (in contrast to the case of a rivulet that de-pins only at the advancing contact line) is thickened and narrowed as τ is increased from τ_{depin}. The corresponding profiles for a shear-

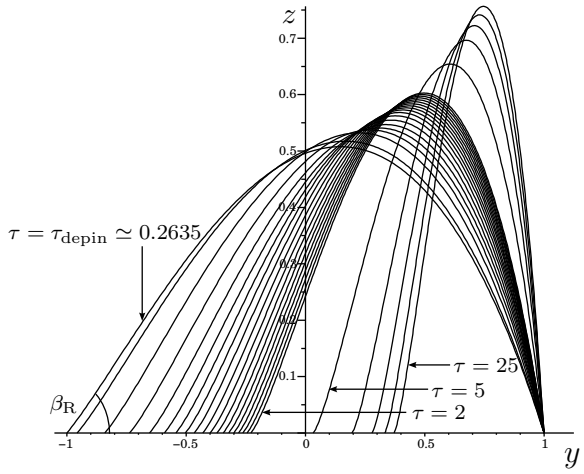

Figure 1.23: Free surface profiles $z = h(y)$ of a gravity-driven rivulet with receding contact angle $\beta_1 = \beta_{\rm R} = 0.5$ for $\tau = \tau_{\rm depin} \simeq 0.2635$, 0.3, 0.4, 0.5, ..., 1.7, 1.8, 2, 5, 10, 15, 20 and 25. The corresponding profiles for a shear-driven rivulet and for a ridge are qualitatively similar.

	Gravity-driven Rivulet	Shear-driven Rivulet	Ridge
$\tau_{\rm yield}$	0.2340	0.2338	0.2342
$a_{\rm yield}$	1.0259	1.0264	1.0250
$h_{\rm m}$	0.5029	0.5032	0.5025
$y_{\rm m}$	0.1460	0.1461	0.1458

Table 1.5: Values of $\tau_{\rm yield}$ and the corresponding values of $a_{\rm yield}$, $h_{\rm m}$ and $y_{\rm m}$ when $\tau = \tau_{\rm yield}$ for each of the three problems in the case $\beta_{\rm R} = 0.5$ and $\beta_{\rm A} = 1.3$.

driven rivulet and for a ridge are qualitatively similar and hence are omitted for brevity.

Except in the cases $\beta_{\mathrm{R}} = 0$ and $\beta_{\mathrm{A}} = \infty$ considered above, in general as τ is increased from zero de-pinning will eventually occur at *both* contact lines. Beyond this critical "yield" value of τ, denoted by τ_{yield}, no equilibrium solution exists and the rivulet/ridge will evolve unsteadily. From (1.110), τ_{yield} and the corresponding critical "yield" value of a, denoted by a_{yield}, are related by

$$\beta_{\mathrm{A}}^2 - \beta_{\mathrm{R}}^2 = 6 a_{\mathrm{yield}} \tau_{\mathrm{yield}}, \tag{1.117}$$

Table 1.5 gives the values of τ_{yield} and the corresponding values of a_{yield}, h_{m} and y_{m} when $\tau = \tau_{\mathrm{yield}}$ for each of the three problems in the case $\beta_{\mathrm{R}} = 0.5$ and $\beta_{\mathrm{A}} = 1.3$.

1.6 Rings of Fluid

In Chapter 5 of this thesis we will consider a ring of fluid subject to a uniform azimuthal surface shear stress that flows round the entire circumference of a large, stationary horizontal cylinder. Many authors have studied the related problem of fluid flow on a rotating horizontal cylinder. In particular, the two-dimensional case of a film on the outside of a rotating cylinder (known as coating flow) as well as the problem of a film on the inside of a rotating cylinder (known as rimming flow) has received attention. In these studies, the rotation of the cylinder prevents either the fluid from draining off the bottom of the cylinder (in the case of coating flow), or collecting at the bottom of the cylinder (in the case of rimming flow), because of the effects of gravity. Pukhnachev [76] derived an equation for the film thickness in unsteady coating flow using lubrication theory including the effects of surface tension, gravity and viscosity. Moffatt [60] used lubrication theory to determine that for a given rotation speed, there is a maximum mass of fluid on the outer surface of a cylinder which can be supported against gravity. Moffatt [60] also experimentally observed that the film thickness may not be independent of the axial coordinate and showed the occurrence of slight humps in the free surface which can develop into rings of fluid along the cylinder. Johnson [41] considered rimming flow of a power-law fluid in a rotating cylinder and found four classes of steady-state solutions. In two of these solutions the film covers the entire cylinder, and of the other two, the fluid coats one side of the cylinder in one, and in the other, gravity dominates such that all the fluid collects at the bottom of the cylinder.

The papers by Pukhnachev [76], Moffatt [60] and Johnson [41] have motivated a great deal of further work on fluid flow on a rotating cylinder by a wide range of authors; however, there has been less attention given to the case where a pressure gradient or shear stress is present. Tirumkudulu and Acrivos [94] included the hydrostatic pressure gradient in the model studied by Moffatt [60] for a film on the

inside of a rotating cylinder and showed that the numerically computed film profile compares favourably with their experimental results for a wide range of rotation speeds. Villegas-Diaz, Power and Riley [103] studied the steady rimming flow of a thin film on the inside of a rotating cylinder subject to a uniform longitudinal surface shear stress, including the effects of gravity but not surface tension. There exists a maximum volume flux such that the film wets the entire cylinder and it is found that this maximum flux is four times greater in the case of rotation with no shear stress present compared to the case of shear stress with no rotation. Discontinuous solutions with shocks (that is, one or more jumps in the film thickness) are possible both when the shear stress and the rotation are in the same or in opposite directions and, in particular, when they are in opposite directions then these shocks can occur anywhere on the cylinder. To gain further insight into the feasibility of these shock solutions in practice, Villegas-Diaz, Power and Riley [104] then extended the lubrication model to include surface tension and higher-order gravity effects, and offered analytical and numerical results to support the claim that these compressive shock solutions are physically relevant.

There have been a number of experimental studies investigating coating and rimming flow. Melo and Douady [56] investigated the rimming flow of a film of oil as the rotation speed of the cylinder is increased and observed the occurrence of three-dimensional patterns, Thoroddsen and Mahadevan [93] observed a wide range of patterns in experiments of flow inside a cylinder, including so-called "shark-teeth" patterns where a wavy film-front develops into having cusp-like fronts as the rotation speed is increased. Chen et al. [10] found that there is a critical volume of fluid inside a cylinder in rimming flow such that, for a uniform film to form, the required rotation speed is a minimum, and that if the volume is below this critical value then shark-teeth patterns are observed while if the volume is above this critical value then finger instabilities and discrete rings of fluid are

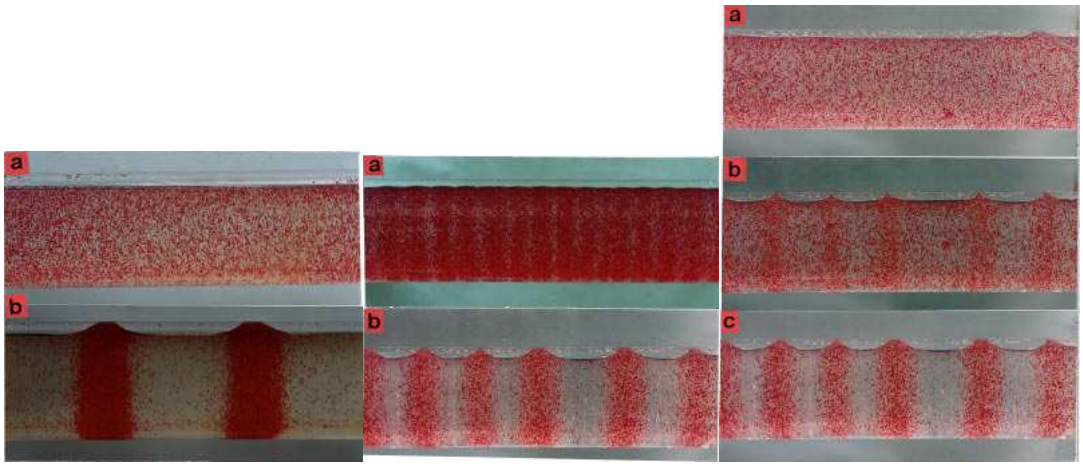

(i) (ii) (iii)

Figure 1.24: Images of rings of particle-laden fluid in a Couette device, formed by rotating the device, found by Tirumkudulu, Tripathi and Acrivos [95]. The patterns formed in (i) are (a) before rotation and (b) after rotation, (ii) for (a) low rotation speed and (b) high rotation speed, and (iii) for constant rotation speed as time increases from (a) through to (c). Reprinted with permission from Tirumkudulu, Tripathi and Acrivos [95], Copyright 1999, American Institute of Physics.

observed. Chicharro, Vazquez and Manasseh [11] also considered fluid flow on the inside of a rotating cylinder but with a much lower volume of fluid than previous studies and again observed rings of fluid at higher rotational speeds. On a slightly different note, Deans and Kucuka [17] observed a uniform film of ammonia-water mixture develop over time into banded films on the outside of a stationary horizontal cylinder. Another area which has received much attention is segregation of particle-laden fluids in coating and rimming flow, and work on this topic is summarised by Seiden and Thomas [85] in their recent review paper. For example, Tirumkudulu, Tripathi and Acrivos [95] constructed a Couette device consisting of two concentric cylinders and partially filled the gap between them with particle-laden fluid; the inner cylinder was then rotated and the particles were observed to form rings, as shown in Figure 1.24.

There have also been a number of three-dimensional analytical studies on coating and rimming flow. Hosoi and Mahadevan [36] numerically computed steady

and unsteady two-dimensional solutions for fluid on the inside of a rotating cylinder and then computed solutions including instability in the free surface in the axial direction to give the three-dimensional shark-teeth pattern observed by Thoroddsen and Mahadevan [93]. Jin and Acrivos [39] extended the two-dimensional model of Tirumkudulu and Acrivos [94] to include an axially varying viscosity for a film inside a rotating cylinder and found that the computed film profiles show good agreement with the results gained from numerically solving the full three-dimensional Stokes equations. Evans, Schwartz and Roy [30] obtained numerical solutions to the three-dimensional model for fluid flow on the outside of a rotating horizontal cylinder derived by Evans, Schwartz and Roy [29], which included the effects of gravity, surface tension, centripetal acceleration and axial variation, and successfully reproduced features observed in their own experiments, namely the formation of fingers and rings of fluid as the rotation speed increases. Noakes, King and Riley [67] studied the three-dimensional linear stability of thin films of fluid on the inside or outside of a rotating horizontal cylinder in the absence of gravity such that the film thickness is uniform all round the cylinder. In the case of rimming flow there is an axial instability resulting in the formation of rings of fluid and in the case of coating flow there is either an axial instability as in the rimming case or an azimuthal instability resulting in the formation of stripes along the cylinder at certain points round its circumference. Pougatch and Frigaard [75] computed three-dimensional numerical solutions for the film profile in rimming flow after the uniform, two-dimensional film becomes unstable, including higher order viscous and gravitational effects as well as leading order surface tension and inertia.

Recently, Leslie, Wilson and Duffy [48] studied the steady flow of a thin ring of fluid with constant non-zero contact angle flowing on the inside or outside of a rotating horizontal cylinder. In particular, it is found that there is a maximum

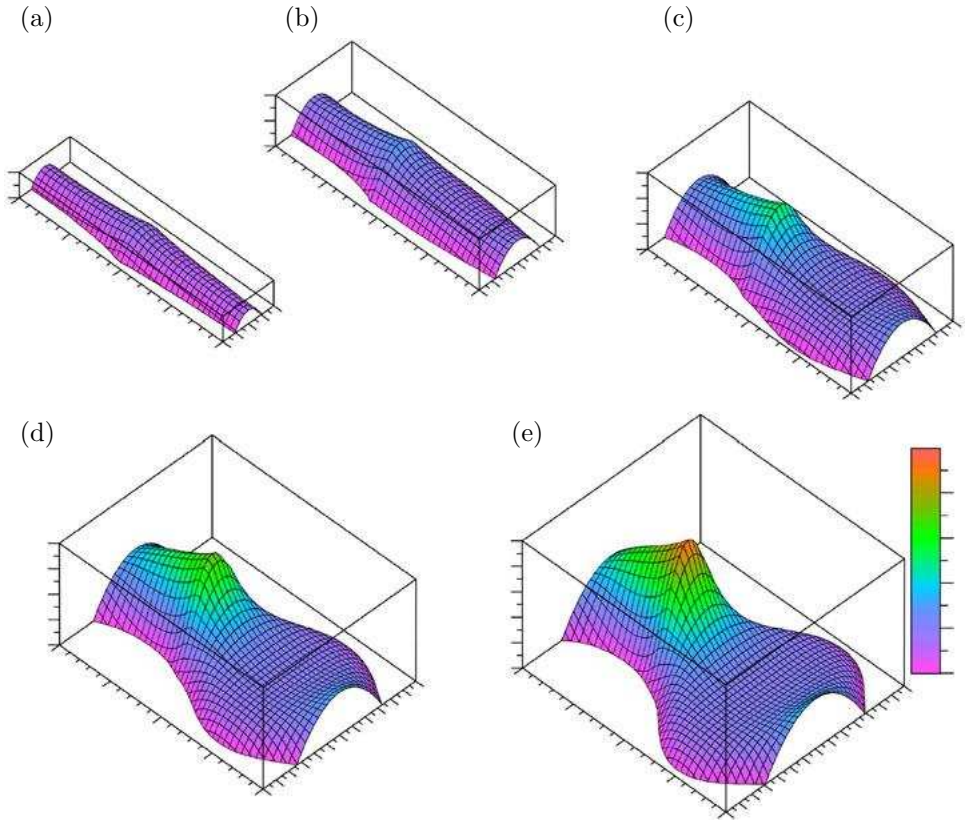

Figure 1.25: Three-dimensional plots of a rivulet with critical mass for a range of prescribed rotation speeds. The prescribed rotation speed increases from the lowest value in (a) to the largest value in (e). Reprinted from Leslie, Wilson and Duffy [48] with permission of Cambridge University Press.

mass of fluid that can be supported against gravity for a given rotation speed or, equivalently, there is a minimum rotation speed required to support a given mass of fluid. At this critical mass (or rotation speed) the free surface of the rivulet exhibits a cusp on the lower half of the cylinder on the side that is rising with rotation. Figure 1.25 shows three-dimensional plots of a rivulet with critical mass for a range of prescribed rotation speeds and, in particular, shows that increasing the rotation speed increases the mass of fluid that can be supported. It was also shown that backflow (that is, the azimuthal velocity in the opposite direction to rotation) is possible near the free surface on the rising side of the cylinder close to the critical solution.

1.7 Outline of Thesis

In this thesis we analyse the behaviour of steady ridges, rivulets and rings of fluid, driven by combinations of gravity, an external pressure gradient and a uniform surface shear stress, where the latter two effects are interpreted as the fluid being subject to an external airflow.

In Chapter 2 we use lubrication theory to describe the steady flow of a thin ridge of fluid with prescribed constant volume on a substrate inclined to the horizontal, including the effects of gravity and surface tension, subject to an external pressure gradient arising from an external airflow that flows tangentially to the substrate far from the ridge. We model the external airflow using classical thin-aerofoil theory as described in Subsection 1.3.2 and obtain the governing equation for the profile of the ridge. We then describe some basic properties of the solution before using a combination of asymptotic and numerical techniques to analyse the effect of varying the strength of the external airflow and the inclination angle of the substrate.

In Chapter 3 we follow the approach of Duffy and Moffatt [23] described in Subsection 1.4.2 and use the solution for the unidirectional flow of a thin rivulet with prescribed constant volume flux down an inclined planar substrate to describe the locally unidirectional flow of a rivulet with constant width (i.e. pinned contact lines) but slowly varying contact angle as well as the possible pinning and subsequent de-pinning of a rivulet with constant contact angle and the possible pinning and subsequent re-pinning of a rivulet with constant width as it flows in the azimuthal direction from the top to the bottom of a large horizontal cylinder.

In Chapter 4 we consider the effect of a uniform azimuthal surface shear stress in the direction opposing gravity in the problem considered in Chapter 3. In particular, we find that the possible flow patterns in the rivulet cross-section are again of the type shown in Figure 1.17. We then obtain a complete description

of the flow in the case of a rivulet with constant contact angle and slowly varying width and in the case of a rivulet with constant width and slowly varying contact angle.

In Chapter 5 we consider a ring of fluid with constant width on a large horizontal cylinder subject to a uniform azimuthal surface shear stress. In particular, we show that there is a critical solution corresponding to a maximum mass of fluid that can be supported against gravity for a given shear stress, and that when the mass is close to its maximum value, backflow (that is, flow in the direction opposite to that of the shear stress) is possible. We use a combination of asymptotic and numerical techniques to analyse both the critical and the sub-critical solution.

Finally, in Chapter 6 we summarise the results and main findings of the thesis, and suggest some directions for future work.

1.8 Presentations and Publications

The work described in Subsection 1.5.4 of Chapter 1 in collaboration with former Ph. D. student Julie M. Sullivan, together with my supervisors, has recently been published in Physics of Fluids [90].

Aspects of the work described in Chapters 2 and 3 have been presented at the British Applied Mathematics Colloquium in Birmingham in 2011 and in London in 2012, at the Scottish Fluid Mechanics Meeting in Glasgow in 2011 and in Edinburgh in 2012, at the Society for Industrial and Applied Mathematics Annual Meeting in Minneapolis, USA in 2012, and at the Thin Liquid Films and Fluid Interfaces: Models, Experiments and Applications workshop in Banff, Canada in 2012. A full account of the work in Chapter 2 has been submitted for publication in Physics of Fluids and a full account of the work in Chapter 3 has recently been published in the European Journal of Mechanics - B/Fluids [73].

Aspects of the work described in Chapters 4 and 5 have been presented at the British Applied Mathematics Colloquium in London in 2012 and at the Scottish Fluid Mechanics Meeting in Edinburgh in 2012. A full account of the work in Chapter 4 has been submitted for publication in the Quarterly Journal of Mechanics and Applied Mathematics, while a full account of the work in Chapter 5 is currently in preparation for publication.

In addition, I participated in the Physics with Industry Workshop in Leiden in October 2010, studying the problem of removing droplets of fluid left on the surface of microchips during the production process using a jet of air. Details of the work completed can be found in the workshop proceedings [100].

Chapter 2

Strongly-coupled interaction between a ridge of fluid and an external airflow

In this Chapter we study the steady flow of a thin ridge of fluid with prescribed constant volume on a substrate inclined to the horizontal, including the effects of gravity and surface tension, subject to an external pressure gradient arising from an external airflow.

2.1 Problem Formulation

Consider a steady thin ridge (or, equivalently, a two-dimensional droplet) of fluid on a planar substrate inclined at an angle α ($0 \leq \alpha \leq \pi$) to the horizontal, in the presence of a steady external airflow, as sketched in Figure 2.1. Values of α satisfying $0 \leq \alpha < \pi/2$ correspond to a sessile ridge sitting on an inclined substrate (as shown in Figure 2.1), values of α satisfying $\pi/2 < \alpha \leq \pi$ correspond to a pendent ridge hanging from an inclined substrate, while the value $\alpha = \pi/2$

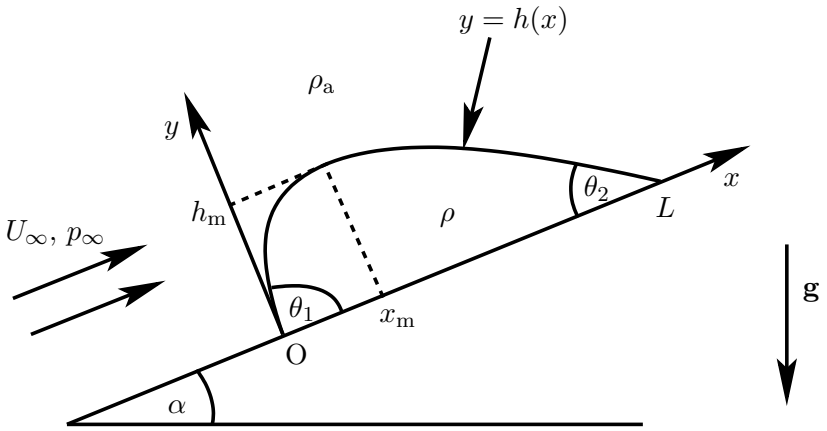

Figure 2.1: Sketch of a steady thin ridge of fluid on an inclined substrate in the presence of a steady external airflow which flows tangentially to the substrate far from the ridge with constant speed U_∞ and ambient pressure p_∞.

corresponds to the special case of a ridge on a vertical substrate. We assume that the fluid in the ridge has constant density ρ and coefficient of surface tension σ, and that the ridge is subject to an external flow of inviscid air of constant density ρ_a which flows tangentially to the substrate far from the ridge with constant speed U_∞ and ambient pressure p_∞. The airflow is perturbed by the presence of the ridge, resulting in a non-uniform external pressure gradient that depends in a non-trivial way on the unknown free surface profile of the ridge. Referred to Cartesian coordinates Oxy with the x and y directions taken to be parallel and normal to the substrate, respectively, as indicated in Figure 2.1, the ridge has free surface profile $y = h(x)$ for $0 \leq x \leq L$, width L in the transverse (i.e. in the x) direction, volume per unit length in the longitudinal (i.e. in the z) direction V, maximum thickness $h = h_m$ at $x = x_m$, and downslope and upslope contact angles $\theta_1 = h'(0)$ (≥ 0) and $\theta_2 = -h'(L)$ (≥ 0), respectively. The pressure in both the air and the ridge is denoted by $p = p(x, y)$.

In order to analyse the problem we introduce the following non-dimensionalised

and scaled variables:

$$\begin{gathered} x = L_0 x^*, \quad x_{\mathrm{m}} = L_0 x^*_{\mathrm{m}}, \quad L = L_0 L^*, \quad y = \epsilon L_0 y^*, \quad y = L_0 Y^*, \\ h = \epsilon L_0 h^*, \quad h_{\mathrm{m}} = \epsilon L_0 h^*_{\mathrm{m}}, \quad V = \epsilon L_0^2 V^*, \quad p - p_\infty = \frac{\epsilon\sigma}{L_0} p^*, \end{gathered} \tag{2.1}$$

where L_0 is the characteristic transverse length scale (discussed in more detail below) and $\epsilon = V/L_0^2 \ll 1$ is the (small) transverse aspect ratio of the ridge, giving $V^* = 1$ without loss of generality. Hence in what follows we set $V^* = 1$ in all of the numerical calculations, but retain V^* explicitly in all of the analytical results for clarity. Note that, since the problem has two different length scales in the y direction, two different non-dimensional y-coordinates, namely y^* and Y^*, are required. The coordinate y^* corresponding to the characteristic thickness scale for the ridge ϵL_0 ($\ll L_0$) is required to describe the behaviour of the ridge, and, in particular, the internal pressure in the ridge denoted by $p^* = p^*(x^*, y^*)$. On the other hand, the coordinate Y^* corresponding to the characteristic length scale L_0 (i.e. the same length scale as in the x-direction) is required to describe the behaviour of the external airflow, and, in particular, the external pressure in the air denoted by $p^* = P(x^*, Y^*)$. For clarity, we immediately drop the star superscripts on non-dimensional variables in what follows.

The external airflow consists of a uniform stream with constant speed U_∞ in the positive x-direction plus a non-uniform perturbation due to the presence of the ridge, which we obtain using thin-aerofoil theory (as in Subsection 1.3.2). The velocity potential and stream function of the external airflow $\phi(x, Y)$ and $\psi(x, Y)$ (both non-dimensionalised with $L_0 U_\infty$) are given in terms of the unknown free surface profile of the ridge by (from (1.29) and (1.40), and using the fact that $\phi_x = \psi_Y$ and $\phi_Y = -\psi_x$)

$$\phi(x, Y) = x + \frac{\epsilon}{2\pi} \int_0^L h'(\xi) \ln\left[(x-\xi)^2 + Y^2\right] \, \mathrm{d}\xi, \tag{2.2}$$

$$\psi(x, Y) = Y + \frac{\epsilon}{\pi} \int_0^L h'(\xi) \tan^{-1}\left(\frac{Y}{x-\xi}\right) \, \mathrm{d}\xi, \tag{2.3}$$

satisfying $\psi(x,0) = 0$, where a prime denotes differentiation with respect to argument. Using either (2.2) or (2.3) together with Bernoulli's theorem yields an expression for the leading order external pressure $P(x,Y)$, namely

$$P(x,Y) = -\Lambda \int_0^L \frac{(x-\xi)h'(\xi)}{(x-\xi)^2+Y^2}\,\mathrm{d}\xi, \tag{2.4}$$

where the non-dimensional parameter Λ (≥ 0), defined by

$$\Lambda = \frac{\rho_{\mathrm{a}} L_0 U_\infty^2}{\pi\sigma}, \tag{2.5}$$

is the appropriate measure of the strength of the external airflow. Note that, since U_∞ occurs in (2.5) only via the term U_∞^2, the sign of U_∞ is unimportant and hence the profile of the ridge will be the same whether the external airflow is directed tangentially up or tangentially down the substrate; for definiteness we take the external airflow to be directed tangentially up the substrate, as indicated in Figure 2.1. Note also that, since the inviscid external airflow imposes a pressure gradient but no shear stress on the free surface of the ridge, there is no flow within the ridge. Hence, the internal pressure p satisfies the equations

$$\epsilon p_x = -\left(\frac{L_0}{\ell}\right)^2 \sin\alpha, \quad p_y = -\left(\frac{L_0}{\ell}\right)^2 \cos\alpha \tag{2.6}$$

(that is, equation (1.46) with $L = L_0$ and $u = 0$ since there is no surface shear stress to drive flow within the ridge) subject to the leading order normal-stress balance at the free surface $y = h$, namely $p = P - h''$ at $Y = 0$, where $\ell = (\sigma/\rho g)^{1/2}$ denotes the usual capillary length, in which g denotes the constant magnitude of gravitational acceleration. Integrating (2.6b) subject to the boundary condition gives

$$p = \left(\frac{L_0}{\ell}\right)^2 (h-y)\cos\alpha + P - h'' \tag{2.7}$$

(that is, equation (1.49) with $L = L_0$ and $\cos\alpha \neq 1$ since $\alpha = O(1)$ at this stage). Substituting this solution for the internal pressure p into (2.6a) and evaluating the

expression for the external pressure P given in (2.4) at $Y = 0$ yields the governing linear singular integro-differential equation for the ridge profile h, namely

$$h''' - \left(\frac{L_0}{\ell}\right)^2 h' \cos\alpha - \left(\frac{L_0}{\ell}\right)^2 \frac{\sin\alpha}{\epsilon} + \Lambda \frac{\mathrm{d}}{\mathrm{d}x} \int_0^L \frac{h'(\xi)}{x-\xi}\,\mathrm{d}\xi = 0 \tag{2.8}$$

(that is, analogous to equation (1.51) with $\alpha = O(1)$ and in the absence of surface shear stress), where the integral is of Cauchy principal-value type. Equation (2.8) is to be solved subject to boundary conditions of zero thickness at both contact lines and of prescribed constant volume, namely

$$h(0) = 0, \quad h(L) = 0, \quad V = \int_0^L h\,\mathrm{d}x. \tag{2.9}$$

Note that not all of the terms in (2.8) are necessarily of the same order in the thin-film limit $\epsilon \to 0$, and so the appropriate form of (2.8) depends on the particular physical situation under investigation.

2.2 A Large Sessile Ridge

When the substrate is nearly horizontal (specifically, when $\alpha = O(\epsilon)$), the transverse component of gravity is relatively weak and so a relatively "large" ridge of width comparable to the capillary length ℓ can be supported against gravity by capillary and/or external pressure forces. In this case it is appropriate to choose $L_0 = \ell$ as the characteristic transverse length scale so that the transverse aspect ratio is $\epsilon = V/\ell^2 \ll 1$, the characteristic pressure scale is $\epsilon\sigma/\ell = \epsilon\rho g\ell = \rho g V/\ell$, and at leading order in the limit $\epsilon \to 0$ equation (2.8) becomes

$$h''' - h' - \hat{\alpha} + \Lambda \frac{\mathrm{d}}{\mathrm{d}x} \int_0^L \frac{h'(\xi)}{x-\xi}\,\mathrm{d}\xi = 0, \tag{2.10}$$

where

$$\Lambda = \frac{\rho_\mathrm{a} \ell U_\infty^2}{\pi\sigma} \tag{2.11}$$

and the non-dimensional parameter $\hat{\alpha}$ (≥ 0), defined by

$$\hat{\alpha} = \frac{\alpha}{\epsilon}, \tag{2.12}$$

is an appropriately scaled version of the angle of inclination of the substrate to the horizontal. Equation (2.10) is analysed in detail below and in Sections 2.3 and 2.4. The corresponding equations in the pendent case (specifically, when $\pi - \alpha = O(\epsilon)$) and in the case of a small ridge (specifically, when $\alpha = O(1)$) are discussed briefly in Sections 2.5 and 2.6, respectively.

2.2.1 Local Behaviour near the Contact Lines

Local analysis of (2.10) reveals that near the downslope contact line h behaves according to

$$h \sim \theta_1 x - \frac{\Lambda\theta_1}{2} x^2 \ln x + \frac{\kappa_1}{2} x^2 \quad \text{as} \quad x \to 0^+, \tag{2.13}$$

while near the upslope contact line h behaves according to

$$h \sim \theta_2 (L - x) - \frac{\Lambda\theta_2}{2} (L - x)^2 \ln(L - x) + \frac{\kappa_2}{2} (L - x)^2 \quad \text{as} \quad x \to L^-, \tag{2.14}$$

where the contact angles θ_1 and θ_2 and the constants κ_1 and κ_2 are determined globally (rather than locally). In particular, (2.13) and (2.14) show that h'' (but not h or h') is logarithmically singular at both contact lines for non-zero θ_1 and θ_2.

2.2.2 Transverse Force Balance

Multiplying the governing equation (2.10) by h, integrating with respect to x from 0 to L, and using the local behaviour (2.13) and (2.14) yields a statement of the transverse force balance on the ridge, namely

$$\theta_1^2 - \theta_2^2 - \int_0^L \fint_0^L \frac{h'(x)h'(\xi)}{x - \xi} \, \mathrm{d}\xi \, \mathrm{d}x = 2V\hat{\alpha}. \tag{2.15}$$

A simple change of variables shows that the double integral in (2.15) is identically zero for regular (non-singular) $h'(x)$ in $0 \leq x \leq L$. Hence, since in the present problem, as in that studied by Durbin [26] but *not* in that studied by King and Tuck [42], there are finite contact angles at both contact lines, the transverse force balance (2.15) reduces to simply

$$\theta_1^2 - \theta_2^2 = 2V\hat{\alpha}. \tag{2.16}$$

Note that Durbin's [26] equation (A6) is equivalent to the present equation (2.16).

The transverse force balance (2.16) is a very useful relationship which (since $V > 0$ and $\hat{\alpha} \geq 0$) shows immediately that $0 \leq \theta_2 \leq \theta_1$, i.e. that a ridge on an inclined substrate is always skewed in the downslope direction, with $\theta_1 = \theta_2$ only in the special case of a horizontal substrate, $\hat{\alpha} = 0$. Moreover, there is a critical ridge profile which occurs when $\theta_2 = 0$ (i.e. when the upslope contact angle is zero). For a prescribed value of $\hat{\alpha}$, this critical profile occurs at a critical maximum external airflow strength Λ, denoted by $\Lambda = \Lambda_{\max}(\hat{\alpha})$, above which there are no physically realisable steady solutions and, conversely, for a prescribed value of Λ, it occurs at a critical maximum angle of inclination of the substrate $\hat{\alpha}$, denoted by $\hat{\alpha} = \hat{\alpha}_{\max}(\Lambda)$, above which there are again no physically realisable steady solutions. The critical quantities $\Lambda_{\max}$ and $\hat{\alpha}_{\max}$ will be discussed in Sections 2.3 and 2.4.

2.2.3 General Form of the Solution for the Ridge Profile

Inspection of (2.9) and (2.10) reveals that the general form of the solution for the ridge profile $h = h(x)$ is a linear function of V and $\hat{\alpha}$, namely

$$h = Vh_0 + \hat{\alpha}h_1, \tag{2.17}$$

with

$$h_0(0) = h_0(L) = h_1(0) = h_1(L) = 0, \quad \int_0^L h_0 \, \mathrm{d}x = 1, \quad \int_0^L h_1 \, \mathrm{d}x = 0, \tag{2.18}$$

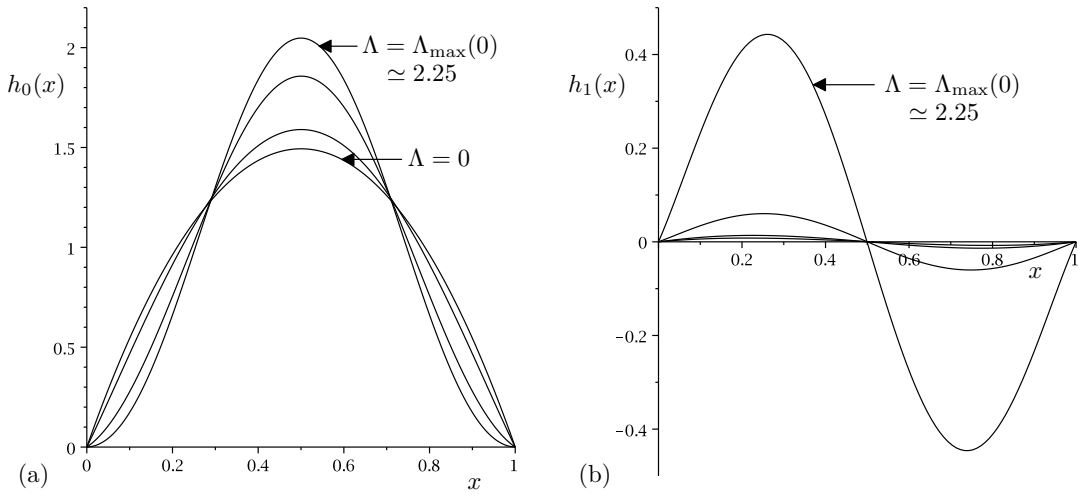

Figure 2.2: Plots of the functions (a) $h_0(x)$ and (b) $h_1(x)$ appearing in the solution for the ridge profile (2.17) for $\Lambda = 0$, 1, 2, $\Lambda_{\max}(0) \simeq 2.25$ when $L = 1$.

where the function $h_0 = h_0(x)$, which represents the ridge profile in the case of a horizontal substrate $\hat{\alpha} = 0$, is positive and symmetric about $x = L/2$, and the function $h_1 = h_1(x)$ is antisymmetric about $x = L/2$. In general, we must solve (2.10) subject to (2.9) for h numerically, and we do this using the finite difference method detailed in Appendix A. Figure 2.2 shows numerically calculated plots of (a) h_0 and (b) h_1 when $L = 1$ for various values of Λ satisfying $\Lambda \leq \Lambda_{\max}(0) \simeq 2.25$. In particular, since h_1 is positive for $0 < x < L/2$ and negative for $L/2 < x < L$, Figure 2.2 shows that increasing $\hat{\alpha}$ (i.e. tilting the substrate) always skews the ridge in the downslope direction so that the maximum thickness h_{m} increases, the location of the maximum thickness x_{m} decreases (i.e. moves downslope), the downslope contact angle θ_1 increases, and the upslope contact angle θ_2 decreases.

2.3 Strengthening the External Airflow

In this Section we investigate the quasi-static evolution of a large sessile ridge of prescribed constant volume V on a substrate inclined at a constant angle $\hat{\alpha}$ to the

horizontal as the external airflow is gradually strengthened (i.e. as Λ is gradually increased from zero). In Subsection 2.3.1 we consider a pinned ridge with pinned contact lines, and hence constant width L but variable contact angles θ_1 and θ_2. In reality, the contact lines will not remain pinned for all values of $\Lambda \leq \Lambda_{\max}$ (i.e. for all values of $\theta_2 \geq 0$). In practice (as, for example, Dussan V. [99] and Blake and Ruschak [9] describe), eventually one or both of the contact angles θ_1 and θ_2 will reach either the receding contact angle, θ_{R}, or the advancing contact angle, θ_{A}, (as defined in Subsection 1.3.1) and the corresponding contact line or lines will de-pin. For definiteness we assume that θ_1 and θ_2 satisfy $\theta_{\mathrm{R}} \leq \theta_{1,2} \leq \theta_{\mathrm{A}}$ when $\Lambda = 0$, i.e. that the ridge is always pinned in the absence of the external airflow. We will find that increasing the strength of the external airflow Λ decreases the contact angles θ_1 and θ_2, and so, while neither θ_1 nor θ_2 can ever reach θ_{A}, they may reach θ_{R}. However, as previously noted, the transverse force balance (2.16) shows that $\theta_2 \leq \theta_1$, and so (except in the special case $\hat{\alpha} = 0$ in which $\theta_1 = \theta_2$), θ_2 will always reach θ_{R} before θ_1 does (i.e. the upslope contact line with always de-pin before the downslope one). After de-pinning we assume that θ_2 remains equal to θ_{R}, and hence from (2.16) that $\theta_1 = (\theta_{\mathrm{R}}^2 + 2V\hat{\alpha})^{1/2}$ ($\geq \theta_{\mathrm{R}}$). Thus in Subsection 2.3.2 we consider a ridge that de-pins at its upslope contact line, and hence after de-pinning has variable width L but constant contact angles $\theta_1 = (\theta_{\mathrm{R}}^2 + 2V\hat{\alpha})^{1/2}$ and $\theta_2 = \theta_{\mathrm{R}}$.

2.3.1 A Pinned Ridge

In this Subsection we study a pinned ridge with constant width L but variable contact angles θ_1 and θ_2 for increasing Λ.

2.3.1.1 The Special Case of No External Airflow ($\Lambda = 0$)

In the special case of no external airflow, $\Lambda = 0$, the ridge profile, denoted by $h = H_0 = H_0(x)$, is given by (from (2.17))

$$H_0 = Vh_0 + \hat{\alpha}h_1, \tag{2.19}$$

where the functions $h_0 = h_0(x)$ and $h_1 = h_1(x)$ are given by

$$h_0 = \frac{\sinh\dfrac{L-x}{2}\sinh\dfrac{x}{2}}{\dfrac{L}{2}\cosh\dfrac{L}{2} - \sinh\dfrac{L}{2}} \tag{2.20}$$

and

$$h_1 = \frac{L\cosh\dfrac{L-x}{2}\sinh\dfrac{x}{2}}{\sinh\dfrac{L}{2}} - x, \tag{2.21}$$

respectively. From (2.19)–(2.21) it may readily be deduced that

$$\theta_{1,2} = V\gamma \pm \frac{\hat{\alpha}}{2\gamma}, \tag{2.22}$$

where the + sign is taken for θ_1 and the − sign is taken for θ_2, where the function $\gamma = \gamma(L)$ (> 0) is defined by

$$\gamma = \frac{1}{2}\left(\frac{L}{2}\coth\frac{L}{2} - 1\right)^{-1}. \tag{2.23}$$

Inspection of (2.23) reveals that γ is a strictly positive, monotonically decreasing function of L and satisfies $\gamma \sim 6/L^2 \to \infty$ as $L \to 0^+$ and $\gamma \sim 1/L \to 0^+$ as $L \to \infty$, as shown in Figure 2.3. Hence from (2.22) it can be deduced that as L is increased both contact angles decrease, with θ_2 reaching zero and θ_1 reaching the non-zero value $\theta_1 = 2V\gamma = \hat{\alpha}/\gamma$ when $\hat{\alpha} = 2V\gamma^2$, and hence the critical maximum value of $\hat{\alpha}$ when $\Lambda = 0$ is given by $\hat{\alpha}_{\max}(0) = 2V\gamma^2$.

Figure 2.4(a) shows plots of the profile of a pinned ridge in the case of no external airflow, H_0, for various values of $\hat{\alpha}$ when $L = 1$, in which case $\hat{\alpha}_{\max}(0) \simeq 74.40$. In particular, Figure 2.4(a) shows that, as expected, in the absence of an external airflow tilting the substrate skews the ridge in the downslope direction.

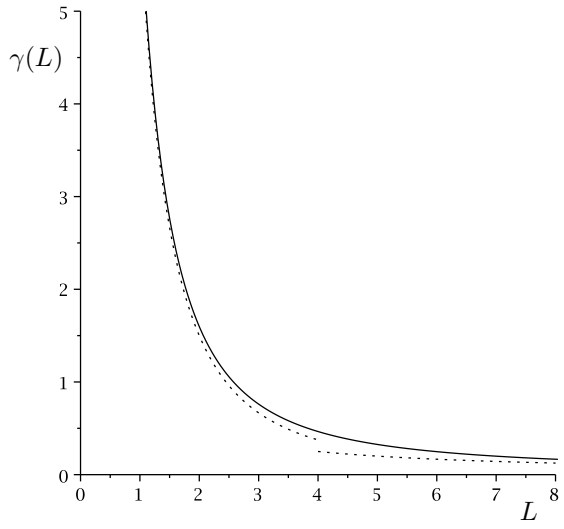

Figure 2.3: Plot of the function $\gamma(L)$ given by (2.23). The dotted curves show the leading order asymptotic behaviour $\gamma \sim 6/L^2 \to \infty$ as $L \to 0^+$ and $\gamma \sim 1/L \to 0^+$ as $L \to \infty$.

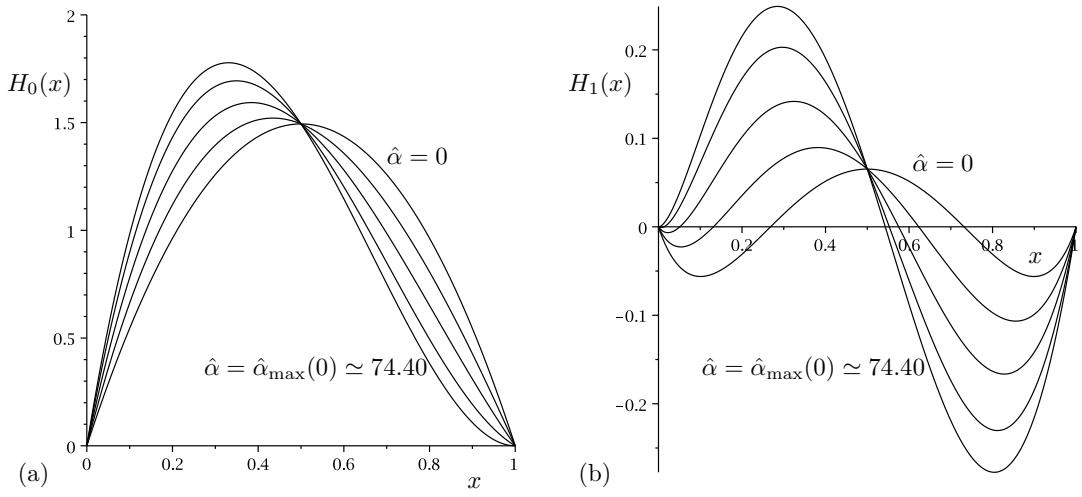

Figure 2.4: Plots of (a) the leading order term, $H_0(x)$, and (b) the first order term, $H_1(x)$, in the asymptotic solution for the profile of a pinned ridge in the limit of a weak external airflow, $\Lambda \to 0^+$, given by (2.24) for $\hat{\alpha} = 0$, 20, 40, 60, $\hat{\alpha}_{\max}(0) \simeq 74.40$ when $L = 1$.

2.3.1.2 The Limit of a Weak External Airflow ($\Lambda \to 0^+$)

In the limit of a weak external airflow, $\Lambda \to 0^+$, the ridge profile takes the form

$$h = H_0 + \Lambda H_1 + O(\Lambda^2), \tag{2.24}$$

where the leading order term, $H_0 = H_0(x)$, is simply the solution in the special case of no external airflow, $\Lambda = 0$, given by (2.19)–(2.21) and the first order term, $H_1 = H_1(x)$, satisfies

$$H_1''' - H_1' + \frac{\mathrm{d}}{\mathrm{d}x}\int_0^L \frac{H_0'(\xi)}{x-\xi}\,\mathrm{d}\xi = 0 \tag{2.25}$$

subject to

$$H_1(0) = 0, \quad H_1(L) = 0, \quad \int_0^L H_1\,\mathrm{d}x = 0. \tag{2.26}$$

Figure 2.4(b) shows numerically calculated plots of the first order term in the asymptotic solution for the profile of a pinned ridge, H_1, for various values of $\hat{\alpha}$ when $L = 1$. In the special case of a horizontal substrate, $\hat{\alpha} = 0$, H_1 is symmetric about $x = L/2$ with $H_1 > 0$ and $H_1' = 0$ at $x = x_\mathrm{m} = L/2$, and $-H_1'(L) = H_1'(0) < 0$. Therefore, in this case the effect of a weak external airflow is to slightly decrease both contact angles θ_1 and θ_2 equally, and to slightly increase the maximum thickness h_m (which always occurs at $x = x_\mathrm{m} = L/2$), i.e. to push the ridge down at its edges and pull it up at its middle. In the general case of a tilted substrate, $0 < \hat{\alpha} \leq \hat{\alpha}_\mathrm{max}$, H_1 is no longer symmetric about $x = L/2$, with $x = x_\mathrm{m}$ satisfying $0 < x_\mathrm{m} < L/2$, and $-H_1'(L) < H_1'(0) \leq 0$ with $H_1'(0) = 0$ at $\hat{\alpha} = \hat{\alpha}_\mathrm{max}(0)$. Therefore, in this case the effect of a weak external airflow is to slightly decrease both contact angles (but to decrease θ_2 more than θ_1), and to slightly increase the maximum thickness h_m and to move the position at which it occurs x_m slightly downslope, i.e. to skew the ridge downslope while simultaneously pushing it down at its edges and pulling it up at its middle as in the case of a horizontal substrate. We will consider the effect of the external airflow in more detail in Subsection 2.3.1.3 below.

2.3.1.3 The General Case of Non-Zero External Airflow ($\Lambda > 0$)

Figure 2.5(a) shows plots of the profile of a pinned ridge as Λ is increased from $\Lambda = 0$ to $\Lambda = \Lambda_{\max} \simeq 1.50$ when $\hat{\alpha} = 20$ and $L = 1$. Figures 2.5(b)–(d) show how the contact angles θ_1 and θ_2, the maximum thickness $h_{\rm m}$ and the relative location of the maximum thickness $x_{\rm m}/L$ vary with Λ for a range of values of $\hat{\alpha}$. In particular, Figure 2.5(b) shows that both θ_1 and θ_2 decrease monotonically with Λ, and that $\mathrm{d}\theta_1/\mathrm{d}\Lambda = 0$ when $\theta_2 = 0$ (i.e. at $\Lambda = \Lambda_{\max}$). Furthermore, Figures 2.5(c) and 2.5(d) show that $h_{\rm m}$ increases monotonically and $x_{\rm m}/L$ decreases monotonically (i.e. the ridge is skewed downslope) except in the special case of a horizontal substrate, $\hat{\alpha} = 0$, in which the ridge is symmetric about $x = x_{\rm m} = L/2$ for all Λ.

Figure 2.6 shows the relationship between $\hat{\alpha}_{\max}$ and $\Lambda_{\max}$ (i.e. between the critical values of $\hat{\alpha}$ and Λ and for which $\theta_2 = 0$) for various values of L; this plot may be interpreted as giving either $\Lambda_{\max}$ as a function of $\hat{\alpha}$ or $\hat{\alpha}_{\max}$ as a function of Λ. In particular, Figure 2.6 shows that, for a given value of L, the largest possible value of $\hat{\alpha}_{\max}$ occurs at $\Lambda = 0$ (i.e. is equal to $\hat{\alpha}_{\max}(0)$), and the largest possible value of $\Lambda_{\max}$ occurs at $\hat{\alpha} = 0$ (i.e. is equal to $\Lambda_{\max}(0)$). For example, in Figures 2.5(b)–(d) the largest possible value of Λ is $\Lambda_{\max}(0) \simeq 2.25$, and the largest possible value of $\hat{\alpha}$ is $\hat{\alpha}_{\max}(0) \simeq 74.40$.

The results shown in Figure 2.5 confirm the trend evident in the limit of a weak external airflow described in Subsection 2.3.1.2, namely that the effect of strengthening the external airflow is to skew the ridge downslope while simultaneously pushing it down at its edges and pulling it up at its middle. In order to understand why the external airflow has this effect on the ridge it is instructive to investigate the external pressure due to the external airflow given by (2.4) in more detail.

Figure 2.7(a) shows the external pressure at the free surface of the ridge and the substrate, $P(x, 0)$, plotted as a function of x for various values of Λ when $\hat{\alpha} = 20$

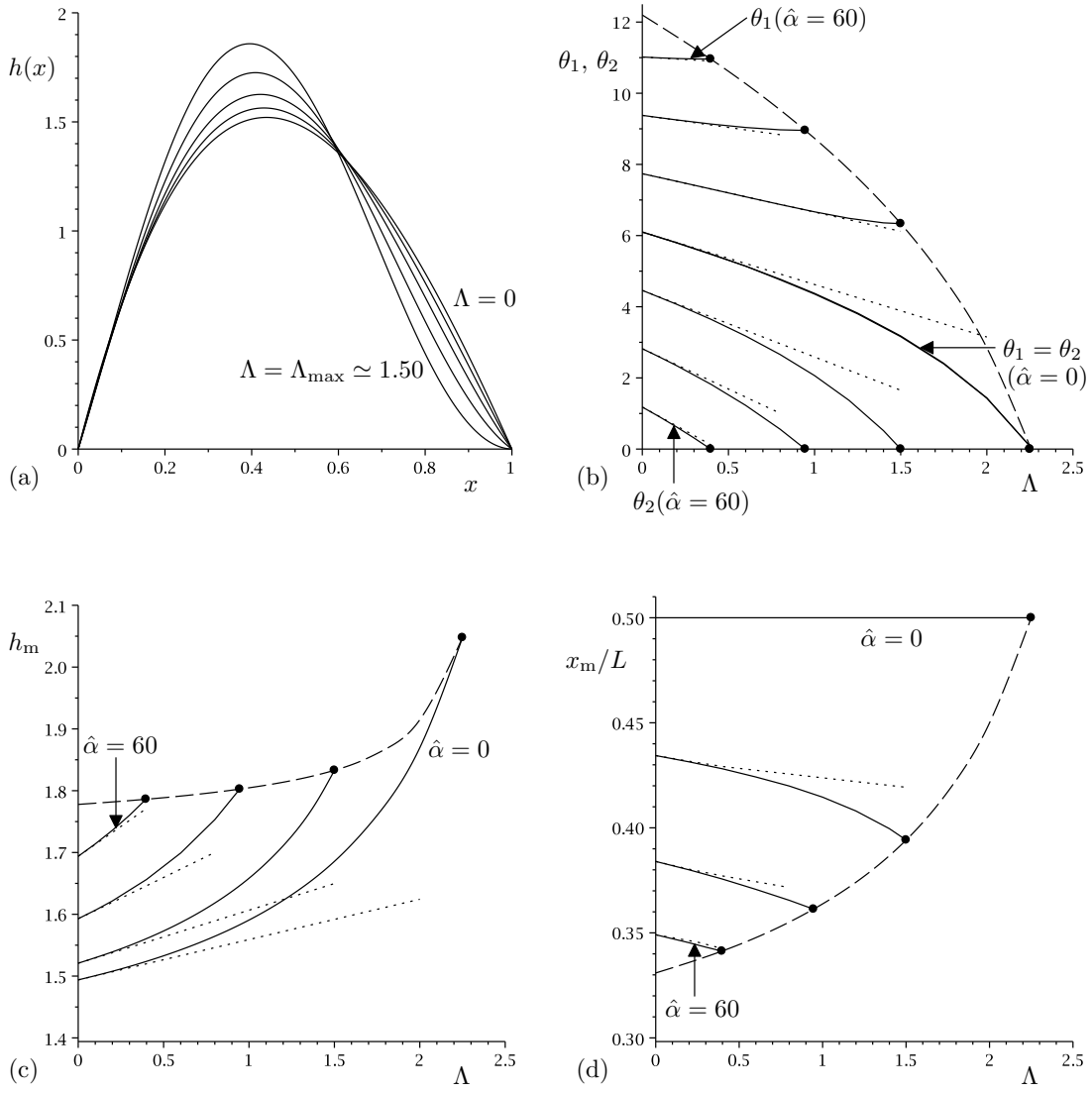

Figure 2.5: Plots of (a) the profile of a pinned ridge for $\Lambda = 0$, 0.4, 0.8, 1.2, $\Lambda_{\max} \simeq 1.50$ when $\hat{\alpha} = 20$ and $L = 1$, together with (b) the contact angles θ_1 and θ_2, (c) the maximum thickness h_{m} and (d) the relative location of the maximum thickness x_{m}/L, all plotted as functions of Λ for a pinned ridge for $\hat{\alpha} = 0$, 20, 40, 60 when $L = 1$ (in which case $\Lambda_{\max}(0) \simeq 2.25$ and $\hat{\alpha}_{\max}(0) \simeq 74.40$). In (b)–(d) the dots indicate the points at which $\theta_2 = 0$ (i.e. when $\Lambda = \Lambda_{\max}$), the dashed lines show the curves on which $\Lambda = \Lambda_{\max}$, and the dotted lines show the first-order-accurate asymptotic solutions in the limit of a weak external airflow, $\Lambda \to 0^+$.

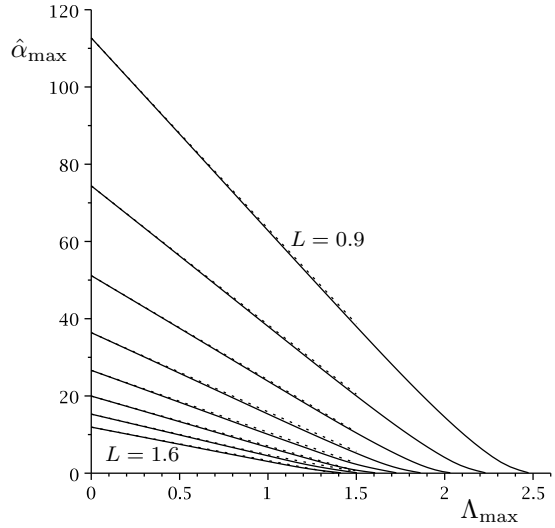

Figure 2.6: Plot of the relationship between the critical inclination angle $\hat{\alpha}_{\max}$ and the critical external airflow strength $\Lambda_{\max}$ for $L = 0.9$, 1, 1.1, 1.2, 1.3, 1.4, 1.5, 1.6. The dotted lines show the first-order-accurate asymptotic solutions in the limit of a weak external airflow, $\Lambda \to 0^+$.

and $L = 1$ (i.e. for the pinned ridge whose profile is shown in Figure 2.5(a)). In particular, Figure 2.7(a) shows that the external pressure near $x = x_{\rm m}$ is lower than the ambient pressure far from the ridge, and that the external pressure near the downslope (leading) and upslope (trailing) edges of the ridge is higher than the ambient pressure. Using the local behaviour (2.13) and (2.14) shows that near the downslope contact line P behaves according to

$$P(x,0) \sim -\Lambda\theta_1 \ln x \to \infty \quad \text{as} \quad x \to 0^+ \tag{2.27}$$

for $\theta_1 > 0$, while near the upslope contact line P behaves according to

$$P(x,0) \sim -\Lambda\theta_2 \ln(L-x) \to \infty \quad \text{as} \quad x \to L^- \tag{2.28}$$

for $\theta_2 > 0$ and

$$P(x,0) \sim \Lambda_{\max}\kappa_2 L = O(1) \quad \text{as} \quad x \to L^- \tag{2.29}$$

for $\theta_2 = 0$, i.e. a non-zero contact angle leads to a logarithmic singularity in $P(x,0)$ at the corresponding contact line. Figure 2.7(b) shows the external pressure, $P(x,Y)$, plotted as a function of Y for various values of x in the range

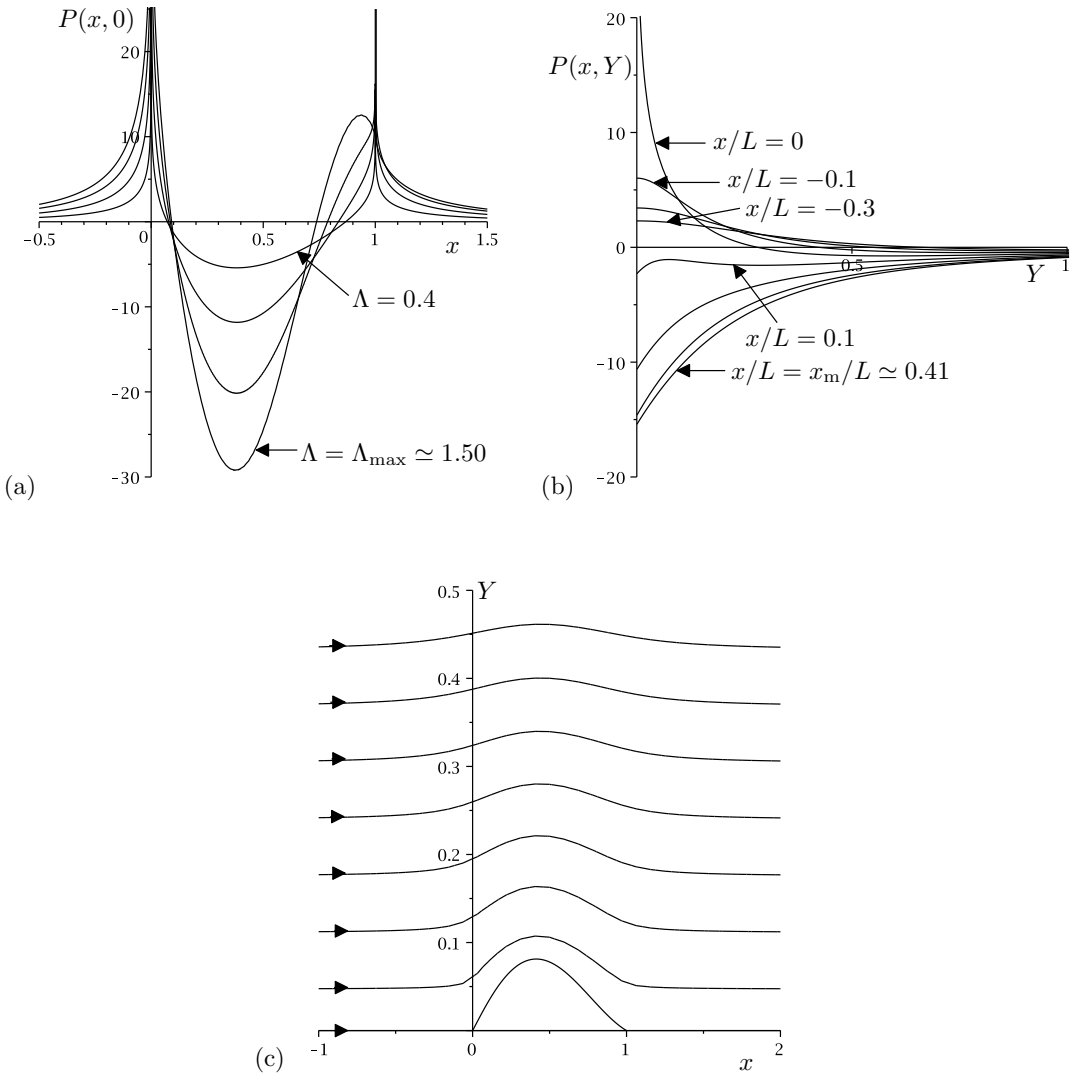

Figure 2.7: Plots of (a) the external pressure at the free surface of the ridge and the substrate, $P(x,0)$, as a function of x for $\Lambda = 0$, 0.4, 0.8, 1.2, $\Lambda_{\max} \simeq 1.50$ when $\hat{\alpha} = 20$ and $L = 1$, (b) the external pressure, $P(x,Y)$, as a function of Y at $x/L = -0.3$, -0.2, -0.1, 0, 0.1, 0.2, 0.3, $x_{\rm m}/L \simeq 0.41$ when $\Lambda = 1$, $\hat{\alpha} = 20$ and $L = 1$, and (c) the streamlines of the external airflow passing over the ridge when $\Lambda = 1$, $\hat{\alpha} = 20$, $L = 1$ and $\epsilon = 0.05$.

$-0.3 \leq x/L \leq x_{\rm m}/L \simeq 0.41$ when $\Lambda = 1$, $\hat{\alpha} = 20$ and $L = 1$. In particular, Figure 2.7(b) shows that $P(x_{\rm m}, Y)$ is negative at $Y = 0$ and increases monotonically towards zero as Y increases. Figure 2.7(b) also shows that $P(0, Y)$ is large and positive near $Y = 0$ and decreases towards zero as Y increases. $P(L, Y)$ has qualitatively the same behaviour as $P(0, Y)$, but for clarity values of x/L greater than $x_{\rm m}/L \simeq 0.41$ are not shown in Figure 2.7(b). Figure 2.7(c) shows the streamlines of the external airflow passing over the ridge plotted using (2.2) when $\Lambda = 1$, $\hat{\alpha} = 20$, $L = 1$ and $\epsilon = 0.05$. Far upstream and downstream of the ridge the flow is uniform and so the streamlines are parallel to the substrate, while near $x = x_{\rm m}$ the curvature of the streamlines is (slightly) negative and so, given that the pressure increases in the direction away from the centre of curvature, the pressure there is (slightly) smaller than that of the uniform stream. Hence, the free surface tends to be pulled up near $x = x_{\rm m}$ (i.e. $h_{\rm m}$ increases). Similarly, near the contact lines the streamline curvature is (slightly) positive and so the pressure near the contact lines is (slightly) larger than that of the uniform stream. Hence, the free surface tends to be pushed down (i.e. both θ_1 and θ_2 decrease) near the contact lines.

2.3.2 A Ridge that De-Pins at its Upslope Contact Line

In this Subsection we study a ridge that de-pins at its upslope contact line for increasing Λ.

As the strength of the external airflow is increased from zero the ridge initially deforms but remains pinned with constant width as described in Subsection 2.3.1. However, since the contact angles θ_1 and θ_2 ($\leq \theta_1$) are both monotonically decreasing functions of Λ, eventually at a critical external airflow strength denoted by $\Lambda = \Lambda_{\rm R}$ and satisfying $\Lambda_{\rm R} \leq \Lambda_{\rm max}$, the upslope contact angle θ_2 becomes equal to the retreating contact angle $\theta_{\rm R}$ and the upslope contact line de-pins. As the strength of the external airflow is increased from $\Lambda = \Lambda_{\rm R}$ the ridge continues to

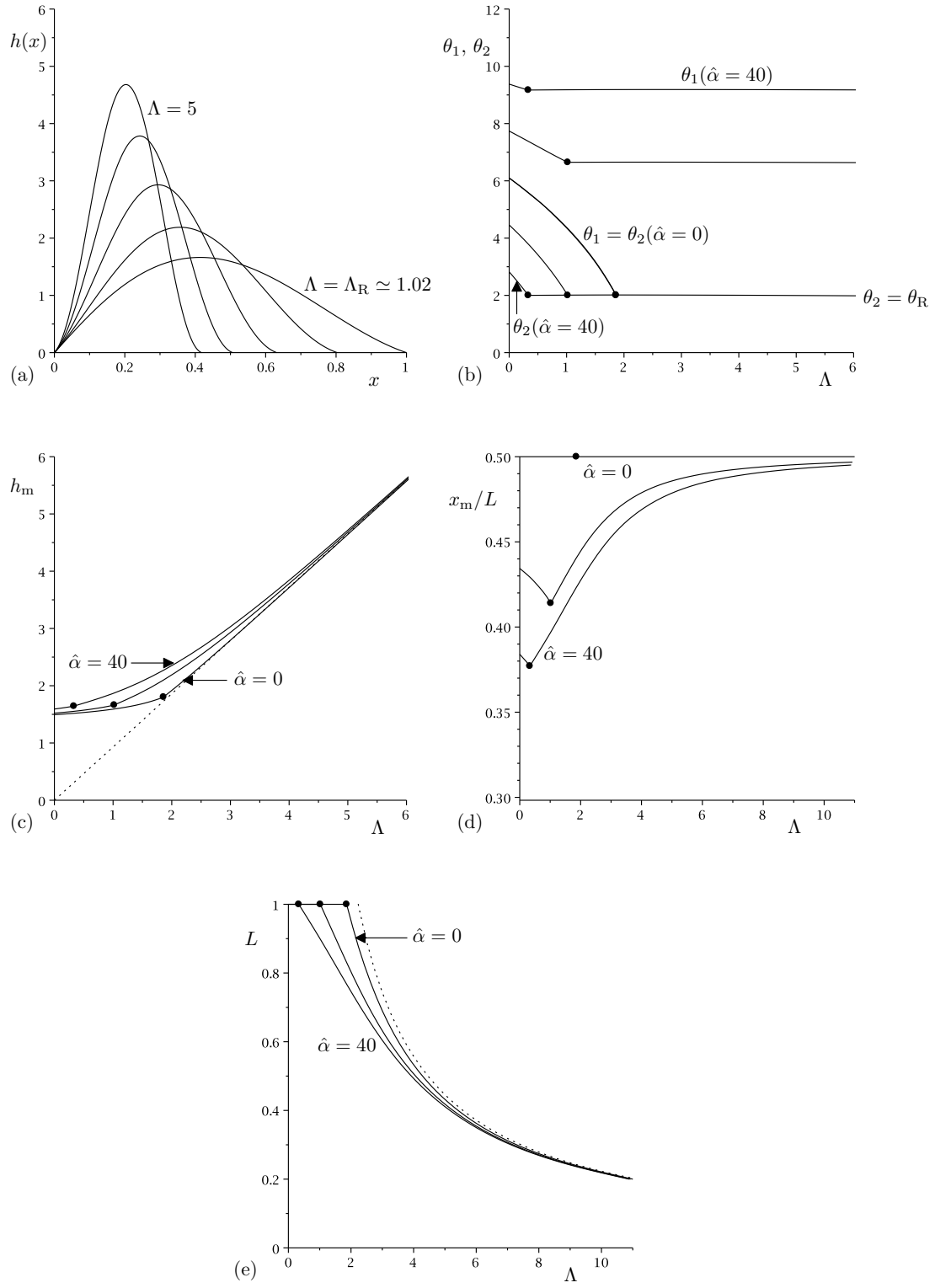

Figure 2.8: Plots of (a) the profile of a de-pinned ridge for $\Lambda = \Lambda_{\rm R} \simeq 1.02$, 2, 3, 4, 5 when $\hat{\alpha} = 20$ and $\theta_{\rm R} = 2$, together with (b) the contact angles θ_1 and θ_2, (c) the maximum thickness $h_{\rm m}$, (d) the relative location of the maximum thickness $x_{\rm m}/L$ and (e) the width L, all plotted as functions of Λ for a ridge whose upslope contact line de-pins for $\hat{\alpha} = 0$, 20, 40 when $\theta_{\rm R} = 2$ (in which case $\hat{\alpha}_{\max}(0) \simeq 50.01$). In (b)–(e) the dots indicate the points at which the upslope contact line de-pins (i.e. when $\Lambda = \Lambda_{\rm R}$ and $\theta_2 = \theta_{\rm R}$), and in (c)–(e) the dotted lines show the leading order asymptotic solutions in the limit of a strong airflow, $\Lambda \to \infty$, given by (c) $h_{\rm m} \simeq 0.94\Lambda \to \infty$, (d) $x_{\rm m}/L = 1/2$ (which coincides with the solution in the case $\hat{\alpha} = 0$) and (e) $L \simeq 2.20\Lambda^{-1} \to 0^+$ for all $\hat{\alpha}$.

deform but now with varying width L. Figure 2.8(a) shows plots of the profile of a de-pinned ridge as Λ is increased from $\Lambda = \Lambda_{\rm R} \simeq 1.02$ when $\hat{\alpha} = 20$ and $\theta_{\rm R} = 2$. Note that for clarity the corresponding pinned ridge profiles for $0 \leq \Lambda < \Lambda_{\rm R}$ are not shown in Figure 2.8(a), but examples are, of course, shown in Figure 2.5(a). Figures 2.8(b)–(e) show how the contact angles θ_1 and θ_2, the maximum thickness $h_{\rm m}$, the relative location of the maximum thickness $x_{\rm m}/L$ and the width L vary with Λ for a range of values of $\hat{\alpha}$ when $\theta_{\rm R} = 2$. Note that for $\Lambda < \Lambda_{\rm R}$ (i.e. to the left of the dots denoting the points at which the upslope contact line de-pins), the curves in Figures 2.8(b)–(d) are, of course, identical to the corresponding curves for a pinned ridge shown in Figures 2.5(b)–(d). In particular, Figure 2.8(b) shows that after the contact line has de-pinned (i.e. for $\Lambda > \Lambda_{\rm R}$) the contact angles $\theta_1 = (\theta_{\rm R}^2 + 2V\hat{\alpha})^{1/2}$ and $\theta_2 = \theta_R$ are both independent of the value of Λ. Moreover, Figures 2.8(c)–(e) show that while $h_{\rm m}$ and L are monotonically increasing and decreasing functions of Λ, respectively, $x_{\rm m}/L$ decreases to a minimum value at $\Lambda = \Lambda_{\rm R}$ before increasing towards the limiting value of $x_{\rm m}/L = 1/2$ as Λ becomes large.

In the limit of a strong external airflow, $\Lambda \to \infty$, the numerically calculated solutions shown in Figure 2.8 suggest that the ridge becomes infinitely narrow like $L = O(\Lambda^{-1}) \to 0^+$ and infinitely thick like $h_{\rm m} = O(\Lambda) \to \infty$ with $x_{\rm m}/L \to 1/2^-$. To investigate the behaviour of the ridge in this limit we therefore rescale the variables according to

$$\begin{gathered} L = \Lambda^{-1}\bar{L}, \quad x = \Lambda^{-1}\bar{L}\bar{x}, \quad x_{\rm m} = \Lambda^{-1}\bar{L}\bar{x}_{\rm m}, \quad \xi = \Lambda^{-1}\bar{L}\bar{\xi}, \\ h = \Lambda\bar{L}^{-1}\bar{h}, \quad h_{\rm m} = \Lambda\bar{L}^{-1}\bar{h}_{\rm m}. \end{gathered} \tag{2.30}$$

At leading order in the limit $\Lambda \to \infty$ the effect of gravity is negligible, and equations (2.10) and (2.9) become

$$\bar{h}''' + \bar{L}\frac{\rm d}{{\rm d}\bar{x}}\int_0^1 \frac{\bar{h}'(\bar{\xi})}{\bar{x} - \bar{\xi}}\,{\rm d}\bar{\xi} = 0 \tag{2.31}$$

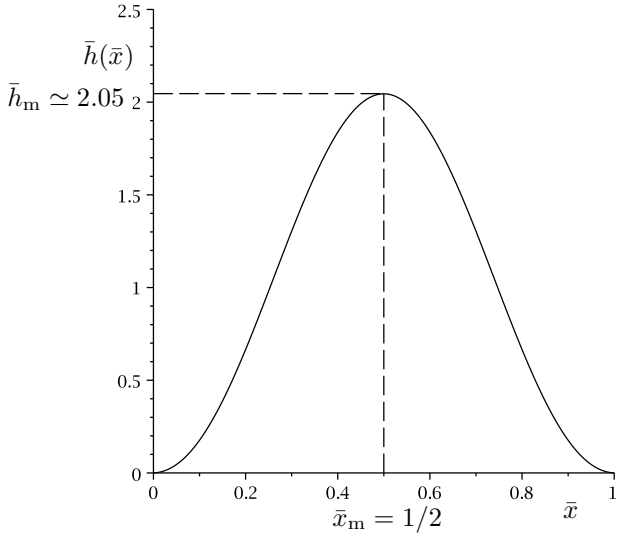

Figure 2.9: Plot of the leading order scaled ridge profile $\bar{h}(\bar{x})$ in the limit of a strong external airflow, $\Lambda \to \infty$, obtained by solving (2.31) subject to (2.32) numerically.

subject to

$$\bar{h}(0) = 0, \quad \bar{h}(1) = 0, \quad \bar{h}'(1) = 0, \quad \int_0^1 \bar{h}\,\mathrm{d}\bar{x} = V, \tag{2.32}$$

where the scaled width $\bar{L}$ must be calculated as part of the solution. Equation (2.31) was solved subject to (2.32) numerically to obtain the solution for the leading order scaled ridge profile $\bar{h} = \bar{h}(\bar{x})$, and, in particular, the leading order values $\bar{L} \simeq 2.20$, $\bar{h}_{\rm m} \simeq 2.05$ and $\bar{x}_{\rm m} = 1/2$. Figure 2.9 shows $\bar{h}$ plotted as a function of $\bar{x}$, and, in particular, shows that $\bar{h}$ is symmetric about $\bar{x} = \bar{x}_{\rm m} = 1/2$. The leading order asymptotic solutions for $h_{\rm m} \simeq 0.94\Lambda \to \infty$ and $L \simeq 2.20\Lambda^{-1} \to 0^+$ are shown with dotted lines in Figures 2.8(c) and 2.8(e), while in Figure 2.8(d) the leading order asymptotic solution for $x_{\rm m}/L = 1/2$ coincides with the solution in the case $\hat{\alpha} = 0$. In particular, this asymptotic solution shows how the ridge becomes infinitely narrow and thick and symmetric in the limit of a strong external airflow. While this asymptotic solution is formally valid for arbitrarily large values of Λ, the underlying thin-film approximation will, of course, eventually fail when Λ becomes too large.

2.4 Tilting the Substrate

In this Section we investigate the quasi-static evolution of a large sessile ridge of prescribed constant volume V in the presence of an external airflow of constant strength Λ as the substrate is gradually tilted (i.e. as the angle of inclination of the substrate $\hat{\alpha}$ to the horizontal is gradually increased from zero). Like in Subsection 2.3.1, in Subsection 2.4.1 we again consider a pinned ridge with pinned contact lines, and hence constant width L but variable contact angles θ_1 and θ_2. However, unlike in Subsection 2.3.1, in which we found that increasing Λ decreases both θ_1 and θ_2, we will find that increasing $\hat{\alpha}$ increases θ_1 and decreases θ_2; moreover, as the general form of the solution for the ridge profile (2.17) shows, θ_1 and θ_2 both vary linearly with $\hat{\alpha}$. Like in Section 2.3, in reality, the contact lines will not remain pinned for all values of $\hat{\alpha} \leq \hat{\alpha}_{\max}$ (i.e. for all values of $\theta_2 \geq 0$). In practice, either θ_1 will reach θ_{A} or θ_2 will reach θ_{R} and the corresponding contact line or lines will de-pin. For definiteness we assume that θ_1 and θ_2 satisfy $\theta_{\mathrm{R}} \leq \theta_{1,2} \leq \theta_{\mathrm{A}}$ when $\hat{\alpha} = 0$, i.e. that the ridge is always pinned when the substrate is horizontal. Unlike in Section 2.3, in which, in general, θ_2 always reaches θ_{R} first as Λ is increased, now it is possible *either* for θ_2 to reach θ_{R} *or* for θ_1 to reach θ_{A} first as $\hat{\alpha}$ is increased. After de-pinning we assume that either θ_2 remains equal to θ_{R} and hence from (2.16) that $\theta_1 = (\theta_{\mathrm{R}}^2 + 2V\hat{\alpha})^{1/2}$ $(\geq \theta_{\mathrm{R}})$ is an increasing function of $\hat{\alpha}$, or θ_1 remains equal to θ_{A} and hence from (2.16) that $\theta_2 = (\theta_{\mathrm{A}}^2 - 2V\hat{\alpha})^{1/2}$ $(\leq \theta_{\mathrm{A}})$ is a decreasing function of $\hat{\alpha}$, as appropriate. In Subsection 2.4.2 we consider the general situation in which both contact lines eventually de-pin, while in Subsections 2.4.3 and 2.4.4 we consider the special cases in which only the downslope contact line de-pins and only the upslope contact line de-pins, respectively.

2.4.1 A Pinned Ridge

Figure 2.10(a) shows plots of the profile of a pinned ridge as $\hat{\alpha}$ is increased from $\hat{\alpha} = 0$ to $\hat{\alpha}_{\max} \simeq 38.02$ when $\Lambda = 1$ and $L = 1$. Figures 2.10(b)–(d) show how θ_1, θ_2, $h_{\rm m}$ and $x_{\rm m}/L$ vary with $\hat{\alpha}$ for a range of values of Λ. In particular, Figure 2.10(b) shows that θ_1 increases linearly and θ_2 decreases linearly with $\hat{\alpha}$. Furthermore, Figures 2.10(c) and 2.10(d) show that $h_{\rm m}$ increases monotonically and $x_{\rm m}/L$ decreases monotonically with $\hat{\alpha}$ (i.e. the ridge is skewed downslope as the substrate is tilted). Note that, as in Figures 2.5(b)–(d) discussed previously in Subsection 2.4.1 (which correspond to the same values of L and V), in Figures 2.10(b)–(d) the largest possible value of Λ is $\Lambda_{\max}(0) \simeq 2.25$, and the largest possible value of $\hat{\alpha}$ is $\hat{\alpha}_{\max}(0) \simeq 74.40$.

2.4.2 A Ridge that Eventually De-Pins at Both of its Contact Lines

In the general case in which $\theta_{\rm A}$ is finite and $\theta_{\rm R}$ is non-zero, the ridge eventually de-pins at both of its contact lines for increasing $\hat{\alpha}$, but the order in which the contact lines de-pin depends on the value of Λ. Specifically, if θ_1 reaches $\theta_{\rm A}$ at some value $\hat{\alpha} = \hat{\alpha}_{\rm A}(\Lambda)$ $(< \hat{\alpha}_{\max}(\Lambda))$, before θ_2 reaches $\theta_{\rm R}$, then the downslope contact line will de-pin first, but if θ_2 reaches $\theta_{\rm R}$ at some value $\hat{\alpha} = \hat{\alpha}_{\rm R}(\Lambda)$ $(< \hat{\alpha}_{\max}(\Lambda))$, before θ_1 reaches $\theta_{\rm A}$, then the upslope contact line will de-pin first. Regardless of which contact line de-pins first, the second contact line de-pins when *both* $\theta_1 = \theta_{\rm A}$ *and* $\theta_2 = \theta_{\rm R}$, and hence from the transverse force balance (2.16) this always occurs at $\hat{\alpha} = \hat{\alpha}_{\rm AR}$, where

$$\hat{\alpha}_{\rm AR} = \frac{\theta_{\rm A}^2 - \theta_{\rm R}^2}{2V}, \tag{2.33}$$

which is independent of the value of Λ, and for $\hat{\alpha} > \hat{\alpha}_{\rm AR}$ there are no steady solutions of the kind considered here. There is a critical value of Λ, denoted by

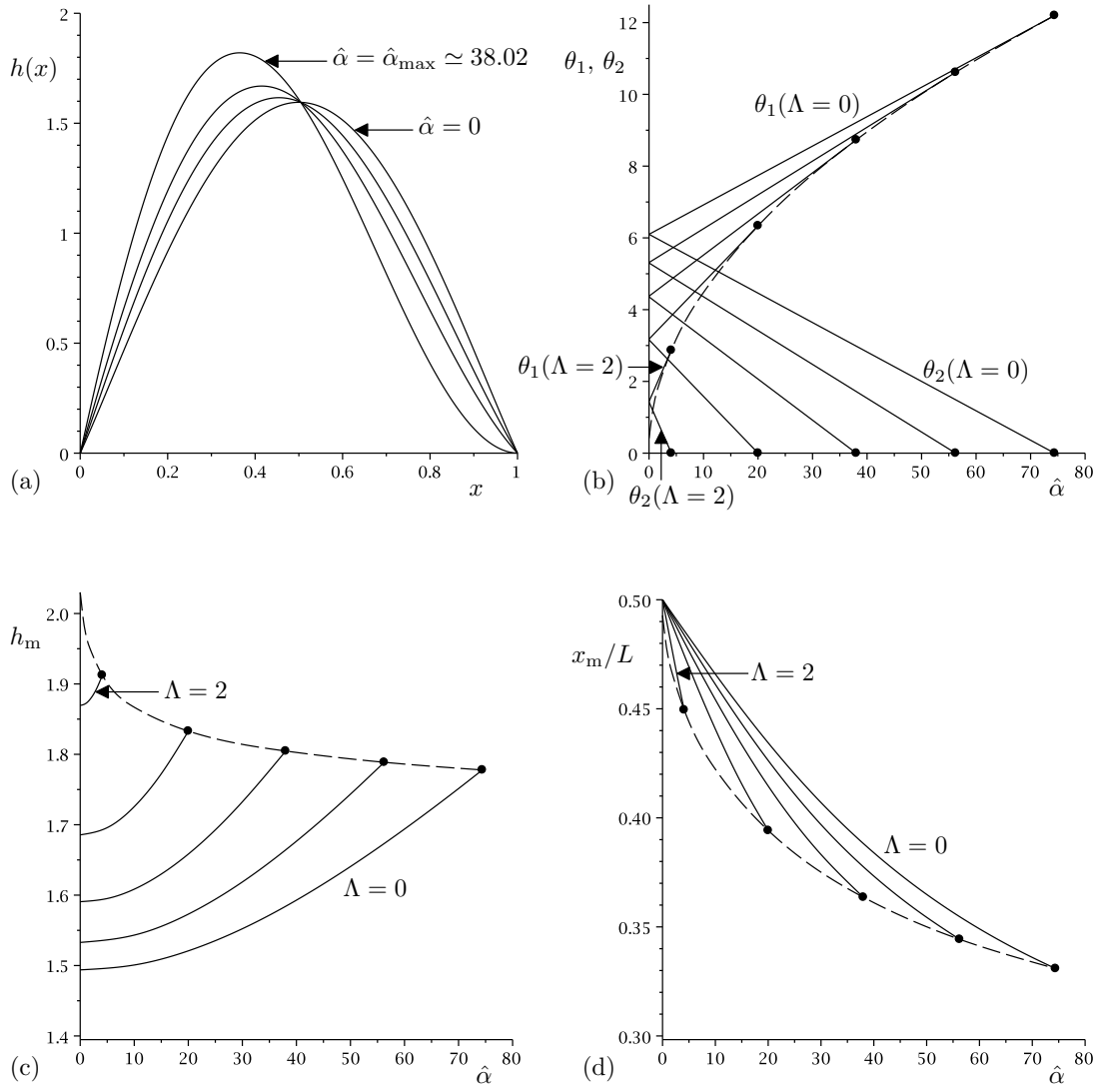

Figure 2.10: Plots of (a) the profile of a pinned ridge for $\hat{\alpha} = 0$, 10, 20, $\hat{\alpha}_{\max} \simeq 38.02$ when $\Lambda = 1$ and $L = 1$, together with (b) the contact angles θ_1 and θ_2, (c) the maximum thickness h_m and (d) the relative location of the maximum thickness x_m/L, all plotted as functions of $\hat{\alpha}$ for a pinned ridge for $\Lambda = 0$, 0.5, 1, 1.5 and 2 when $L = 1$ (in which case $\Lambda_{\max}(0) \simeq 2.25$ and $\hat{\alpha}_{\max}(0) \simeq 74.40$). In (b)–(d) the dots indicate the points at which $\theta_2 = 0$ (i.e. when $\hat{\alpha} = \hat{\alpha}_{\max}$) and the dashed lines show the curves on which $\hat{\alpha} = \hat{\alpha}_{\max}$.

$\Lambda_{\rm AR}$, for which both contact lines de-pin simultaneously as $\hat{\alpha}$ is increased (i.e. $\theta_1 = \theta_{\rm A}$ and $\theta_2 = \theta_{\rm R}$ simultaneously for the first time at $\hat{\alpha} = \hat{\alpha}_{\rm AR}$), and the value of $\Lambda_{\rm AR}$ determines which of the two contact lines de-pin first for increasing $\hat{\alpha}$. Specifically, if $\Lambda < \Lambda_{\rm AR}$ then the downslope contact line de-pins first, while if $\Lambda > \Lambda_{\rm AR}$ then the upslope contact line de-pins first.

Figures 2.11(a) and 2.11(b) show plots of the profile of a ridge as $\hat{\alpha}$ is increased from $\hat{\alpha} = 0$ to $\hat{\alpha} = \hat{\alpha}_{\rm AR} = 45/2 = 22.50$ in the cases $\Lambda < \Lambda_{\rm AR}$ and $\Lambda > \Lambda_{\rm AR}$, respectively, when $\theta_{\rm A} = 7$ and $\theta_{\rm R} = 2$. Figures 2.11(c)–(f) show how θ_1 and θ_2, $h_{\rm m}$, $x_{\rm m}/L$ and L vary with $\hat{\alpha}$ for a range of values of Λ when $\theta_{\rm A} = 7$ and $\theta_{\rm R} = 2$. Note that until the first contact line de-pins (i.e. to the left of the leftmost dots denoting the points at which the first contact line de-pins), the curves in Figures 2.11(c)–(e) are, of course, identical to the corresponding curves for a pinned ridge shown in Figures 2.10(b)–(d). In particular, Figures 2.11(c) and 2.11(f) show that if $\Lambda < \Lambda_{\rm AR} \simeq 0.93$ then the downslope contact line de-pins first and the width of the ridge increases after de-pinning, if $\Lambda > \Lambda_{\rm AR}$ then the upslope contact line de-pins first and the width of the ridge decreases after de-pinning, and if $\Lambda = \Lambda_{\rm AR}$ then both contact lines de-pin simultaneously.

2.4.3 A Ridge that De-Pins Only at its Downslope Contact Line

In the special case when $\theta_{\rm R} = 0$ the upslope contact line remains pinned for all values of $\theta_2 \geq 0$, while the downslope contact line de-pins at $\hat{\alpha} = \hat{\alpha}_{\rm A}$. Figure 2.12(a) shows plots of the profile of a ridge which has de-pinned at its downslope contact line as $\hat{\alpha}$ is increased from $\hat{\alpha} = \hat{\alpha}_{\rm A} \simeq 23.08$ to $\hat{\alpha} = \hat{\alpha}_{\rm Amax} = 49/2 = 24.50$ when $\Lambda = 1$, $\theta_{\rm A} = 7$ and $\theta_{\rm R} = 0$. Figures 2.12(b)–(e) show how θ_1 and θ_2, $h_{\rm m}$, $x_{\rm m}/L$ and L vary with $\hat{\alpha}$ for a range of values of Λ when $\theta_{\rm A} = 7$ and $\theta_{\rm R} = 0$. In particular, Figure 2.12(f) shows that the width of the ridge always increases with

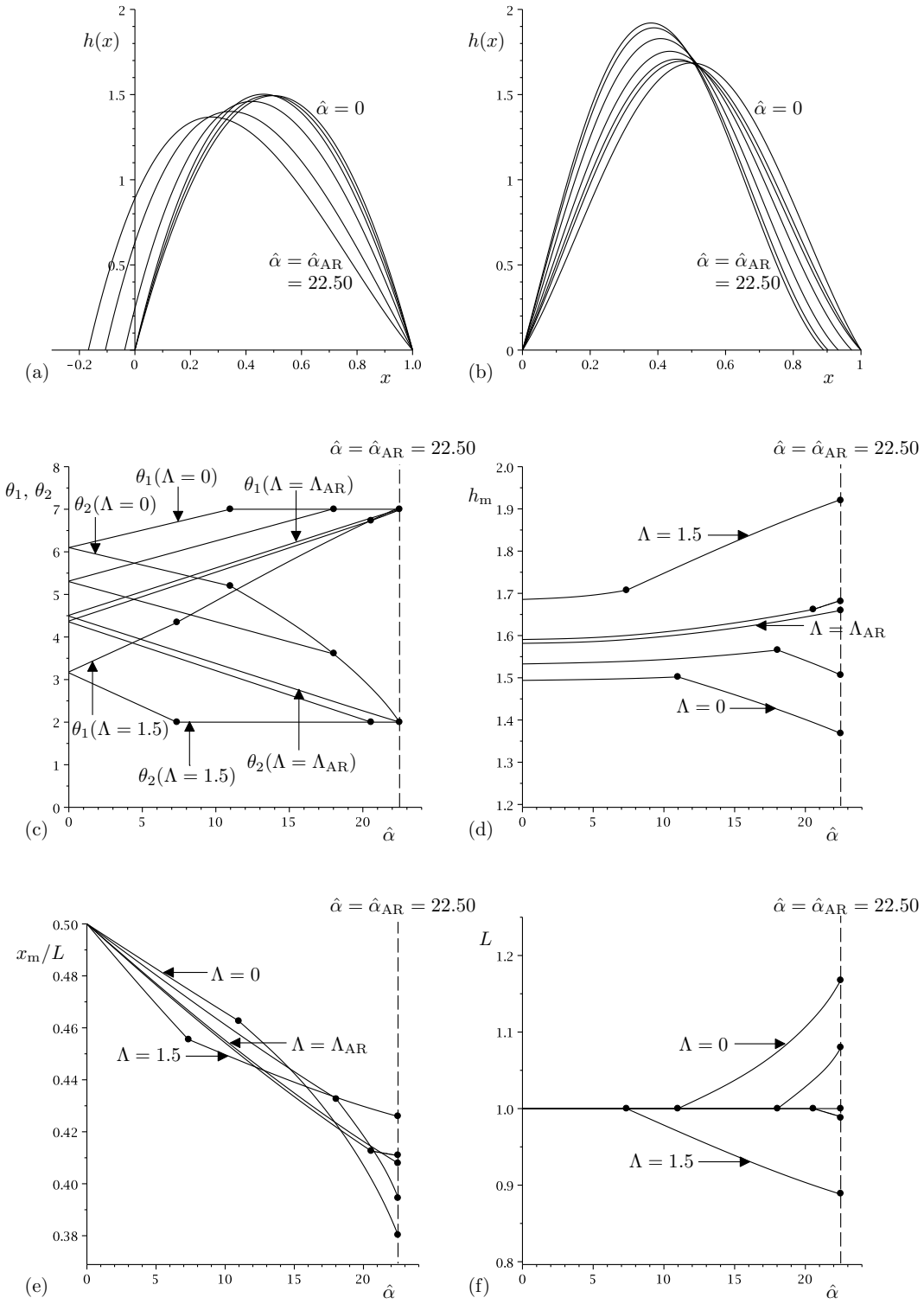

Figure 2.11: Plots of (a) the profile of a ridge which first de-pins at its downslope contact line for $\hat{\alpha} = 0$, 5, $\hat{\alpha}_{\rm A} \simeq 10.99$, 15, 20, $\hat{\alpha}_{\rm AR} = 22.50$ and $\Lambda = 0$ ($< \Lambda_{\rm AR} \simeq 0.93$), (b) the profile of a ridge which first de-pins at its upslope contact line for $\hat{\alpha} = 0$, 5, $\hat{\alpha}_{\rm R} \simeq 7.34$, 10, 15, 20, $\hat{\alpha}_{\rm AR} = 22.50$ and $\Lambda = 1.5$ ($> \Lambda_{\rm AR}$), when $\theta_{\rm A} = 7$ and $\theta_{\rm R} = 2$, together with (c) the contact angles θ_1 and θ_2, (d) the maximum thickness $h_{\rm m}$, (e) the relative location of the maximum thickness $x_{\rm m}/L$, and (f) the width L, all plotted as functions of $\hat{\alpha}$ for a ridge whose upslope and downslope contact lines de-pin for $\Lambda = 0$, 0.5, $\Lambda_{\rm AR} \simeq 0.93$, 1, 1.5 when $\theta_{\rm A} = 7$ and $\theta_{\rm R} = 2$. In (c)–(f) the first (i.e. the leftmost) dot on each curve indicates the point at which the first contact line (which can be either the upslope or downslope contact line) de-pins, the second (i.e. the rightmost) dot indicates the point $\hat{\alpha} = \hat{\alpha}_{\rm AR}$ at which the second contact line de-pins, and the vertical dashed line indicates the value $\hat{\alpha} = \hat{\alpha}_{\rm AR} = 22.50$ beyond which there are no steady solutions of the kind considered here.

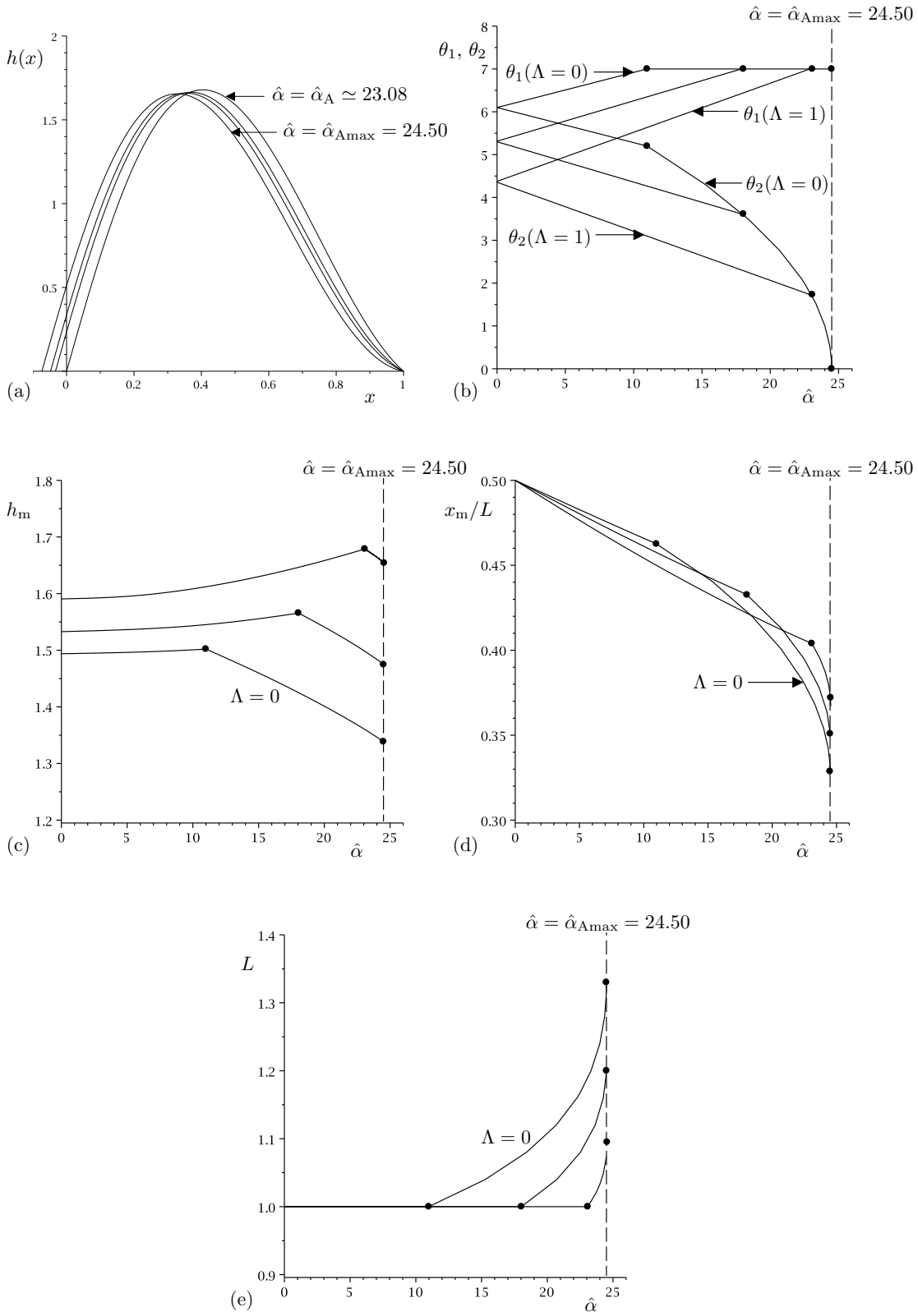

Figure 2.12: Plots of (a) the profile of a ridge which has de-pinned at its downslope contact line for $\hat{\alpha} = \hat{\alpha}_{\rm A} \simeq 23.08$, 24, 24.25, $\hat{\alpha}_{\rm Amax} = 24.50$ when $\Lambda = 1$, $\theta_{\rm A} = 7$ and $\theta_{\rm R} = 0$, together with (b) the contact angles θ_1 and θ_2, (c) the maximum thickness $h_{\rm m}$, (d) the relative location of the maximum thickness $x_{\rm m}/L$ and (e) the width L, all plotted as functions of $\hat{\alpha}$ for a ridge whose downslope contact line de-pins for $\Lambda = 0$, 0.5, 1 when $\theta_{\rm A} = 7$ and $\theta_{\rm R} = 0$. In (b)–(e) the first (i.e. the leftmost) dot on each curve indicates the point at which the downslope contact de-pins, the second (i.e. the rightmost) dot indicates the point $\hat{\alpha} = \hat{\alpha}_{\rm Amax}$ at which $\theta_2 = 0$, and the vertical dashed line indicates the value $\hat{\alpha} = \hat{\alpha}_{\rm Amax} = 24.50$ beyond which there are no steady solutions on the kind considered here.

$\hat{\alpha}$ after de-pinning.

The upslope contact angle eventually reaches the value $\theta_2 = \theta_R = 0$ when $\theta_A^2 = 2V\hat{\alpha}$, and so, as Figures 2.12(b)–(e) show, there is a maximum value of $\hat{\alpha} = \hat{\alpha}_{Amax} = \theta_A^2/2V$ ($= \hat{\alpha}_{AR}$ evaluated at $\theta_R = 0$), which is independent of the value of Λ, at which the ridge achieves its maximum width and beyond which there are no steady solutions of the kind considered here.

2.4.4 A Ridge that De-Pins Only at its Upslope Contact Line

In the special case when $\theta_A = \infty$ the downslope contact line remains pinned for all values of θ_1, while the upslope contact line de-pins at $\hat{\alpha} = \hat{\alpha}_R$. Figure 2.13(a) shows plots of profile of a ridge which has de-pinned at its upslope contact line as $\hat{\alpha}$ is increased from $\hat{\alpha} = \hat{\alpha}_R \simeq 20.58$ when $\Lambda = 1$, $\theta_A = \infty$ and $\theta_R = 2$. Figures 2.13(b)–(e) show how θ_1 and θ_2, h_m, x_m/L and L vary with $\hat{\alpha}$ for a range of values of Λ when $\theta_A = \infty$ and $\theta_R = 2$. In particular, Figure 2.13(f) shows that the width of the ridge always decreases with $\hat{\alpha}$ after de-pinning.

In the limit of a large angle of inclination of the substrate, $\hat{\alpha} \to \infty$, the numerically calculated solutions shown in Figure 2.13 suggest that the ridge becomes infinitely narrow like $L = O(\hat{\alpha}^{-1/4}) \to 0^+$ and infinitely thick like $h_m = O(\hat{\alpha}^{1/4}) \to \infty$ with $x_m/L \to 1/3^+$. To investigate the behaviour of the ridge in this limit we therefore rescale the variables according to

$$\begin{gathered} L = \hat{\alpha}^{-1/4}\bar{L}, \quad x = \hat{\alpha}^{-1/4}\bar{L}\bar{x}, \quad x_m = \hat{\alpha}^{-1/4}\bar{L}\bar{x}_m, \quad \xi = \hat{\alpha}^{-1/4}\bar{L}\bar{\xi}, \\ h = \hat{\alpha}^{1/4}\bar{L}^{-1}\bar{h}, \quad h_m = \hat{\alpha}^{1/4}\bar{L}^{-1}\bar{h}_m, \quad \theta_1 = \hat{\alpha}^{1/2}\bar{L}^{-2}\bar{\theta}_1. \end{gathered} \tag{2.34}$$

At leading order in the limit $\hat{\alpha} \to \infty$ the effects of the external airflow and of the normal component of gravity are negligible, and equations (2.10) and (2.9) become

$$\bar{h}''' - \bar{L}^4 = 0 \tag{2.35}$$

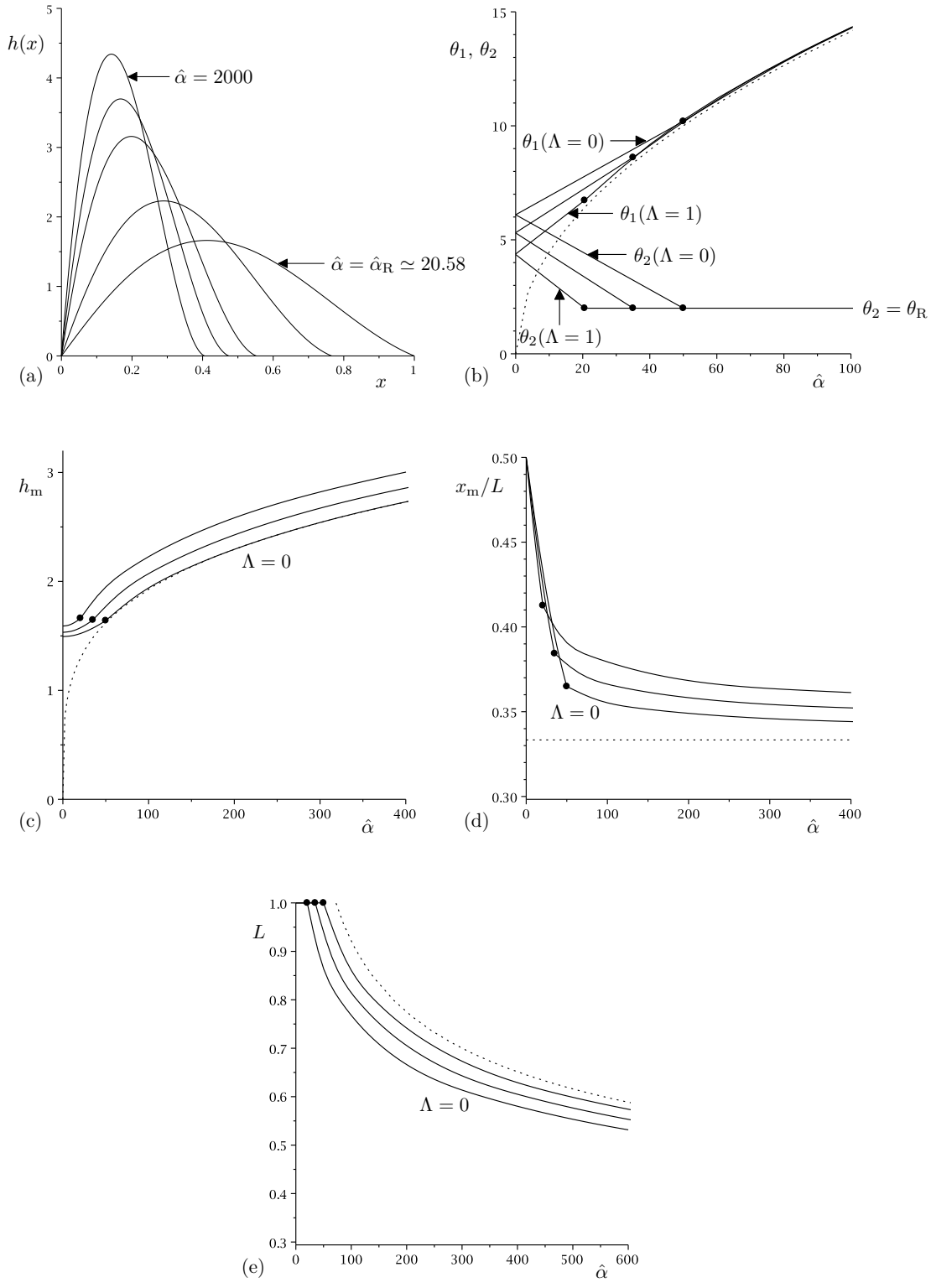

Figure 2.13: Plots of (a) the profile of a ridge which has de-pinned at its upslope contact line for $\hat{\alpha} = \hat{\alpha}_{\rm R} \simeq 20.58$, 100, 500, 1000, 2000 when $\Lambda = 1$, $\theta_{\rm A} = \infty$ and $\theta_{\rm R} = 2$, together with (b) the contact angles θ_1 and θ_2, (c) the maximum thickness $h_{\rm m}$, (d) the relative location of the maximum thickness $x_{\rm m}/L$ and (e) the width L, all plotted as functions of $\hat{\alpha}$ for a ridge whose upslope contact line de-pins for $\Lambda = 0$, 0.5, 1 when $\theta_{\rm A} = \infty$ and $\theta_{\rm R} = 2$. In (b)–(e) the dots on each curve indicate the point at which the upslope contact de-pins, and the dotted curves show the leading order asymptotic solutions in the limit of a large angle of inclination of the substrate, $\hat{\alpha} \to \infty$, given by (b) $\theta_1 \simeq 1.41\hat{\alpha}^{1/2} \to \infty$, (c) $h_{\rm m} \simeq 0.61\hat{\alpha}^{1/4} \to \infty$, (d) $x_{\rm m}/L \to 1/3^+$ and (e) $L \simeq 2.91\hat{\alpha}^{-1/4} \to 0^+$ for all Λ.

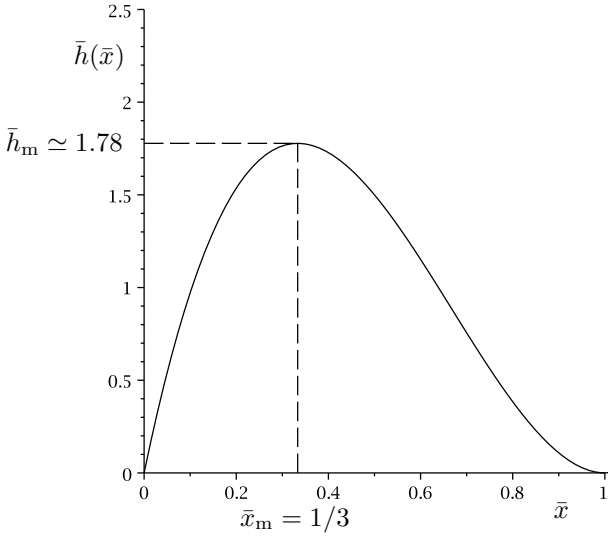

Figure 2.14: Plot of the scaled ridge profile $\bar{h}(\bar{x})$ in the limit of a large angle of inclination of the substrate, $\hat{\alpha} \to \infty$, given by (2.37) and (2.38).

subject to

$$\bar{h}(0) = 0, \quad \bar{h}(1) = 0, \quad \bar{h}'(1) = 0, \quad \int_0^1 \bar{h}\,\mathrm{d}\bar{x} = V, \tag{2.36}$$

where the scaled width $\bar{L}$ must be calculated as part of the solution. Equations (2.35) and (2.36) have the simple exact solution

$$\bar{h} = \frac{\bar{L}^4}{6}\bar{x}(1-\bar{x})^2 \quad \text{where} \quad \bar{L} = (72V)^{1/4} \simeq 2.91V^{1/4}, \tag{2.37}$$

which gives the values

$$\bar{\theta}_1 = \frac{\bar{L}^4}{6} = 12V, \quad \bar{h}_{\rm m} = \frac{2\bar{L}^4}{81} = \frac{16V}{9} \simeq 1.78V, \quad \bar{x}_{\rm m} = \frac{1}{3}. \tag{2.38}$$

Figure 2.14 shows $\bar{h}$ plotted as a function of $\bar{x}$, and, in particular, shows that $\bar{h}$ is skewed downslope with $\bar{x}_{\rm m} = 1/3$. The leading order asymptotic solutions for $\theta_1 = (2V\hat{\alpha})^{1/2} \simeq 1.41\hat{\alpha}^{1/2} \to \infty$, $\theta_2 = 0$, $h_{\rm m} = (16/9)(V^3\hat{\alpha}/72)^{1/4} \simeq 0.61\hat{\alpha}^{1/4} \to \infty$, $x_{\rm m}/L = 1/3$ and $L = (72V/\hat{\alpha})^{1/4} \simeq 2.91\hat{\alpha}^{-1/4} \to 0^+$ are shown with dotted lines in Figures 2.13(b)–(e). In particular, this asymptotic solution shows how the ridge becomes infinitely narrow and thick and is skewed downslope with infinitely large downslope contact angle in the limit of a large angle of inclination of the substrate.

Like the solution in the limit of strong external airflow discussed in Subsection 2.3.2, while this asymptotic solution is formally valid for arbitrarily large values of $\hat{\alpha}$, the underlying thin-film approximation will, of course, eventually fail when $\hat{\alpha}$ becomes too large.

2.5 A Large Pendent Ridge

The equation for the profile of a large pendent ridge on a nearly horizontal substrate (specifically, when $\pi - \alpha = O(\epsilon)$), differs from the corresponding equation for a large sessile ridge (2.10) derived in Section 2.2 only in the sign of the h' term (i.e. the term corresponding to the normal component of gravity), where Λ is again given by (2.11) and $\hat{\alpha}$ (≥ 0) is now defined by

$$\hat{\alpha} = \frac{\pi - \alpha}{\epsilon}. \tag{2.39}$$

This equation is again subject to the boundary conditions (2.9), and equations (2.13)–(2.18) again hold.

In the special case of no external airflow, $\Lambda = 0$, the ridge profile is again given by (2.19), where the functions $h_0 = h_0(x)$ and $h_1 = h_1(x)$ are now given by

$$h_0 = \frac{\sin\dfrac{L-x}{2}\sin\dfrac{x}{2}}{\sin\dfrac{L}{2} - \dfrac{L}{2}\cos\dfrac{L}{2}} \tag{2.40}$$

and

$$h_1 = x - \frac{L\cos\dfrac{L-x}{2}\sin\dfrac{x}{2}}{\sin\dfrac{L}{2}}, \tag{2.41}$$

respectively. The contact angles θ_1 and θ_2 are again given by (2.22), where the function $\gamma = \gamma(L)$ is now defined by

$$\gamma = \frac{1}{2}\left(1 - \frac{L}{2}\cot\frac{L}{2}\right)^{-1}. \tag{2.42}$$

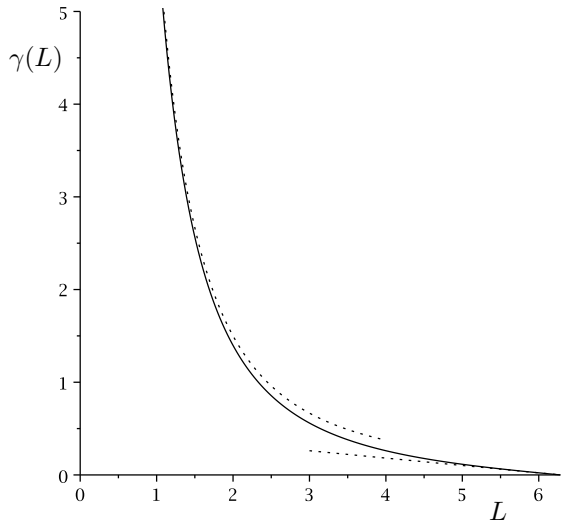

Figure 2.15: Plot of the function $\gamma(L)$ given by (2.42). The dotted curves show the leading order asymptotic behaviour $\gamma \sim 6/L^2 \to \infty$ as $L \to 0^+$ and $\gamma \sim (2\pi - L)/4\pi \to 0^+$ as $L \to 2\pi^-$.

Inspection of (2.42) reveals that, unlike for a sessile ridge (2.23), for a pendent ridge there are multiple branches of solutions. However, γ is a strictly positive, monotonically decreasing function of L in the only interval in which the solutions for h are physically realisable, namely $0 < L \leq 2\pi$, and satisfies $\gamma \sim 6/L^2 \to \infty$ as $L \to 0^+$ and $\gamma \sim (2\pi - L)/4\pi \to 0^+$ as $L \to 2\pi^-$, as shown in Figure 2.15.

The quasi-static evolution of a large pendent ridge as the external airflow is gradually strengthened and as the substrate is gradually tilted is very similar to that of a large sessile ridge described in Sections 2.3 and 2.4, respectively. For example, Figure 2.16 shows how θ_1, θ_2, h_m, x_m/L and L vary with Λ for a range of values of $\hat{\alpha}$ when $\theta_\mathrm{R} = 2$ for both a large sessile and a large pendent ridge. In particular, Figure 2.16 shows that there is little difference between the behaviour of the ridge in the two situations, with the pendent ridge (shown with the dashed lines) generally being slightly thicker, de-pinning at a slightly smaller value of Λ_R, and (after de-pinning occurs) being slightly narrower than the corresponding sessile ridge (shown with the solid lines). Moreover, as Figure 2.16 also shows, at leading order in the limit of a strong external airflow, $\Lambda \to \infty$, the effect of

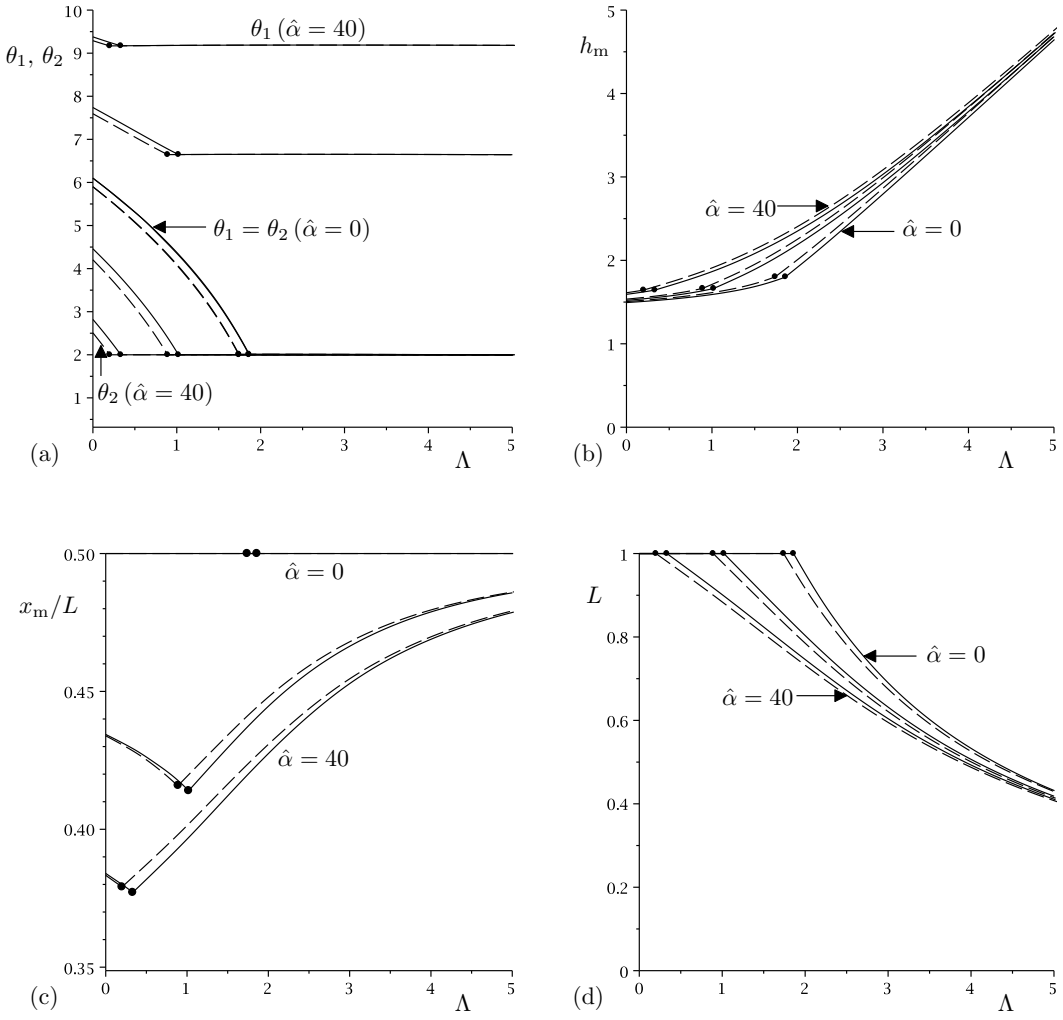

Figure 2.16: Plots of (a) the contact angles θ_1 and θ_2, (b) the maximum thickness $h_{\rm m}$, (c) the relative location of the maximum thickness $x_{\rm m}/L$, and (d) the width L, all plotted as functions of Λ for a ridge whose upslope contact line de-pins for $\hat{\alpha}=0$, 20, 40 when $\theta_{\rm R}=2$. The dots indicate the points at which the upslope contact line de-pins (i.e. when $\Lambda=\Lambda_{\rm R}$ and $\theta=\theta_{\rm R}$). The solid lines show the results for a large sessile ridge for which $\hat{\alpha}=\alpha/\epsilon=O(1)$ and the dashed lines show the results for a large pendent ridge for which $\hat{\alpha}=(\pi-\alpha)/\epsilon=O(1)$.

gravity is negligible and both sessile and pendent ridges behave according to the asymptotic behaviour described in Subsection 2.3.2.

2.6 A Small Ridge

When the substrate is not restricted to being nearly horizontal (specifically, when $\alpha = O(1)$), in both sessile and pendent cases the transverse component of gravity is relatively strong and so only a relatively "small" ridge of width much less than the capillary length ℓ can be supported against gravity by capillary and/or external pressure forces. In this case it is appropriate to choose $L_0 = \sqrt{\epsilon}\ell = V^{1/4}\sqrt{\ell}$ as the characteristic transverse length scale so that the aspect ratio is $\epsilon = \sqrt{V}/\ell \ll 1$, the characteristic pressure scale is $\sqrt{\epsilon}\sigma/\ell = \sqrt{\epsilon}\rho g\ell = \rho g V^{1/4}\sqrt{\ell}$, and at leading order in the limit $\epsilon \to 0$ equation (2.8) becomes

$$h''' - \sin\alpha + \Lambda \frac{\mathrm{d}}{\mathrm{d}x}\int_0^L \frac{h'(\xi)}{x-\xi}\,\mathrm{d}\xi = 0, \tag{2.43}$$

where

$$\Lambda = \frac{\rho_\mathrm{a} U_\infty^2 \sqrt{\epsilon}\ell}{\pi\sigma} = \frac{\rho_\mathrm{a} U_\infty^2 V^{1/4}\sqrt{\ell}}{\pi\sigma}. \tag{2.44}$$

Inspection of (2.43) reveals that $h(x,\alpha) = h(x,\pi-\alpha)$, i.e. a small sessile ridge and a small pendent ridge have the same profile. Comparing (2.43) with the equation for h in the case of a large sessile ridge (2.10) reveals that, as expected, the normal component of gravity (i.e. the h' term) is negligible for a small ridge, while the dimensionless variable $\hat{\alpha}$ is replaced by $\sin\alpha$. Also, comparing (2.44) with (2.11) reveals that U_∞ must be much greater in the case of a small ridge than in the case of a large ridge for the integral term to balance the other terms in (2.43) (since $V^{1/4}\sqrt{\ell} \ll \ell$); physically, this is because the external airflow must be stronger to balance the relatively larger effect of surface tension on a smaller ridge. Near to the contact lines, h again behaves according to (2.13) and (2.14), while the force

balance in the x direction and the form of the free surface are now given by (2.16) and (2.17), respectively, with $\sin\alpha$ replacing $\hat{\alpha}$. In the special case of no external airflow, $\Lambda = 0$,

$$\begin{aligned} h_0 &= \frac{6x\,(L-x)}{L^3}, \\ h_1 &= \frac{x}{12}\,(L-x)\,(L-2x) \end{aligned} \tag{2.45}$$

and

$$\theta_{1,2} = \frac{6V}{L^2} \pm \frac{L^2 \sin\alpha}{12}, \tag{2.46}$$

where again the + sign is taken for θ_1 and the − sign is taken for θ_2. It may readily be deduced from (2.46) that the condition

$$\sin\alpha \leq \frac{72V}{L^4} \tag{2.47}$$

must hold for physically realisable solutions (i.e. for $\theta_2 \geq 0$), and that, unlike in the case of a large ridge, θ_2 will not reach zero for all combinations of prescribed values of L and V, specifically if $72V/L^4 > 1$. The solution for $\Lambda = 0$, given by (2.45)–(2.47), was found by Hocking and Miksis [34] albeit with a slightly different scaling. In the limit of a weak external airflow, $\Lambda \to 0^+$, h is given by (2.24), where H_0 is the $\Lambda = 0$ solution and

$$H_1 = V H_{10} + \sin\alpha\; H_{11}, \tag{2.48}$$

where the functions $H_{10} = H_{10}(x)$ and $H_{11} = H_{11}(x)$ are given by

$$\begin{aligned} H_{10} &= \ln L - \frac{5x\,(L-x)}{2L^2} - \frac{x^2(3L-2x)}{L^3}\ln x - \frac{(L-x)^2\,(L+2x)}{L^3}\ln(L-x)\,, \\ H_{11} &= \frac{Lx}{48}\,(L-2x)\,(L-x) - \frac{x^2(L-x)^2}{24}\ln x + \frac{x^2\,(L-x)^2}{24}\ln(L-x)\,. \end{aligned} \tag{2.49}$$

The plots of H_0 and H_1 are qualitatively similar to those shown in Figure 2.4 except when $72V/L^4 > 1$, in which case $H_0'(L)$ is strictly positive (rather than simply non-negative) and $H_1'(0)$ is strictly negative (rather than simply non-positive).

As previously mentioned, $h(x,\alpha) = h(x,\pi-\alpha)$, and hence we consider only the case of a small sessile ridge with $0 \le \alpha \le \pi/2$ (including the case of a vertical substrate $\alpha = \pi/2$). In Subsection 2.4.2 we found that for a large ridge for sufficiently large $\hat{\alpha}$, both contact lines will de-pin (namely when $\theta_1 = \theta_{\rm A}$ and $\theta_2 = \theta_{\rm R}$). For a small ridge the forcing term in (2.43), namely $\sin\alpha$, is bounded and the contact lines will de-pin at both ends only if $\theta_{\rm A}^2 - \theta_{\rm R}^2 \le 2V$. Figures 2.17(a) and 2.17(b) give numerically calculated plots showing how θ_1 and θ_2 behave as α is increased for various values of Λ with $L = 2$ in the case of a small ridge. In Figure 2.17(a) the values $\theta_{\rm A} = 1.7$ and $\theta_{\rm R} = 1$ were chosen so that $\theta_{\rm A}^2 - \theta_{\rm R}^2 < 2$ and $\sin\alpha_{\rm AR} = (1.7^2 - 1)/2 = 0.945$ (or $\alpha_{\rm AR} \simeq 1.24$, the value of α at which both contact lines de-pin). As in Subsection 2.4.2, the value of Λ is crucial to determining which contact line de-pins first: if $\Lambda < \Lambda_{\rm AR}$ then the downslope contact line de-pins first, if $\Lambda > \Lambda_{\rm AR}$ then the upslope contact line de-pins first, and if $\Lambda = \Lambda_{\rm AR}$ then the contact lines de-pin at the same value of α, namely at $\alpha = \alpha_{\rm AR}$. For these particular parameter values, $\Lambda_{\rm AR} \simeq 0.19$. In Figure 2.17(b) the values $\theta_{\rm A} = 1.7$ and $\theta_{\rm R} = 0.8$ were chosen so that $\theta_{\rm A}^2 - \theta_{\rm R}^2 > 2$. In this case, the value of Λ determines whether the ridge remains pinned, it de-pins only at the upslope contact line, or it de-pins only at the downslope contact line, and an example of each possibility is shown.

Figures 2.18(a) and 2.18(b) show plots of the values of $\sin\alpha_{\rm AR}$ at which the contact lines de-pin. In Figure 2.18(a), $\sin\alpha_{\rm AR}$ is plotted as a function of $\theta_{\rm R}$ for various values of $\theta_{\rm A}$. If $\theta_{\rm A} < \sqrt{2}$ then the range of values that $\sin\alpha_{\rm AR}$ may take is limited, but if $\theta_{\rm A} \ge \sqrt{2}$ then it is possible for $\sin\alpha_{\rm AR}$ to lie anywhere in the interval $0 \le \sin\alpha_{\rm AR} \le 1$. The region to the left of each curve corresponds to the case when only the downslope contact line de-pins. There are no solutions for $\theta_{\rm R} > \theta_{\rm A}$ and there are no solutions "above" each curve since no steady solutions exist for $\alpha > \alpha_{\rm AR}$. In Figure 2.18(b), $\sin\alpha_{\rm AR}$ is plotted as a function of $\theta_{\rm A}$ for

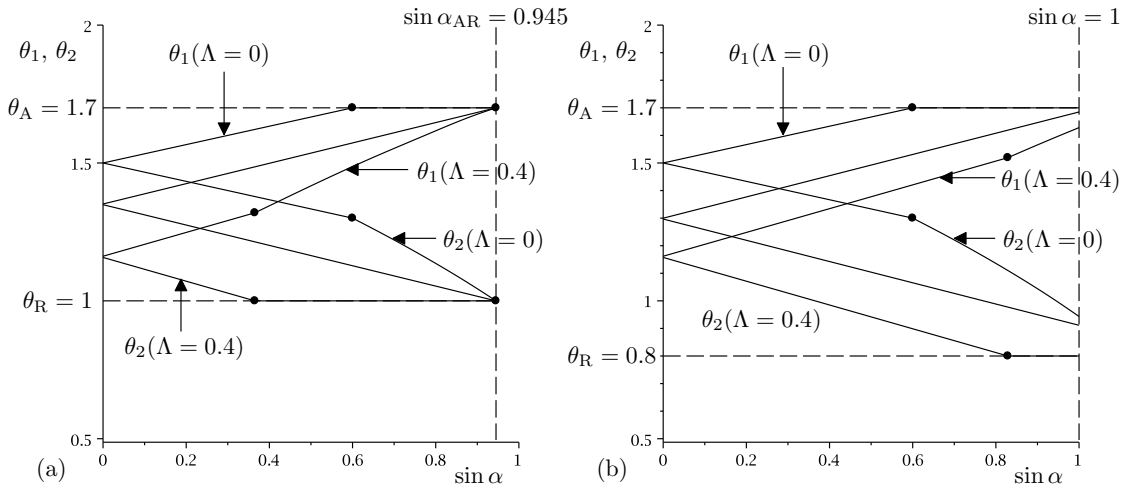

Figure 2.17: Plots of the contact angles θ_1 and θ_2 as functions of $\sin\alpha$ for (a) $\Lambda = 0$, $\Lambda_{\rm AR} \simeq 0.19$, 0.4 when $L = 2$, $\theta_{\rm A} = 1.7$ and $\theta_{\rm R} = 1$ (i.e. $\theta_{\rm A}^2 - \theta_{\rm R}^2 < 2$), and (b) $\Lambda = 0$, 0.2, 0.4 when $L = 2$, $\theta_{\rm A} = 1.7$ and $\theta_{\rm R} = 0.8$ (i.e. $\theta_{\rm A}^2 - \theta_{\rm R}^2 > 2$). The first (i.e. the leftmost) dot on each curve indicates the point at which the first contact line (which can be either the upslope or downslope contact line) de-pins and in (a), the second dot indicates the point $\sin\alpha_{\rm AR} = (1.7^2 - 1)/2 = 0.945$ at which the second contact line de-pins.

various values of $\theta_{\rm R}$. There are no solutions for $\theta_{\rm A} < \theta_{\rm R}$ and there are also no solutions "above" each curve since this corresponds to $\alpha > \alpha_{\rm AR}$. The region to the right of each curve corresponds to the case when only the upslope contact line de-pins. Figure 2.18(c) shows a parameter-plane plot of Λ as a function of L at $\alpha = \pi/2$ (i.e. a vertical substrate) for various values of $\theta_{\rm A}$ and $\theta_{\rm R}$ such that $\theta_{\rm A}^2 - \theta_{\rm R}^2 = 2$. Since θ_1 reaches a maximum and θ_2 reaches a minimum at $\alpha = \pi/2$ then this corresponds to critical value pairs of Λ and L required for the contact lines to de-pin. In the limit of a strong airflow, $\Lambda \to \infty$, $L = O(\Lambda^{-1}) \to \infty$ as given in Subsection 2.3.2. Note that there is a maximum value that L can take so that the contact lines may de-pin, namely $L = (72V)^{1/4} \simeq 2.91V^{1/4}$, as deduced from (2.47), and occurring when $\Lambda = 0$, $\theta_{\rm A} = \sqrt{2}$ and $\theta_{\rm R} = 0$. The regions to the left and to the right of each curve in Figure 2.18(c) are considered separately. In the region to the left of each curve, if $\theta_2 = \theta_{\rm R}$ then $\theta_1 > \theta_{\rm A}$, which means that no steady solutions exist at $\alpha = \pi/2$ since $\sin\alpha_{\rm AR} < 1$; however, if $\theta_1 = \theta_{\rm A}$ then

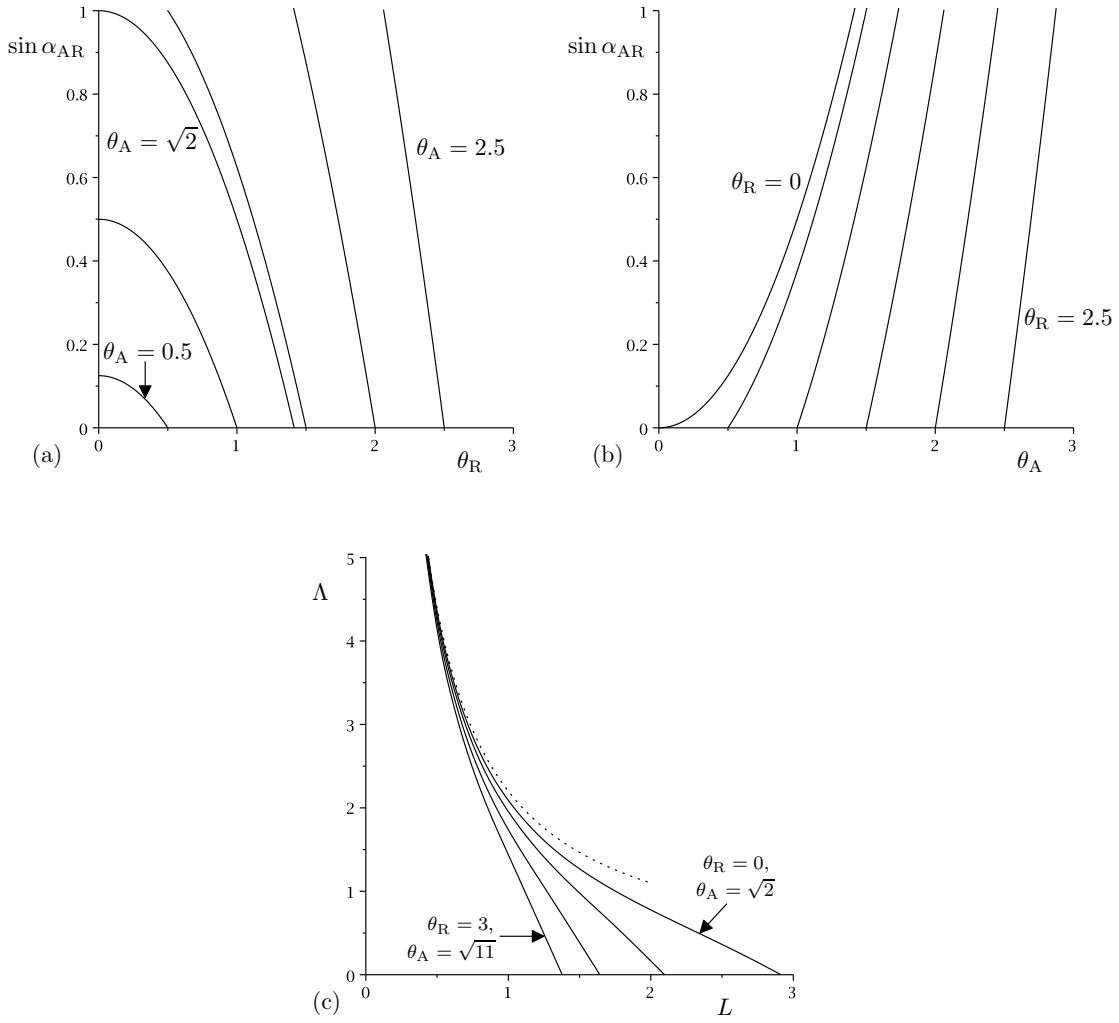

Figure 2.18: (a) and (b) are plots of $\sin\alpha_{AR}$ as a function of θ_R for $\theta_A = 0.5$, 1, $\sqrt{2}$, 1.5, 2, 2.5 and θ_A for $\theta_R = 0$, 0.5, 1, 1.5, 2, 2.5, respectively, and (c) is a parameter-plane plot of the strength of the external airflow Λ as a function of the width L for a ridge on a vertical wall $\alpha = \pi/2$ that de-pins at the contact lines when $\theta_R = 0$, 1, 2, 3 (corresponding to $\theta_A = \sqrt{2}$, $\sqrt{3}$, $\sqrt{6}$, $\sqrt{11}$). The dotted line is the leading order asymptotic solution in the limit of strong airflow $\Lambda \to \infty$, given by $L \simeq 2.20\Lambda^{-1}$.

$\theta_2 > \theta_{\mathrm{R}}$, which means that only the downslope contact line de-pins. In the region to the right of each curve, if $\theta_1 = \theta_{\mathrm{A}}$ then $\theta_2 < \theta_{\mathrm{R}}$, which means that no steady solutions exist at $\alpha = \pi/2$ since $\sin\alpha_{\mathrm{AR}} < 1$; however, if $\theta_2 = \theta_{\mathrm{R}}$ then $\theta_1 < \theta_{\mathrm{A}}$, which means that only the upslope contact line de-pins.

In summary, the main difference between the behaviour of a large ridge and a small ridge is that the contact lines of a large ridge will always de-pin for large enough $\hat{\alpha}$ whereas a small ridge may remain pinned at one or both ends depending on the values of θ_{A}, θ_{R}, Λ and L.

2.7 Conclusions

In the present Chapter we investigated the behaviour of a steady thin ridge of fluid with prescribed constant volume on a substrate inclined at an angle α to the horizontal, including the effects of gravity and surface tension, subject to an external pressure gradient arising from an external airflow. When the substrate is nearly horizontal (specifically, when $\alpha = O(\epsilon)$, where ϵ is the small aspect ratio of the ridge), a relatively "large" ridge of width comparable to the capillary length may be supported in a steady state, either sitting on the substrate (the sessile case), or hanging from it (the pendent case). When the substrate is not restricted to being nearly horizontal (specifically, when $\alpha = O(1)$), only a relatively "small" ridge of width much less than the capillary length may be supported in a steady state. The governing equation for the ridge profile is different in the case of a large sessile ridge, a large pendent ridge, and a small (sessile or pendent) ridge; however, the behaviour in each of the three cases is similar. Hence we gave a complete description of the behaviour of a large sessile ridge in Sections 2.2–2.4 and then briefly considered the other two problems in Sections 2.5 and 2.6, highlighting the differences between the three cases. In their study, King and Tuck [42] considered

only the case when surface tension is negligible for their numerical simulations, that is, the ridge width is much larger than the capillary length and so necessarily $\alpha = O(\epsilon)$ (i.e. a nearly horizontal substrate) for a steady solution. Conversely, in their study of the stability of a ridge on an inclined substrate, Hocking and Miksis [34] considered the case when the ridge width is much smaller than the capillary length and, as such, found steady solutions for $\alpha = O(1)$ (i.e. a substrate that is not restricted to being nearly horizontal).

In Section 2.3 we described the quasi-static evolution of solutions with prescribed constant volume as the external airflow is gradually strengthened. Unlike King and Tuck [42], who found that zero, one or two values of the strength of the external airflow yield a steady solution for each value of the substrate inclination, as described in Subsection 1.3.3, in the present problem we found that a range of possible values of the strength of the external airflow are possible for each value of the substrate inclination. In Subsection 2.3.1 we studied a pinned ridge with pinned contact lines (i.e. constant width) and varying contact angles and found that both contact angles decrease, the maximum thickness increases and the ridge becomes skewed downslope as the airflow is strengthened, as shown in Figure 2.5(a). For a constant angle of inclination, there is a maximum airflow strength that corresponds to the upslope contact angle attaining its minimum physically realisable value of zero. In practice, the upslope contact angle will reach the receding angle at some value of the airflow strength less than this maximum and the upslope contact line will de-pin. Hence in Subsection 2.3.2 we considered a ridge of variable width whose upslope contact line de-pins with an assumed constant upslope contact angle (specifically, the receding angle). In the limit of a strong airflow, the ridge becomes narrow and thick with the downslope contact angle remaining constant, as seen in Figure 2.8(a).

In Section 2.4 we described the quasi-static evolution of solutions with pre-

scribed constant volume as the substrate is gradually tilted. In Subsection 2.4.1 we studied a pinned ridge with pinned contact lines and varying contact angles and found that the downslope contact angle increases, the upslope contact angle decreases and the maximum thickness increases, so that the ridge becomes skewed downslope as the substrate is tilted, as shown in Figure 2.10(a). Like in Section 2.3, for a constant airflow strength there is a maximum possible angle of inclination that again corresponds to the upslope contact angle attaining its minimum physically realisable value of zero. In practice, one or both of the contact lines will de-pin before the upslope contact angle reaches zero. In Subsection 2.4.2 we considered the general case in which both contact lines de-pin and in Subsections 2.4.3 and 2.4.4 we considered the special cases in which only the downslope contact line de-pins and only the upslope contact line de-pins, respectively. For a ridge whose contact lines de-pin at both ends, we found that the value of the inclination of the substrate at which this double de-pinning occurs is independent of the strength of the external airflow, as shown in Figure 2.11, with no steady solutions of the kind considered here existing beyond this value. A ridge whose downslope contact line de-pins while its upslope contact line remains pinned becomes wider and shallower and there is a maximum value of the inclination of the substrate beyond which no steady solutions of the kind considered here exist (corresponding to the upslope contact angle attaining its minimum physically realisable value of zero). This maximum inclination value is independent of both the strength of the external airflow and of the ridge width, as shown in Figure 2.12. A ridge whose upslope contact line de-pins while its downslope contact line remains pinned becomes narrower and thicker as the inclination of the substrate is increased, with steady solutions existing for all values of the substrate inclination, as shown in Figure 2.13.

In Section 2.5 we found that a large pendent ridge has smaller contact angles

and greater maximum thickness than a large sessile ridge for a given strength of external airflow and angle of inclination of the substrate. Hence, the value of the airflow strength at which the upslope contact angle de-pins (for a given receding angle) is smaller for a large pendent ridge than it is for a large sessile ridge as the airflow is gradually strengthened, as shown in Figure 2.16.

In Section 2.6 we found that, unlike in the case of a large ridge, it is possible that a small ridge (of width much less than the capillary length) may exist for any angle of inclination of the substrate. In particular, the upslope contact angle achieves a minimum at $\alpha = \pi/2$ (i.e. a vertical substrate) and so if this minimum upslope contact angle is greater than zero then a steady solution is possible for all α. Similarly, the ridge will de-pin at one or both contact lines only if the advancing and/or receding angles are attained for $\alpha \leq \pi/2$.

Chapter 3

Pinning, de-pinning and re-pinning of a slowly varying rivulet

In this Chapter we show how the solutions for the unidirectional flow of a rivulet with prescribed volume flux down an inclined planar substrate can be used to describe the locally unidirectional flow of a rivulet with constant width but variable contact angle (i.e. pinned contact lines) as well as the possible pinning and subsequent de-pinning of a rivulet with constant contact angle and the possible de-pinning and subsequent re-pinning of a rivulet with constant width as they flow in the azimuthal direction from the top to the bottom of a large horizontal cylinder.

3.1 Unidirectional Flow of a Thin Rivulet

Consider the steady unidirectional flow of a thin symmetric rivulet with semi-width a and volume flux $Q\,(>0)$ down a planar substrate inclined at an angle

α ($0 \leq \alpha \leq \pi$) to the horizontal. We assume that the fluid is Newtonian with constant viscosity μ, density ρ and coefficient of surface tension γ, and choose Cartesian coordinates $Oxyz$ with the x axis down the line of greatest slope, the y axis horizontal, and the z axis normal to the substrate $z = 0$. The velocity $\mathbf{u} = u(y, z)\mathbf{i}$ and the pressure (relative to its ambient value) $p = p(y, z)$ satisfy the familiar mass-conservation and Navier–Stokes equations subject to the usual normal and tangential stress balances and the kinematic condition at the free surface $z = h(y)$, the no-slip condition at the substrate $z = 0$, and the condition of zero thickness at the contact lines (i.e. $h(\pm a) = 0$). The contact angle is denoted by $\beta = \mp h'(\pm a)\,(\geq 0)$, where the dash denotes differentiation with respect to argument, and the maximum thickness of the rivulet, which always occurs at $y = 0$, is denoted by $h_{\mathrm{m}} = h(0)$. We non-dimensionalise y and a with ℓ, z, h and h_{m} with $\delta\ell$, u with $U = \delta^2\rho g\ell^2/\mu$, Q with $\delta\ell^2 U = \delta^3\rho g\ell^4/\mu$, and p with $\delta\rho g\ell$, where g is the magnitude of gravitational acceleration, $\ell = (\gamma/\rho g)^{1/2}$ is the capillary length, and δ is the transverse aspect ratio. There is some freedom regarding the definition of δ. When $\beta > 0$ we could define δ using the value of the contact angle by choosing $\delta = \beta$, corresponding to taking $\beta = 1$ without loss of generality. Alternatively, we could define δ using the prescribed value of the flux, denoted by $\bar{Q}\,(> 0)$, by choosing $\delta = (\mu\bar{Q}/\rho g\ell^4)^{1/3}$, corresponding to taking $\bar{Q} = 1$ without loss of generality. However, for the moment we leave δ unspecified and retain both β and $\bar{Q}$ in order to keep the subsequent presentation as general as possible.

In the general case of non-zero contact angle $\beta > 0$ Duffy and Moffatt [23] showed that at leading order in the limit of small transverse aspect ratio $\delta \to 0$ (i.e. for a thin rivulet) the governing equations are readily solved to yield the velocity $u = \sin\alpha(2h - z)z/2$, the pressure $p = \cos\alpha(h - z) - h''$, the free surface

shape

$$h(y) = \beta \times \begin{cases} \dfrac{\cosh ma - \cosh my}{m \sinh ma} & \text{for} \quad 0 \le \alpha < \dfrac{\pi}{2}, \\ \dfrac{a^2 - y^2}{2a} & \text{for} \quad \alpha = \dfrac{\pi}{2}, \\ \dfrac{\cos my - \cos ma}{m \sin ma} & \text{for} \quad \dfrac{\pi}{2} < \alpha \le \pi, \end{cases} \tag{3.1}$$

the maximum thickness of the rivulet

$$h_{\mathrm{m}} = \beta \times \begin{cases} \dfrac{1}{m} \tanh\left(\dfrac{ma}{2}\right) & \text{for} \quad 0 \le \alpha < \dfrac{\pi}{2}, \\ \dfrac{a}{2} & \text{for} \quad \alpha = \dfrac{\pi}{2}, \\ \dfrac{1}{m} \tan\left(\dfrac{ma}{2}\right) & \text{for} \quad \dfrac{\pi}{2} < \alpha \le \pi, \end{cases} \tag{3.2}$$

and the volume flux

$$Q = \frac{\beta^3 \sin\alpha}{9m^4} f(ma), \tag{3.3}$$

where $m = |\cos\alpha|^{1/2}$. The function $f = f(ma)$ appearing in (3.3) is given by

$$f(ma) = \begin{cases} 15ma \coth^3 ma - 15 \coth^2 ma - 9ma \coth ma + 4 & \text{for} \quad 0 \le \alpha < \dfrac{\pi}{2}, \\ \dfrac{12}{35}(ma)^4 & \text{for} \quad \alpha = \dfrac{\pi}{2}, \\ -15ma \cot^3 ma + 15 \cot^2 ma - 9ma \cot ma + 4 & \text{for} \quad \dfrac{\pi}{2} < \alpha \le \pi, \end{cases} \tag{3.4}$$

and satisfies $f \sim 12(ma)^4/35 \to 0$ as $ma \to 0$, $f \sim 6ma - 11 \to \infty$ as $ma \to \infty$ for $0 \le \alpha < \pi/2$, and $f \sim 15\pi(\pi - ma)^{-3} \to \infty$ as $ma \to \pi$ for $\pi/2 < \alpha \le \pi$.

In the special case of zero contact angle $\beta = 0$ we recover the solution for a perfectly wetting fluid described by Duffy and Wilson [24], namely that there is no solution for $0 \le \alpha \le \pi/2$, but

$$a = \frac{\pi}{m}, \quad h = \frac{h_{\mathrm{m}}}{2}(1 + \cos my), \quad Q = \frac{5\pi \sin\alpha \, h_{\mathrm{m}}^3}{24m} \quad \text{for} \quad \frac{\pi}{2} < \alpha \le \pi. \tag{3.5}$$

3.2 A Rivulet with Constant Contact Angle

3.2.1 The General Case of Non-Zero Contact Angle $\beta = \bar{\beta} > 0$

Duffy and Moffatt [23] used the solution (3.1)–(3.4) to describe the locally unidirectional flow with prescribed flux $Q = \bar{Q}$ down a slowly varying substrate, specifically the flow in the azimuthal direction from the top $\alpha = 0$ to the bottom $\alpha = \pi$ of a large horizontal cylinder, of a rivulet with constant non-zero contact angle $\beta = \bar{\beta} > 0$ but slowly varying semi-width a. Note that here and henceforth "slowly varying" means that the longitudinal aspect ratio $\epsilon = \ell/R$, where R is the radius of the cylinder, satisfies $\epsilon \ll \delta$ so that $\epsilon/\delta \to 0$ in the limit $\epsilon \to 0$. Imposing the conditions of prescribed flux, $Q = \bar{Q}$ with Q given by (3.3), and of constant non-zero contact angle, $\beta = \bar{\beta} > 0$, yields a non-linear algebraic equation for the semi-width a which can, in general, be solved only numerically or asymptotically. Figure 3.1(a) shows a sketch of the scaled semi-width a/π as a function of the scaled azimuthal angle α/π when $\beta = \bar{\beta} > 0$. For all values of $\bar{Q}$ there is a slowly varying rivulet that runs all the way from $\alpha = 0$ [where $a = O(\alpha^{-1}) \to \infty$ and $h_{\rm m} \to 1^+$ as $\alpha \to 0^+$] to $\alpha = \pi$ [where $a \to \pi^-$ and $h_{\rm m} = O(\pi - \alpha)^{-1/3} \to \infty$ as $\alpha \to \pi^-$].

The rivulet does not have top-to-bottom symmetry; its semi-width a has a single minimum, denoted by $a = a_{\rm min}\,(< \pi)$ and occurring at $\alpha = \alpha_{\rm min}$, on the lower half of the cylinder (i.e. for $\pi/2 < \alpha \leq \pi$), and its maximum thickness $h_{\rm m}$ either increases monotonically or has a single maximum and a single minimum on the upper half of the cylinder (i.e. for $0 \leq \alpha < \pi/2$). Furthermore, in the limit of small flux, $\bar{Q} \to 0^+$, the rivulet satisfies $a = O(\bar{Q}^{1/4})$ and $h_{\rm m} = O(\bar{Q}^{1/4})$ while in the limit of large flux, $\bar{Q} \to \infty$, it satisfies $a = O(\bar{Q})$ and $h_{\rm m} = O(1)$ on the upper half of the cylinder, $a = O(\bar{Q}^{1/4})$ and $h_{\rm m} = O(\bar{Q}^{1/4})$ at $\alpha = \pi/2$, and $a = O(1)$

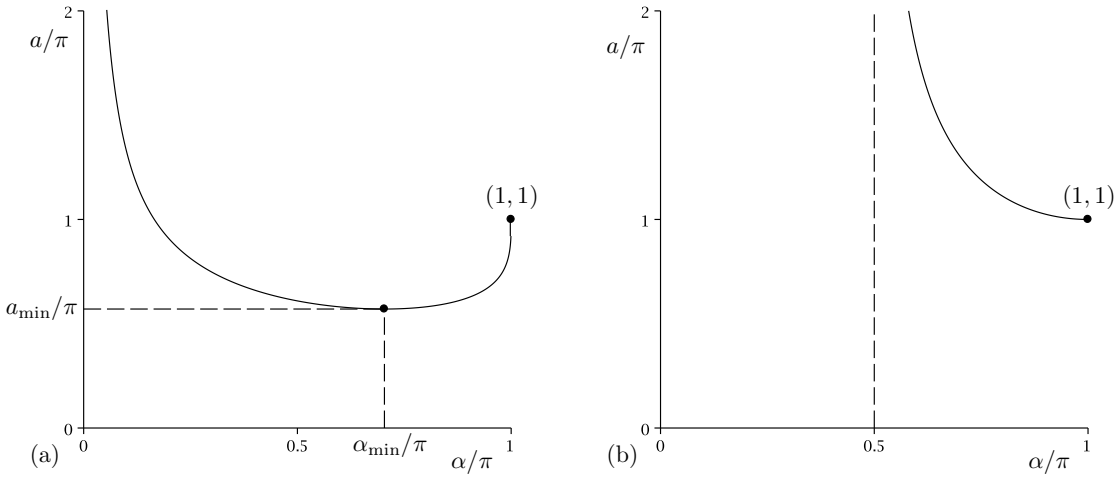

Figure 3.1: Sketches of the scaled semi-width a/π as a function of the scaled azimuthal angle α/π for a rivulet with (a) constant non-zero contact angle $\beta = \bar{\beta} > 0$ and (b) constant zero contact angle $\beta = \bar{\beta} = 0$.

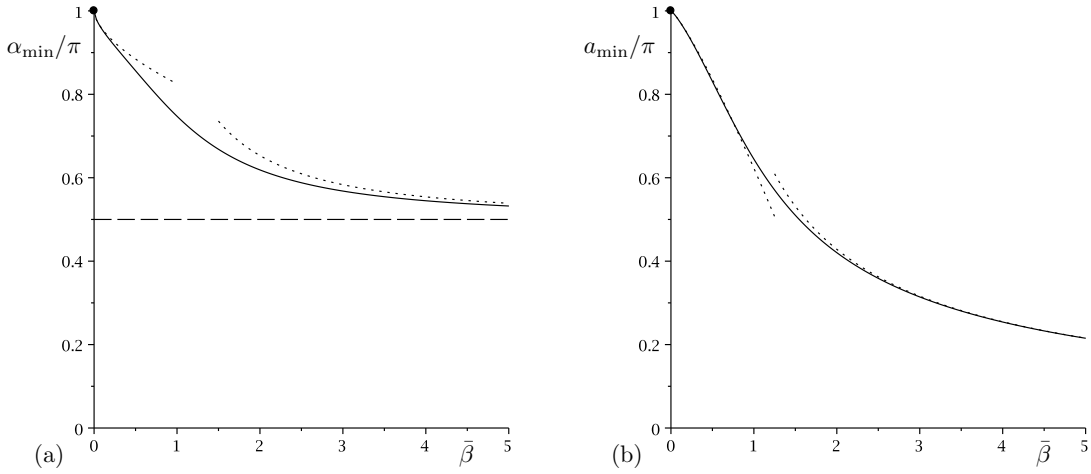

Figure 3.2: Plots of (a) $\alpha_{\min}/\pi$ and (b) $a_{\min}/\pi$ as functions of the constant contact angle $\bar{\beta}$ when $\bar{Q} = 1$, together with their asymptotic behaviour in the limits $\bar{\beta} \to 0^+$ given by (3.6) and $\bar{\beta} \to \infty$ given by (3.7), shown with dotted lines.

and $h_{\rm m} = O(\bar{Q}^{1/3})$ on the lower half of the cylinder. Since the location and value of the minimum semi-width are important in what follows, Figure 3.2 shows plots of $\alpha_{\rm min}/\pi$ and $a_{\rm min}/\pi$ as functions of the constant contact angle $\bar{\beta}$, and shows that both are monotonically decreasing functions of $\bar{\beta}$ satisfying

$$\alpha_{\rm min} \sim \pi - \left(\frac{40\bar{\beta}^3}{81\pi^2\bar{Q}}\right)^{\frac{1}{5}} \to \pi^- \quad \text{and} \quad a_{\rm min} \sim \pi - \frac{5\pi}{4}\left(\frac{40\bar{\beta}^3}{81\pi^2\bar{Q}}\right)^{\frac{2}{5}} \to \pi^- \tag{3.6}$$

as $\bar{\beta} \to 0^+$, and

$$\alpha_{\rm min} \sim \frac{\pi}{2} + \frac{2}{9}\left(\frac{105\bar{Q}}{4\bar{\beta}^3}\right)^{\frac{1}{2}} \to \frac{\pi^+}{2} \quad \text{and} \quad a_{\rm min} \sim \left(\frac{105\bar{Q}}{4\bar{\beta}^3}\right)^{\frac{1}{4}} \to 0^+ \tag{3.7}$$

as $\bar{\beta} \to \infty$.

3.2.2 The Special Case of Zero Contact Angle $\beta = \bar{\beta} = 0$

Duffy and Wilson [24] used the solution (3.5) to describe the corresponding flow of a rivulet with zero contact angle $\beta = \bar{\beta} = 0$ (i.e. a perfectly wetting fluid). Specifically, imposing the condition of prescribed flux, $Q = \bar{Q}$ with Q given by (3.5), yields an explicit solution for the maximum thickness $h_{\rm m} = h_{\rm m0}$, where

$$h_{\rm m0} = \left(\frac{24\bar{Q}m}{5\pi\sin\alpha}\right)^{\frac{1}{3}} = \left(\frac{24\bar{Q}|\cos\alpha|^{1/2}}{5\pi\sin\alpha}\right)^{\frac{1}{3}}. \tag{3.8}$$

Figure 3.1(b) shows a sketch of the scaled semi-width a/π as a function of the scaled azimuthal angle α/π when $\beta = \bar{\beta} = 0$. For all values of $\bar{Q}$ there is a slowly varying rivulet on the lower half of the cylinder with monotonically decreasing semi-width $a = \pi/m$ and monotonically increasing maximum thickness $h_{\rm m} = h_{\rm m0}$ that runs from $\alpha = \pi/2^+$ (where $a = O(\alpha - \pi/2)^{-1/2} \to \infty$ and $h_{\rm m} = O(\alpha - \pi/2)^{1/6} \to 0^+$ as $\alpha \to \pi/2^+$) to $\alpha = \pi$ (where $a \to \pi^+$ and $h_{\rm m} = O(\pi - \alpha)^{-1/3} \to \infty$ as $\alpha \to \pi^-$). Note that, unlike in the general case of non-zero contact angle $\bar{\beta} > 0$, in which there is an infinite mass of fluid on the cylinder, in the special case of

zero contact angle $\beta = \bar{\beta} = 0$ the mass of fluid on the cylinder, denoted by M and non-dimensionalised with $\delta\rho\ell^2 R$, is given by

$$M = \int_{\frac{\pi}{2}}^{\pi} \int_{-a}^{+a} h \, \mathrm{d}y \, \mathrm{d}\alpha = \int_{\frac{\pi}{2}}^{\pi} \frac{\pi h_{\mathrm{m}}}{m} \, \mathrm{d}\alpha = \left(\frac{6\pi^2 \bar{Q}}{5} \right)^{\frac{1}{3}} C, \tag{3.9}$$

where the constant C is given by

$$C = \int_0^{\pi} \frac{\mathrm{d}\alpha}{(\sin\alpha)^{\frac{1}{3}}} = \frac{\sqrt{\pi}\,\Gamma\left(\frac{1}{3}\right)}{\Gamma\left(\frac{5}{6}\right)} \simeq 4.2065. \tag{3.10}$$

3.3 A Rivulet with Constant Width

The solutions (3.1)–(3.4) and (3.5) can also be used to describe the locally unidirectional flow with prescribed flux $Q = \bar{Q}$ from the top $\alpha = 0$ to the bottom $\alpha = \pi$ of a large horizontal cylinder of a rivulet with *constant semi-width* $a = \bar{a}\,(> 0)$ *(i.e. pinned contact lines) but slowly varying contact angle* $\beta\,(\geq 0)$. Imposing the conditions of prescribed flux, $Q = \bar{Q}$ with Q given by (3.3), and of constant semi-width, $a = \bar{a}$, yields an explicit solution for the contact angle β, namely

$$\beta = \left(\frac{9\bar{Q}m^4}{f(m\bar{a})\sin\alpha} \right)^{\frac{1}{3}} = \left(\frac{9\bar{Q}\cos^2\alpha}{f(|\cos\alpha|^{1/2}\bar{a})\sin\alpha} \right)^{\frac{1}{3}}. \tag{3.11}$$

The solution (3.11) reveals that, unlike in the case of constant contact angle described in Section 3.2 (in which the dependence of a on $\bar{Q}$ is not straightforward), in this case β is simply proportional to $\bar{Q}^{1/3}$ for all values of α and $\bar{a}$. Moreover, as in the case of constant contact angle, the rivulet does not have top-to-bottom symmetry. Inspection of the solution (3.11) also reveals that, unlike in the case of constant contact angle (in which the behaviour is qualitatively the same for all values of the contact angle), the behaviour of the rivulet is qualitatively different for a "narrow" rivulet with $a = \bar{a} < \pi$, in the marginal case $a = \bar{a} = \pi$, and for a "wide" rivulet with $a = \bar{a} > \pi$. We shall therefore describe the behaviour of the rivulet in each of these three cases separately in the next three Subsections.

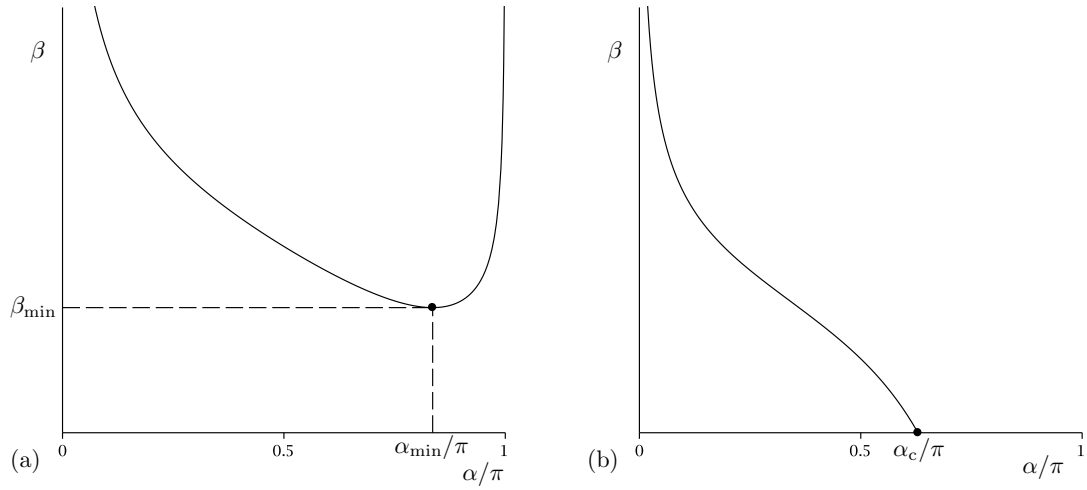

Figure 3.3: Sketches of the contact angle β as a function of the scaled azimuthal angle α/π for (a) a "narrow" rivulet with constant semi-width $a = \bar{a} < \pi$ and (b) a "wide" rivulet with constant semi-width $a = \bar{a} > \pi$. For brevity, the marginal case $a = \bar{a} = \pi$ is not shown.

3.3.1 A Narrow Rivulet with $a = \bar{a} < \pi$

Figure 3.3(a) shows a sketch of the contact angle β as a function of the scaled azimuthal angle α/π for a narrow rivulet with constant semi-width $a = \bar{a} < \pi$. When $\bar{a} < \pi$ for all values of $\bar{Q}$ there is a slowly varying rivulet that runs all the way from $\alpha = 0$ to $\alpha = \pi$, and its contact angle β has a single minimum, denoted by $\beta = \beta_{\min}$ and occurring at $\alpha = \alpha_{\min}$, on the lower half of the cylinder (i.e. for $\pi/2 < \alpha < \pi$)[1], and its maximum thickness h_{m} has a single minimum on the upper half of the cylinder (i.e. for $0 < \alpha < \pi/2$). Since the location and value of the minimum contact angle are important in what follows, Figure 3.4 shows plots of $\alpha_{\min}/\pi$ and $\beta_{\min}$ as functions of the scaled constant semi-width $\bar{a}/\pi$, and shows that $\alpha_{\min}$ is a monotonically increasing function of $\bar{a}$ and $\beta_{\min}$ is a monotonically decreasing function of $\bar{a}$ satisfying

$$\alpha_{\min} \sim \frac{\pi}{2} + \frac{2\bar{a}^2}{9} \to \frac{\pi}{2}^+ \quad \text{and} \quad \beta_{\min} \sim \left(\frac{105\bar{Q}}{4\bar{a}^4}\right)^{\frac{1}{3}} \to \infty \tag{3.12}$$

[1]Note that $\alpha_{\min}$ is independent of $\bar{Q}$.

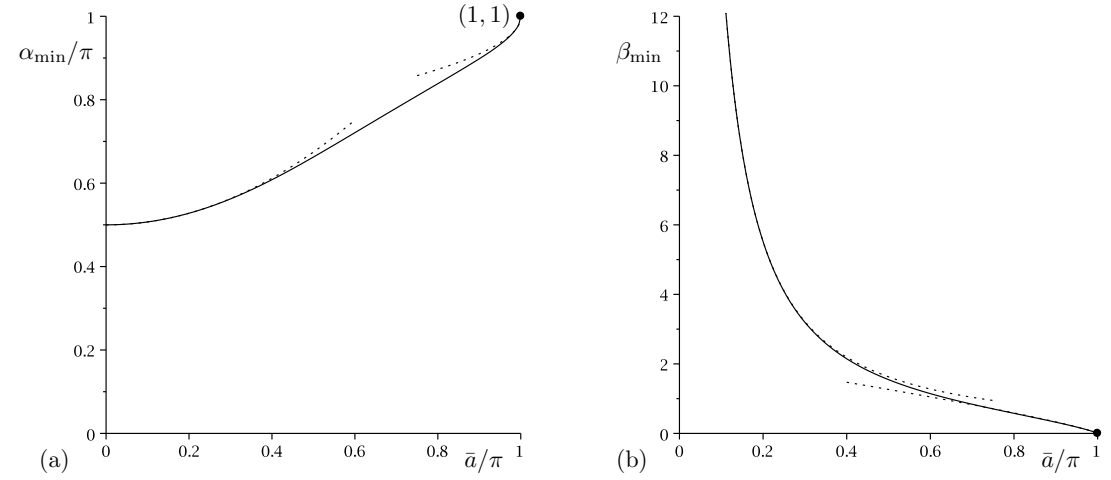

Figure 3.4: Plots of (a) $\alpha_{\min}/\pi$ and (b) $\beta_{\min}$ as functions of the scaled constant semi-width $\bar{a}/\pi$ when $\bar{Q} = 1$, together with their asymptotic behaviour in the limits $\bar{a} \to 0^+$ given by (3.12) and $\bar{a} \to \infty$ given by (3.13), shown with dotted lines.

as $\bar{a} \to 0^+$, and

$$\alpha_{\min} \sim \pi - \left(\frac{4(\pi - \bar{a})}{5\pi}\right)^{\frac{1}{2}} \to \pi^- \quad \text{and} \quad \beta_{\min} \sim \frac{6}{5}\left(\frac{9\bar{Q}^2}{20\pi}\right)^{\frac{1}{6}} (\pi - \bar{a})^{\frac{5}{6}} \to 0^+ \tag{3.13}$$

as $\bar{a} \to \pi^-$. The rivulet becomes deep near the top and the bottom of the cylinder according to

$$\beta \sim \left(\frac{9\bar{Q}}{f(\bar{a})\alpha}\right)^{\frac{1}{3}} \to \infty \quad \text{and} \quad h_{\mathrm{m}} \sim \left(\frac{9\bar{Q}}{f(\bar{a})\alpha}\right)^{\frac{1}{3}} \tanh\left(\frac{\bar{a}}{2}\right) \to \infty \tag{3.14}$$

as $\alpha \to 0^+$, and

$$\beta \sim \left(\frac{9\bar{Q}}{f(\bar{a})(\pi - \alpha)}\right)^{\frac{1}{3}} \to \infty \quad \text{and} \quad h_{\mathrm{m}} \sim \left(\frac{9\bar{Q}}{f(\bar{a})(\pi - \alpha)}\right)^{\frac{1}{3}} \tan\left(\frac{\bar{a}}{2}\right) \to \infty \tag{3.15}$$

as $\alpha \to \pi^-$ (so that the thin-film approximation ultimately fails in these limits); also β and h_{m} take the $O(1)$ values

$$\beta = \left(\frac{105\bar{Q}}{4\bar{a}^4}\right)^{\frac{1}{3}} \quad \text{and} \quad h_{\mathrm{m}} = \left(\frac{105\bar{Q}}{32\bar{a}}\right)^{\frac{1}{3}} \tag{3.16}$$

at $\alpha = \pi/2$. In the limit of a narrow rivulet, $\bar{a} \to 0^+$, the rivulet becomes narrow and deep everywhere according to

$$\beta \sim \left(\frac{105\bar{Q}}{4\bar{a}^4 \sin\alpha}\right)^{\frac{1}{3}} \to \infty \quad \text{and} \quad h_{\mathrm{m}} \sim \left(\frac{105\bar{Q}}{32\bar{a}\sin\alpha}\right)^{\frac{1}{3}} \to \infty. \tag{3.17}$$

3.3.2 The Marginal Case $a = \bar{a} = \pi$

In the marginal case $a = \bar{a} = \pi$ (not shown in Figure 3.3 for brevity) the rivulet behaves qualitatively the same as in the case of a narrow rivulet with $a = \bar{a} < \pi$ described in Subsection 3.3.1, except that, since in this case $\beta = 0$ at $\alpha = \pi$, instead of satisfying (3.15) the rivulet becomes deep with zero contact angle and finite semi-width π near the bottom of the cylinder according to

$$\beta \sim \left(\frac{3\pi^2\bar{Q}(\pi-\alpha)^5}{320}\right)^{\frac{1}{3}} \to 0^+ \quad \text{and} \quad h_{\mathrm{m}} \sim \left(\frac{24\bar{Q}}{5\pi(\pi-\alpha)}\right)^{\frac{1}{3}} \to \infty \tag{3.18}$$

as $\alpha \to \pi^-$.

3.3.3 A Wide Rivulet with $a = \bar{a} > \pi$

Figure 3.3(b) shows a sketch of the contact angle β as a function of the scaled azimuthal angle α/π for a wide rivulet with constant semi-width $a = \bar{a} > \pi$. Unlike when $\bar{a} \leq \pi$, when $\bar{a} > \pi$ for all values of $\bar{Q}$ there is a slowly varying rivulet that runs from $\alpha = 0$ only as far as a critical azimuthal angle $\alpha = \alpha_{\mathrm{c}}$ on the lower half of the cylinder (i.e. for $\pi/2 < \alpha < \pi$)[2], and its contact angle β is a monotonically decreasing function of α, attaining its minimum physically realisable value of zero at $\alpha = \alpha_{\mathrm{c}}$, where the critical azimuthal angle α_{c} is given by solving $m\bar{a} = \pi$ to obtain

$$\alpha_{\mathrm{c}} = \cos^{-1}\left(-\frac{\pi^2}{\bar{a}^2}\right) \quad \text{for} \quad \bar{a} > \pi \tag{3.19}$$

and is a monotonically decreasing function of $\bar{a}$ satisfying $\alpha_{\mathrm{c}} = \pi + O(\bar{a}-\pi)^{1/2} \to \pi^-$ as $\bar{a} \to \pi^+$ and $\alpha_{\mathrm{c}} = \pi/2 + O(\bar{a}^{-2}) \to \pi/2^+$ as $\bar{a} \to \infty$. Figure 3.5 shows the scaled critical azimuthal angle α_{c}/π plotted as a function of the scaled constant semi-width $\bar{a}/\pi$. The rivulet again becomes deep near the top of the cylinder according to (3.14) and again β and h_{m} take the $O(1)$ values given by (3.16) at

[2]Note that α_{c} is independent of $\bar{Q}$.

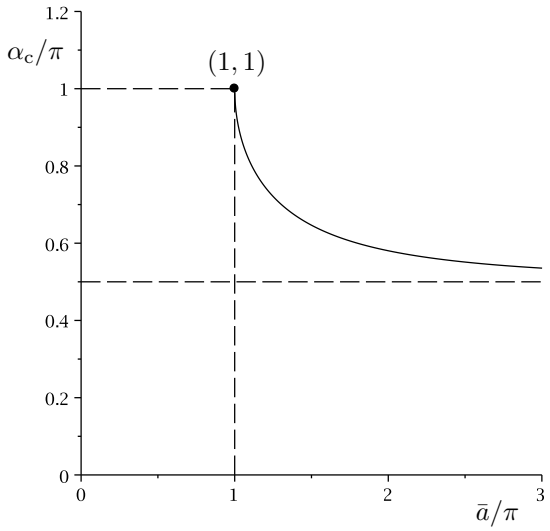

Figure 3.5: Plot of the scaled critical azimuthal angle α_c/π as a function of the scaled constant semi-width $\bar{a}/\pi$.

$\alpha = \pi/2$. At $\alpha = \alpha_c$ the rivulet has zero contact angle $\beta = 0$, semi-width $a = \bar{a}$, and maximum thickness $h_m = h_{mc}$, where

$$h_{mc} = \left(\frac{24\bar{Q}}{5\bar{a}\sin\alpha_c}\right)^{\frac{1}{3}} = \left(\frac{24\bar{a}\bar{Q}}{5\sqrt{\bar{a}^4 - \pi^4}}\right)^{\frac{1}{3}}. \tag{3.20}$$

In particular, as $\alpha \to \alpha_c^-$ we find that $\beta \to 0^+$ according to

$$\beta = \left(\frac{3(\bar{a}^4 - \pi^4)\bar{Q}}{40\bar{a}^2}\right)^{\frac{1}{3}} (\alpha_c - \alpha) + O(\alpha_c - \alpha)^2, \tag{3.21}$$

$a \equiv \bar{a}$, and $h_m \to h_{mc}^-$ according to

$$h_m = h_{mc} + \frac{(\bar{a}^4 + \pi^4)h_{mc}}{6\pi^2\sqrt{\bar{a}^4 - \pi^4}}(\alpha - \alpha_c) + O(\alpha - \alpha_c)^2. \tag{3.22}$$

However, beyond $\alpha = \alpha_c$ the solution for β given by (3.11) is no longer physically realisable because it always predicts that $h < 0$ somewhere in the interval $y = -\bar{a}$ to $y = +\bar{a}$, and so an alternative description of the behaviour beyond $\alpha = \alpha_c$ is required. Physically it is possible that the rivulet simply falls off the cylinder at $\alpha = \alpha_c$ or that the flow becomes unsteady beyond $\alpha = \alpha_c$. However, an alternative (and possibly more likely) scenario in which steady rivulet flow still occurs is that the hitherto pinned contact lines of the rivulet de-pin at $\alpha = \alpha_c$, and that the

rivulet runs from $\alpha = \alpha_c$ to the bottom of the cylinder $\alpha = \pi$ with zero contact angle according to the solution in the case $\beta = 0$ given by (3.5) and (3.8), with monotonically decreasing semi-width $a = \pi/m$ ($\pi \leq a \leq \bar{a}$) and monotonically increasing maximum thickness $h_m = h_{m0}\,(\geq h_{mc})$. In particular, as $\alpha \to \alpha_c^+$ we find that $\beta \equiv 0$, $a \to \bar{a}^-$ according to

$$a = \bar{a} - \frac{\bar{a}\sqrt{\bar{a}^4 - \pi^4}}{2\pi^2}(\alpha - \alpha_c) + O(\alpha - \alpha_c)^2, \tag{3.23}$$

and $h_m \to h_{mc}^+$ according to (3.22), so that the solutions in $\alpha < \alpha_c$ and $\alpha > \alpha_c$ join continuously (but not smoothly) at $\alpha = \alpha_c$. This latter scenario is a special case of the behaviour which will be discussed in Section 3.5, in which we consider the de-pinning and re-pinning of a rivulet with constant width at a prescribed (and, in general, non-zero) value of the contact angle $\beta = \bar{\beta}\,(\geq 0)$. In particular, when the rivulet de-pins at zero contact angle $\beta = \bar{\beta} = 0$ it becomes deep with zero contact angle and finite semi-width π near the bottom of the cylinder according to

$$a = \pi + \frac{\pi}{4}(\pi - \alpha)^2 + O(\pi - \alpha)^4 \to \pi^+ \quad \text{and} \quad h_m \sim \left(\frac{24\bar{Q}}{5\pi(\pi - \alpha)}\right)^{\frac{1}{3}} \to \infty \tag{3.24}$$

as $\alpha \to \pi^-$, and in the limit of a wide rivulet on the upper half of the cylinder, $\bar{a} \to \infty$, (in which $\alpha_c \to \pi/2^+$) the rivulet becomes wide and flat on the upper half of the cylinder according to

$$\beta \sim \left(\frac{3\bar{Q}m^3}{2\bar{a}\sin\alpha}\right)^{\frac{1}{3}} \to 0^+ \quad \text{and} \quad h_m \sim \left(\frac{3\bar{Q}}{2\bar{a}\sin\alpha}\right)^{\frac{1}{3}} \to 0^+ \tag{3.25}$$

and is given by the solution in the case $\beta = 0$ given by (3.5) and (3.8) on the lower half of the cylinder.

3.3.4 Rivulet Profiles

The behaviour for both $\bar{a} \leq \pi$ and $\bar{a} > \pi$ is illustrated in Figure 3.6, which shows plots of the contact angle β, the scaled semi-width a/π, and the maximum

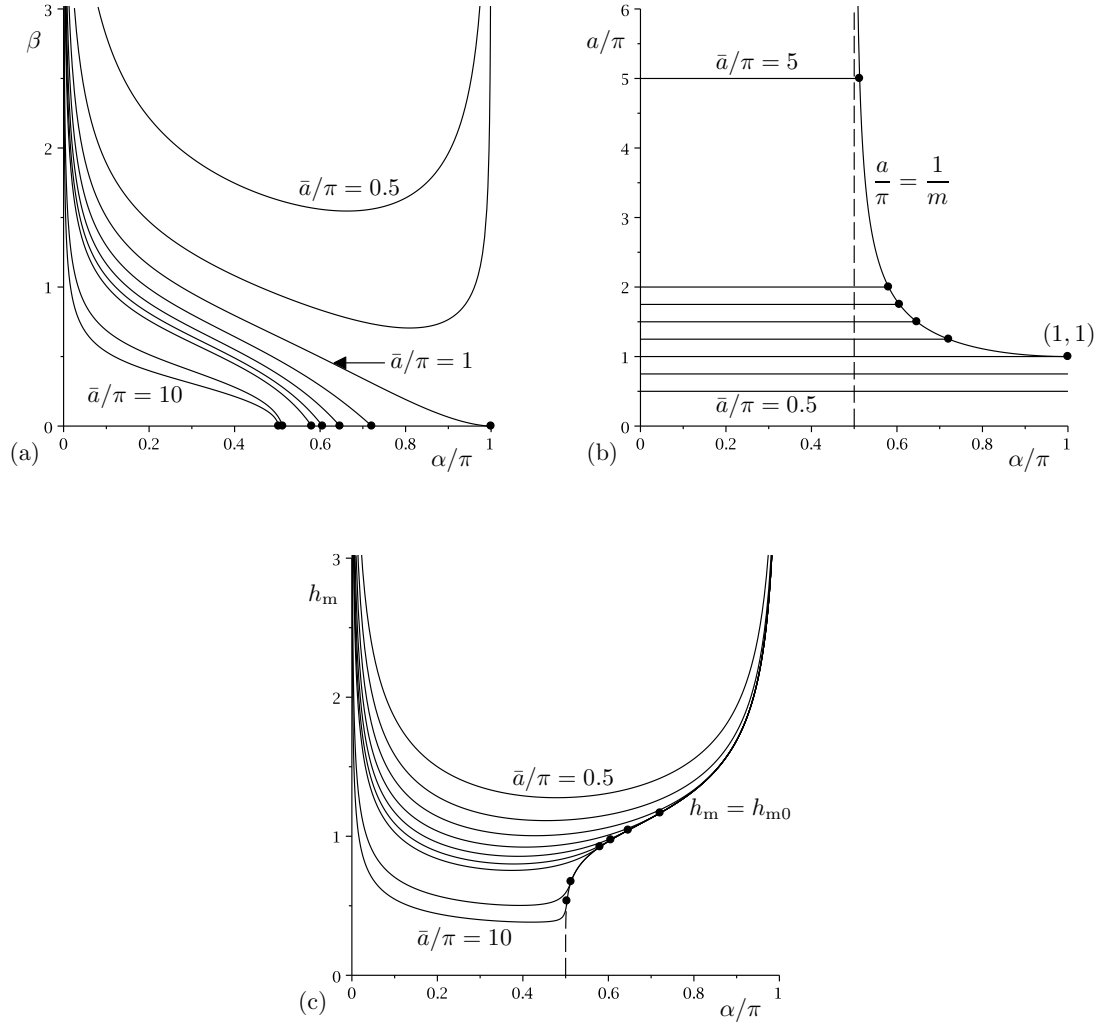

Figure 3.6: Plots of (a) the contact angle β, (b) the scaled semi-width a/π, and (c) the maximum thickness $h_{\rm m}$ as functions of the scaled angle α/π for $\bar{a}/\pi = 0.5$, 0.75, 1, 1.25, 1.5, 1.75, 2, 5, 10 when $\bar{Q} = 1$ for a rivulet whose contact lines de-pin at zero contact angle $\beta = \bar{\beta} = 0$. The corresponding solutions for a rivulet with zero contact angle $\beta = 0$ given by (3.5) and (3.8) are shown with dashed lines (visible only in part (c)). De-pinning occurs at $\alpha = \alpha_{\rm c}$ for $\bar{a}/\pi > 1$, and the points at which this happens are denoted by dots.

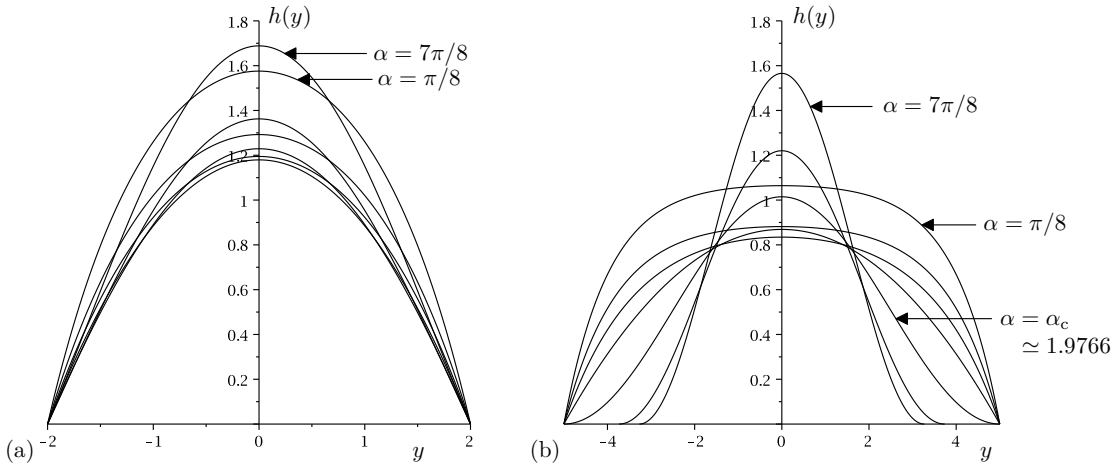

Figure 3.7: Cross-sectional profiles $h(y)$ when $\bar{Q} = 1$ in the cases (a) $\bar{a} = 2\,(< \pi)$ for $\alpha = \pi/8$, $\pi/4$, $3\pi/8$, $\pi/2$, $5\pi/8$, $3\pi/4$, $7\pi/8$ and (b) $\bar{a} = 5\,(> \pi)$ for $\alpha = \pi/8$, $\pi/4$, $3\pi/8$, $\pi/2$, $\alpha_{\rm c} \simeq 1.9766$, $3\pi/4$, $7\pi/8$. For clarity, the two parts of this figure use the same vertical but different horizontal ranges.

thickness $h_{\rm m}$ as functions of the scaled angle α/π for a range of values of $\bar{a}/\pi$ when $\bar{Q} = 1$. In particular, Figure 3.6 shows that de-pinning occurs at $\alpha = \alpha_{\rm c}$ for $\bar{a}/\pi > 1$. Figure 3.7 shows typical cross-sectional profiles of the rivulet in the cases (a) $\bar{a} = 2\,(< \pi)$ and (b) $\bar{a} = 5\,(> \pi)$, and Figure 3.8 shows sketches of the rivulet in the same two cases, namely (a) $\bar{a} < \pi$, in which the rivulet is never de-pinned, and (b) $\bar{a} > \pi$, in which the rivulet is de-pinned and has zero contact angle in the interval $\alpha_{\rm c} < \alpha \leq \pi$.

3.4 Pinning and De-Pinning of a Rivulet with Constant Contact Angle $\beta = \bar{\beta}$ at $a = \bar{a}$

As we described in Section 3.2, the semi-width a of a slowly varying rivulet with constant non-zero contact angle $\beta = \bar{\beta} > 0$ is unbounded at $\alpha = 0$ (i.e. the rivulet is infinitely wide at the top of the cylinder), has a single minimum value of $a = a_{\rm min}\,(< \pi)$ at $\alpha = \alpha_{\rm min}$ on the lower half of the cylinder and takes the value $a = \pi$ at $\alpha = \pi$, while in the special case of zero contact angle $\beta = \bar{\beta} = 0$

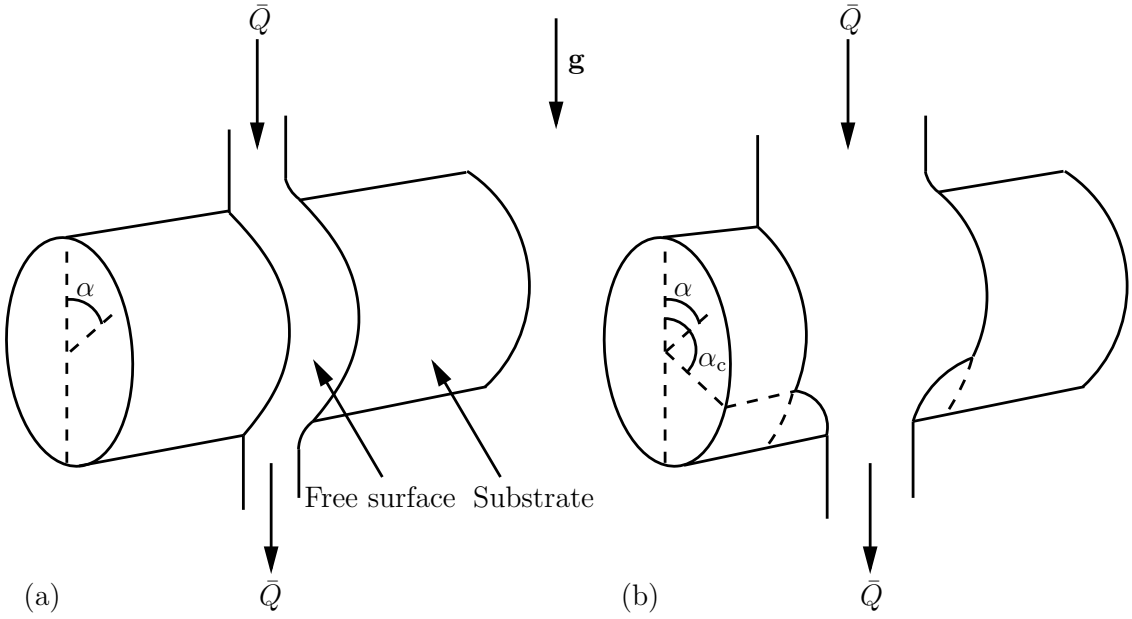

Figure 3.8: Sketches of a slowly varying rivulet with prescribed flux $\bar{Q}$ with (when not de-pinned with zero contact angle $\beta = 0$ and slowly varying semi-width a) constant semi-width $a = \bar{a}$ and slowly varying contact angle β that runs from the top $\alpha = 0$ to the bottom $\alpha = \pi$ of a large horizontal cylinder, in the cases (a) $\bar{a} < \pi$, in which the rivulet is never de-pinned, and (b) $\bar{a} > \pi$, in which the rivulet is de-pinned and has zero contact angle in the interval $\alpha_c < \alpha \leq \pi$.

the semi-width is unbounded at $\alpha = \pi/2$ and decreases to the value $a = \pi$ at $\alpha = \pi$. In practice, however, there could be a minimum physically realisable value of the semi-width, denoted by $a = \bar{a}$, at which the contact lines become pinned. Evidently the behaviour of the rivulet in this situation will be qualitatively different for $\bar{a} \leq \pi$ and $\bar{a} > \pi$.

3.4.1 $\bar{a} \leq \pi$

When $\bar{a} \leq a_{\min} (< \pi)$ the semi-width is always greater than or equal to $\bar{a}$ and hence pinning and de-pinning do not occur, and so the rivulet behaves exactly as described in Section 3.2. However, when $a_{\min} < \bar{a} < \pi$ the rivulet runs from $\alpha = 0$ with constant non-zero contact angle $\beta = \bar{\beta} > 0$ but decreasing semi-width a as described in Section 3.2 until it reaches the value $a = \bar{a}$ at $\alpha = \alpha_{\text{pin}}$ $(0 < \alpha_{\text{pin}} < \alpha_{\min})$ at which the contact lines pin. The rivulet then runs from $\alpha = \alpha_{\text{pin}}$ with constant semi-width $a = \bar{a}$ but varying contact angle β as described in Section 3.3 until it reaches $\alpha = \alpha_{\text{depin}}$ $(\alpha_{\min} < \alpha_{\text{depin}} < \pi)$ at which the contact lines de-pin. The rivulet then runs from $\alpha = \alpha_{\text{depin}}$ to $\alpha = \pi$ with constant contact angle $\beta = \bar{\beta} > 0$ but increasing semi-width a as described in Section 3.2. Here $\alpha = \alpha_{\text{pin}}$ and $\alpha = \alpha_{\text{depin}}$ are the appropriate solutions of the equation $Q = \bar{Q}$ with Q given by (3.3), $a = \bar{a}$ and $\beta = \bar{\beta}$. In the marginal case $\bar{a} = \pi$ we have $\alpha_{\text{depin}} = \pi$ and so de-pinning does not occur. Expressed another way, in the general case of constant non-zero contact angle $\bar{\beta} > 0$ pinning and de-pinning occur when $\bar{\beta} > \bar{\beta}_{\text{c}}$, where the value of $\bar{\beta}_{\text{c}}$ corresponds to $a_{\min} = \bar{a}$. In the special case of pinning at zero contact angle $\beta = \bar{\beta} = 0$ we have $a = \pi/m \geq \pi \geq \bar{a}$, and so pinning and de-pinning do not occur. In the limit $\bar{\beta} \to \infty$ we have $\alpha_{\text{pin}} \to 0^+$ and $\alpha_{\text{depin}} \to \pi^-$ and so recover the solution for a rivulet with constant semi-width $a = \bar{a} \leq \pi$ described in Section 3.3.

The behaviour when $\bar{a} \leq \pi$ is illustrated in Figure 3.9, which shows plots of the

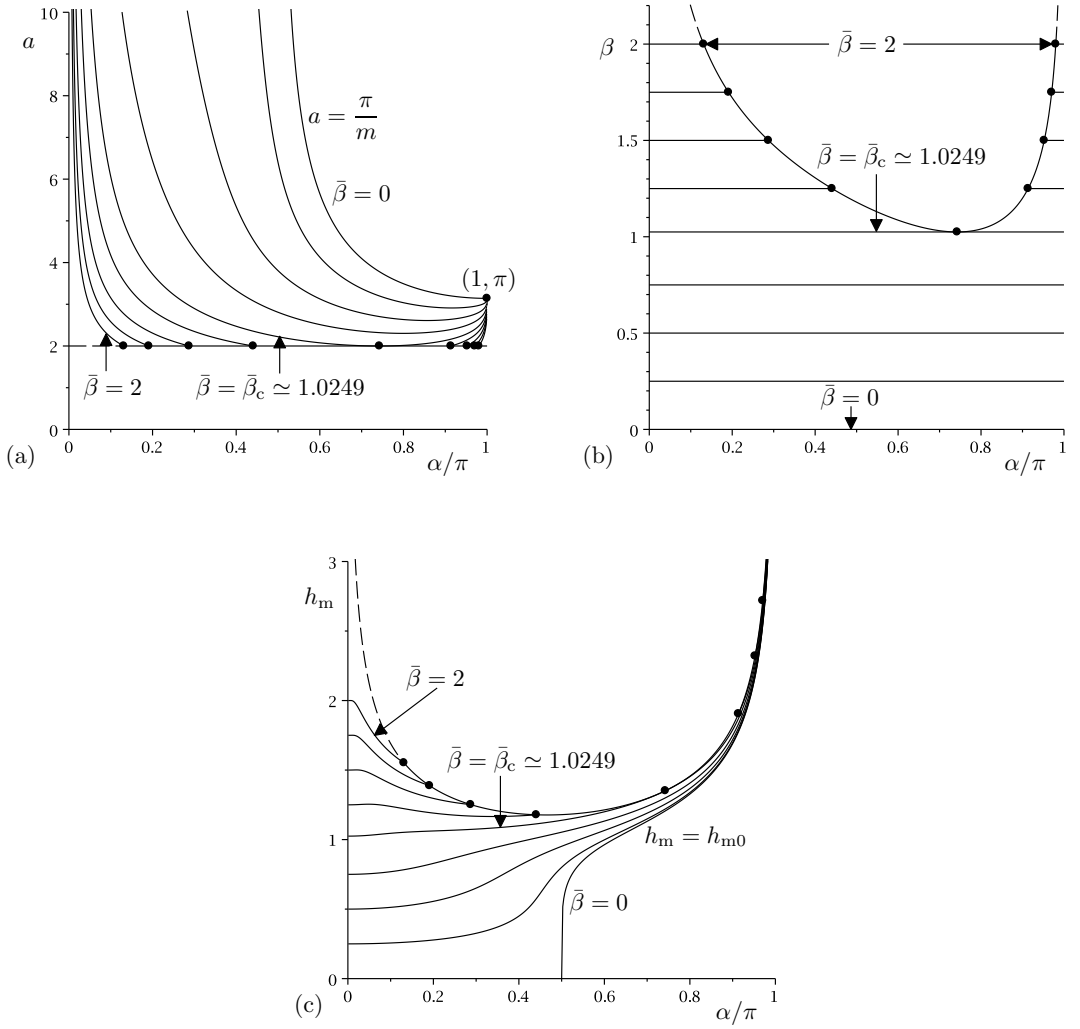

Figure 3.9: Plots of (a) the semi-width a, (b) the contact angle β, and (c) the maximum thickness $h_{\rm m}$ as functions of the scaled angle α/π for $\bar{\beta} = 0$, 0.25, 0.5, 0.75, $\bar{\beta}_{\rm c} \simeq 1.0249$, 1.25, 1.5, 1.75, 2 when $\bar{Q} = 1$ for a rivulet whose contact lines pin at $a = \bar{a} = 2\,(< \pi)$. The corresponding solutions for a rivulet with constant semi-width $\bar{a} = 2$ are shown with dashed lines. Pinning and de-pinning occur for $\bar{\beta} > \bar{\beta}_{\rm c} \simeq 1.0249$, and the points at which this happens are denoted by dots.

semi-width a, the contact angle β, and the maximum thickness h_{m} as functions of the scaled angle α/π for a range of values of $\bar{\beta}$ when $\bar{Q} = 1$ and $\bar{a} = 2\,(< \pi)$. In particular, Figure 3.9 shows that in this case pinning and de-pinning occur for $\bar{\beta} > \bar{\beta}_{\mathrm{c}} \simeq 1.0249$.

3.4.2 $\bar{a} > \pi$

When $\bar{a} > \pi$, as in the case $a_{\min} < \bar{a} \leq \pi$, the rivulet runs from $\alpha = 0$ with constant non-zero contact angle $\beta = \bar{\beta} > 0$ but decreasing semi-width a as described in Section 3.2 until it reaches the value $a = \bar{a}$ at $\alpha = \alpha_{\mathrm{pin}}$ $(0 < \alpha_{\mathrm{pin}} < \alpha_{\mathrm{c}})$ at which the contact lines pin. The rivulet then runs from $\alpha = \alpha_{\mathrm{pin}}$ with constant semi-width $a = \bar{a}$ but decreasing contact angle β as described in Section 3.3 until, unlike in the case $a_{\min} < \bar{a} \leq \pi$, it reaches the critical azimuthal angle $\alpha = \alpha_{\mathrm{c}}$ $(\pi/2 < \alpha_{\mathrm{c}} < \pi)$ at which the contact angle β reaches the value zero and the contact lines de-pin. The rivulet then runs from $\alpha = \alpha_{\mathrm{c}}$ to $\alpha = \pi$ with zero contact angle $\beta = 0$, decreasing semi-width $a = \pi/m$ and increasing maximum thickness $h_{\mathrm{m}} = h_{\mathrm{m0}}$ as described in Section 3.2. In the special case of pinning at zero contact angle $\beta = \bar{\beta} = 0$ pinning and de-pinning do not occur. In the limit $\bar{\beta} \to \infty$ we have $\alpha_{\mathrm{pin}} \to 0^{+}$ and so recover the solution for a rivulet with constant semi-width $a = \bar{a} > \pi$ described in Section 3.3.

The behaviour when $\bar{a} > \pi$ is illustrated in Figure 3.10, which shows plots of the semi-width a, the contact angle β, and the maximum thickness h_{m} as functions of the scaled angle α/π for a range of values of $\bar{\beta}$ when $\bar{Q} = 1$ and $\bar{a} = 5\,(> \pi)$. In particular, Figure 3.10 shows that pinning and de-pinning occur for all $\bar{\beta} > 0$, and that in this case de-pinning occurs at the scaled critical azimuthal angle $\alpha_{\mathrm{c}}/\pi \simeq 0.6292$ for all $\bar{\beta} > 0$.

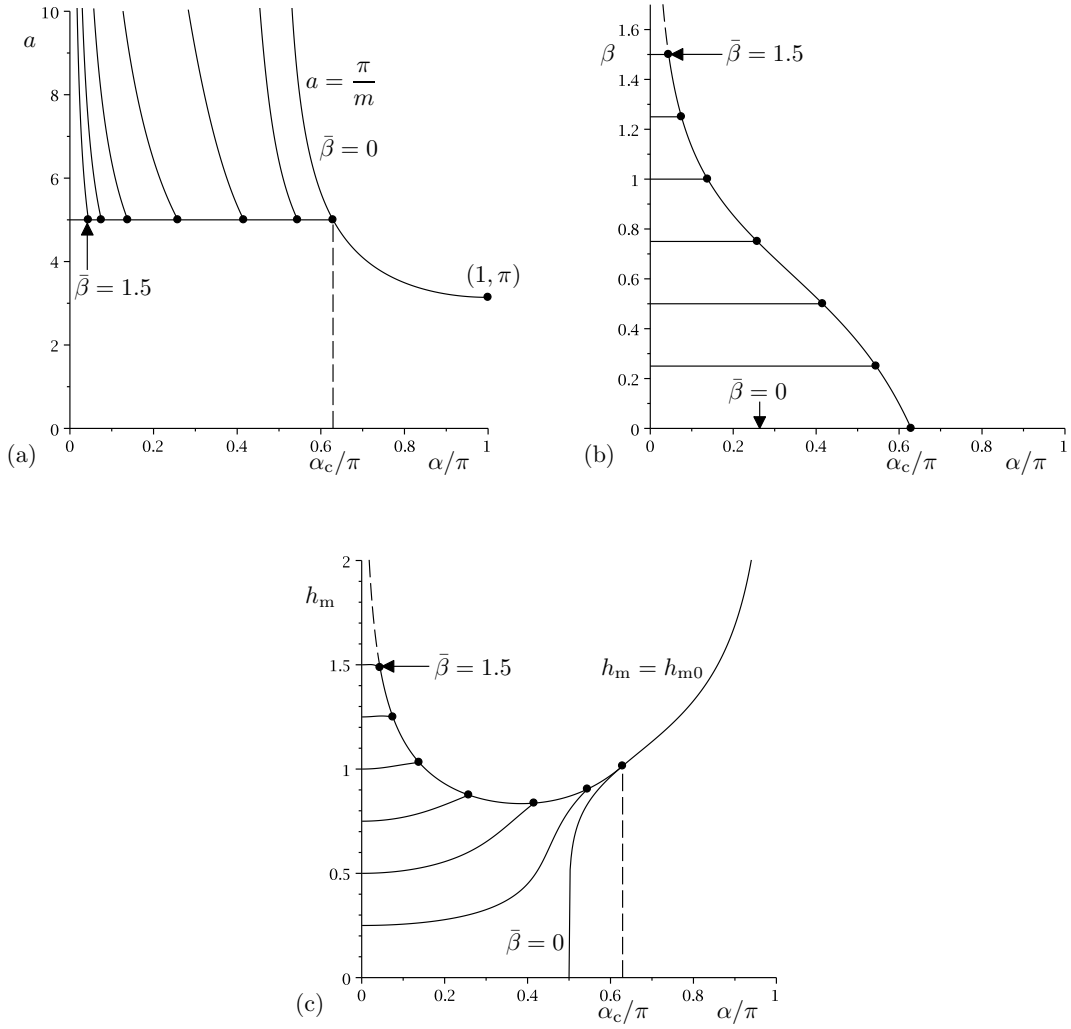

Figure 3.10: Plots of (a) the semi-width a, (b) the contact angle β, and (c) the maximum thickness h_m as functions of the scaled angle α/π for $\bar{\beta} = 0$, 0.25, ..., 1.5 when $\bar{Q} = 1$ for a rivulet whose contact lines pin at $a = \bar{a} = 5\,(> \pi)$. The corresponding solutions for a rivulet with constant semi-width $\bar{a} = 5$ are shown with dashed lines. Pinning and de-pinning occur for all $\bar{\beta} > 0$, and the points at which this happens are denoted by dots. The vertical dashed lines show the scaled critical azimuthal angle $\alpha_c/\pi \simeq 0.6292$ at which de-pinning occurs for all $\bar{\beta} > 0$.

3.4.3 Rivulet Profiles

Figure 3.11 shows typical cross-sectional profiles of the rivulet in the cases (a) $\bar{a} = 2\,(< \pi)$ and $\bar{\beta} = 0.5\,(< \bar{\beta}_{\rm c} \simeq 1.0249)$, (b) $\bar{a} = 2\,(< \pi)$ and $\bar{\beta} = 1.5\,(> \bar{\beta}_{\rm c})$, and (c) $\bar{a} = 5\,(> \pi)$ and $\bar{\beta} = 1$, and, in order to clarify what might appear to be a rather complicated situation, Figure 3.12 shows sketches of the rivulet in the same three cases, namely (a) $\bar{a} < \pi$ and $0 < \bar{\beta} < \bar{\beta}_{\rm c}$, in which the rivulet is never pinned, (b) $\bar{a} < \pi$ and $\bar{\beta} > \bar{\beta}_{\rm c}$, in which the rivulet is pinned in the interval $\alpha_{\rm pin} < \alpha < \alpha_{\rm depin}$, and (c) $\bar{a} > \pi$, in which the rivulet is pinned in the interval $\alpha_{\rm pin} < \alpha < \alpha_{\rm c}$ and has zero contact angle in the interval $\alpha_{\rm c} \leq \alpha \leq \pi$.

3.5 De-Pinning and Re-Pinning of a Rivulet with Constant Width $a = \bar{a}$ at $\beta = \bar{\beta}$

In Section 3.4 we described the pinning and de-pinning of a rivulet with constant contact angle $\beta = \bar{\beta}$ at $a = \bar{a}$. In this Section we describe the corresponding situation involving the de-pinning and re-pinning of a rivulet with constant width $a = \bar{a}$ at $\beta = \bar{\beta} > 0$. As we described in Section 3.3, for a narrow rivulet with $\bar{a} < \pi$ the contact angle β of a slowly varying rivulet with constant semi-width $a = \bar{a}$ is unbounded at $\alpha = 0$ and $\alpha = \pi$, and has a single minimum value of $\beta = \beta_{\rm min}$ at $\alpha = \alpha_{\rm min}$ on the lower half of the cylinder, while for a wide rivulet with $\bar{a} > \pi$ the contact angle is unbounded at $\alpha = 0$ and decreases to the value zero at $\alpha = \alpha_{\rm c}$. In Section 3.3 we showed how there can be steady flow of a wide rivulet all the way from $\alpha = 0$ to $\alpha = \pi$ when the contact lines de-pin when the contact angle reaches its minimum physically realisable value of zero, i.e. at $\alpha = \alpha_{\rm c}$. More generally, however, the contact lines could de-pin at a non-zero value of the contact angle, denoted by $\beta = \bar{\beta} > 0$. Evidently, as in Section 3.4, the behaviour of the rivulet

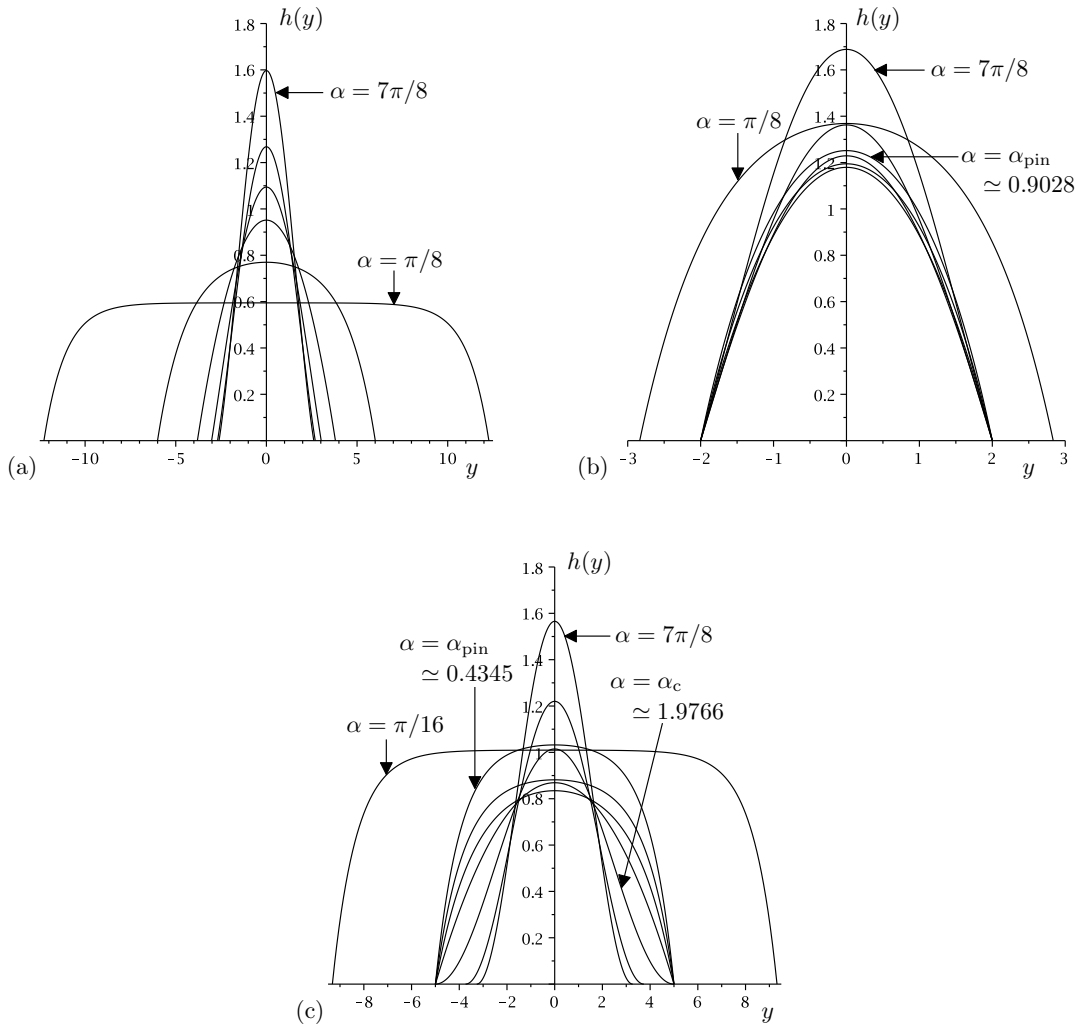

Figure 3.11: Cross-sectional profiles $h(y)$ when $\bar{Q} = 1$ in the cases (a) $\bar{a} = 2\,(< \pi)$ and $\bar{\beta} = 0.5\,(< \bar{\beta}_{\rm c} \simeq 1.0249)$ for $\alpha = \pi/8$, $\pi/4$, $3\pi/8$, $\pi/2$, $5\pi/8$, $3\pi/4$, $7\pi/8$, (b) $\bar{a} = 2\,(< \pi)$ and $\bar{\beta} = 1.5\,(> \bar{\beta}_{\rm c})$ for $\alpha = \pi/8$, $\alpha_{\rm pin} \simeq 0.9028$, $3\pi/8$, $\pi/2$, $5\pi/8$, $3\pi/4$, $7\pi/8$, and (c) $\bar{a} = 5\,(> \pi)$ and $\bar{\beta} = 1$ for $\alpha = \pi/16$, $\alpha_{\rm pin} \simeq 0.4345$, $\pi/4$, $3\pi/8$, $\pi/2$, $\alpha_{\rm c} \simeq 1.9766$, $3\pi/4$, $7\pi/8$. For clarity, in part (b) no profiles are shown in the interval $\alpha_{\rm depin} \simeq 2.9923 \leq \alpha \leq \pi$, and the three parts of this figure use the same vertical but different horizontal ranges.

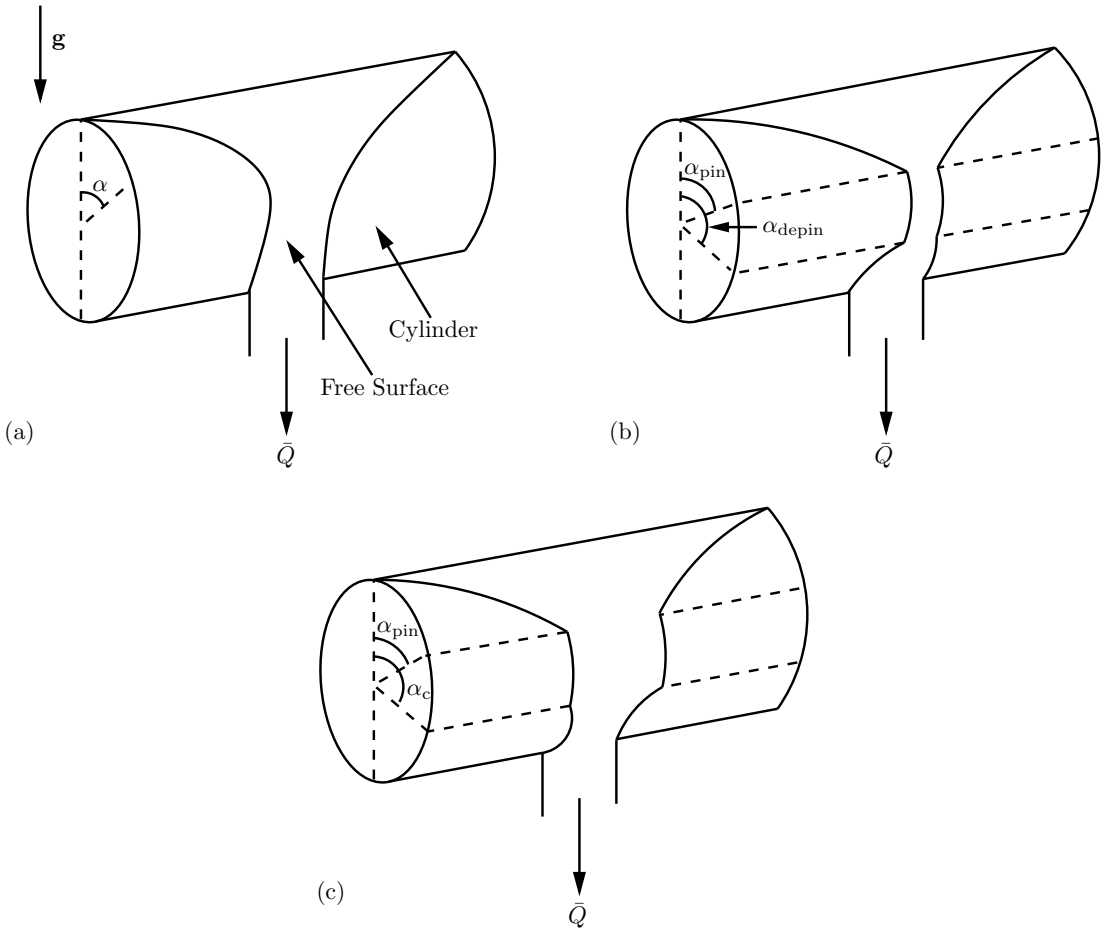

Figure 3.12: Sketches of a slowly varying rivulet with prescribed flux $\bar{Q}$ with (when not pinned with constant semi-width $a = \bar{a}$ and slowly varying contact angle β) constant non-zero contact angle $\beta = \bar{\beta} > 0$ and slowly varying semi-width a that runs from the top $\alpha = 0$ to the bottom $\alpha = \pi$ of a large horizontal cylinder, in the cases (a) $\bar{a} < \pi$ and $0 < \bar{\beta} < \bar{\beta}_{\rm c}$, in which the rivulet is never pinned, (b) $\bar{a} < \pi$ and $\bar{\beta} > \bar{\beta}_{\rm c}$, in which the rivulet is pinned in the interval $\alpha_{\rm pin} < \alpha < \alpha_{\rm depin}$, and (c) $\bar{a} > \pi$, in which the rivulet is pinned in the interval $\alpha_{\rm pin} < \alpha < \alpha_{\rm c}$ and has zero contact angle in the interval $\alpha_{\rm c} \leq \alpha \leq \pi$.

in this situation will be qualitatively different for $\bar{a} \leq \pi$ and $\bar{a} > \pi$.

3.5.1 $\bar{a} \leq \pi$

When $\bar{a} < \pi$ and $\bar{\beta} < \beta_{\min}$ the contact angle is always greater than or equal to $\bar{\beta}$ and hence de-pinning and re-pinning do not occur, and so the rivulet behaves exactly as described in Section 3.3. However, when $\bar{a} < \pi$ and $\bar{\beta} \geq \beta_{\min}$ the rivulet runs from $\alpha = 0$ with constant semi-width $a = \bar{a}$ but decreasing contact angle β as described in Section 3.3 until it reaches the value $\beta = \bar{\beta}$ at $\alpha = \alpha_{\text{depin}}$ ($0 < \alpha_{\text{depin}} < \alpha_{\min}$) at which the contact lines de-pin. The rivulet then runs from $\alpha = \alpha_{\text{depin}}$ with constant contact angle $\beta = \bar{\beta}$ but varying semi-width a as described in Section 3.2 until it reaches $\alpha = \alpha_{\text{repin}}$ ($\alpha_{\min} < \alpha_{\text{repin}} < \pi$) at which the contact lines re-pin. The rivulet then runs from $\alpha = \alpha_{\text{repin}}$ to $\alpha = \pi$ with constant semi-width $a = \bar{a}$ but increasing contact angle β as described in Section 3.3. Here $\alpha = \alpha_{\text{depin}}$ and $\alpha = \alpha_{\text{repin}}$ are the appropriate solutions of the equation $Q = \bar{Q}$ with Q given by (3.3), $a = \bar{a}$ and $\beta = \bar{\beta}$. In the marginal case $\bar{a} = \pi$ we have $\alpha_{\text{repin}} = \pi$ and so re-pinning does not occur. Expressed another way, de-pinning and re-pinning occur when $\bar{a} > \bar{a}_{\text{c}}$, where the value of $\bar{a}_{\text{c}}$ corresponds to $\beta_{\min} = \bar{\beta}$. In the limit $\bar{a} \to \infty$ we have $\alpha_{\text{depin}} \to 0^+$ and $\alpha_{\text{repin}} \to \pi^-$ and so recover the solution for a rivulet with constant non-zero contact angle $\beta = \bar{\beta} > 0$ described in Section 3.2.

3.5.2 $\bar{a} > \pi$

When $\bar{a} > \pi$, as in the case $\bar{a} \leq \pi$, the rivulet runs from $\alpha = 0$ with constant semi-width $a = \bar{a}$ but decreasing contact angle β as described in Section 3.3 until it reaches the value $\beta = \bar{\beta} > 0$ at $\alpha = \alpha_{\text{depin}}$ ($0 < \alpha_{\text{depin}} < \alpha_{\text{c}}$) at which the contact lines de-pin. The rivulet then runs from $\alpha = \alpha_{\text{depin}}$ with contact angle $\beta = \bar{\beta} > 0$ but varying semi-width a as described in Section 3.2 until, unlike in

the case $\bar{a} \leq \pi$, it reaches $\alpha = \pi$. In the limit $\bar{a} \to \infty$ we have $\alpha_{\text{depin}} \to 0^+$ and so again recover the solution for a rivulet with constant non-zero contact angle $\beta = \bar{\beta} > 0$ described in Section 3.2.

3.5.3 Rivulet Profiles

The behaviour for $\bar{\beta} > 0$ for both $\bar{a} \leq \pi$ and $\bar{a} > \pi$ is illustrated in Figure 3.13, which shows plots of the contact angle β, the scaled semi-width a/π, and the maximum thickness h_{m} as functions of the scaled angle α/π for a range of values of $\bar{a}/\pi$ when $\bar{Q} = 1$ and $\bar{\beta} = 1$. In particular, Figure 3.13 shows that in this case de-pinning and re-pinning occur for $\bar{a}/\pi > \bar{a}_{\text{c}}/\pi \simeq 0.6446$ and de-pinning but no re-pinning occurs for $\bar{a}/\pi > 1$. Figure 3.14 shows typical cross-sectional profiles of the rivulet in the cases (a) $\bar{\beta} = 1$ and $\bar{a} = 2\,(< \bar{a}_{\text{c}} \simeq 2.0252)$ (b) $\bar{\beta} = 1$ and $\bar{a} = 2.5$ $(\bar{a}_{\text{c}} < \bar{a} < \pi)$, and (c) $\bar{\beta} = 1$ and $\bar{a} = 5\,(> \pi)$, and, in order to clarify what might again appear to be a rather complicated situation, Figure 3.15 shows sketches of the rivulet in the same three cases, namely (a) $\bar{a} < \bar{a}_{\text{c}} < \pi$, in which the rivulet is never de-pinned, (b) $\bar{a}_{\text{c}} < \bar{a} < \pi$, in which the rivulet is de-pinned in the interval $\alpha_{\text{depin}} < \alpha < \alpha_{\text{repin}}$, and (c) $\bar{a} > \pi$, in which the rivulet is de-pinned in the interval $\alpha_{\text{depin}} < \alpha \leq \pi$.

3.5.4 Mass of Fluid on the Cylinder

The mass of fluid on the cylinder M is given by

$$M = \int_0^{\pi} \int_{-a}^{+a} h \, \mathrm{d}y \, \mathrm{d}\alpha = \int_0^{\frac{\pi}{2}} \frac{2\beta(ma \coth ma - 1)}{m^2} \, \mathrm{d}\alpha + \int_{\frac{\pi}{2}}^{\pi} \frac{2\beta(1 - ma \cot ma)}{m^2} \, \mathrm{d}\alpha. \tag{3.26}$$

Figure 3.16 shows M plotted as a function of the logarithm of the scaled semi-width $\log(\bar{a}/\pi)$ for a range of values of $\bar{\beta}$, and shows that M is a monotonically increasing function of $\bar{a}$. Figure 3.16 also shows that in the limit of a narrow

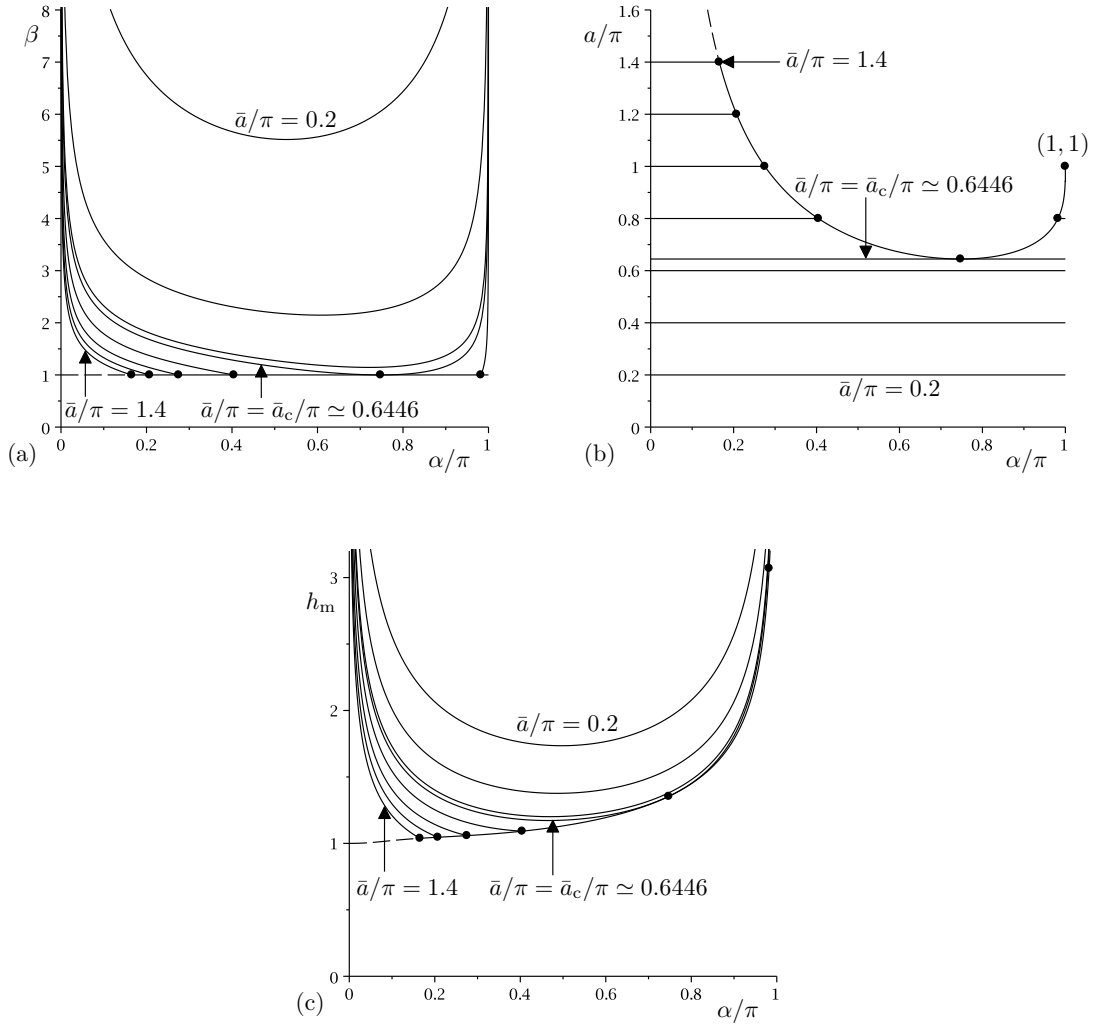

Figure 3.13: Plots of (a) the contact angle β, (b) the scaled semi-width $\bar{a}/\pi$, and (c) the maximum thickness $h_{\rm m}$ as functions of the scaled angle α/π for $\bar{a}/\pi = 0.2$, 0.4, 0.6, $\bar{a}_{\rm c}/\pi \simeq 0.6446$, 0.8, 1, 1.2, 1.4 when $\bar{Q} = 1$ for a rivulet whose contact lines de-pin at non-zero contact angle $\beta = \bar{\beta} = 1$. The corresponding solutions for a rivulet with constant contact angle $\beta = \bar{\beta} = 1$ are shown with dashed lines. De-pinning and re-pinning occur for $\bar{a}/\pi > \bar{a}_{\rm c}/\pi \simeq 0.6446$, de-pinning but no re-pinning occurs for $\bar{a}/\pi > 1$, and the points at which this happens are denoted by dots.

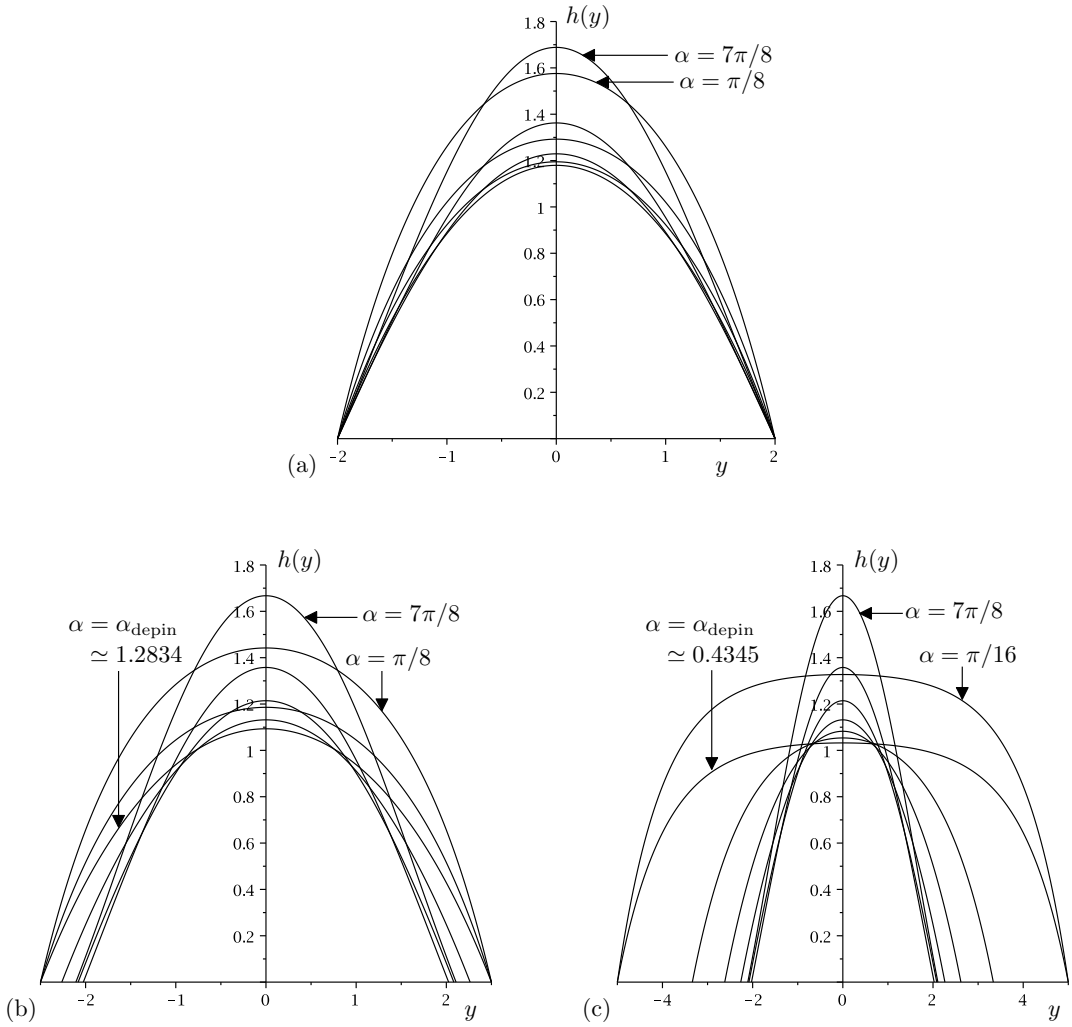

Figure 3.14: Cross-sectional profiles $h(y)$ when $\bar{Q} = 1$ in the cases (a) $\bar{\beta} = 1$ and $\bar{a} = 2\,(< \bar{a}_c \simeq 2.0252)$ for $\alpha = \pi/8$, $\pi/4$, $3\pi/8$, $\pi/2$, $5\pi/8$, $3\pi/4$, $7\pi/8$, (b) $\bar{\beta} = 1$ and $\bar{a} = 2.5$ $(\bar{a}_c < \bar{a} < \pi)$ for $\alpha = \pi/8$, $\pi/4$, $\alpha_{\rm depin} \simeq 1.2834$, $3\pi/8$, $\pi/2$, $5\pi/8$, $3\pi/4$, $7\pi/8$, and (c) $\bar{\beta} = 1$ and $\bar{a} = 5\,(> \pi)$ for $\alpha = \pi/16$, $\alpha_{\rm depin} \simeq 0.4345$, $\pi/4$, $3\pi/8$, $\pi/2$, $5\pi/8$, $3\pi/4$, $7\pi/8$. For clarity, in part (b) no profiles are shown in the interval $\alpha_{\rm repin} \simeq 3.0814 \leq \alpha \leq \pi$, and the three parts of this figure use the same vertical but different horizontal ranges.

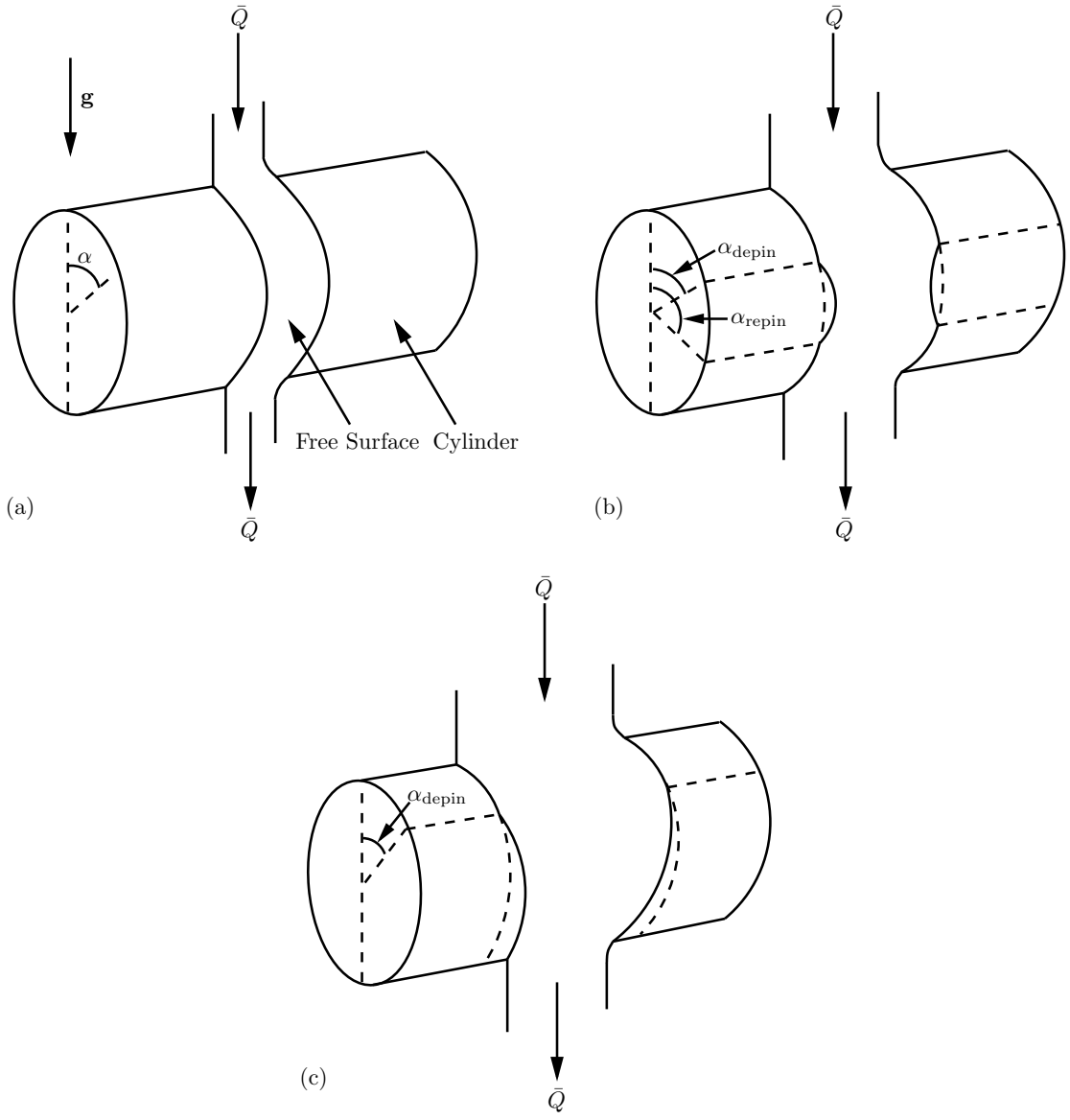

Figure 3.15: Sketches of a slowly varying rivulet with prescribed flux $\bar{Q}$ with (when not de-pinned with non-zero constant contact angle $\beta = \bar{\beta} > 0$ and slowly varying semi-width a) constant semi-width $a = \bar{a}$ and slowly varying contact angle β that runs from the top $\alpha = 0$ to the bottom $\alpha = \pi$ of a large horizontal cylinder, in the cases (a) $\bar{a} < \bar{a}_{\text{c}} < \pi$, in which the rivulet is never de-pinned, (b) $\bar{a}_{\text{c}} < \bar{a} < \pi$, in which the rivulet is de-pinned in the interval $\alpha_{\text{depin}} < \alpha < \alpha_{\text{repin}}$, and (c) $\bar{a} > \pi$, in which the rivulet is de-pinned in the interval $\alpha_{\text{depin}} < \alpha \leq \pi$.

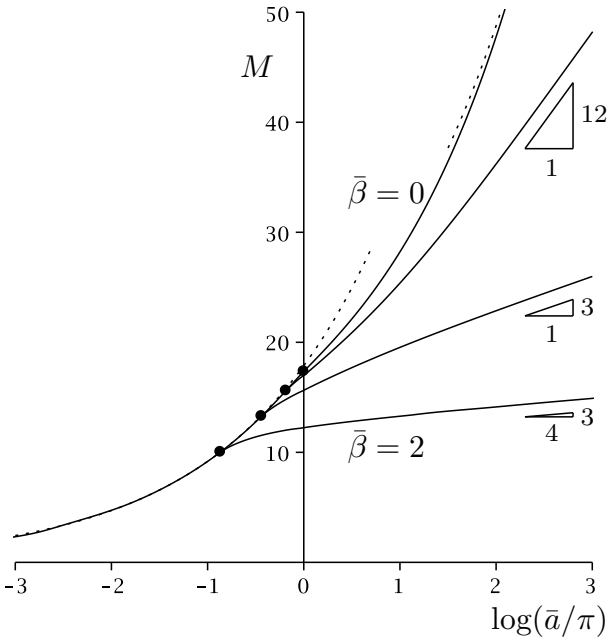

Figure 3.16: The mass of fluid on the cylinder M for a rivulet whose contact lines de-pin at contact angle $\beta = \bar{\beta}$ plotted as a function of the logarithm of the scaled semi-width $\log(\bar{a}/\pi)$ for $\bar{\beta} = 0$, 1/2, 1, 2 when $\bar{Q} = 1$, together with its leading order asymptotic behaviour in the limits $\bar{a} \to 0^+$ given by (3.27) and $\bar{a} \to \infty$ when $\bar{\beta} = 0$ given by (3.28), shown with dotted lines. The triangles indicate the slopes $3\bar{Q}/\bar{\beta}^2 = 12$, 3, 3/4, confirming the leading order asymptotic behaviour in the limit $\bar{a} \to \infty$ when $\bar{\beta} > 0$ given by (3.29). De-pinning and re-pinning occur for $\bar{a}/\pi > \bar{a}_c/\pi$, de-pinning but no re-pinning occurs for $\bar{a}/\pi > 1$, and the points at which de-pinning first occurs are denoted by dots.

rivulet, $\bar{a} \to 0^+$, $M \to 0^+$ according to

$$M \sim \left(\frac{70\bar{a}^2\bar{Q}}{9}\right)^{\frac{1}{3}} C \to 0^+, \tag{3.27}$$

while in the limit of a wide rivulet on the upper half of the cylinder, $\bar{a} \to \infty$, $M \to \infty$ according to

$$M \sim \left(\frac{3\bar{a}^2\bar{Q}}{2}\right)^{\frac{1}{3}} C \to \infty \tag{3.28}$$

when $\bar{\beta} = 0$ and

$$M \sim \frac{3\bar{Q}}{\bar{\beta}^2} \log \bar{a} \to \infty \tag{3.29}$$

when $\bar{\beta} > 0$, where the constant C is again given by (3.10).

3.6 Conclusions

In the present Chapter we showed how the solutions for the unidirectional flow of a thin rivulet with prescribed volume flux down an inclined planar substrate can be used to describe the locally unidirectional flow of a rivulet with constant width (i.e. pinned contact lines) but slowly varying contact angle as well as the possible pinning and subsequent de-pinning of a rivulet with constant contact angle and the possible de-pinning and subsequent re-pinning of a rivulet with constant width as they flow in the azimuthal direction from the top $\alpha = 0$ to the bottom $\alpha = \pi$ of a large horizontal cylinder. We found that, despite being the same locally, the global behaviour of a rivulet with constant width can be very different from that of a rivulet with constant contact angle described by Duffy and Moffatt [23] and Duffy and Wilson [24]. Specifically, while a rivulet with constant non-zero contact angle $\beta = \bar{\beta} > 0$ can always run from the top to the bottom of the cylinder, the behaviour of a rivulet with constant width $\bar{a}$ depends on the value of $\bar{a}$. In particular, while a narrow rivulet with constant semi-width $a = \bar{a} \leq \pi$ can run all the way from the top to the bottom of the cylinder, a wide rivulet with constant

semi-width $a = \bar{a} > \pi$ can run from the top of the cylinder only to a critical azimuthal angle $\alpha = \alpha_c$ given by (3.19). In Section 3.3 we discussed the scenario in which the hitherto pinned contact lines of the rivulet de-pin at $\alpha = \alpha_c$ and the rivulet runs from $\alpha = \alpha_c$ to the bottom of the cylinder with zero contact angle but slowly varying semi-width $a = \pi/m$, as sketched in Figure 3.8.

In Section 3.4 we described the pinning and de-pinning of a rivulet with constant contact angle $\beta = \bar{\beta}$ at $a = \bar{a}$. In particular, we showed that when $\bar{a} \leq \pi$ the rivulet is pinned in the interval $\alpha_{\rm pin} < \alpha < \alpha_{\rm depin}$ for $\bar{\beta} > \bar{\beta}_c$, but that when $\bar{a} > \pi$ the rivulet is pinned in the interval $\alpha_{\rm pin} < \alpha < \alpha_c$ and has zero contact angle in the interval $\alpha_c \leq \alpha \leq \pi$ for all $\bar{\beta} > 0$, as sketched in Figure 3.12. In Section 3.5 we described the corresponding situation involving the de-pinning and re-pinning of a rivulet with constant semi-width $a = \bar{a}$ at a non-zero contact angle $\beta = \bar{\beta} > 0$ which generalises the de-pinning at zero contact angle discussed in Section 3.3. In particular, we showed that when $\bar{a} \leq \pi$ the rivulet is de-pinned in the interval $\alpha_{\rm depin} < \alpha < \alpha_{\rm repin}$ for $\bar{a} > \bar{a}_c$, but that when $\bar{a} > \pi$ the rivulet is de-pinned in the interval $\alpha_{\rm depin} < \alpha \leq \pi$, as sketched in Figure 3.15. In the latter situation, the mass of fluid on the cylinder was found to be a monotonically increasing function of the constant semi-width $\bar{a}$.

Chapter 4

Rivulet flow round a horizontal cylinder subject to a uniform surface shear stress

In Chapter 3 we considered the possible pinning, de-pinning and re-pinning of a gravity-driven rivulet with prescribed constant volume flux as it flows in the azimuthal direction from the top to the bottom of a large horizontal cylinder. In this Chapter, this is extended to include a prescribed uniform surface shear stress due to an external airflow in the direction opposing gravity, and we consider both the case of a rivulet with constant contact angle but variable width (i.e. de-pinned contact lines) and the case of a rivulet with constant width but variable contact angle (i.e. pinned contact lines).

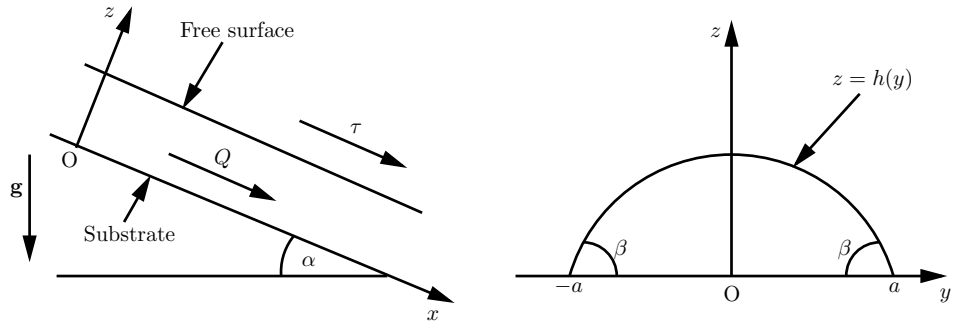

Figure 4.1: Sketch of a thin rivulet with semi-width a, contact angle β and volume flux Q flowing on a planar substrate inclined at an angle α to the horizontal subject to a prescribed uniform longitudinal surface shear stress τ.

4.1 Unidirectional Flow on a Planar Substrate

4.1.1 Problem Formulation

Consider the steady unidirectional flow of a thin symmetric rivulet with semi-width a and volume flux Q on a planar substrate inclined at an angle α ($0 \leq \alpha < 2\pi$) to the horizontal subject to a prescribed uniform longitudinal surface shear stress τ. We assume that the fluid is Newtonian with constant viscosity μ, density ρ and coefficient of surface tension γ, and choose Cartesian coordinates $Oxyz$ with the x axis down the line of greatest slope for $0 < \alpha < \pi$ or up the line of greatest slope for $\pi < \alpha < 2\pi$, the y axis horizontal, and the z axis normal to the substrate $z = 0$, such that $\tau > 0$ corresponds to a shear stress in the positive x direction, as sketched in Figure 4.1.

In dimensionless variables the velocity $\mathbf{u} = u(y, z)\mathbf{i}$ and the pressure (relative to its ambient value) $p = p(y, z)$ satisfy the familiar lubrication and mass-conservation equations (given by (1.16) with y and z replacing x and y, respectively) subject to the normal stress balance $p = -h''$ (that is, equation (1.20) where the dash now means differentiation with respect to y), the tangential stress balance $u_z = \tau$ (analogous to equation (1.21) but now including the shear stress τ at the free

surface) and the kinematic condition at the free surface $z = h(y)$ (that is, equation (1.22) with y replacing x and with $h_t = 0$ for steady flow), the no-slip condition $u = 0$ at the substrate $z = 0$ (analogous to equation (1.17)), and the condition of zero thickness at the contact lines (i.e. $h(\pm a) = 0$), where a dash denotes differentiation with respect to argument. The contact angle is denoted by $\beta = \mp h'(\pm a)$ (≥ 0) and the maximum thickness of the rivulet, which always occurs at $y = 0$, is denoted by $h_{\rm m} = h(0)$. In the above, and in what follows, we have non-dimensionalised as follows:

$$\begin{gathered} y^* = \ell y, \quad a^* = \ell a, \quad z^* = \delta \ell z, \quad h^* = \delta \ell h, \quad h^*_{\rm m} = \delta \ell h_{\rm m}, \\ u^* = \frac{\delta^2 \rho g \ell^2}{\mu} u, \quad Q^* = \frac{\delta^3 \rho g \ell^4}{\mu} Q, \quad p^* - p^*_\infty = \delta \rho g \ell p, \quad \tau^* = \delta^2 \rho g \ell, \end{gathered} \tag{4.1}$$

where star subscripts denote dimensional variables, g is the magnitude of gravitational acceleration, $\ell = (\gamma/\rho g)^{1/2}$ is the capillary length, and δ is the transverse aspect ratio. There is some freedom regarding the definition of δ; however, for the moment we leave δ unspecified in order to keep the subsequent presentation as general as possible. At leading order in the limit of small transverse aspect ratio $\delta \to 0$ (i.e. for a thin rivulet) the governing equations (given by (1.16) with y and z replacing x and y, respectively) are readily solved to yield the pressure

$$p = \cos\alpha (h - z) - h'' \tag{4.2}$$

and the velocity

$$u = \frac{\sin\alpha}{2}(2h - z)z + \tau z, \tag{4.3}$$

so that the local flux $\bar{u} = \bar{u}(y)$ is given by

$$\bar{u} = \int_0^h u \, {\rm d}z = \frac{\sin\alpha}{3} h^3 + \frac{\tau}{2} h^2. \tag{4.4}$$

We may differentiate (4.2) with respect to y and use the fact that $p_y = 0$ to obtain a third order ordinary differential equation for the free surface, namely

$$(h\cos\alpha - h'')' = 0, \tag{4.5}$$

which is to be solved subject to the contact-line conditions $h(\pm a) = 0$ and $\mp h'(\pm a) = \beta\,(\geq 0)$.

4.1.2 The General Case of Non-Zero Contact Angle $\beta > 0$

In the general case of non-zero contact angle $\beta > 0$ we may solve (4.5) subject to the contact-line conditions to obtain the free surface shape

$$h = \beta \times \begin{cases} \dfrac{\cosh ma - \cosh my}{m \sinh ma} & \text{for} \quad 0 \leq \alpha < \dfrac{\pi}{2},\ \dfrac{3\pi}{2} < \alpha < 2\pi, \\ \dfrac{a^2 - y^2}{2a} & \text{for} \quad \alpha = \dfrac{\pi}{2},\ \dfrac{3\pi}{2}, \\ \dfrac{\cos my - \cos ma}{m \sin ma} & \text{for} \quad \dfrac{\pi}{2} < \alpha < \dfrac{3\pi}{2}, \end{cases} \tag{4.6}$$

so that the maximum thickness of the rivulet is given by

$$h_{\mathrm{m}} = \frac{\beta}{m} \times \begin{cases} \tanh\left(\dfrac{ma}{2}\right) & \text{for} \quad 0 \leq \alpha < \dfrac{\pi}{2},\ \dfrac{3\pi}{2} < \alpha < 2\pi, \\ \dfrac{ma}{2} & \text{for} \quad \alpha = \dfrac{\pi}{2},\ \dfrac{3\pi}{2}, \\ \tan\left(\dfrac{ma}{2}\right) & \text{for} \quad \dfrac{\pi}{2} < \alpha < \dfrac{3\pi}{2}, \end{cases} \tag{4.7}$$

and the volume flux is given by

$$Q = \int_{-a}^{a} \bar{u}\,\mathrm{d}y = \frac{\beta^3 \sin\alpha}{9m^4} f(ma) + \frac{\beta^2 \tau}{2m^3} g(ma), \tag{4.8}$$

where we have written $m = |\cos\alpha|^{1/2}$. The functions $f = f(ma)$ and $g = g(ma)$ appearing in (4.8) are defined by

$$f(ma) = \begin{cases} 15ma\coth^3 ma - 15\coth^2 ma - 9ma\coth ma + 4 & \text{for} \quad 0 \leq \alpha < \dfrac{\pi}{2}, \\ & \qquad \dfrac{3\pi}{2} < \alpha < 2\pi, \\ \dfrac{12}{35}(ma)^4 & \text{for} \quad \alpha = \dfrac{\pi}{2},\ \dfrac{3\pi}{2}, \\ -15ma\cot^3 ma + 15\cot^2 ma - 9ma\cot ma + 4 & \text{for} \quad \dfrac{\pi}{2} < \alpha < \dfrac{3\pi}{2} \end{cases} \tag{4.9}$$

and

$$g(ma) = \begin{cases} 3ma\coth^2 ma - 3\coth ma - ma & \text{for} \quad 0 \le \alpha < \dfrac{\pi}{2},\ \dfrac{3\pi}{2} < \alpha < 2\pi, \\ \dfrac{4}{15}(ma)^3 & \text{for} \quad \alpha = \dfrac{\pi}{2},\ \dfrac{3\pi}{2}, \\ 3ma\cot^2 ma - 3\cot ma + ma & \text{for} \quad \dfrac{\pi}{2} < \alpha < \dfrac{3\pi}{2}. \end{cases} \tag{4.10}$$

Note that the function $f(ma)$ was first obtained by Duffy and Moffatt [23] (their equation (14) and denoted as $F(B)$) and the function $g(ma)$ was first obtained by Sullivan, Wilson and Duffy [91] (their equation (2.16)). For $0 \le \alpha < \pi/2$ and $3\pi/2 < \alpha < 2\pi$ both f and g are positive, monotonically increasing functions, increasing from zero at $ma = 0$ to infinity as $ma \to \infty$, while their derivatives f' and g' are also positive, monotonically increasing functions, increasing from zero at $ma = 0$ to 6 and 2, respectively, as $ma \to \infty$. Figure 4.2(a) shows plots of f, g, f', and g' as functions of ma for $0 \le \alpha < \pi/2$ and $3\pi/2 < \alpha < 2\pi$. For $\pi/2 < \alpha < 3\pi/2$ both f and g have multiple branches, but we restrict our attention to the branches in the interval $0 \le ma < \pi$ since these are the only ones for which the solution is physically realisable (specifically, for which $h \ge 0$ everywhere in the interval $y = -a$ to $y = +a$). Then f and g and their derivatives f' and g' are all positive, monotonically increasing functions, increasing from zero at $ma = 0$ to infinity as $ma \to \pi^-$. Figure 4.2(b) shows plots of f, g, f', and g' as functions of ma/π for $\pi/2 < \alpha < 3\pi/2$. For future reference it is useful to note that in the limit $ma \to 0^+$

$$f(ma) = \begin{cases} \dfrac{12}{35}(ma)^4 - \dfrac{8}{105}(ma)^6 + O(ma)^8 & \text{for} \quad 0 \le \alpha < \dfrac{\pi}{2},\ \dfrac{3\pi}{2} < \alpha < 2\pi, \\ \dfrac{12}{35}(ma)^4 + \dfrac{8}{105}(ma)^6 + O(ma)^8 & \text{for} \quad \dfrac{\pi}{2} < \alpha < \dfrac{3\pi}{2} \end{cases} \tag{4.11}$$

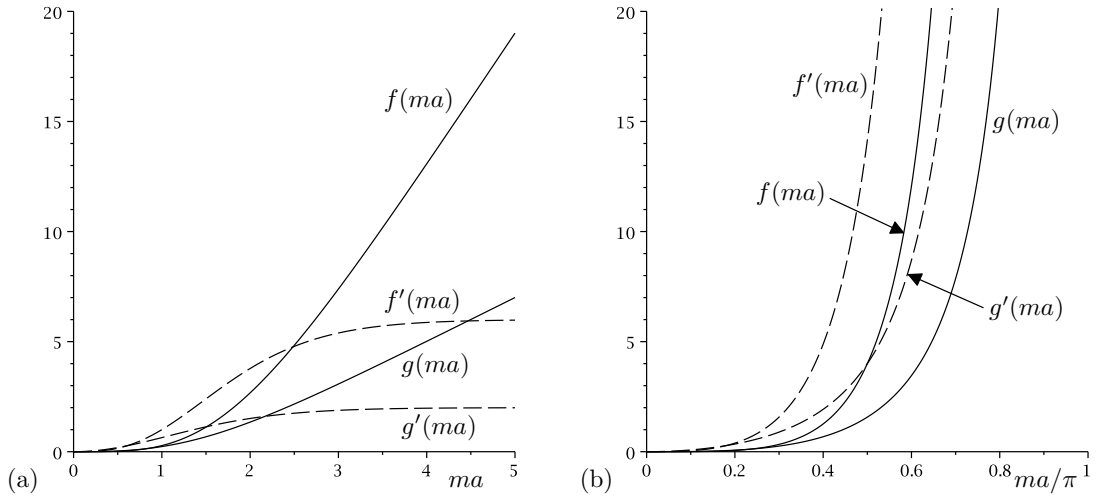

Figure 4.2: Plots of f and g (solid lines), defined by (4.9) and (4.10), respectively, together with their derivatives f' and g' (dashed lines) as (a) functions of ma for $0 \le \alpha < \pi/2$ and $3\pi/2 < \alpha < 2\pi$ when $0 \le ma < \infty$, and (b) functions of ma/π for $\pi/2 < \alpha < 3\pi/2$ when $0 \le ma < \pi$.

and

$$g(ma) = \begin{cases} \dfrac{4}{15}(ma)^3 - \dfrac{4}{105}(ma)^5 + O(ma)^7 & \text{for} \quad 0 \le \alpha < \dfrac{\pi}{2}, \ \dfrac{3\pi}{2} < \alpha < 2\pi, \\ \dfrac{4}{15}(ma)^3 + \dfrac{4}{105}(ma)^5 + O(ma)^7 & \text{for} \quad \dfrac{\pi}{2} < \alpha < \dfrac{3\pi}{2}. \end{cases} \tag{4.12}$$

In the limit $ma \to \infty$ for $0 \le \alpha < \pi/2$ and $3\pi/2 < \alpha < 2\pi$

$$f(ma) = 6ma - 11 + O(ma \exp(-2ma)) \tag{4.13}$$

and

$$g(ma) = 2ma - 3 + O(ma \exp(-2ma)). \tag{4.14}$$

In the limit $ma \to \pi^-$ for $\pi/2 < \alpha < 3\pi/2$

$$f(ma) = \frac{15\pi}{(\pi - ma)^3} + O(\pi - ma)^{-1} \tag{4.15}$$

and

$$g(ma) = \frac{3\pi}{(\pi - ma)^2} + O(1). \tag{4.16}$$

4.1.3 The Special Case of Zero Contact Angle $\beta = 0$

In the special case of zero contact angle $\beta = 0$ we recover the solution for a rivulet of perfectly wetting fluid analysed by Sullivan, Wilson and Duffy [91], namely that there is no solution for $0 \leq \alpha \leq \pi/2$ and $3\pi/2 \leq \alpha < 2\pi$, but

$$a = \frac{\pi}{m}, \quad h = \frac{h_{\mathrm{m}}}{2}\left(1 + \cos my\right), \quad Q = \frac{\pi}{24m}\left(5\sin\alpha h_{\mathrm{m}} + 9\tau\right)h_{\mathrm{m}}^2 \tag{4.17}$$

for $\pi/2 < \alpha < 3\pi/2$.

4.1.4 Cross-Sectional Flow Patterns

All of the possible cross-sectional flow patterns that can occur within the rivulet may be categorised into five types which, following the notation used by Wilson and Duffy [108] and Sullivan, Wilson and Duffy [91], we denote as type I to type V. The flow patterns for a rivulet on a substrate inclined at an angle α for $0 < \alpha < \pi$ with shear stress τ and volume flux Q are equivalent to those for $\pi < \alpha < 2\pi$ with shear stress $-\tau$ and volume flux $-Q$, and hence, without loss of generality, in the rest of this Subsection we restrict our attention to the interval $0 < \alpha < \pi$.

Figure 1.17 in Chapter 1 shows sketches of these five different types of flow pattern when $\beta > 0$ at $\alpha = \pi/2$, for which the rivulet has a parabolic profile. Regions with $u > 0$ (i.e. downwards flow for $0 < \alpha < \pi$) are shaded and regions with $u < 0$ are unshaded. When $\beta = 0$ and/or $\alpha \neq \pi/2$ the rivulet profile is not parabolic; however, the flow patterns in these cases are qualitatively the same as those shown in Figure 1.17. The locations of the maximum and minimum velocities are marked with dots, and expressions for these points for each flow type are the same as those given by Sullivan, Wilson and Duffy [91] and hence are not reproduced here for brevity. When $\tau > 0$ the shear stress acts down the substrate in co-operation with gravity and so the velocity is downwards throughout the rivulet (type-I flow), but when $\tau < 0$ the shear stress acts up the substrate in opposition

to gravity, and the velocity is always upwards near the contact lines (types-II–V flow). The velocity within the rivulet is zero on the curve $z = 2(h - \tau/\sin\alpha)$; with $z = h = h_{\rm m}$ this shows, in particular, that type-III flow occurs when $h_{\rm m} = -2\tau/\sin\alpha$. For flow types II–IV this curve of zero velocity meets the substrate when $y = \pm b$, and for flow type II it meets the free surface when $y = \pm c$, where b is given by

$$b = \begin{cases} \dfrac{1}{m}\cosh^{-1}\left[\cosh ma + \dfrac{\tau m \sinh ma}{\beta \sin\alpha}\right] & \text{for} \quad 0 < \alpha < \dfrac{\pi}{2}, \\ \left(a^2 + \dfrac{2\tau a}{\beta}\right)^{\frac{1}{2}} & \text{for} \quad \alpha = \dfrac{\pi}{2}, \\ \dfrac{1}{m}\cos^{-1}\left[\cos ma - \dfrac{\tau m \sin ma}{\beta \sin\alpha}\right] & \text{for} \quad \dfrac{\pi}{2} < \alpha < \pi, \end{cases} \tag{4.18}$$

and c is given by (4.18) with τ replaced by 2τ.

4.2 Locally Unidirectional Flow Round a Horizontal Cylinder

In the remainder of the present Chapter we use the steady unidirectional flow solutions (4.6)–(4.10) and (4.17) to describe the steady, locally unidirectional flow of a slowly varying rivulet with prescribed flux $Q = \bar{Q}$ on a slowly varying substrate, specifically the flow in the azimuthal direction round a large stationary horizontal cylinder, subject to a prescribed uniform azimuthal surface shear stress τ. Note that here and henceforth "slowly varying" means that the longitudinal aspect ratio $\epsilon = \ell/R$, where R is the radius of the cylinder, satisfies $\epsilon \ll \delta$, so that $\epsilon/\delta \to 0$ in the limit $\epsilon \to 0$. The angle α is now interpreted as the local slope of the cylinder, with $\alpha = 0$ at the top, increasing down the right-hand side to $\alpha = \pi$ at the bottom, and up the left-hand side to $\alpha = 2\pi$ at the top again. Since a solution with shear stress τ and volume flux $\bar{Q}$ on one side of the cylinder is equivalent to a solution

with shear stress $-\tau$ and volume flux $-\bar{Q}$ on the other side, in the remainder of the present Chapter we will, without loss of generality, restrict our attention to the case of positive prescribed flux, $\bar{Q} > 0$ (corresponding to a clockwise flux in the figures shown later).

In practice, when a rivulet flows round a cylinder it is possible that either its contact lines are de-pinned and free to move such that its contact angle remains constant but its width varies, or its contact lines are pinned such that its width remains constant but its contact angle varies. We will therefore consider both of these scenarios in the present Chapter and, in particular, we will show that they have qualitatively different behaviour. Firstly, in Section 4.3 we describe a rivulet with constant non-zero contact angle $\beta = \bar{\beta} > 0$ but slowly varying semi-width $a = a(\alpha)$. Imposing the condition of prescribed flux $Q = \bar{Q}$ means that (4.8) is a transcendental equation for a which is solved asymptotically in various physically relevant limits and numerically. Secondly, in Section 4.4 we describe a rivulet with constant semi-width $a = \bar{a}$ but slowly varying contact angle $\beta = \beta(\alpha)\,(\geq 0)$. Imposing the condition of prescribed flux $Q = \bar{Q}$ means that (4.8) is a cubic polynomial equation for β which may be solved exactly. We analyse this solution and, in particular, explore its behaviour in various physically relevant limits.

Figure 4.3 shows a representative selection of rivulet solutions for various values of τ plotted as functions of the scaled angle α/π ($0 \leq \alpha < 2\pi$) when $Q = \bar{Q} = 1$. Expressed in another way, Figure 4.3 shows contours of the expression for the shear stress τ given by (4.8) in the α/π–a, α/π–β and α/π–h_{m} planes, as appropriate, when $Q = \bar{Q} = 1$. Specifically, Figures 4.3(a) and 4.3(b) show the semi-width a and maximum thickness h_{m} for a rivulet with constant non-zero contact angle $\beta = \bar{\beta} = 1$, Figures 4.3(c) and 4.3(d) show the contact angle β and maximum thickness h_{m} for a "narrow" rivulet with constant semi-width $a = \bar{a} = 2\,(< \pi)$, and Figures 4.3(e) and 4.3(f) show the contact angle β and maximum thickness

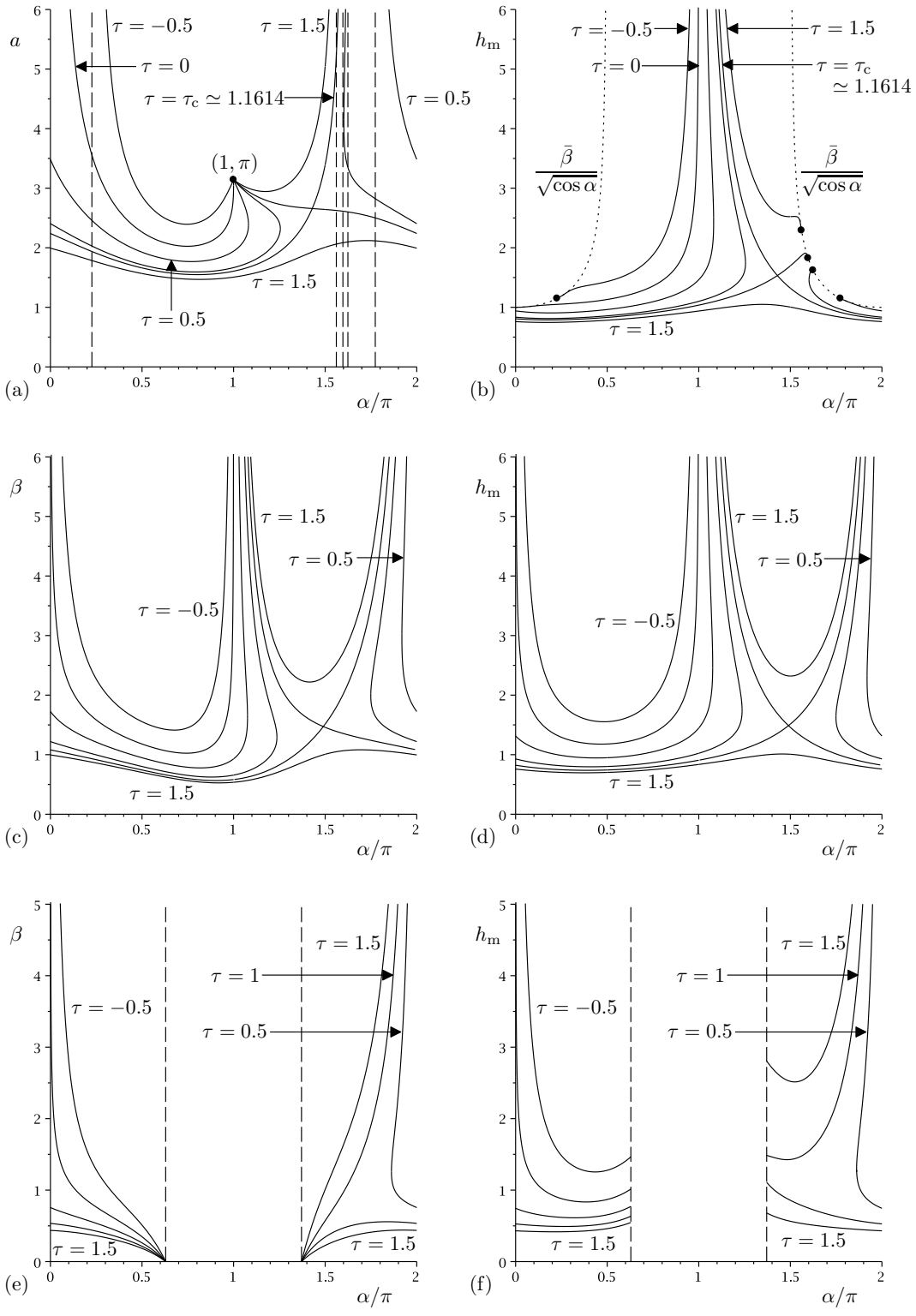

Figure 4.3: Plots of (a) the semi-width a, (c,e) the contact angle β, and (b,d,f) the maximum thickness $h_{\rm m}$ as functions of α/π ($0 \le \alpha < 2\pi$) when $Q = \bar{Q} = 1$ for (a,b) $\tau = -0.5$, 0, 0.5, 1, $\tau_{\rm c} \simeq 1.1614$, 1.5 for a rivulet with constant contact angle $\beta = \bar\beta = 1$, (c,d) $\tau = -0.5$, 0, 0.5, 1, $\tau_{\rm c} \simeq 1.2741$, 1.5 for a "narrow" rivulet with constant semi-width $a = \bar{a} = 2\,(< \pi)$, and (e,f) $\tau = -0.5$, 0, 0.5, 1, 1.5 for a "wide" rivulet with constant semi-width $a = \bar{a} = 5\,(> \pi)$. We solve equation (4.8) to plot parts (a), (c) and (e), and we use equation (4.7) to plot parts (b), (d) and (f). In (a) the vertical dashed lines indicate the values of α/π at which $a \to \infty$, and in (b) the dots denote the corresponding values of $h_{\rm m}$ which lie on the curves $h_{\rm m} = \bar\beta/\sqrt{\cos\alpha}$ for $0 \le \alpha < \pi/2$ and $3\pi/2 < \alpha < 2\pi$, which are denoted with dotted lines. In (e) and (f) the vertical dashed lines correspond to the values of α/π at which $\beta = 0$, namely $\alpha/\pi = \alpha_{\rm depin}/\pi \simeq 0.6292$ and $\alpha/\pi = 2 - \alpha_{\rm depin}/\pi \simeq 1.3708$.

h_{m} for a "wide" rivulet with constant semi-width $a = \bar{a} = 5\,(> \pi)$, all plotted as functions of α/π for various values of τ. In particular, Figure 4.3 shows that neither in the case of constant non-zero contact angle nor in the case of constant width does the rivulet have top-to-bottom symmetry (i.e. symmetry about $\alpha = \pi/2$ and $\alpha = 3\pi/2$). As Figure 4.3 shows, there are various kinds of rivulet solution, some of which exist only in a restricted range of values of α. In particular, in Figures 4.3(a) and 4.3(b) there is no physically realisable rivulet solution with $\beta = \bar{\beta} = 1$ when $\tau = -0.5$ in the interval $0 \leq \alpha \leq \alpha_{\infty}$, where $\alpha_{\infty}/\pi \simeq 0.2264$. This behaviour (which occurs for all $\tau < 0$) will be discussed in greater detail in Section 4.3, where it will be interpreted as the presence of an infinitely wide sheet of fluid. Similarly, in Figures 4.3(e) and 4.3(f) there are no physically realisable rivulet solutions with $a = \bar{a} = 5$ for all values of τ shown in the interval $\alpha_{\mathrm{depin}} < \alpha < 2\pi - \alpha_{\mathrm{depin}}$, where $\alpha_{\mathrm{depin}}/\pi \simeq 0.6292$ and $2 - \alpha_{\mathrm{depin}}/\pi \simeq 1.3708$. This behaviour (which occurs for all values of τ when $\bar{a} > \pi$) will be discussed in greater detail in Section 4.4, where it will be interpreted as the occurrence of contact-line de-pinning. Comparison of Figures 4.3(c) and 4.3(d) with Figures 4.3(e) and 4.3(f) shows that, just as was found in Chapter 3 in the special case of no shear stress, $\tau = 0$, unlike a rivulet with constant non-zero contact angle, a "narrow" rivulet with constant semi-width $a = \bar{a} < \pi$ behaves qualitatively differently from a "wide" rivulet with constant semi-width $a = \bar{a} > \pi$. Figure 4.3 also shows the existence of a positive critical shear stress, $\tau_{\mathrm{c}}\,(> 0)$, such that "full-ring" solutions (i.e. solutions for which a, β and h_{m} are continuous, finite and non-negative for all $0 \leq \alpha < 2\pi$ and $-a \leq y \leq a$), analogous to those studied by Leslie, Wilson and Duffy [48] in the case of flow on a rotating cylinder in the absence of surface shear stress, exist when $\tau \geq \tau_{\mathrm{c}}$ but not when $\tau < \tau_{\mathrm{c}}$.

In the remainder of the present Chapter we focus on just one of the kinds of solution shown in Figure 4.3, namely the case of non-positive shear stress, $\tau \leq 0$,

in which there is always a solution corresponding to a rivulet flowing down at least part of the right-hand side of the cylinder (where the shear stress acts in opposition to gravity, but it is still possible to sustain a positive flux), but never any solutions corresponding to flow on the left-hand side of the cylinder (where the shear stress acts in co-operation with gravity, making it impossible to sustain a positive flux).

4.3 A Rivulet with Constant Non-Zero Contact Angle $\beta = \bar{\beta} > 0$

In this Section we describe the steady, locally unidirectional flow of a slowly varying rivulet with constant non-zero contact angle $\beta = \bar{\beta} > 0$ but slowly varying semi-width $a = a(\alpha)$ on the right-hand side of a large horizontal cylinder subject to a non-positive uniform azimuthal surface shear stress $\tau\,(\leq 0)$ acting in opposition to gravity.

In the special case of no shear, $\tau = 0$, the rivulet becomes infinitely wide at the top of the cylinder (i.e. $a \to \infty$ as $\alpha \to 0^+$) and it runs all the way from the top $\alpha = 0$ to the bottom $\alpha = \pi$ of the cylinder; however, as we saw in Figure 4.3(a), in the general case of strictly negative shear, $\tau < 0$, the rivulet becomes infinitely wide at the station $\alpha = \alpha_\infty$ away from the top of the cylinder (i.e. $a \to \infty$ as $\alpha \to \alpha_\infty^+$) and there is no physically realisable rivulet solution in the interval $0 \leq \alpha \leq \alpha_\infty$. The value of α_∞ ($0 \leq \alpha_\infty < \pi/2$) is determined by the leading order balance in (4.8) when $a \to \infty$, namely

$$2\bar{\beta}\sin\alpha + 3m\tau = 0 \tag{4.19}$$

evaluated at $\alpha = \alpha_\infty$, and is therefore given by

$$\alpha_\infty = \cos^{-1}\left(\frac{\sqrt{81\tau^4 + 64\bar{\beta}^4} - 9\tau^2}{8\bar{\beta}^2}\right), \tag{4.20}$$

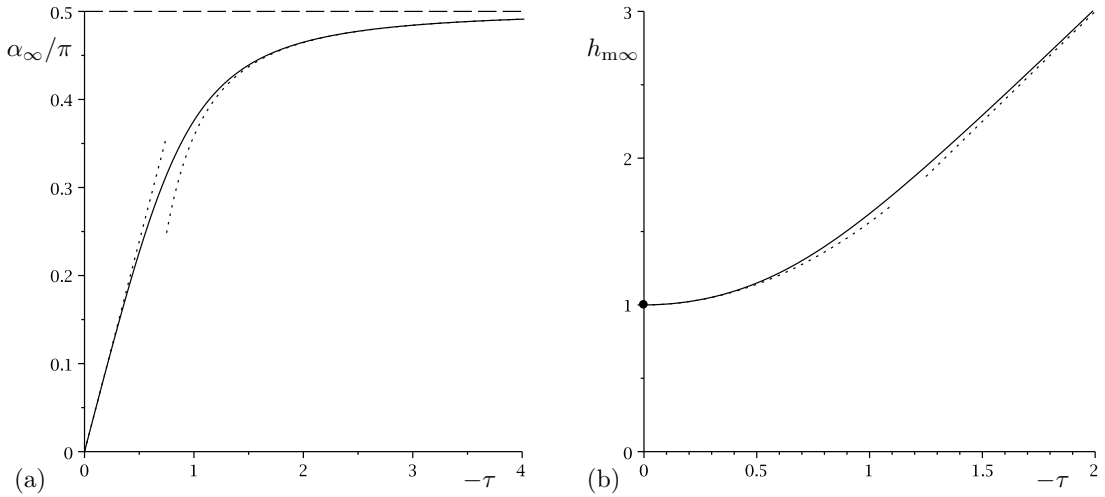

Figure 4.4: Plots of (a) the scaled azimuthal angle at which the rivulet becomes infinitely wide, α_∞/π, given by (4.20), and (b) the corresponding maximum thickness, $h_{m\infty}$, given by (4.21), as functions of $-\tau\,(\geq 0)$ when $\bar{\beta} = 1$. The dotted curves show the asymptotic results in the limits of weak shear, $-\tau \to 0^+$, and strong shear, $-\tau \to \infty$, given by (4.22) and (4.23), respectively.

while the corresponding value of the maximum thickness $h_m = h_{m\infty}$ is given by

$$h_{m\infty} = \frac{\bar{\beta}}{\sqrt{\cos\alpha_\infty}} = \frac{\left[\sqrt{81\tau^4 + 64\bar{\beta}^4} + 9\tau^2\right]^{\frac{1}{2}}}{2\sqrt{2}}. \tag{4.21}$$

Figure 4.4 shows plots of α_∞/π and $h_{m\infty}$ as functions of $-\tau\,(\geq 0)$ when $\bar{\beta} = 1$, and shows that both α_∞ and $h_{m\infty}$ are monotonically increasing functions of $-\tau$. In particular, in the limit of weak shear, $\tau \to 0^-$, the rivulet becomes infinitely wide near the top of the cylinder and correspondingly its maximum thickness approaches the finite value $\bar{\beta}$ from above according to

$$\alpha_\infty \sim -\frac{3\tau}{2\bar{\beta}} \to 0^+ \quad \text{and} \quad h_{m\infty} \sim \bar{\beta} + \frac{9\tau^2}{16\bar{\beta}} \to \bar{\beta}^+, \tag{4.22}$$

while in the limit of strong shear, $\tau \to -\infty$, the rivulet becomes infinitely wide near the middle of the cylinder and correspondingly its maximum thickness becomes infinite according to

$$\alpha_\infty \sim \frac{\pi}{2} - \frac{4\bar{\beta}^2}{9\tau^2} \to \frac{\pi}{2}^- \quad \text{and} \quad h_{m\infty} \sim -\frac{3\tau}{2} \to \infty. \tag{4.23}$$

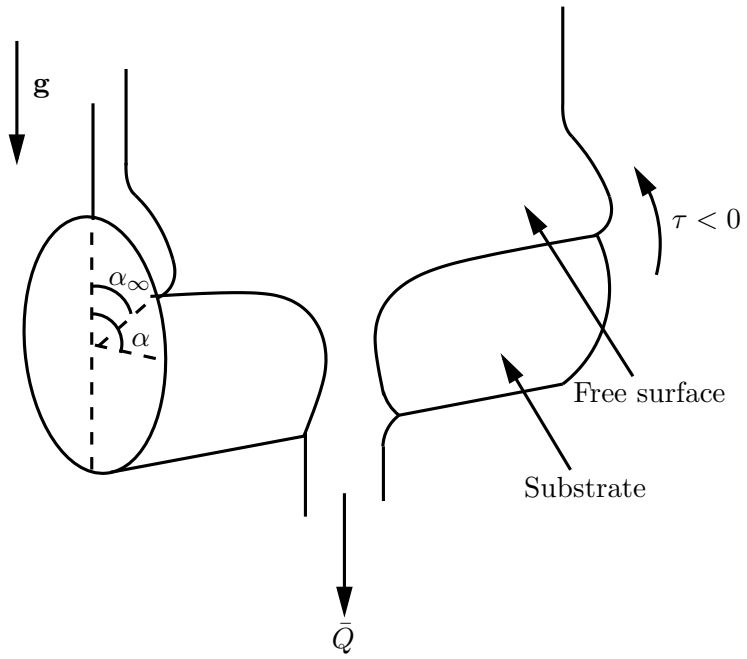

Figure 4.5: Sketch of the scenario considered in Section 4.3, namely an infinitely wide two-dimensional film of uniform thickness $H = H(\alpha)$ covers the cylinder from $\alpha = 0$ to $\alpha = \alpha_\infty$, where it "breaks" into a single rivulet with prescribed flux $Q = \bar{Q}$, constant contact angle $\beta = \bar{\beta}\,(> 0)$ and slowly varying semi-width a that runs from $\alpha = \alpha_\infty$ to $\alpha = \pi$.

Since there is no physically realisable rivulet solution in the interval $0 \leq \alpha \leq \alpha_\infty$, an alternative description of the behaviour is required there. Perhaps the most natural scenario is that an infinitely wide two-dimensional film of uniform thickness $H = H(\alpha)$ covers the cylinder from $\alpha = 0$ to $\alpha = \alpha_\infty$, where it "breaks" into a single rivulet with prescribed flux $Q = \bar{Q}$ that runs from $\alpha = \alpha_\infty$ to the bottom of the cylinder $\alpha = \pi$. This scenario is sketched in Figure 4.5 and is the one that we will consider here. The appropriate form of H, determined by setting $\bar{u} = 0$ and $h = H$ in (4.4), is

$$H = -\frac{3\tau}{2\sin\alpha}\,(> 0). \tag{4.24}$$

In particular, (4.24) shows that the film becomes deep near the top of the cylinder according to

$$H \sim -\frac{3\tau}{2\alpha} \to \infty \tag{4.25}$$

as $\alpha \to 0^+$, and that it approaches the finite thickness $h_{\mathrm{m}\infty}$ from above according to

$$H \sim h_{\mathrm{m}\infty} - \frac{2\bar{\beta}^2}{3\tau}\,(\alpha_\infty - \alpha) \to h^+_{\mathrm{m}\infty} \tag{4.26}$$

as $\alpha \to \alpha^-_\infty$. Similarly, (4.8) shows that the rivulet becomes infinitely wide according to

$$a \sim \frac{4\left[3(\cos\alpha_\infty)^{\frac{3}{2}}\bar{Q} - \bar{\beta}^2\tau\right]}{\bar{\beta}\sqrt{81\tau^4 + 64\bar{\beta}^4}\,(\alpha - \alpha_\infty)} \to \infty \tag{4.27}$$

and (4.7) shows that it approaches the finite maximum thickness $h_{\mathrm{m}\infty}$ from above according to

$$h_{\mathrm{m}} \sim h_{\mathrm{m}\infty} + \frac{h_{\mathrm{m}\infty}\tan\alpha_\infty}{2}\,(\alpha - \alpha_\infty) \to h^+_{\mathrm{m}\infty} \tag{4.28}$$

as $\alpha \to \alpha^+_\infty$, so that the infinitely wide film in $0 \leq \alpha \leq \alpha_\infty$ and the finite-width rivulet in $\alpha_\infty < \alpha \leq \pi$ join continuously (but not smoothly) at the station $\alpha = \alpha_\infty$. In the special case of no shear, $\tau = 0$, the rivulet becomes deep with finite semi-

width π near the bottom of the cylinder according to

$$a \sim \pi - \left(\frac{5\bar{\beta}^3(\pi-\alpha)}{3\bar{Q}}\right)^{\frac{1}{3}} \to \pi^- \quad \text{and} \quad h_{\rm m} \sim \left(\frac{24\bar{Q}}{5(\pi-\alpha)}\right)^{\frac{1}{3}} \to \infty \tag{4.29}$$

as $\alpha \to \pi^-$, while in the general case of strictly negative shear, $\tau < 0$, the rivulet again becomes deep with finite semi-width π near the bottom of the cylinder, but now according to

$$a \sim \pi + \frac{10\bar{\beta}(\pi-\alpha)}{9\tau} \to \pi^- \quad \text{and} \quad h_{\rm m} \sim -\frac{9\tau}{5(\pi-\alpha)} \to \infty \tag{4.30}$$

as $\alpha \to \pi^-$.

The behaviour of the present solution is illustrated in Figure 4.6, which shows plots of the semi-width a and the maximum thickness $h_{\rm m}$ as functions of α/π when $\bar{\beta} = 1$ for (a,b) various values of $\tau\,(\leq 0)$ when $\bar{Q} = 1$ and for (c,d) various values of $\bar{Q}$ when $\tau = -0.5$.

In Subsection 4.3.1 we present examples of free surface profiles of the film and the rivulet, and in Subsections 4.3.2–4.3.5 we describe the behaviour in the limits of weak shear, $\tau \to 0^-$, strong shear, $\tau \to -\infty$, small flux, $\bar{Q} \to 0^+$, and large flux, $\bar{Q} \to \infty$, respectively.

4.3.1 Free Surface Profiles

Figure 4.7 shows examples of cross-sectional free surface profiles of the film and the rivulet in the case $\bar{\beta} = 1$, $\tau = -0.5$ and $\bar{Q} = 1$. For these parameter values we obtain $\alpha_\infty \simeq 0.7112$, and so the profile shown for $\alpha = \pi/8 < \alpha_\infty \simeq 0.7112$ is simply a horizontal line that corresponds to an infinitely wide film of uniform thickness $H \simeq 1.9598$.

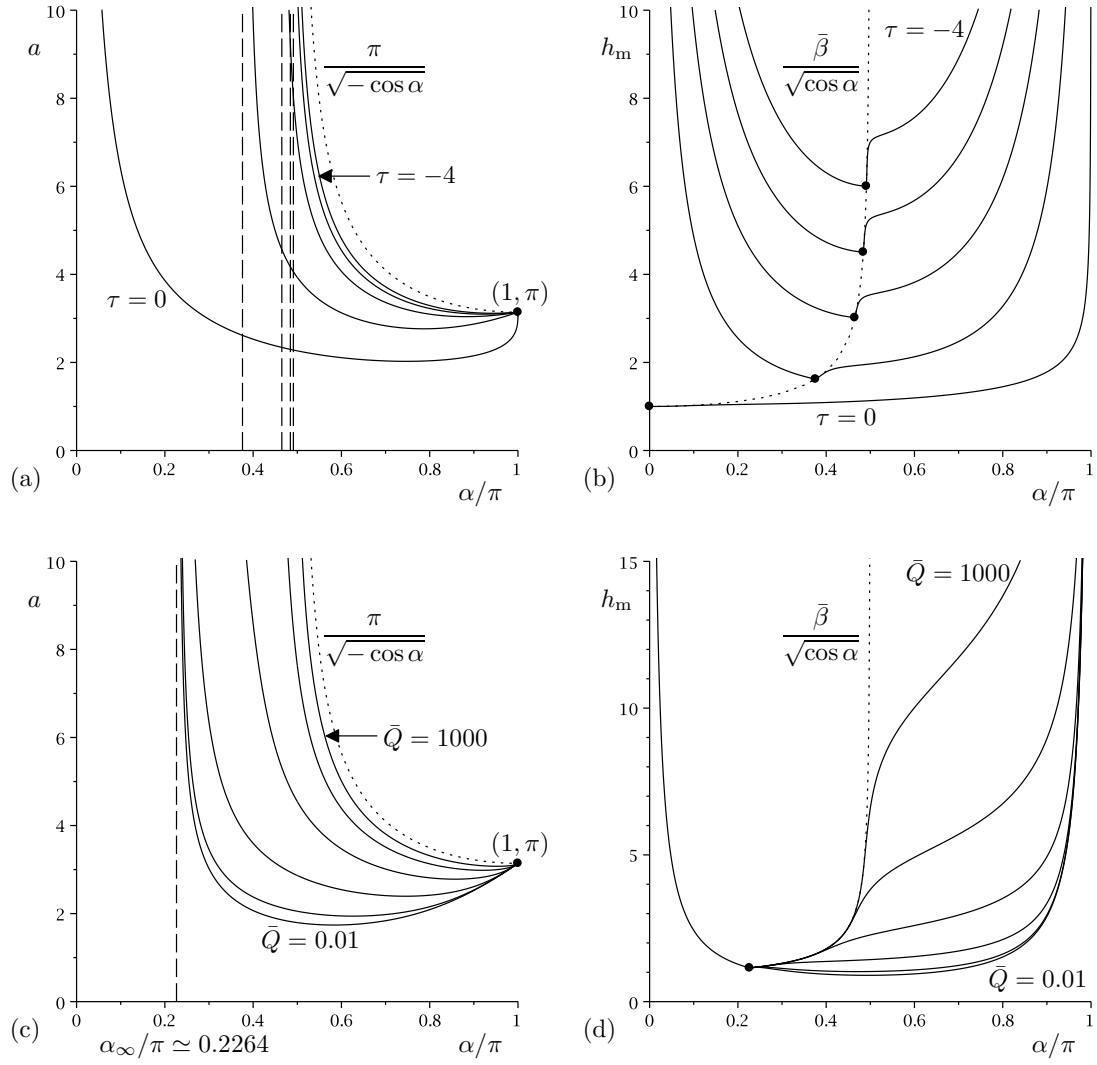

Figure 4.6: Plots of (a,c) the semi-width a and (b,d) the maximum thickness $h_{\rm m}$ as functions of the scaled angle α/π when $\bar\beta = 1$ for (a,b) $\tau = -4, -3, \ldots, 0$ when $\bar Q = 1$ and (c,d) $\bar Q = 0.01, 0.1, \ldots, 1000$ when $\tau = -0.5$. In (a) and (c) the vertical dashed lines indicate the values of $\alpha/\pi = \alpha_\infty/\pi$, given by (4.20), at which $a \to \infty$, and in (b) and (d) the dots denote the corresponding values of $h_{\rm m}$ which lie on the curve $h_{\rm m} = \bar\beta/\sqrt{\cos\alpha}$ for $0 \le \alpha < \pi/2$, which is denoted with a dotted line. In (a) and (c) the dotted lines denote the solution $a = \pi/\sqrt{-\cos\alpha}$ for $\pi/2 < \alpha \le \pi$ attained at leading order in the asymptotic limits $\tau \to -\infty$ and $\bar Q \to \infty$, respectively.

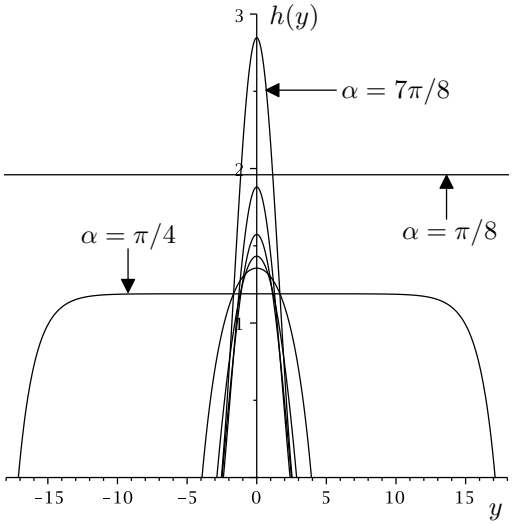

Figure 4.7: Cross-sectional free surface profiles of the film H and the rivulet $h(y)$ when $\bar{\beta} = 1$, $\tau = -0.5$ and $\bar{Q} = 1$ at $\alpha = \pi/8$, $\pi/4$, $3\pi/8$, $\pi/2$, $5\pi/8$, $3\pi/4$, $7\pi/8$. Note that in this case $\pi/8 < \alpha_\infty \simeq 0.7112 < \pi/4$, and so the profile in the case $\alpha = \pi/8$ is that of an infinitely wide film of uniform thickness $H \simeq 1.9598$ rather than that of a finite-width rivulet.

4.3.2 The Limit of Weak Shear ($\tau \to 0^-$)

In the limit of weak shear, $\tau \to 0^-$, $\alpha_\infty \to 0^+$ according to (4.22) and the rivulet behaves according to

$$a \sim a_{\tau 0} - \frac{9g(ma_{\tau 0})\tau}{2\bar{\beta}\sin\alpha f'(ma_{\tau 0})} \to a_{\tau 0}^+ \quad \text{and} \quad h_{\rm m} \sim \frac{\bar{\beta}}{m}\tanh\left(\frac{ma_{\tau 0}}{2}\right) = O(1) \quad (4.31)$$

on the upper half of the cylinder,

$$a \sim \left(\frac{105\bar{Q}}{4\bar{\beta}^3}\right)^{\frac{1}{4}} - \frac{7\tau}{8\bar{\beta}} \to \left(\frac{105\bar{Q}}{4\bar{\beta}^3}\right)^{\frac{1}{4}+} \quad \text{and} \quad h_{\rm m} \sim \left(\frac{105\bar{Q}\bar{\beta}}{64}\right)^{\frac{1}{4}} - \frac{7\tau}{16} \to \left(\frac{105\bar{Q}\bar{\beta}}{64}\right)^{\frac{1}{4}+} \quad (4.32)$$

at $\alpha = \pi/2$, and according to (4.31) with "tanh" replaced by "tan" in the expression for $h_{\rm m}$ on the lower half of the cylinder, where $a_{\tau 0}$ is the semi-width in the special case of no shear, that is, the form of a when $\tau = 0$.

4.3.3 The Limit of Strong Shear ($\tau \to -\infty$)

In the limit of strong shear, $\tau \to -\infty$, $\alpha_\infty \to \pi/2^-$ according to (4.23) and the film becomes deep according to $H = -3\tau/(2\sin\alpha) \to \infty$ on the upper half of the cylinder, while the rivulet becomes wide and deep according to

$$a \sim -\frac{7\tau}{2\bar{\beta}} \to \infty \quad \text{and} \quad h_{\mathrm{m}} \sim -\frac{7\tau}{4} \to \infty \tag{4.33}$$

at $\alpha = \pi/2$, and deep with finite width according to

$$a \sim \frac{\pi}{m} + \frac{10\bar{\beta}\sin\alpha}{9m^2\tau} \to \frac{\pi}{m}^- \quad \text{and} \quad h_{\mathrm{m}} \sim -\frac{9\tau}{5\sin\alpha} \to \infty \tag{4.34}$$

on the lower half of the cylinder. Note that a changes from $O(\tau)$ to $O(1)$ in a narrow transition layer of width $O(\tau^{-2})$ near $\alpha = \pi/2^+$.

4.3.4 The Limit of Small Flux ($\bar{Q} \to 0^+$)

In the limit of small flux, $\bar{Q} \to 0^+$, the rivulet behaves according to

$$a \sim a_{\mathrm{Q0}} + \frac{18m^3\bar{Q}}{\bar{\beta}^2\left[2\bar{\beta}\sin\alpha f'(ma_{\mathrm{Q0}}) + 9m\tau g'(ma_{\mathrm{Q0}})\right]} \to a_{\mathrm{Q0}}^+ \tag{4.35}$$

and

$$h_{\mathrm{m}} \sim \frac{\bar{\beta}}{m}\tanh\left(\frac{ma_{\mathrm{Q0}}}{2}\right) = O(1) \tag{4.36}$$

on the upper half of the cylinder for $\alpha_\infty < \alpha < \pi/2$,

$$a \sim -\frac{7\tau}{2\beta} - \frac{30\bar{Q}}{49\tau^3} \to -\frac{7\tau}{2\bar{\beta}}^+ \quad \text{and} \quad h_{\mathrm{m}} \sim -\frac{7\tau}{4} - \frac{15\bar{\beta}\bar{Q}}{49\tau^3} \to -\frac{7\tau}{4}^+ \tag{4.37}$$

at $\alpha = \pi/2$, and according to (4.35) and (4.36) with "tanh" replaced by "tan" on the lower half of the cylinder, where a_{Q0} is the semi-width in the special case of zero flux, that is, the form of a when $\bar{Q} = 0$.

4.3.5 The Limit of Large Flux ($\bar{Q} \to \infty$)

In the limit of large flux, $\bar{Q} \to \infty$, the rivulet becomes wide with finite thickness according to

$$a \sim \frac{3m^3\bar{Q}}{\bar{\beta}^2\left[2\bar{\beta}\sin\alpha + 3m\tau\right]} \to \infty \quad \text{and} \quad h_{\rm m} \sim \frac{\bar{\beta}}{m}\tanh\left(\frac{3m^4\bar{Q}}{2\bar{\beta}^2\left[2\bar{\beta}\sin\alpha + 3m\tau\right]}\right) \to \frac{\bar{\beta}}{m}^{-} \tag{4.38}$$

on the upper half of the cylinder for $\alpha_\infty < \alpha < \pi/2$, wide and deep according to

$$a \sim \left(\frac{105\bar{Q}}{4\bar{\beta}^3}\right)^{\frac{1}{4}} - \frac{7\tau}{8\bar{\beta}} \to \infty \quad \text{and} \quad h_{\rm m} \sim \left(\frac{105\bar{Q}\bar{\beta}}{64}\right)^{\frac{1}{4}} - \frac{7\tau}{16} \to \infty \tag{4.39}$$

at $\alpha = \pi/2$, and deep with finite width according to

$$a \sim \frac{\pi}{m} - \left(\frac{5\pi\bar{\beta}^3\sin\alpha}{3m^7\bar{Q}}\right)^{\frac{1}{3}} \to \frac{\pi}{m}^{-} \quad \text{and} \quad h_{\rm m} \sim \left(\frac{24\bar{Q}m}{5\pi\sin\alpha}\right)^{\frac{1}{3}} \to \infty \tag{4.40}$$

on the lower half of the cylinder; note that a and $h_{\rm m}$ in (4.40) are independent of τ to the orders given. Note also that a changes from $O(\bar{Q})$ to $O(1)$ and $h_{\rm m}$ changes from $O(1)$ to $O(\bar{Q}^{1/3})$ in a narrow transition layer of width $O(\bar{Q}^{-1/2})$ near $\alpha = \pi/2$.

4.4 A Rivulet with Constant Semi-Width $a = \bar{a}$

In this Section we describe the steady, locally unidirectional flow of a slowly varying rivulet with constant semi-width $a = \bar{a}$ but slowly varying contact angle $\beta = \beta(\alpha)\,(\geq 0)$ on the right-hand side of a large horizontal cylinder subject to a non-positive uniform azimuthal surface shear stress $\tau\,(\leq 0)$ acting in opposition to gravity.

Unlike in the case of constant non-zero contact angle described in Section 4.3 in which the behaviour is qualitatively the same for all values of the contact angle, the behaviour is qualitatively different for a narrow rivulet with $a = \bar{a} < \pi$, in the marginal case $a = \bar{a} = \pi$, and for a wide rivulet with $a = \bar{a} > \pi$, and hence

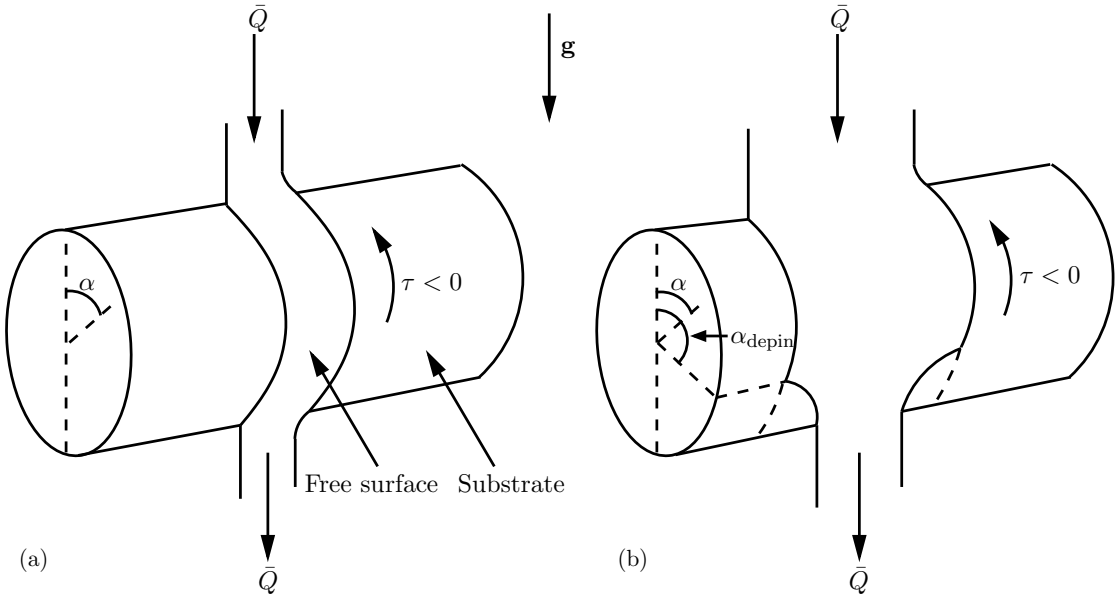

Figure 4.8: Sketch of the scenario considered in Section 4.4, namely a rivulet with prescribed flux $\bar{Q}$ and (when not de-pinned with zero contact angle $\beta = \bar{\beta} = 0$ but slowly varying semi-width $a = \pi/m$) constant semi-width $a = \bar{a}$ but slowly varying contact angle β that runs from $\alpha = 0$ to $\alpha = \pi$, in the cases (a) $a = \bar{a} < \pi$, in which the rivulet is never de-pinned, and (b) $a = \bar{a} > \pi$, in which the rivulet is de-pinned and has zero contact angle in the interval $\alpha_{\text{depin}} \leq \alpha \leq \pi$.

in Subsections 4.4.1–4.4.3 we describe the behaviour in each of these three cases separately. In Subsection 4.4.4 we present examples of free surface profiles of the rivulet, and in Subsections 4.4.5–4.4.8 we describe the behaviour in the limits of weak shear, $\tau \to 0^-$, strong shear, $\tau \to -\infty$, small flux, $\bar{Q} \to 0^+$, and large flux, $\bar{Q} \to \infty$, respectively.

4.4.1 A Narrow Rivulet with $a = \bar{a} < \pi$

For a narrow rivulet with $a = \bar{a} < \pi$ for all values of $\bar{Q}$ and $\tau\,(\leq 0)$ there is a slowly varying rivulet that runs all the way from the top of the cylinder $\alpha = 0$ to the bottom of the cylinder $\alpha = \pi$, and its contact angle β has a single minimum on the lower half of the cylinder and its maximum thickness h_{m} has a single minimum on the upper half of the cylinder. This scenario is sketched in Figure 4.8(a).

4.4.1.1 The Special Case of No Shear ($\tau = 0$)

In the special case of no shear, $\tau = 0$, the real positive solution of (4.8) for the contact angle β is given by (3.11) in Chapter 3 and the maximum thickness $h_{\rm m}$ is given by (4.7) with β given by (3.11). The rivulet becomes deep near the top and the bottom of the cylinder according to (3.14) in Chapter 3 as $\alpha \to 0^+$ and (3.15) in Chapter 3 as $\alpha \to \pi^-$; also β and $h_{\rm m}$ take the $O(1)$ values (3.16) in Chapter 3 at $\alpha = \pi/2$. In the limit of a very narrow rivulet, $\bar{a} \to 0^+$, the rivulet becomes narrow and deep everywhere according to (3.17) in Chapter 3.

4.4.1.2 The General Case of Strictly Negative Shear ($\tau < 0$)

In the general case of strictly negative shear, $\tau < 0$, the real positive solution of (4.8) for the contact angle β is

$$\beta = -\frac{3\tau m g(m\bar{a})}{2\sin\alpha f(m\bar{a})}\left\{1 + 2\cosh\left[\frac{1}{3}\cosh^{-1}\left(1 - \frac{4\bar{Q}m\sin^2\alpha f^2(m\bar{a})}{3\tau^3 g^3(m\bar{a})}\right)\right]\right\}, \quad (4.41)$$

and the maximum thickness $h_{\rm m}$ is given by (4.7) with β given by (4.41). The rivulet becomes deep near the top and the bottom of the cylinder according to

$$\beta \sim -\frac{9\tau g(\bar{a})}{2\alpha f(\bar{a})} \to \infty \quad \text{and} \quad h_{\rm m} \sim -\frac{9\tau g(\bar{a})}{2\alpha f(\bar{a})}\tanh\left(\frac{\bar{a}}{2}\right) \to \infty \quad (4.42)$$

as $\alpha \to 0^+$ and

$$\beta \sim -\frac{9\tau g(\bar{a})}{2(\pi-\alpha) f(\bar{a})} \to \infty \quad \text{and} \quad h_{\rm m} \sim -\frac{9\tau g(\bar{a})}{2(\pi-\alpha) f(\bar{a})}\tan\left(\frac{\bar{a}}{2}\right) \to \infty \quad (4.43)$$

as $\alpha \to \pi^-$; also β and $h_{\rm m}$ take the $O(1)$ values

$$\beta = -\frac{7\tau}{6\bar{a}}\left\{1 + 2\cosh\left[\frac{1}{3}\cosh^{-1}\left(1 - \frac{405\bar{Q}}{49\tau^3\bar{a}}\right)\right]\right\} \quad \text{and} \quad h_{\rm m} = \frac{\beta\bar{a}}{2} \quad (4.44)$$

at $\alpha = \pi/2$. In the limit of a very narrow rivulet, $\bar{a} \to 0^+$, the rivulet becomes narrow and deep everywhere according to (3.17) in Chapter 3 (showing that, rather unexpectedly, its behaviour is independent of τ).

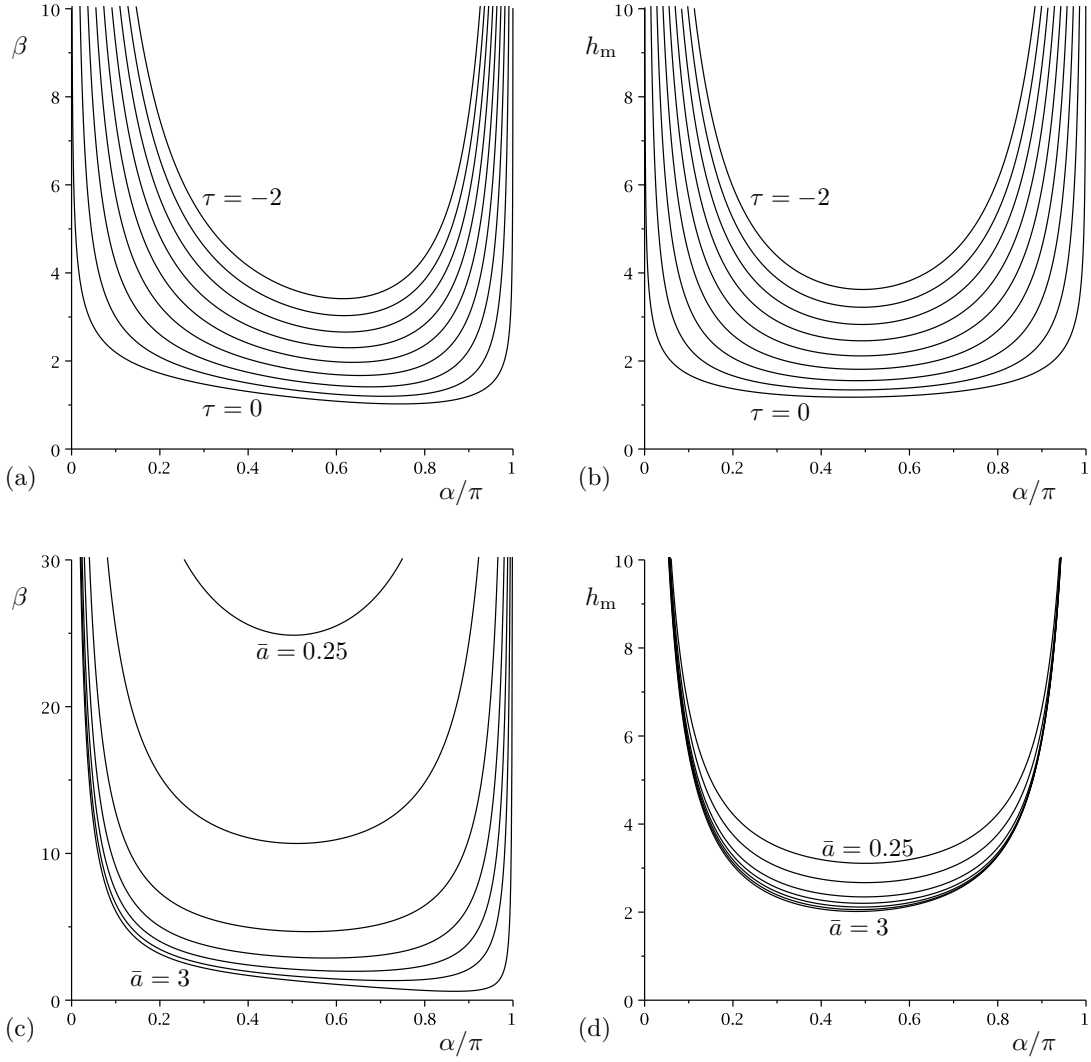

Figure 4.9: Plots of (a,c) the contact angle β and (b,d) the maximum thickness $h_{\rm m}$ as functions of the scaled angle α/π when $\bar{Q} = 1$ for (a,b) $\tau = -2, -1.75, \ldots, 0$ when $\bar{a} = 2\,(< \pi)$, and (c,d) $\bar{a} = 0.25, 0.5, 1, \ldots, 3$ when $\tau = -1$.

The behaviour of the present solution when $a = \bar{a} < \pi$ is illustrated in Figure 4.9, which shows plots of the contact angle β and the maximum thickness $h_{\rm m}$ as functions of α/π when $\bar{Q} = 1$ for (a,b) various values of $\tau\,(\leq 0)$ when $\bar{a} = 2\,(< \pi)$ and for (c,d) various values of $\bar{a}$ satisfying $\bar{a} < \pi$ when $\tau = -1$.

4.4.2 The Marginal Case $a = \bar{a} = \pi$

In the marginal case $a = \bar{a} = \pi$ the rivulet behaves qualitatively as in the case of a narrow rivulet with $a = \bar{a} < \pi$ except that, since in this case $\beta = 0$ at $\alpha = \pi$, instead of satisfying (3.15) in Chapter 3 in the special case of no shear, $\tau = 0$, or (4.43) in the general case of strictly negative shear, $\tau < 0$, the rivulet becomes deep with zero contact angle and finite semi-width π near the bottom of the cylinder according to (3.18) in Chapter 3 when $\tau = 0$ and

$$\beta \sim -\frac{9\pi\tau(\pi - \alpha)}{40} \to 0^+ \quad \text{and} \quad h_{\rm m} \sim -\frac{9\tau}{5(\pi - \alpha)} \to \infty \tag{4.45}$$

when $\tau < 0$, as $\alpha \to \pi^-$.

4.4.3 A Wide Rivulet with $a = \bar{a} > \pi$

Unlike for a narrow rivulet with $a = \bar{a} < \pi$, for a wide rivulet with $a = \bar{a} > \pi$ for all values of $\bar{Q}$ and $\tau\,(\leq 0)$ there is a slowly varying rivulet that runs from the top of the cylinder $\alpha = 0$ only as far as a station $\alpha = \alpha_{\rm depin}$ $(\pi/2 < \alpha_{\rm depin} < \pi)$ on the lower half of the cylinder, and its contact angle β, again given by (3.11) in Chapter 3 in the special case of no shear, $\tau = 0$, or (4.41) in the general case of strictly negative shear, $\tau < 0$, is a monotonically decreasing function of α, attaining its minimum physically realisable value of zero at the station $\alpha = \alpha_{\rm depin}$, where $\alpha_{\rm depin}$ is given by

$$\alpha_{\rm depin} = \cos^{-1}\left(-\frac{\pi^2}{\bar{a}^2}\right) \quad \text{for} \quad \bar{a} > \pi. \tag{4.46}$$

Note that, rather unexpectedly, $\alpha_{\rm depin}$ is independent of both τ and $\bar{Q}$, and hence coincides exactly with the corresponding angle found in Chapter 3 in the special case of no shear, $\tau = 0$. The rivulet again becomes deep near the top of the cylinder according to (3.14) in Chapter 3 when $\tau = 0$ or (4.42) when $\tau < 0$, and again β and $h_{\rm m}$ take the $O(1)$ values given by (3.16) in Chapter 3 when $\tau = 0$ or (4.44) when $\tau < 0$ at $\alpha = \pi/2$. At $\alpha = \alpha_{\rm depin}$ the rivulet has zero contact angle $\beta = 0$, semi-width $a = \bar{a} > \pi$, and maximum thickness $h_{\rm m} = h_{\rm mdepin}$, where $h_{\rm mdepin}\,(> 0)$ is the real positive solution of (4.17c) when $\alpha = \alpha_{\rm depin}$, namely

$$h_{\rm mdepin} = \left(\frac{24\bar{Q}\bar{a}}{5\sqrt{\bar{a}^4 - \pi^4}}\right)^{\frac{1}{3}} \tag{4.47}$$

when $\tau = 0$ and

$$h_{\rm mdepin} = -\frac{3\tau\bar{a}^2}{5\sqrt{\bar{a}^4 - \pi^4}}\left\{1 + 2\cosh\left[\frac{1}{3}\cosh^{-1}\left(1 - \frac{100\bar{Q}(\bar{a}^4 - \pi^4)}{9\tau^3\bar{a}^5}\right)\right]\right\} \tag{4.48}$$

when $\tau < 0$. Furthermore, as $\alpha \to \alpha_{\rm depin}^-$ we find that $\beta \to 0^+$ according to

$$\beta = \beta_{\rm depin}\,(\alpha_{\rm depin} - \alpha) + O(\alpha_{\rm depin} - \alpha)^2, \tag{4.49}$$

$a \equiv \bar{a}$, and $h_{\rm m} \to h_{\rm mdepin}^-$ according to

$$h_{\rm m} = h_{\rm mdepin} + \frac{5(\bar{a}^4 + \pi^4)h_{\rm mdepin}^2 + 9\tau\bar{a}^2\sqrt{\bar{a}^4 - \pi^4}h_{\rm mdepin}}{6\pi^2(5\sqrt{\bar{a}^4 - \pi^4}h_{\rm mdepin} + 6\tau\bar{a}^2)}\,(\alpha - \alpha_{\rm depin}) + O(\alpha - \alpha_{\rm depin})^2, \tag{4.50}$$

where the coefficient $\beta_{\rm depin}\,(> 0)$ in (4.49) is the real positive solution of the cubic polynomial equation that is obtained from (4.8) in the limit $\alpha \to \alpha_{\rm depin}^-$, and is given by

$$\beta_{\rm depin} = \frac{\sqrt{\bar{a}^4 - \pi^4}}{4\bar{a}}\,h_{\rm mdepin}, \tag{4.51}$$

together with (4.47) or (4.48), as appropriate.

Since there is no physically realisable rivulet solution in the interval $\alpha_{\rm depin} < \alpha \leq \pi$, an alternative description of the behaviour is required there. The scenario we will consider is the one proposed in Chapter 3, namely that for $0 \leq \alpha <$

α_{depin} the rivulet behaves according to the description of a narrow rivulet given in Subsection 4.4.1, but that the contact lines de-pin at $\alpha = \alpha_{\text{depin}}$, and the rivulet runs from $\alpha = \alpha_{\text{depin}}$ to the bottom of the cylinder $\alpha = \pi$ with zero contact angle according to the solution in the case $\beta = \bar{\beta} = 0$ given by (4.17), with monotonically decreasing semi-width $a = \pi/m$ ($\pi \leq a \leq \bar{a}$) and monotonically increasing maximum thickness $h_{\text{m}} \geq h_{\text{mdepin}}$. This scenario is sketched in Figure 4.8(b). In particular, as $\alpha \to \alpha^{+}_{\text{depin}}$ we find that $\beta \equiv 0$, $a \to \bar{a}^{-}$ according to (3.23) in Chapter 3, that is, it is independent of τ, and $h_{\text{m}} \to h^{+}_{\text{mdepin}}$ according to (4.50), so that the solutions in $\alpha < \alpha_{\text{depin}}$ and $\alpha > \alpha_{\text{depin}}$ join continuously (but not smoothly) at the station $\alpha = \alpha_{\text{depin}}$. Note that in Chapter 3 the more general scenario of de-pinning and re-pinning at a non-zero contact angle was considered, but for simplicity we restrict our attention to the simplest case of de-pinning at zero contact angle here.

4.4.3.1 The Special Case of No Shear ($\tau = 0$)

In the special case of no shear, $\tau = 0$, the real positive solution of (4.17c) for the maximum thickness h_{m} in the interval $\alpha_{\text{depin}} \leq \alpha \leq \pi$ is

$$h_{\text{m}} = \left(\frac{24\bar{Q}m}{5\pi \sin \alpha} \right)^{\frac{1}{3}}. \tag{4.52}$$

Near the bottom of the cylinder the rivulet becomes deep with finite semi-width π according to (3.24) in Chapter 3 as $\alpha \to \pi^{-}$. Also, in the limit of a very wide rivulet, $\bar{a} \to \infty$, for which $\alpha_{\text{depin}} \to \pi/2^{+}$, the rivulet becomes wide and flat according to (3.25) in Chapter 3 on the upper half of the cylinder, and behaves according to the solution in the case $\beta = \bar{\beta} = 0$ given by (4.17) and (4.52) on the lower half of the cylinder.

4.4.3.2 The General Case of Strictly Negative Shear ($\tau < 0$)

In the general case of strictly negative shear, $\tau < 0$, the real positive solution of (4.17c) for the maximum thickness $h_{\rm m}$ in the interval $\alpha_{\rm depin} \le \alpha \le \pi$ is

$$h_{\rm m} = -\frac{3\tau}{5\sin\alpha}\left\{1 + 2\cosh\left[\frac{1}{3}\cosh^{-1}\left(1 - \frac{100\bar{Q}m\sin^2\alpha}{9\pi\tau^3}\right)\right]\right\}. \tag{4.53}$$

Near the bottom of the cylinder the rivulet has finite semi-width a that approaches the value π again according to (3.24) in Chapter 3 and becomes deep according to

$$h_{\rm m} \sim -\frac{9\tau}{5(\pi - \alpha)} \to \infty \tag{4.54}$$

as $\alpha \to \pi^-$. At leading order in the limit of a very wide rivulet, $\bar{a} \to \infty$, for which $\alpha_{\rm depin} \to \pi/2^+$, on the upper half of the cylinder β and $h_{\rm m}$ take the $O(1)$ forms

$$\beta = -\frac{3m\tau}{2\sin\alpha} \quad \text{and} \quad h_{\rm m} = -\frac{3\tau}{2\sin\alpha} \tag{4.55}$$

and the rivulet behaves according to the solution in the case $\beta = \bar{\beta} = 0$ given by (4.17) and (4.53) on the lower half of the cylinder.

The behaviour of the present solution when $a = \bar{a} > \pi$ is illustrated in Figure 4.10, which shows plots of the contact angle β, the maximum thickness $h_{\rm m}$ and the semi-width a as functions of α/π when $\bar{Q} = 1$ for (a,b) various values of $\tau\,(\le 0)$ when $\bar{a} = 5\,(> \pi)$ and for (c,d) various values of $\bar{a}$ satisfying $\bar{a} \ge \pi$ when $\tau = -1$.

4.4.4 Free Surface Profiles

Figure 4.11 shows examples of cross-sectional free surface profiles of the rivulet when $\tau = -1$ and $\bar{Q} = 1$ in the cases (a) $\bar{a} = 2\,(< \pi)$ and (b) $\bar{a} = 5\,(> \pi)$.

4.4.5 The Limit of Weak Shear ($\tau \to 0^-$)

In the limit of weak shear, $\tau \to 0^-$, β and $h_{\rm m}$ take the forms

$$\beta = \beta_0 + \tau\beta_1 + O(\tau^2) \quad \text{and} \quad h_{\rm m} = h_{\rm m0} + \tau h_{\rm m1} + O(\tau^2). \tag{4.56}$$

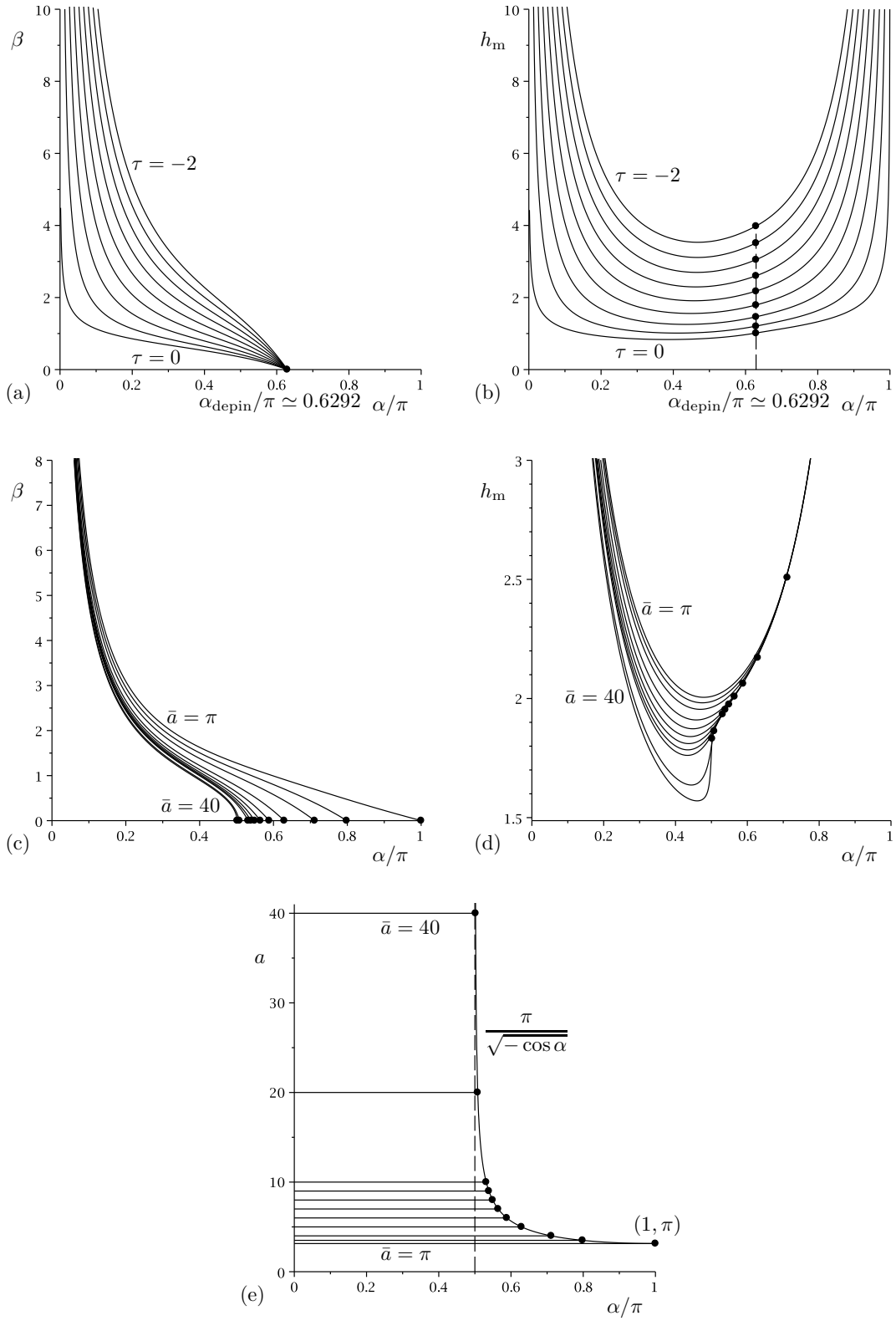

Figure 4.10: Plots of (a,c) the contact angle β, (b,d) the maximum thickness $h_{\rm m}$ and (e) the semi-width a, all as functions of α/π ($0 \le \alpha \le \pi$) for (a,b) $\tau = -2, -1.75, \ldots, 0$ when $\bar{a} = 5\,(> \pi)$ and $\bar{Q} = 1$ and (c,d,e) $\bar{a} = \pi$, 3.5, 4, 5, …, 10, 20, 40 when $\tau = -1$ and $\bar{Q} = 1$. The dots indicate the corresponding values of $\alpha_{\rm depin}/\pi$ given by (4.46) at which the contact lines de-pin.

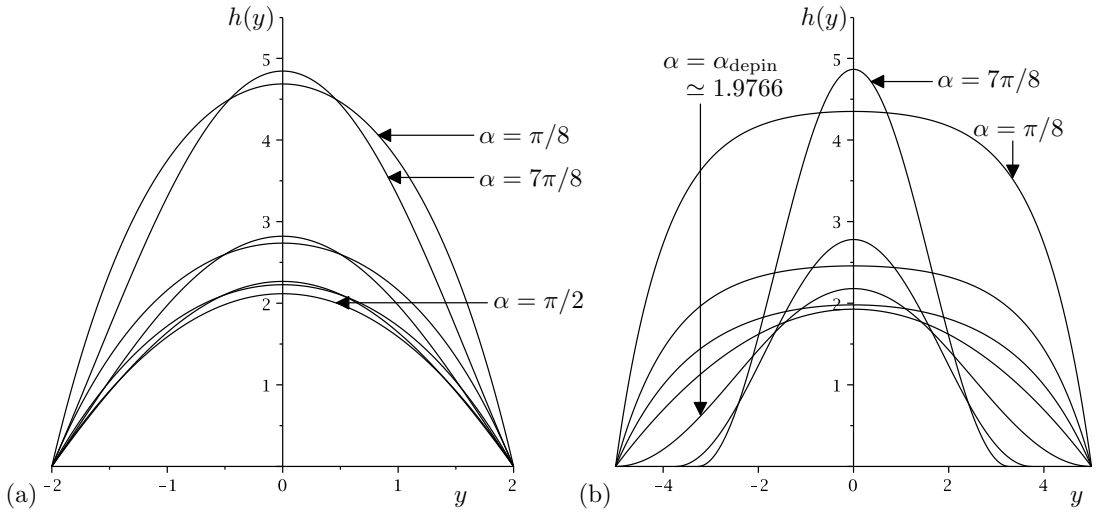

Figure 4.11: Cross-sectional free surface profiles $h(y)$ when $\tau = -1$ and $\bar{Q} = 1$ in the cases (a) $\bar{a} = 2\,(< \pi)$ at $\alpha = \pi/8,\ \pi/4,\ 3\pi/8,\ \pi/2,\ 5\pi/8,\ 3\pi/4,\ 7\pi/8$ and (b) $\bar{a} = 5\,(> \pi)$ at $\alpha = \pi/8,\ \pi/4,\ 3\pi/8,\ \pi/2,\ \alpha_{\rm depin} = \cos^{-1}(-\pi^2/25) \simeq 1.9766,\ 3\pi/4$ and $7\pi/8$. For clarity, the two parts of this figure use the same vertical but different horizontal ranges.

The leading order terms β_0 and $h_{\rm m0}$ are the forms of the contact angle and maximum thickness in the special case of no shear, $\tau = 0$, given by (3.11) in Chapter 3 and (4.7), respectively, for $0 \le \alpha < \alpha_{\rm depin}$, and by (4.52) on the lower half of the cylinder for $\alpha_{\rm depin} \le \alpha \le \pi$. The first order terms β_1 and $h_{\rm m1}$ are given by

$$\beta_1 = -\frac{3mg(m\bar{a})}{2f(m\bar{a})\sin\alpha} \quad \text{and} \quad h_{\rm m1} = -\frac{3g(m\bar{a})}{2f(m\bar{a})\sin\alpha}\tanh\left(\frac{m\bar{a}}{2}\right) \tag{4.57}$$

on the upper half of the cylinder,

$$\beta_1 = -\frac{7}{6\bar{a}} \quad \text{and} \quad h_{\rm m1} = -\frac{7}{12} \tag{4.58}$$

at $\alpha = \pi/2$, (4.57) with "tanh" replaced by "tan" in the expression for $h_{\rm m1}$ on the lower half of the cylinder for $\pi/2 < \alpha < \alpha_{\rm depin}$, and

$$h_{\rm m1} = -\frac{3}{5\sin\alpha} \tag{4.59}$$

on the lower half of the cylinder for $\alpha_{\rm depin} \le \alpha \le \pi$.

4.4.6 The Limit of Strong Shear ($\tau \to -\infty$)

In the limit of strong shear, $\tau \to -\infty$, the rivulet becomes deep according to

$$\beta \sim -\frac{9m\tau g(m\bar{a})}{2f(m\bar{a})\sin\alpha} \to \infty \quad \text{and} \quad h_{\rm m} \sim -\frac{9\tau g(m\bar{a})}{2f(m\bar{a})\sin\alpha}\tanh\left(\frac{m\bar{a}}{2}\right) \to \infty \quad (4.60)$$

on the upper half of the cylinder,

$$\beta \sim -\frac{7\tau}{2\bar{a}} \to \infty \quad \text{and} \quad h_{\rm m} \sim -\frac{7\tau}{4} \to \infty \quad (4.61)$$

at $\alpha = \pi/2$, (4.60) with "tanh" replaced by "tan" in the expression for $h_{\rm m}$ on the lower half of the cylinder for $\pi/2 < \alpha < \alpha_{\rm depin}$, and

$$h_{\rm m} \sim -\frac{9\tau}{5\sin\alpha} \to \infty \quad (4.62)$$

on the lower half of the cylinder for $\alpha_{\rm depin} \le \alpha \le \pi$. Note that β changes from $O(\tau)$ to zero in a narrow transition layer of width $O(\tau^{-1})$ near $\alpha = \alpha^{-}_{\rm depin}$.

4.4.7 The Limit of Small Flux ($\bar{Q} \to 0^{+}$)

In the limit of small flux, $\bar{Q} \to 0^{+}$, the contact angle β behaves according to

$$\beta \sim \beta_{\rm Q0} - \frac{2m^3\bar{Q}}{\beta_{\rm Q0}\tau g(m\bar{a})} \to \beta^{+}_{\rm Q0}, \quad (4.63)$$

and the maximum thickness $h_{\rm m}$ behaves according to (4.7) with β given by (4.63) for $0 \le \alpha < \alpha_{\rm depin}$, and

$$h_{\rm m} \sim -\frac{9\tau}{5\sin\alpha} + \frac{40m\bar{Q}\sin\alpha}{27\pi\tau^2} \to \left(-\frac{9\tau}{5\sin\alpha}\right)^{+} \quad (4.64)$$

on the lower half of the cylinder for $\alpha_{\rm depin} \le \alpha < \pi$, where $\beta_{\rm Q0}$ is the contact angle in the special case of zero flux, namely

$$\beta_{\rm Q0} = -\frac{9m\tau g(m\bar{a})}{2\sin\alpha f(m\bar{a})}. \quad (4.65)$$

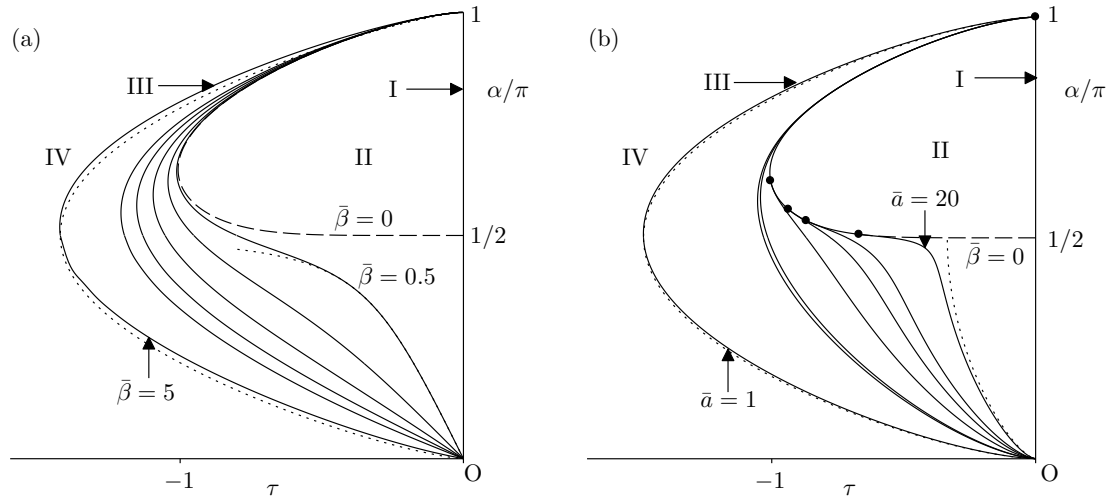

Figure 4.12: Plots showing how the α/π–τ parameter plane is divided by curves corresponding to type-I and type-III flows into regions in which the solutions have the cross-sectional flow patterns of types I–IV described in Subsection 4.1.4 when $\bar{Q} = 1$ for (a) $\beta = \bar{\beta} = 0.5, 1, 1.5, 2, 2.5, 5$ and (b) $a = \bar{a} = 1, 3, \pi, 5, 7, 9, 20$. The dashed curves correspond to the special case of zero contact angle, $\beta = \bar{\beta} = 0$, given by (4.66), and in (b) the locations at which the curves corresponding to wide rivulets with $a = \bar{a} \geq \pi$ join this curve are marked with dots. The dotted curves show the solution in the limits of (a) small contact angle, $\bar{\beta} \to 0^+$, given by (4.67) for $0 \leq \alpha < \pi/2$ and plotted on the $\bar{\beta} = 0.5$ curve and large contact angle, $\bar{\beta} \to \infty$, given by (4.68) and plotted on the $\bar{\beta} = 5$ curve, and (b) a narrow rivulet, $\bar{a} \to 0^+$, given by (4.69) and plotted on the $\bar{a} = 1$ curve and a wide rivulet, $\bar{a} \to \infty$, given by (4.70) for $0 \leq \alpha < \pi/2$ and plotted on the $\bar{a} = 20$ curve.

4.4.8 The Limit of Large Flux ($\bar{Q} \to \infty$)

In the limit of large flux, $\bar{Q} \to \infty$, the contact angle and maximum thickness become large (i.e. $\beta \to \infty$ and $h_{\rm m} \to \infty$, respectively) according to the solution in the special case of no shear, $\tau = 0$, given by (3.11) in Chapter 3 and (4.7) for $0 \leq \alpha < \alpha_{\rm depin}$, and by (4.52) for $\alpha_{\rm depin} \leq \alpha \leq \pi$. Note that β changes from $O(\bar{Q}^{1/3})$ to zero in a narrow transition layer of width $O(\bar{Q}^{-1/3})$ near $\alpha = \alpha^-_{\rm depin}$.

4.5 Flow Patterns Revisited

Figures 4.12(a) and 4.12(b) show how the α/π–τ parameter plane is divided by curves corresponding to type-I and type-III flows into regions in which the solu-

tions have the cross-sectional flow patterns of types I–IV described in Subsection 4.1.4 when $\bar{Q} = 1\,(> 0)$ for rivulets with various constant contact angles $\beta = \bar{\beta}$ and various constant semi-widths $a = \bar{a}$, respectively. In particular, Figure 4.12 includes the curves corresponding to type-III flow in the special case of zero contact angle, $\beta = \bar{\beta} = 0$, namely

$$\tau = -\left(\frac{6\bar{Q}m\sin^2\alpha}{\pi}\right)^{\frac{1}{3}}, \tag{4.66}$$

obtained using the fact that $h_{\rm m} = -2\tau/\sin\alpha$ for type-III flow (as mentioned in Subsection 4.1.4), together with (4.53). The maximum strength of (negative) shear such that type-III flow exists at some station $\alpha =$ constant on the cylinder is denoted by $\tau = \tau_{\rm IIIm}$. As Figure 4.12 shows, there are two stations ($\alpha = \alpha_{\rm III1}$ and $\alpha = \alpha_{\rm III2} > \pi/2$, where $\alpha_{\rm III1} < \alpha_{\rm III2}$) at which type-III flow exists when $|\tau| < |\tau_{\rm IIIm}|$, one ($\alpha = \alpha_{\rm III} > \pi/2$) when $\tau = \tau_{\rm IIIm}$, and none when $|\tau| > |\tau_{\rm IIIm}|$. In the latter case the flow is always upwards at $z = h_{\rm m}$ (i.e. type IV for all α). Of course, since $\bar{Q} > 0$, type-V flow is not possible here.

For type-III flow, in the limit of small contact angle, $\bar{\beta} \to 0^+$, we have

$$\tau \sim -\frac{\bar{\beta}\sin\alpha}{2m} \to 0^- \tag{4.67}$$

on the upper half of the cylinder and shown as a dotted curve in Figure 4.12(a) when $\bar{\beta} = 0.5$, and (4.66) on the lower half of the cylinder, shown as a dashed curve in Figure 4.12(a). In the limit of large contact angle, $\bar{\beta} \to \infty$, we have

$$\tau \sim -\frac{1}{4}\left(210\bar{Q}\bar{\beta}\sin^3\alpha\right)^{\frac{1}{4}} \to -\infty, \tag{4.68}$$

shown as a dotted curve in Figure 4.12(a) when $\bar{\beta} = 5$. In the limit of a narrow rivulet, $\bar{a} \to 0^+$, we have

$$\tau \sim -\frac{1}{4}\left(\frac{210\bar{Q}\sin^2\alpha}{\bar{a}}\right)^{\frac{1}{3}} \to -\infty, \tag{4.69}$$

shown as a dotted curve in Figure 4.12(b) when $\bar{a} = 1$. In the limit of a wide rivulet, $\bar{a} \to \infty$, we have

$$\tau \sim -\left(\frac{3\bar{Q}\sin^2\alpha}{4\bar{a}}\right)^{\frac{1}{3}} \to 0^-, \tag{4.70}$$

on the upper half of the cylinder and shown as a dotted curve in Figure 4.12(b) when $\bar{a} = 20$, and (4.66) on the lower half of the cylinder, shown as a dashed curve in Figure 4.12(b).

Figure 4.13 shows sketches of the possible flow patterns within the film and the rivulet with constant non-zero contact angle described in Section 4.3 in the vertical cross-section $y = 0$. In particular, Figures 4.13(a) and 4.13(b) show the case $|\tau| < |\tau_{\mathrm{IIIm}}|$, in which $\alpha_\infty < \alpha_{\mathrm{III1}} < \pi/2$ and $\alpha_{\mathrm{III1}} > \pi/2$, respectively, Figure 4.13(c) shows the case $\tau = \tau_{\mathrm{IIIm}}$, and Figure 4.13(d) shows the case $|\tau| > |\tau_{\mathrm{IIIm}}|$. Figure 4.13 also illustrates that the solutions for the film in $0 \leq \alpha \leq \alpha_\infty$ and for the rivulet in $\alpha_\infty < \alpha \leq \pi$ join continuously (but not smoothly) at the station $\alpha = \alpha_\infty$. The flow patterns within the rivulet with constant width described in Section 4.4 are rather similar to those shown in Figure 4.13 and hence are omitted for brevity.

4.6 Conclusions

In the present Chapter we investigated the flow of a slowly varying rivulet with positive prescribed flux $Q = \bar{Q} > 0$ on a slowly varying substrate, specifically the flow in the azimuthal direction round a large stationary horizontal cylinder, subject to a prescribed uniform azimuthal surface shear stress τ. In particular, we focused on the case of non-positive shear stress, $\tau \leq 0$, that is, opposing gravity, in which there is always a solution corresponding to a rivulet flowing down at least part of one side of the cylinder. We considered both a rivulet with constant non-zero contact angle $\beta = \bar{\beta} > 0$ but slowly varying semi-width $a = a(\alpha)$ and a

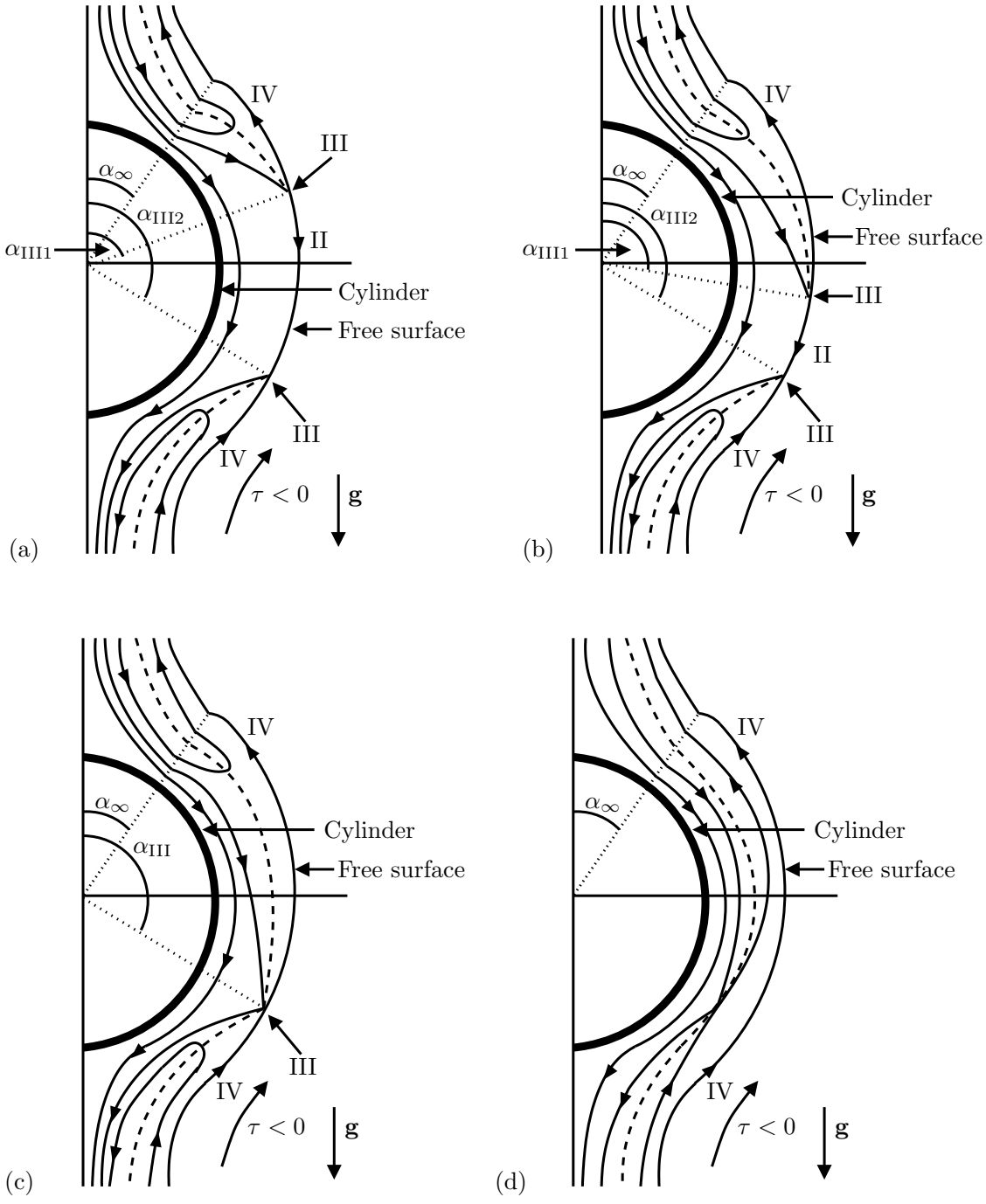

Figure 4.13: Sketches of the possible flow patterns within the film and the rivulet in the vertical cross-section $y = 0$ when (a) $|\tau| < |\tau_{\mathrm{IIIm}}|$ and $\alpha_{\mathrm{III1}} < \pi/2$, (b) $|\tau| < |\tau_{\mathrm{IIIm}}|$ and $\alpha_{\mathrm{III1}} > \pi/2$, (c) $\tau = \tau_{\mathrm{IIIm}}$, and (d) $|\tau| > |\tau_{\mathrm{IIIm}}|$. The dashed curves indicate where $u = 0$.

rivulet with constant semi-width $a = \bar{a}$ but slowly varying contact angle $\beta = \beta(\alpha)$, and showed that they have qualitatively different behaviour.

In Section 4.3 we showed that, unlike in the special case of no shear, $\tau = 0$, considered by Duffy and Moffatt [23], in the general case when shear is present, $\tau < 0$, a rivulet with constant non-zero contact angle $\beta = \bar{\beta} > 0$ can never run all the way from the top to the bottom of the cylinder, and so we considered the scenario sketched in Figure 4.5 in which an infinitely wide two-dimensional film of uniform thickness $H = -3\tau/(2\sin\alpha)\,(> 0)$ covers the cylinder from the top $\alpha = 0$ to the station $\alpha = \alpha_\infty$, where it breaks into a single rivulet with constant non-zero contact angle but slowly varying width that runs from the station $\alpha = \alpha_\infty$ to the bottom $\alpha = \pi$. In particular, we showed that α_∞ is a monotonically increasing function of $-\tau$ which approaches the value $\pi/2$ from below in the limit $-\tau \to \infty$, and hence that as the strength of the (negative) shear increases the film covers an increasingly larger part of the upper half of the cylinder.

In Section 4.4 we showed that, like in the special case of no shear, $\tau = 0$, considered in Chapter 3, while a narrow rivulet with constant semi-width $a = \bar{a} \leq \pi$ can run all the way from the top $\alpha = 0$ to the bottom $\alpha = \pi$ of the cylinder, a wide rivulet with constant semi-width $a = \bar{a} > \pi$ can run from $\alpha = 0$ only to the station $\alpha = \alpha_{\text{depin}}$, where its contact angle becomes zero, and so we considered the scenario sketched in Figure 4.8 in which the contact lines de-pin at $\alpha = \alpha_{\text{depin}}$ and the rivulet flows from $\alpha = \alpha_{\text{depin}}$ to $\alpha = \pi$ with zero contact angle but slowly varying width. In particular, we showed that α_{depin} is independent of τ, and hence that as the strength of the shear is varied the rivulet always de-pins at the same station on the lower half of the cylinder.

As Figure 4.3 shows, the rivulet solutions described in the present Chapter are not the only physically realisable solutions for flow on a stationary cylinder in the presence of a uniform azimuthal surface shear stress. In particular, as we described

in Section 4.2, full-ring solutions that extend all the way round the cylinder, which are impossible in the absence of shear, exist when the shear is sufficiently strong; these solutions will be analysed in Chapter 5.

Chapter 5

A shear-driven ring of fluid on a horizontal cylinder

In this Chapter we study the steady three-dimensional flow in the azimuthal direction of a ring of Newtonian fluid on a large horizontal cylinder subject to a prescribed uniform azimuthal surface shear stress due to an external airflow. Unlike in Chapter 4, where we studied rivulet flow on one side of the cylinder with prescribed volume flux, in the present Chapter we study a ring of fluid that flows round the entire circumference of the cylinder (referred to as a "full ring") in which the volume flux is unknown a priori. Also, in Chapter 4 it was found that the presence of shear simply modifies the rivulet solution that is obtained in the case of no shear studied in Chapter 3; however, in the present Chapter it is found that the presence of shear is required for a full-ring solution to exist. Lastly, in Chapter 4 both the case of a rivulet with constant contact angle but variable width (i.e. de-pinned contact lines) and of a rivulet with constant width but variable contact angle (i.e. pinned contact lines) were considered; however, in the present Chapter we focus on a ring with constant width only and find that, analogously to the case of a rivulet with constant width in Chapter 4, de-pinning of the contact lines of a

sufficiently wide ring is unavoidable for a full ring to exist. The case of constant non-zero contact angle is discussed briefly in Section 6.2.

5.1 Problem Formulation

5.1.1 Geometry of the Problem

Consider the steady three-dimensional flow of a thin, slowly varying ring of fluid (as previously discussed in Sections 1.6 and 4.2) of prescribed constant semi-width $a = \bar{a}$ on the outside of a large stationary horizontal cylinder of radius R subject to a prescribed uniform azimuthal surface shear stress τ. We again take the fluid to be Newtonian with constant viscosity μ, density ρ and coefficient of surface tension γ. The azimuthal angle α ($0 \leq \alpha < 2\pi$) is measured clockwise from the vertical, with $\alpha = 0$ corresponding to the top of the cylinder; values of α in the interval $0 < \alpha < \pi$ ($\pi < \alpha < 2\pi$) correspond to the right-hand (left-hand) side of the cylinder. We choose local Cartesian coordinates $Oxyz$ with the x axis down (up) the line of greatest slope for $0 < \alpha < \pi$ ($\pi < \alpha < 2\pi$), the y axis horizontal, and the z axis normal to the substrate $z = 0$, such that the shear stress $\tau\,(> 0)$ acts in the same (opposite) direction to gravity in $0 < \alpha < \pi$ ($\pi < \alpha < 2\pi$), as sketched in Figure 5.1. At each station $\alpha =$ constant the ring has free surface $z = h(y)$ and its cross-section is symmetric with respect to $y = 0$. The contact angle is denoted by $\beta = \mp h'(\pm\bar{a})\,(\geq 0)$, where a dash denotes differentiation with respect to the argument, and the maximum thickness of the ring, which always occurs at $y = 0$, is denoted by $h_{\rm m} = h(0)$. We consider the situation in which the ring is thin, which means that the transverse aspect ratio, denoted by δ, is small, specifically $\delta \ll 1$. There is some freedom regarding the definition of δ; however, for the moment we leave δ unspecified in order to keep the subsequent presentation as general as possible. In addition, we assume that the ring is slowly varying in α,

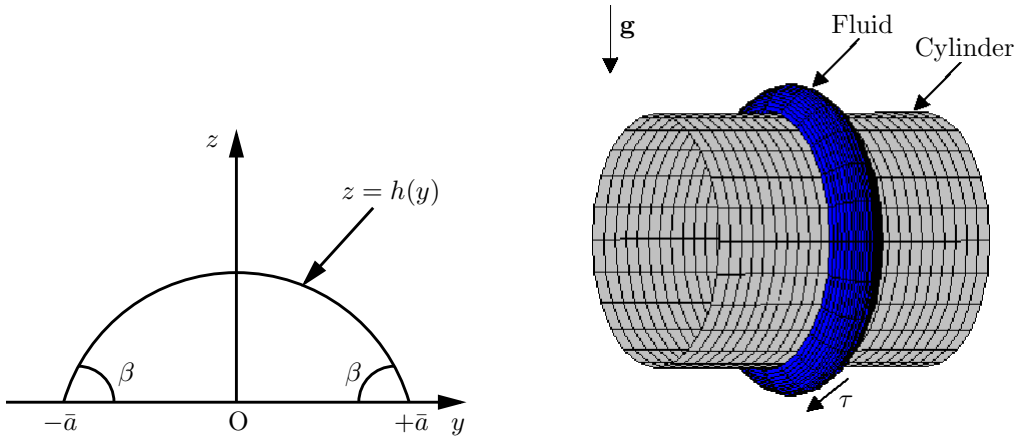

Figure 5.1: Sketch of a thin, slowly varying ring of constant semi-width $a = \bar{a}$ but slowly varying contact angle $\beta = \beta(\alpha)$ flowing on a horizontal cylinder subject to a prescribed uniform azimuthal surface shear stress τ.

which means that the azimuthal aspect ratio, defined by $\epsilon = \ell/R$, satisfies $\epsilon \ll \delta$, so that $\epsilon/\delta \to 0$ in the limit $\epsilon \to 0$, where $\ell = (\gamma/\rho g)^{1/2}$ is the capillary length. Under these assumptions the velocity of the fluid is locally unidirectional (i.e. in the x direction only) and is denoted by $\mathbf{u} = u(y,z)\mathbf{i}$, while the pressure is denoted by $p = p(y,z)$.

We therefore introduce the following non-dimensionalised and scaled variables:

$$\begin{gathered} x = Rx^*, \quad y = \epsilon R y^*, \quad a = \epsilon R a^*, \quad z = \epsilon\delta R z^*, \quad h = \epsilon\delta R h^*, \quad \beta = \delta\beta^*, \\ u = \frac{\epsilon^2\delta^2 R^2\rho g}{\mu}u^*, \quad p - p_\infty = \epsilon\delta R\rho g p^*, \quad \tau = \epsilon\delta^2 R\rho g\tau^*, \\ Q = \frac{\epsilon^4\delta^3 R^4\rho g}{\mu}Q^*, \quad M = \epsilon^2\delta R^3\rho M^*, \end{gathered} \tag{5.1}$$

where p_∞ is the ambient pressure, Q is the azimuthal volume flux of fluid crossing a station $\alpha =$ constant and $M\,(>0)$ is the constant mass of fluid on the cylinder. For clarity, we immediately drop the star superscripts on non-dimensional variables in what follows. Note that, although we consider flow on the outside of the cylinder only, the solution of the related problem of flow on the inside of the cylinder is obtained by simply letting the solution on the upper half of the cylinder in the present problem correspond to the lower half of the cylinder, and vice-versa.

At leading order in ϵ and δ the governing Navier–Stokes equations for the flow on the cylinder are readily solved to yield the pressure and the velocity, again given by (4.2) and (4.3) in Chapter 4, respectively, and the shape of the free surface satisfies the third order ordinary differential equation (4.5) in Chapter 4 subject to the contact-line conditions $h = 0$ and $h' = \mp\beta$ at $y = \pm\bar{a}$, where β is calculated as part of the solution.

In this Chapter we shall be concerned only with so-called "full-ring" solutions, that is, solutions for which $\beta \geq 0$ and $h > 0$ are continuous and finite for all $0 \leq \alpha < 2\pi$ and $-\bar{a} < y < \bar{a}$, analogous to those studied by Leslie, Wilson and Duffy [48] in the case of a full ring with constant, non-zero contact angle but variable width on a rotating horizontal cylinder in the absence of shear stress. These full-ring solutions have constant, non-zero Q which, unlike the rivulet solutions described in Chapter 4, is unknown a priori and instead calculated as part of the solution, and we note that these solutions have neither top-to-bottom, nor left-to-right, symmetry.

5.1.2 The General Case of Non-Zero Contact Angle $\beta > 0$

In the general case of non-zero contact angle $\beta > 0$ the free surface shape $h(y)$ and the maximum thickness h_{m} are again given by (4.6) and (4.7) in Chapter 4, respectively, with $a = \bar{a}$, that is, locally the cross-sectional ring profile is the same as that of a thin rivulet with non-zero contact angle flowing on a planar substrate inclined at an angle α to the horizontal. The volume flux Q is given by

$$Q = \frac{\beta^3 \sin\alpha}{9m^4} f(m\bar{a}) + \frac{\beta^2 \tau}{2m^3} g(m\bar{a}) \tag{5.2}$$

(i.e. equation (4.8) in Chapter 4 with $a = \bar{a}$), where we have written $m = |\cos\alpha|^{1/2}$, and the functions $f = f(m\bar{a})$ and $g = g(m\bar{a})$ are again defined by (4.9) and (4.10) in Chapter 4, respectively, with $a = \bar{a}$. For a given semi-width $\bar{a}$ and shear stress

τ, equation (5.2) is a cubic polynomial equation for β as a function of α in terms of the unknown Q. By considering equation (5.2) at the top $\alpha = 0$ or the bottom $\alpha = \pi$ of the cylinder (i.e. when $\sin\alpha = 0$) we see that if $\tau > 0$ then it immediately follows that $Q > 0$, so that the flux is downwards on the right-hand side of the cylinder and upwards on the left-hand side of the cylinder. On the left-hand side of the cylinder (i.e. when $\sin\alpha < 0$) there are two real positive roots β of (5.2), but only one of these (the one that we shall use) corresponds to the full ring flowing continuously all the way around the cylinder.

5.1.3 The Special Case of Zero Contact Angle $\beta = 0$

In the special case of zero contact angle $\beta = 0$ there is no solution corresponding to a full ring of fluid; however, for future reference we note that there is a solution corresponding to a "half ring" of fluid with slowly varying width (i.e. de-pinned contact lines) on the lower half of the cylinder, namely

$$a = \frac{\pi}{m}, \quad h = \frac{h_{\rm m}}{2}\left(1 + \cos my\right), \quad Q = \frac{\pi}{24m}\left(5\sin\alpha h_{\rm m} + 9\tau\right)h_{\rm m}^2 \tag{5.3}$$

for $\pi/2 < \alpha < 3\pi/2$, but no solution on the upper half of the cylinder for $0 \leq \alpha \leq \pi/2$ and $3\pi/2 \leq \alpha < 2\pi$. Equation (5.3) is identical to (4.17) in Chapter 4, that is, locally the cross-sectional half-ring profile is the same as that of a thin rivulet with zero contact angle flowing on the underside of a planar substrate inclined at an angle α to the horizontal. For a given shear stress τ, equation (5.3c) is a cubic polynomial equation for $h_{\rm m}$ as a function of α in terms of the unknown Q.

5.1.4 Pinned, De-Pinned and Re-Pinned Contact Lines

In the present problem of a full ring with constant semi-width $a = \bar{a}$ but slowly varying contact angle $\beta = \beta(\alpha)$ we find that the behaviour of a "narrow" ring with $\bar{a} < \pi$ is qualitatively different from that of a "wide" ring with $\bar{a} > \pi$. In

particular, we find that a narrow ring can flow around the entire circumference of the cylinder with pinned contact lines whereas for a wide ring de-pinning of the contact lines is unavoidable for a full ring of fluid to exist. Note that this is analogous to the result in Chapters 3 and 4 for rivulet flow on one side of a large horizontal cylinder. Specifically, a wide ring can flow from the top $\alpha = 0$ of the cylinder only as far as a station $\alpha = \alpha_{\text{depin}}$ on the lower right-hand part of the cylinder, where the azimuthal angle α_{depin} is again given by (4.46) in Chapter 4, and from a station $\alpha = \alpha_{\text{repin}}$ on the lower left-hand part of the cylinder back to the top $\alpha = 2\pi$, with pinned contact lines, where $\alpha_{\text{repin}} = 2\pi - \alpha_{\text{depin}}\,(> \alpha_{\text{depin}})$, and $\alpha_{\text{depin}}\,(\pi/2 < \alpha_{\text{depin}} < \pi)$, $\alpha_{\text{repin}}\,(\pi < \alpha_{\text{repin}} < 3\pi/2)$ correspond to the values of α at which the contact angle β attains its minimum physically realisable value of zero. Since equation (5.2) does not provide a physically realisable solution for part of the lower half of the cylinder $\alpha_{\text{depin}} < \alpha < \alpha_{\text{repin}}$ (specifically, the solution with β given by (5.2) predicts that $h < 0$ somewhere in the interval $-\bar{a} < y < \bar{a}$), an alternative description of the behaviour is required there. We will consider a scenario analogous to the one proposed in Chapters 3 and 4, namely that the contact lines de-pin at $\alpha = \alpha_{\text{depin}}$ and that the ring flows with zero contact angle $\beta = \bar{\beta} = 0$ but slowly varying semi-width $a = \pi/m$ according to (5.3) until $\alpha = \alpha_{\text{repin}}$, at which point the contact lines re-pin. The scenarios described above for a narrow and a wide ring are sketched in Figure 5.2. Note that in Chapter 3 we considered the more general scenario of de-pinning and re-pinning at a prescribed non-zero contact angle; however, as in Chapter 4, for simplicity we restrict our attention to the simplest case of de-pinning at zero contact angle here.

5.1.5 Existence of Full Rings

Equation (5.2) is a cubic polynomial equation for the contact angle $\beta = \beta(\alpha)\,(> 0)$ in terms of the unknown volume flux Q when the contact lines are pinned (i.e. for

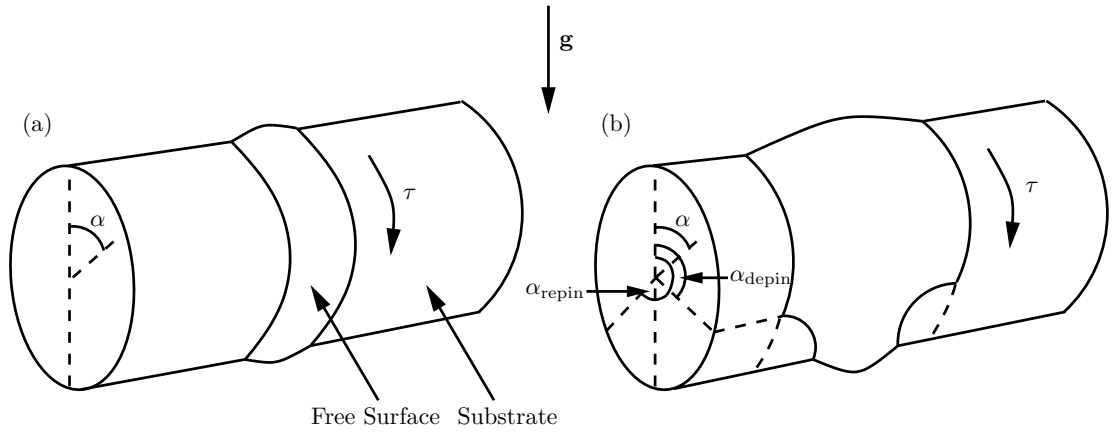

Figure 5.2: Sketches of a slowly varying full ring with constant mass M with (when not de-pinned with zero contact angle $\beta = \bar{\beta} = 0$ but slowly varying semi-width $a = \pi/m$) constant semi-width $a = \bar{a}$ but slowly varying contact angle β that flows round the entire circumference of a large horizontal cylinder $0 \leq \alpha < 2\pi$, in the cases (a) $\bar{a} < \pi$, in which the ring is always pinned, and (b) $\bar{a} > \pi$, in which the ring is de-pinned with $\beta = \bar{\beta} = 0$ on part of the lower half of the cylinder in the interval $\alpha_{\rm depin} \leq \alpha \leq \alpha_{\rm repin}$.

all α when $\bar{a} < \pi$, or for $0 \leq \alpha < \alpha_{\rm depin}$ and $\alpha_{\rm repin} < \alpha < 2\pi$ when $\bar{a} > \pi$), and (5.3c) is a cubic polynomial equation for the maximum thickness $h_{\rm m} = h_{\rm m}(\alpha)\,(> 0)$ in terms of the unknown volume flux Q when the contact lines are de-pinned (i.e. for $\alpha_{\rm depin} \leq \alpha \leq \alpha_{\rm repin}$ when $\bar{a} > \pi$). At the top of the cylinder the flux takes the form $Q = \beta^2 \tau g(\bar{a})/2$ for all $\bar{a}$ while at the bottom of the cylinder it takes the form $Q = \beta^2 \tau g(\bar{a})/2$ for $\bar{a} < \pi$ and $Q = 3\pi\tau h_{\rm m}^2/8$ for $\bar{a} > \pi$. At $\alpha = \pi/2$ and $\alpha = 3\pi/2$ the flux takes the form $Q = 4\beta^3\bar{a}^4/105 + 2\beta^2\tau\bar{a}^3/15$ and $Q = -4\beta^3\bar{a}^4/105 + 2\beta^2\tau\bar{a}^3/15$, respectively, for all $\bar{a}$. By considering the roots of these cubic polynomial equations for β at $\alpha = \pi/2$ and $\alpha = 3\pi/2$ we find that the flux must satisfy $0 < Q \leq 98\tau^3\bar{a}/405$ for full-ring solutions to exist. Note that, in particular, full-ring solutions exist only when shear is present (i.e. $\tau > 0$); this is to be expected, since a non-zero shear is clearly required in order to drive the flow of the fluid against gravity on the left-hand side of the cylinder.

Figure 5.3 shows a representative selection of solutions for various values of $Q =$ constant, plotted as functions of the scaled angle α/π $(0 \leq \alpha < 2\pi)$ when $\tau = 1$.

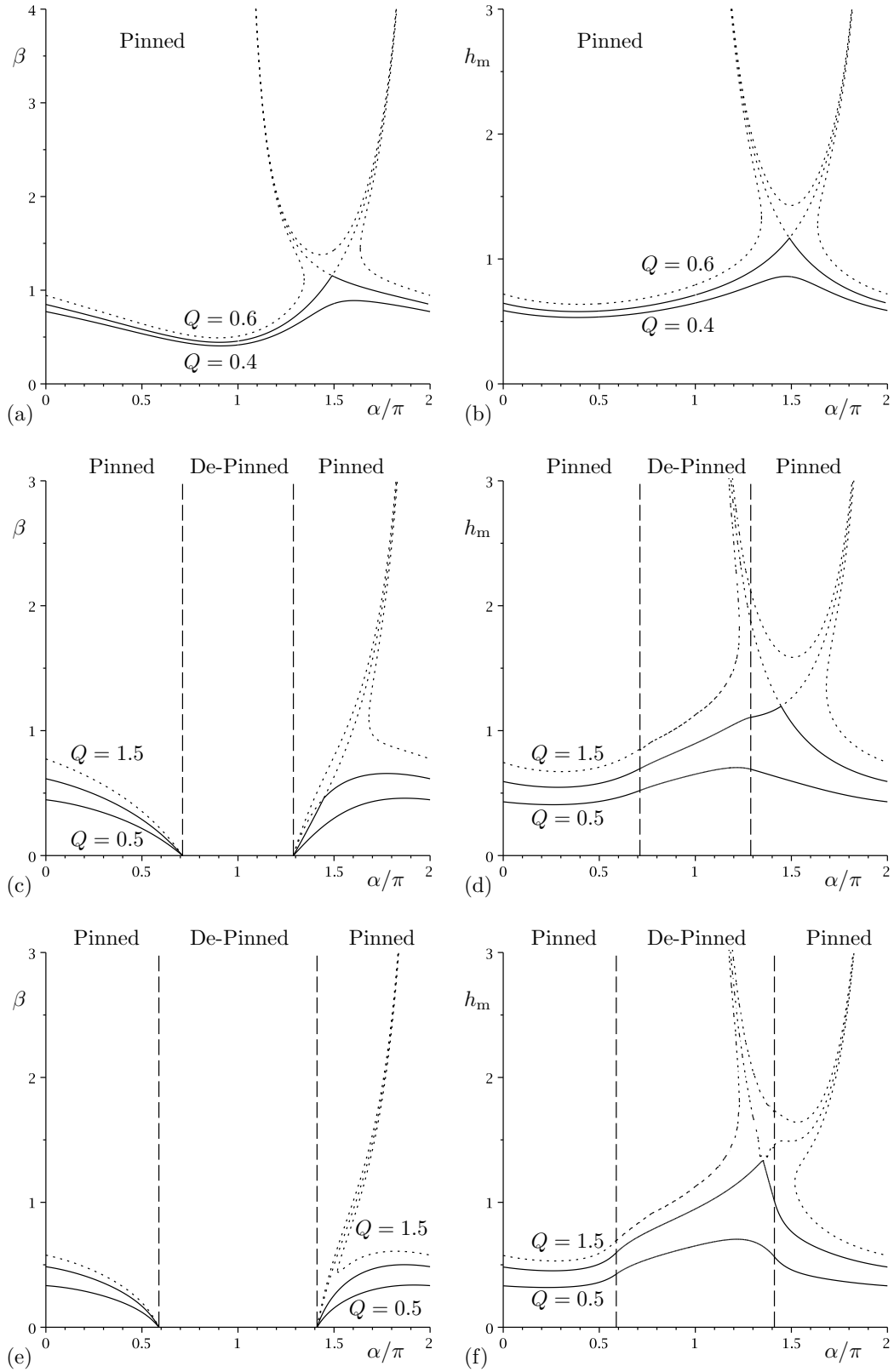

Figure 5.3: Contours of the expression for the flux Q given by (5.2) for pinned contact lines (i.e. for all α when $\bar{a} < \pi$, or for both $0 \le \alpha < \alpha_{\rm depin}$ and $\alpha_{\rm repin} < \alpha < 2\pi$ when $\bar{a} > \pi$) and by (5.3c) for de-pinned contact lines (i.e. when $\bar{a} > \pi$ for $\alpha_{\rm depin} \le \alpha \le \alpha_{\rm repin}$) in the (a,c,e) α/π–β and (b,d,f) α/π–$h_{\rm m}$ planes when $\tau = 1$, plotted for (a) $\bar{a} = 2\,(< \pi)$ and $Q = 0.4,\ Q_{\rm c} \simeq 0.4835,\ 0.6$, (b) $\bar{a} = 4\,(\pi < \bar{a} < 5^{1/4}\pi \simeq 4.6978)$ and $Q = 0.5,\ Q_{\rm c} \simeq 0.9477,\ 1.5$ and (c) $\bar{a} = 6\,(> 5^{1/4}\pi)$ and $Q = 0.5,\ Q_{\rm c} \simeq 1.0570,\ 1.5$. The branches corresponding to full-ring solutions are shown with solid curves, while the other branches are shown with dotted curves. The vertical dashed lines indicate the values $\alpha_{\rm depin}/\pi$ and $\alpha_{\rm repin}/\pi$.

Expressed in another way, Figure 5.3 shows contours of the expression for the flux Q given by (5.2) for pinned contact lines and by (5.3c) for de-pinned contact lines in the α/π–β and α/π–$h_{\rm m}$ planes when $\tau = 1$, plotted for (a) $\bar{a} = 2\,(< \pi)$, (b) $\bar{a} = 4\,(\pi < \bar{a} < 5^{1/4}\pi \simeq 4.6978)$ and (c) $\bar{a} = 6\,(> 5^{1/4}\pi)$. Contours for other values of τ are qualitatively similar, and the significance of the value $\bar{a} = 5^{1/4}\pi$ is discussed in Section 5.2. In particular, only some of these solutions satisfy the criteria to be full-ring solutions, and Figure 5.3 demonstrates a key feature of the present problem, namely the existence of a critical solution with critical flux, denoted by $Q = Q_{\rm c}$, such that a full-ring solution exists when $Q \leq Q_{\rm c}$ but not when $Q > Q_{\rm c}$. Here and henceforth variables in the critical case (e.g. the critical flux) are denoted with a subscript c (e.g. $Q_{\rm c}$), and this critical solution is discussed in detail in Subsection 5.2. Specifically, Figure 5.3 shows that in the case $Q < Q_{\rm c}$ the only branch for which $h_{\rm m} > 0$ everywhere (shown in a solid line) is a full-ring solution, while the other branches (not shown in Figure 5.3) give $h_{\rm m} < 0$ on at least part of the cylinder, and so are not physically realisable. In the case $Q = Q_{\rm c}$ the lower parts of two branches (shown in solid lines) meet to form a corner at $\alpha = \hat{\alpha}_{\rm c}$ and $h_{\rm m} = \hat{h}_{\rm mc}$, where the solution is continuous but not smooth at the corner, while the upper parts of these two branches (shown in dotted lines) are discontinuous and so cannot be full-ring solutions. Here and henceforth variables relating to the corner in the critical case (e.g. the location of the corner) are denoted with both a subscript c and a hat (e.g. $\hat{\alpha}_{\rm c}$). In the case $Q > Q_{\rm c}$ the branches are discontinuous (shown in dotted lines) and so cannot be full-ring solutions. Figures 5.3(c)–(f) also show that the location of the corner can occur either in the interval in which the ring has pinned contact lines (shown in parts (c) and (d)) or in the interval in which the ring has de-pinned contact lines (shown in parts (e) and (f)).

5.1.6 Mass of Fluid

The total mass in the full ring of fluid on the cylinder is finite and is given by

$$\begin{aligned} M &= \int_0^{2\pi} \int_{-\bar{a}}^{\bar{a}} h \, \mathrm{d}y \, \mathrm{d}\alpha \\ &= \int_0^{\frac{\pi}{2}} \frac{2\beta \left(m\bar{a} \coth m\bar{a} - 1 \right)}{m^2} \, \mathrm{d}\alpha + \int_{\frac{\pi}{2}}^{\frac{3\pi}{2}} \frac{2\beta \left(1 - m\bar{a} \cot m\bar{a} \right)}{m^2} \, \mathrm{d}\alpha \\ &+ \int_{\frac{3\pi}{2}}^{2\pi} \frac{2\beta \left(m\bar{a} \coth m\bar{a} - 1 \right)}{m^2} \, \mathrm{d}\alpha. \end{aligned} \tag{5.4}$$

For a prescribed shear stress τ, either the contact angle β is determined in terms of Q by (5.2) for pinned contact lines or the maximum thickness h_{m} is determined in terms of Q by (5.3c) for de-pinned contact lines. The constant value of the flux Q is determined either via a criticality condition in the case of critical flux $Q = Q_{\mathrm{c}}$, where the associated critical mass $M = M_{\mathrm{c}}$ is calculated as part of the solution, as discussed in Section 5.2, or from a condition of prescribed mass from (5.4) in the sub-critical case in which the mass is below its maximum value, $M < M_{\mathrm{c}}$, as discussed in Section 5.3. Note that, by inspection of (4.2), (4.3), (4.6) and (4.7) in Chapter 4, together with (5.2) and (5.3c), we could scale τ out of the problem by defining new dimensionless variables via $z = \tau z^*$, $h = \tau h^*$, $h_{\mathrm{m}} = \tau h_{\mathrm{m}}^*$, $\beta = \tau \beta^*$, $p = \tau p^*$, $u = \tau u^*$, $Q = \tau^3 Q^*$ and $M = \tau M^*$; however, for clarity we retain τ in what follows, and set $\tau = 1$ only in the numerical calculations.

5.2 The Critical Full-Ring Solution

In this Section we describe the behaviour of the critical ring solution with critical flux $Q = Q_{\mathrm{c}}$. In the critical case either the shear stress τ or the mass M may be prescribed with the other being determined by a criticality condition; however, since, as mentioned in Subsection 5.1.6, τ could be scaled out of the problem, in the rest of this Section we assume that τ is prescribed and we determine the

critical mass, $M = M_c$, above which no full-ring solution exists.

As may be seen in Figure 5.3, a key feature of the critical solution is that the expression for the flux Q, given by either (5.2) or (5.3c), has a saddle point at $\alpha = \hat{\alpha}_c$ and $h_m = \hat{h}_{mc}$ which gives rise to a corner in the critical ring profile h_c at $\alpha = \hat{\alpha}_c$. In Subsections 5.2.1 and 5.2.2 we consider separately the cases when the corner occurs in the interval with pinned contact lines and in the interval with de-pinned contact lines, respectively; in Subsection 5.2.3 we determine where the corner occurs for a given ring width, and in Subsection 5.2.4 we consider some properties of the critical solution. For brevity, in the remainder of this Chapter we refer to the interval in which the contact lines are pinned (de-pinned) simply as the "pinned (de-pinned) interval".

5.2.1 Corner in the Pinned Interval

When the corner occurs in the pinned interval, the conditions $\partial Q/\partial\alpha = 0$ and $\partial Q/\partial\beta = 0$, with Q given by (5.2), lead to the criticality conditions

$$4 - 5\sin^2\hat{\alpha}_c - \frac{2\hat{m}_c\bar{a}\sin^2\hat{\alpha}_c f'(\hat{m}_c\bar{a})}{f(\hat{m}_c\bar{a})} + \frac{3\hat{m}_c\bar{a}\sin^2\hat{\alpha}_c g'(\hat{m}_c\bar{a})}{g(\hat{m}_c\bar{a})} = 0 \qquad (5.5)$$

and

$$\hat{\beta}_c = -\frac{3\hat{m}_c\tau g(\hat{m}_c\bar{a})}{\sin\hat{\alpha}_c f(\hat{m}_c\bar{a})}, \qquad (5.6)$$

where we have written $\hat{m}_c = |\cos\hat{\alpha}_c|^{1/2}$. Equation (5.6) shows that $\sin\hat{\alpha}_c < 0$, indicating that the corner is on the left-hand side of the cylinder. Equation (5.5) may be solved for the location of the corner, $\hat{\alpha}_c$, and then the contact angle at the corner, $\hat{\beta}_c$, is given explicitly by (5.6), and the maximum thickness at the corner, $\hat{h}_{mc}$, and critical flux, Q_c, are given explicitly by (4.7) and (5.2), respectively, with $\alpha = \hat{\alpha}_c$ and $\beta = \hat{\beta}_c$.

5.2.2 Corner in the De-Pinned Interval

When the corner occurs in the de-pinned interval, the conditions $\partial Q/\partial\alpha = 0$ and $\partial Q/\partial h_{\rm m} = 0$ obtained from (5.3c) are solved together with (5.3c) itself to yield the solution

$$\frac{\hat{\alpha}_{\rm c}}{\pi} = 1 + \frac{1}{\pi}\cos^{-1}\frac{1}{\sqrt{5}} \simeq 1.3524, \quad \hat{h}_{\rm mc} = \frac{3\tau}{\sqrt{5}} \simeq 1.3416\tau, \quad Q_{\rm c} = \frac{9\pi\tau^3}{5^{3/4}8} \simeq 1.0570\tau^3. \tag{5.7}$$

Equation (5.7) shows that, as in Subsection 5.2.1, the corner is on the left-hand side of the cylinder; note, however, that in this case, $\hat{\alpha}_{\rm c}$, $\hat{h}_{\rm mc}$ and $Q_{\rm c}$ are independent of $\bar{a}$, and $\hat{\alpha}_{\rm c}$ is independent of τ.

5.2.3 Location of the Corner $\hat{\alpha}_{\rm c}$

The value of the constant semi-width $\bar{a}$ for which the corner occurs at the point where the contact lines re-pin (that is, the location at which the pinned and de-pinned intervals meet) is found by solving $\alpha_{\rm repin} = \hat{\alpha}_{\rm c}$ to give

$$\bar{a} = 5^{1/4}\pi \simeq 4.6978\,(> \pi). \tag{5.8}$$

When $\bar{a} < 5^{1/4}\pi$ the corner is in the pinned interval $\alpha_{\rm repin} < \alpha < 2\pi$ and when $\bar{a} \geq 5^{1/4}\pi$ the corner is in the de-pinned interval $\pi < \alpha \leq \alpha_{\rm repin}$.

5.2.4 The Critical Ring for Various Ring Widths

When $\bar{a} < 5^{1/4}\pi$, and with the critical flux $Q_{\rm c}$ obtained from (5.2) with $\alpha = \hat{\alpha}_{\rm c}$ and $\beta = \hat{\beta}_{\rm c}$ from (5.5) and (5.6), the critical contact angle $\beta_{\rm c}$, critical ring profile $h_{\rm c}$, critical maximum thickness $h_{\rm mc}$, critical pressure $p_{\rm c}$, critical velocity $u_{\rm c}$ and critical mass $M_{\rm c}$ may be obtained from (5.2), (4.6), (4.7), (4.2), (4.3) and (5.4), respectively.

When $\bar{a} \geq 5^{1/4}\pi$, and with the critical flux $Q_{\rm c}$ given by (5.7c), the critical maximum thickness $h_{\rm mc}$, critical ring profile $h_{\rm c}$, critical pressure $p_{\rm c}$, critical velocity

u_c and critical mass M_c may be obtained from (5.3c), (5.3b), (4.2), (4.3) and (5.4), respectively.

Figure 5.4 shows the scaled position of the corner in the critical solution, $\hat{\alpha}_c/\pi$, the contact angle at the corner in the critical solution, $\hat{\beta}_c$, the maximum thickness at the corner in the critical solution, $\hat{h}_{mc}$, the critical flux Q_c and the critical mass M_c, all plotted as functions of $\bar{a}$ when $\tau = 1$. In particular, Figure 5.4(a) shows that $\hat{\alpha}_c/\pi$ decreases monotonically from $3/2$ when $\bar{a} = 0$ (for which, of course, there is no solution) to $1+\cos^{-1}(1/\sqrt{5})/\pi \simeq 1.3524$ when $\bar{a} \geq 5^{1/4}\pi$, Figure 5.4(b) shows that $\hat{\beta}_c$ decreases monotonically from infinity when $\bar{a} = 0$ to zero when $\bar{a} \geq 5^{1/4}\pi$, Figure 5.4(c) shows that $\hat{h}_{mc}$ increases monotonically from $7/6 \simeq 1.1667$ when $\bar{a} = 0$ to $3/\sqrt{5} \simeq 1.3416$ when $\bar{a} \geq 5^{1/4}\pi$, Figure 5.4(d) shows that Q_c increases monotonically from zero when $\bar{a} = 0$ to $9\pi/5^{3/4}8 \simeq 1.0570$ when $\bar{a} \geq 5^{1/4}\pi$, and Figure 5.4(e) shows that M_c increases monotonically from zero when $\bar{a} = 0$ to 26.1538 when $\bar{a} = 5^{1/4}\pi$, and then continues to increase monotonically when $\bar{a} > 5^{1/4}\pi$. Figure 5.4 also shows that in the limit of a very narrow ring, $\bar{a} \to 0^+$, the solution at the corner behaves according to

$$\frac{\hat{\alpha}_c}{\pi} \sim \frac{3}{2} - \frac{\bar{a}^2}{126\pi} \to \frac{3^-}{2}, \quad \hat{\beta}_c \sim \frac{7\tau}{3\bar{a}} \to \infty, \quad \hat{h}_{mc} \to \frac{7\tau^+}{6} \simeq 1.1667\tau^+ = O(1), \tag{5.9}$$

and the critical flux and critical mass become small according to

$$Q_c \sim \frac{98\tau^3\bar{a}}{405} \to 0^+, \quad M_c \sim \frac{14\tau\bar{a}}{3}\log\left(2+\sqrt{3}\right) \simeq 6.1458\tau\bar{a} \to 0^+. \tag{5.10}$$

Figure 5.5 shows the critical contact angle β_c and the critical maximum thickness h_{mc} as functions of α/π when $\tau = 1$ for a range of values of $\bar{a}$. In particular, Figure 5.5 shows that there is a corner in the solution for β_c only when $\bar{a} < 5^{1/4}\pi$; this is because the corner is in the de-pinned interval when $\bar{a} > 5^{1/4}\pi$, for which $\beta_c \equiv 0$. In the limit of a very narrow ring, $\bar{a} \to 0^+$, the critical contact angle β_c behaves according to

$$\beta_c \sim \frac{7\tau\tilde{\beta}_c}{6\bar{a}\sin\alpha} \to \infty, \tag{5.11}$$

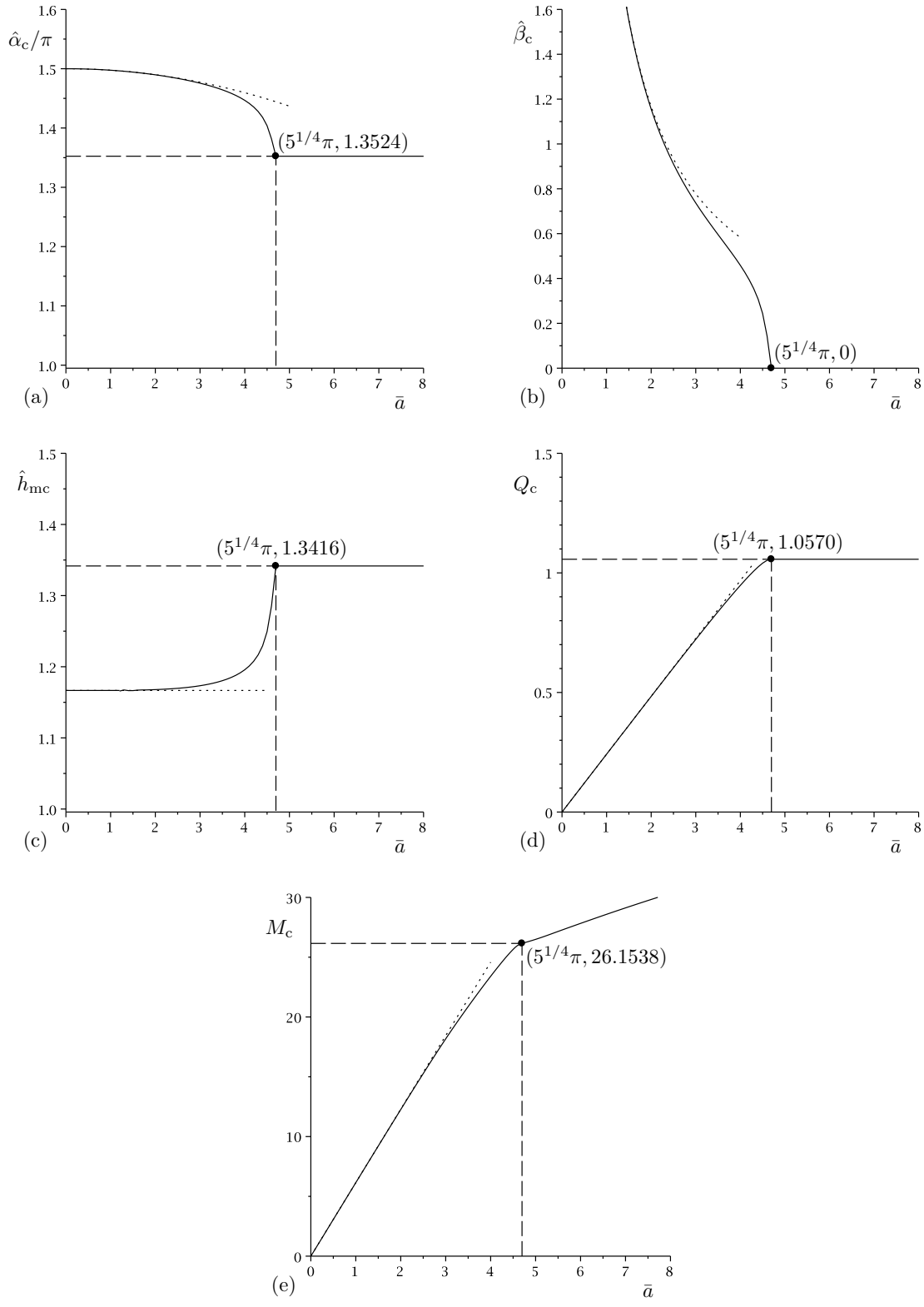

Figure 5.4: Plots of (a) $\hat{\alpha}_c/\pi$, (b) $\hat{\beta}_c$, (c) $\hat{h}_{mc}$, (d) Q_c and (e) M_c as functions of $\bar{a}$ when $\tau = 1$, together with the asymptotic results in the limit of a very narrow ring, $\bar{a} \to 0^+$, given by (5.9) and (5.10), and shown as dotted lines. The dots are located on the curves at the value $\bar{a} = 5^{1/4}\pi \simeq 4.6978$ and the values $\hat{\alpha}_c/\pi \simeq 1.3524$, $\hat{h}_{mc} \simeq 1.3416$ and $Q_c \simeq 1.0570$ here are given by (5.7), while the value $M_c \simeq 26.1538$ is numerically calculated from (5.4) with $\beta = \beta_c$. There is a corner in the pinned interval when $\bar{a} < 5^{1/4}\pi$ and in the de-pinned interval when $\bar{a} \geq 5^{1/4}\pi$.

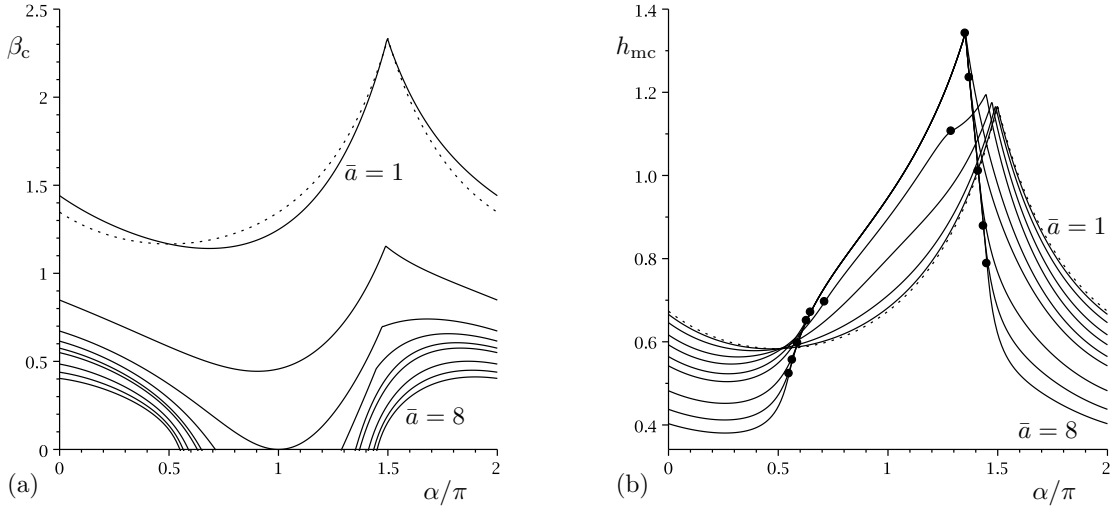

Figure 5.5: Plots of (a) the critical contact angle β_c and (b) the critical maximum thickness h_{mc} as functions of α/π when $\tau = 1$ for $\bar{a} = 1, 2, \pi, 4, 5^{1/4}\pi \simeq 4.6978, 5, 6, 7, 8$. The dotted curves show the asymptotic solution in the limit of a very narrow ring, $\bar{a} \to 0^+$, on the $\bar{a} = 1$ curve. The dots in part (b) indicate the values at which the contact lines de-pin and re-pin (i.e. the values corresponding to $\beta_c = 0$ in part (a)).

where

$$\tilde{\beta}_c = -1 + 2 \times \begin{cases} \cos\left(\dfrac{\pi - 2\alpha}{3}\right) & \text{for} \quad 0 \le \alpha \le \dfrac{3\pi}{2}, \\ \cos\left(\dfrac{\pi + 2\alpha}{3}\right) & \text{for} \quad \dfrac{3\pi}{2} < \alpha < 2\pi, \end{cases} \tag{5.12}$$

and the critical maximum thickness h_{mc} behaves according to (4.7) in Chapter 4 with $\beta = \beta_c$ from (5.11). These asymptotic results are included in Figure 5.5 on the $\bar{a} = 1$ curves and show that the asymptotic solution predicts that both β_c and h_{mc} are smaller than the exact solution on the upper half of the cylinder but larger on the lower half of the cylinder. Figure 5.6 shows plots of β_c and h_{mc} as functions of $\bar{a}$ when $\tau = 1$ for a range of values of α. The behaviour of the full ring at the stations shown in Figure 5.6 in the limits of a very narrow ring, $\bar{a} \to 0^+$, and a very wide ring, $\bar{a} \to \infty$, is detailed in Appendix B. Figure 5.7 shows three-dimensional plots of the critical ring profile h_c when $\tau = 1$ for a range of values of $\bar{a}$. Figures 5.5, 5.6 and 5.7, together with the asymptotics given in Appendix B, show that a larger value of $\bar{a}$ results in a smaller β_c, a smaller h_{mc} on the upper half of the

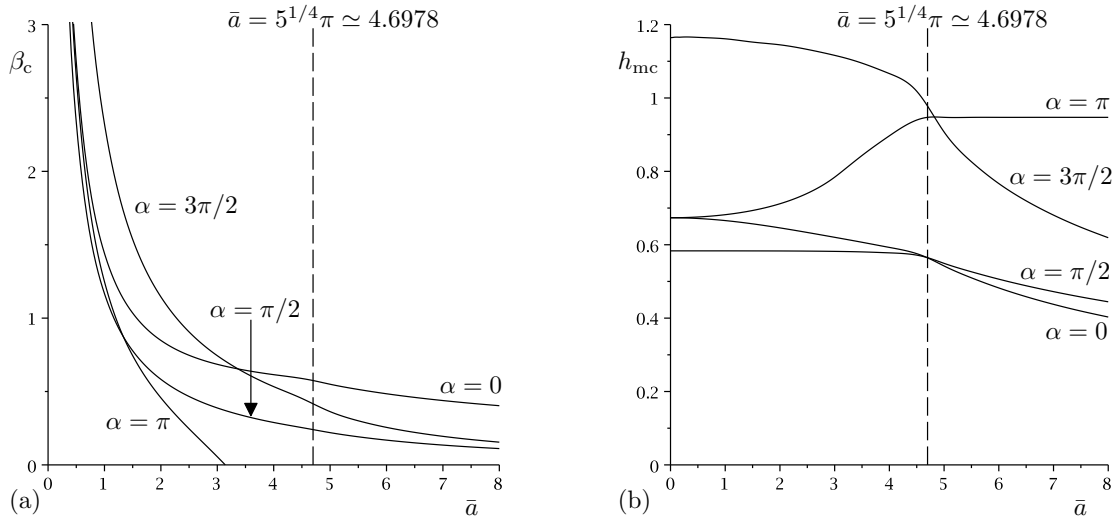

Figure 5.6: Plots of (a) the critical contact angle β_c and (b) the critical maximum thickness h_{mc} as functions of $\bar{a}$ when $\tau = 1$ at $\alpha = 0, \pi/2, \pi, 3\pi/2$.

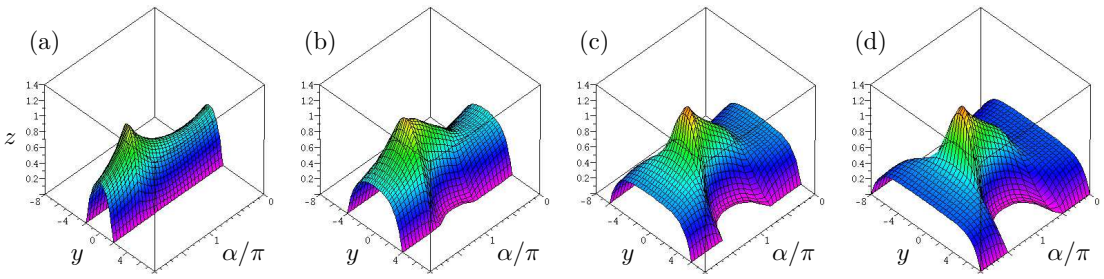

Figure 5.7: Three-dimensional plots of the critical ring profile h_c as a function of y and α/π when $\tau = 1$ for (a) $\bar{a} = 2$, (b) $\bar{a} = 4\,(< 5^{1/4}\pi \simeq 4.6978)$, (c) $\bar{a} = 6\,(> 5^{1/4}\pi)$ and (d) $\bar{a} = 8$.

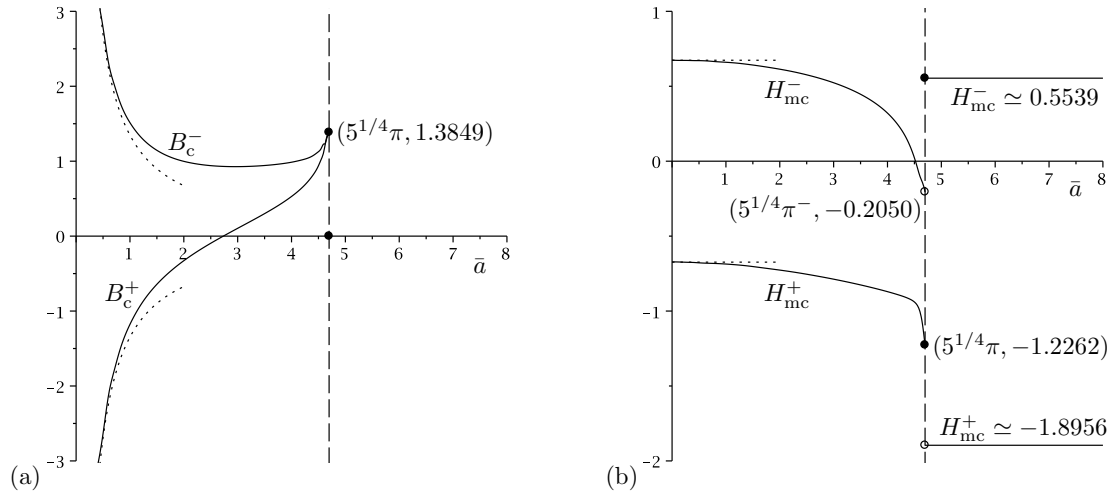

Figure 5.8: (a) The slopes of the critical contact angle β_c as $\alpha \to \hat{\alpha}_c^{\pm}$, $B_c^{\pm}$, and (b) the slopes of the critical maximum thickness h_{mc} as $\alpha \to \hat{\alpha}_c^{\pm}$, $H_{mc}^{\pm}$, plotted as functions of $\bar{a}$ when $\tau = 1$. The vertical dashed lines indicate the value $\bar{a} = 5^{1/4}\pi \simeq 4.6978$, beyond which $\beta_c \equiv 0$ and $B_c^{\pm} = 0$. The dotted curves show the asymptotic results in the limit of a very narrow ring, $\bar{a} \to 0^+$, given by (5.14).

cylinder, and a larger h_{mc} in the pinned interval on the lower half of the cylinder (while, of course, in the de-pinned interval h_{mc} is independent of $\bar{a}$).

The shape of the corner in the critical solution depends on $\bar{a}$; the slopes of the contact angle β_c, ring profile h_c, and maximum thickness h_{mc} on either side of the corner (i.e. as $\alpha \to \hat{\alpha}_c^{\pm}$) are denoted by

$$B_c^{\pm} = \left.\frac{\mathrm{d}\beta_c}{\mathrm{d}\alpha}\right|_{\alpha=\hat{\alpha}_c^{\pm}}, \quad H_c^{\pm} = \left.\frac{\partial h_c}{\partial \alpha}\right|_{\alpha=\hat{\alpha}_c^{\pm}}, \quad H_{mc}^{\pm} = H_c^{\pm}|_{y=0} = \left.\frac{\mathrm{d}h_{mc}}{\mathrm{d}\alpha}\right|_{\alpha=\hat{\alpha}_c^{\pm}}, \tag{5.13}$$

respectively. Figure 5.8 shows plots of $B_c^{\pm}$ and $H_{mc}^{\pm}$ as functions of $\bar{a}$ when $\tau = 1$. In particular, Figure 5.8(a) shows that B_c^- is a positive, monotonically decreasing function of $\bar{a}$ when $\bar{a} < 2.9586$ and a positive, monotonically increasing function of $\bar{a}$ when $2.9586 < \bar{a} < 5^{1/4}\pi \simeq 4.6978$, whereas B_c^+ is a negative, monotonically increasing function of $\bar{a}$ when $\bar{a} < 2.7332$ and a positive, monotonically increasing function of $\bar{a}$ when $2.7332 < \bar{a} < 5^{1/4}\pi$, where $B_c^- = B_c^+ \simeq 1.3849$ when $\bar{a} = 5^{1/4}\pi$, while of course $\hat{\beta}_c = 0$ for $\bar{a} > 5^{1/4}\pi$ and so $B_c^- = B_c^+ = 0$. Also, Figure 5.8(b) shows that H_{mc}^- is a positive, monotonically decreasing function of $\bar{a}$ when

$\bar{a} < 4.5150$, a negative, monotonically decreasing function of $\bar{a}$ when $4.5150 < \bar{a} < 5^{1/4}\pi$, and takes the constant positive value $H_{\rm mc}^{-} \simeq 0.5539$ when $\bar{a} > 5^{1/4}\pi$, whereas $H_{\rm mc}^{+}$ is a negative, monotonically decreasing function of $\bar{a}$ when $\bar{a} < 5^{1/4}\pi$ and takes the constant negative value $H_{\rm mc}^{+} \simeq -1.8956$ when $\bar{a} > 5^{1/4}\pi$. In the limit of a very narrow ring, $\bar{a} \to 0^{+}$, the slopes $B_{\rm c}^{\pm}$ and $H_{\rm mc}^{\pm}$ behave according to

$$B_{\rm c}^{\pm} \sim \mp\frac{7\sqrt{3}\tau}{9\bar{a}} \to \infty \quad \text{and} \quad H_{\rm mc}^{\pm} \sim \mp\frac{7\sqrt{3}\tau}{18} = O(1), \tag{5.14}$$

and these are included in Figure 5.8 as dotted curves.

5.3 The Sub-Critical Full-Ring Solution

In Section 5.2 we described the behaviour of the critical ring solution with maximum mass $M_{\rm c}$ for a prescribed shear stress τ (where the value of $M_{\rm c}$ is found as part of the solution). In this Section we describe the behaviour of a sub-critical full ring when the mass M is also prescribed, in which case a solution exists provided that M satisfies $M < M_{\rm c}$ (i.e. only for values of $\bar{a}$, Q and M that lie below the solid curves in Figures 5.4(d) and 5.4(e)). The behaviour in each of the cases $\bar{a} < \pi$, $\pi < \bar{a} < 5^{1/4}\pi \simeq 4.6978$ and $\bar{a} > 5^{1/4}\pi$ is qualitatively different and so we present results in each of these three cases separately.

As described in Subsection 5.1.4, when $\bar{a} < \pi$ the full ring flows round the entire circumference of the cylinder with pinned contact lines. Figures 5.9(a) and 5.9(b) show plots of the contact angle β and the maximum thickness $h_{\rm m}$ as functions of α/π when $\tau = 1$ and $\bar{a} = 2\,(< \pi)$ for a range of values of $M \leq M_{\rm c} \simeq 12.2613$. When $\bar{a} > \pi$ the full ring flows with pinned contact lines for $0 \leq \alpha < \alpha_{\rm depin}$ and $\alpha_{\rm repin} < \alpha < 2\pi$, and with de-pinned contact lines for $\alpha_{\rm depin} \leq \alpha \leq \alpha_{\rm repin}$. In particular, when $\pi < \bar{a} < 5^{1/4}\pi$ the corner is in the pinned interval $\alpha_{\rm repin} < \alpha < 3\pi/2$, and Figures 5.9(c) and 5.9(d) show plots of β and $h_{\rm m}$ as functions of α/π when $\tau = 1$ and $\bar{a} = 4\,(\pi < \bar{a} < 5^{1/4}\pi)$ for a range of values of $M \leq M_{\rm c} \simeq 23.4027$.

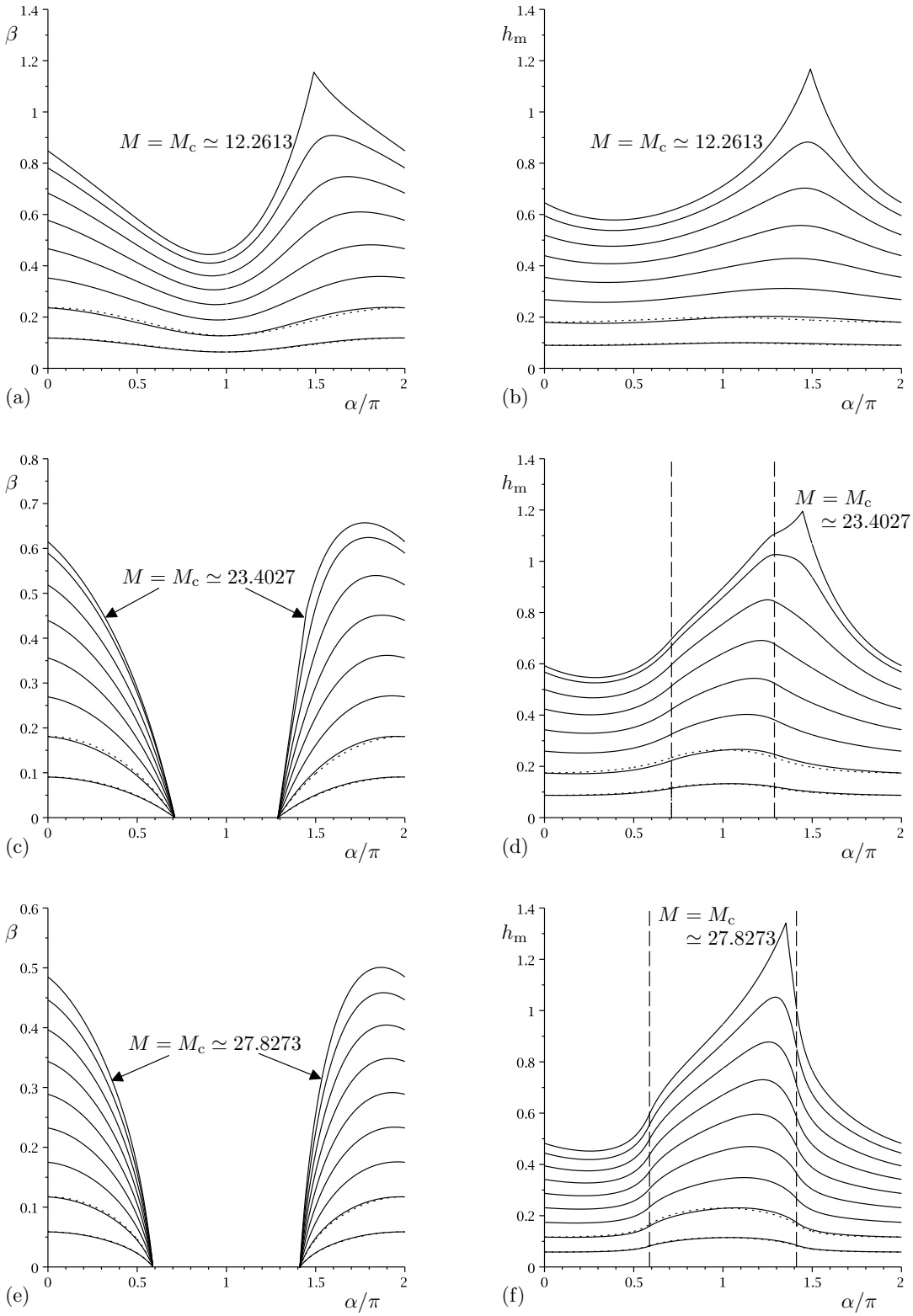

Figure 5.9: Plots of (a,c,e) the contact angle β and (b,d,f) the maximum thickness h_m as functions of α/π when $\tau = 1$ and (a,b) $\bar{a} = 2\,(< \pi)$, $M = 0.5\pi,\ \pi, ..., 3.5\pi,\ M_c \simeq 12.2613$, (c,d) $\bar{a} = 4\,(\pi < \bar{a} < 5^{1/4}\pi \simeq 4.6978)$, $M = \pi,\ 2\pi, ..., 7\pi,\ M_c \simeq 23.4027$ and (e,f) $\bar{a} = 6\,(> 5^{1/4}\pi)$, $M = \pi,\ 2\pi, ..., 8\pi,\ M_c \simeq 27.8273$. The vertical dashed lines in parts (d) and (f) indicate the values $\alpha_{\rm depin}/\pi$ and $\alpha_{\rm repin}/\pi$. The dotted curves show the solution in the limit of small mass, $M \to 0^+$, given in Subsection 5.3.1, for the two smallest values of M in each plot. For clarity the vertical ranges for plots of β in parts (a,c,e) differ from each other; however, the vertical ranges for plots of h_m in parts (b,d,f) are the same.

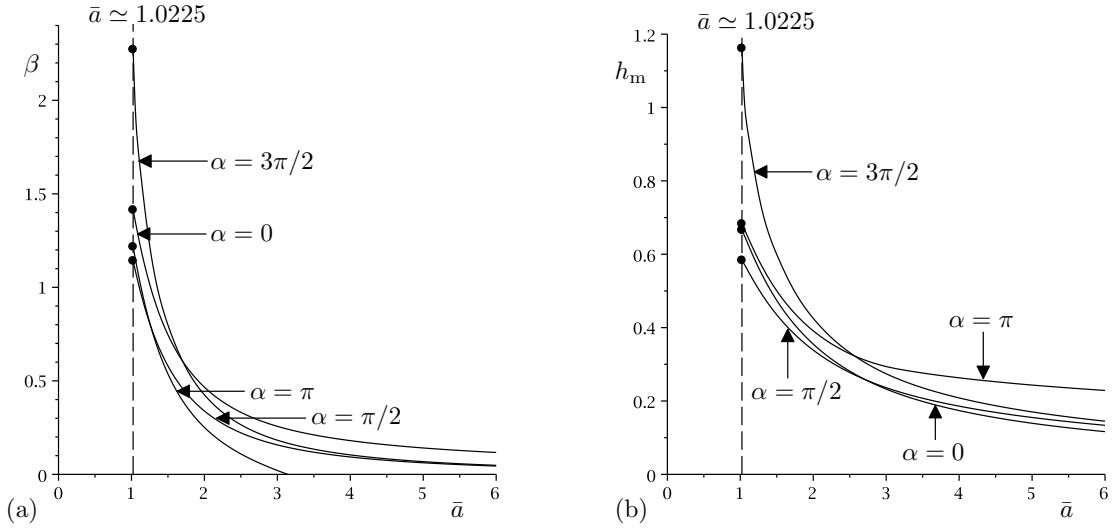

Figure 5.10: Plots of (a) the contact angle β and (b) the maximum thickness $h_{\rm m}$ as functions of $\bar{a}$ when $\tau = 1$ and $M = 2\pi$ for $\alpha = 0, \pi/2, \pi, 3\pi/2$. The vertical dashed lines indicate the value $\bar{a} \simeq 1.0225$, at which value $M_{\rm c} = 2\pi$, so that no full-ring solutions exist when $\bar{a} < 1.0225$.

When $\bar{a} > 5^{1/4}\pi$ the corner is in the de-pinned interval $\pi < \alpha < \alpha_{\rm repin}$, and Figures 5.9(e) and 5.9(f) show plots of β and $h_{\rm m}$ as functions of α/π when $\tau = 1$ and $\bar{a} = 6\,(> 5^{1/4}\pi)$ for a range of values of $M \leq M_{\rm c} \simeq 27.8273$. Figure 5.9(d) shows that, while the corner is in the pinned interval when $\pi < \bar{a} < 5^{1/4}\pi$, the location of the maximum value of $h_{\rm m}$ in a sub-critical case $M < M_{\rm c}$ may occur in either the pinned or the de-pinned interval; however, Figure 5.9(f) shows that the location of the maximum value of $h_{\rm m}$ when $\bar{a} > 5^{1/4}\pi$ always occurs in the de-pinned interval. Also, while the critical maximum thickness at the corner, $\hat{h}_{\rm mc}$, is the maximum value of $h_{\rm mc}$ for most ring widths, there is a small interval of $\bar{a}$ values, namely $4.5150 < \bar{a} < 5^{1/4}\pi \simeq 4.6978$ (obtained by inspection of Figure 5.8(b)) in which this is not the case. Figure 5.10 shows plots of β and $h_{\rm m}$ as functions of $\bar{a}$ when $\tau = 1$ and $M = 2\pi$ for a range of values of α, Figure 5.11 shows plots of β and $h_{\rm m}$ as functions of M when $\tau = 1$ and $\bar{a} = 2, 4, 6$ for a range of values of α, and Figure 5.12 shows three-dimensional plots of the ring profile h when $\tau = 1$ for various values of $\bar{a}$ and $M \leq M_{\rm c}$, clearly illustrating how the

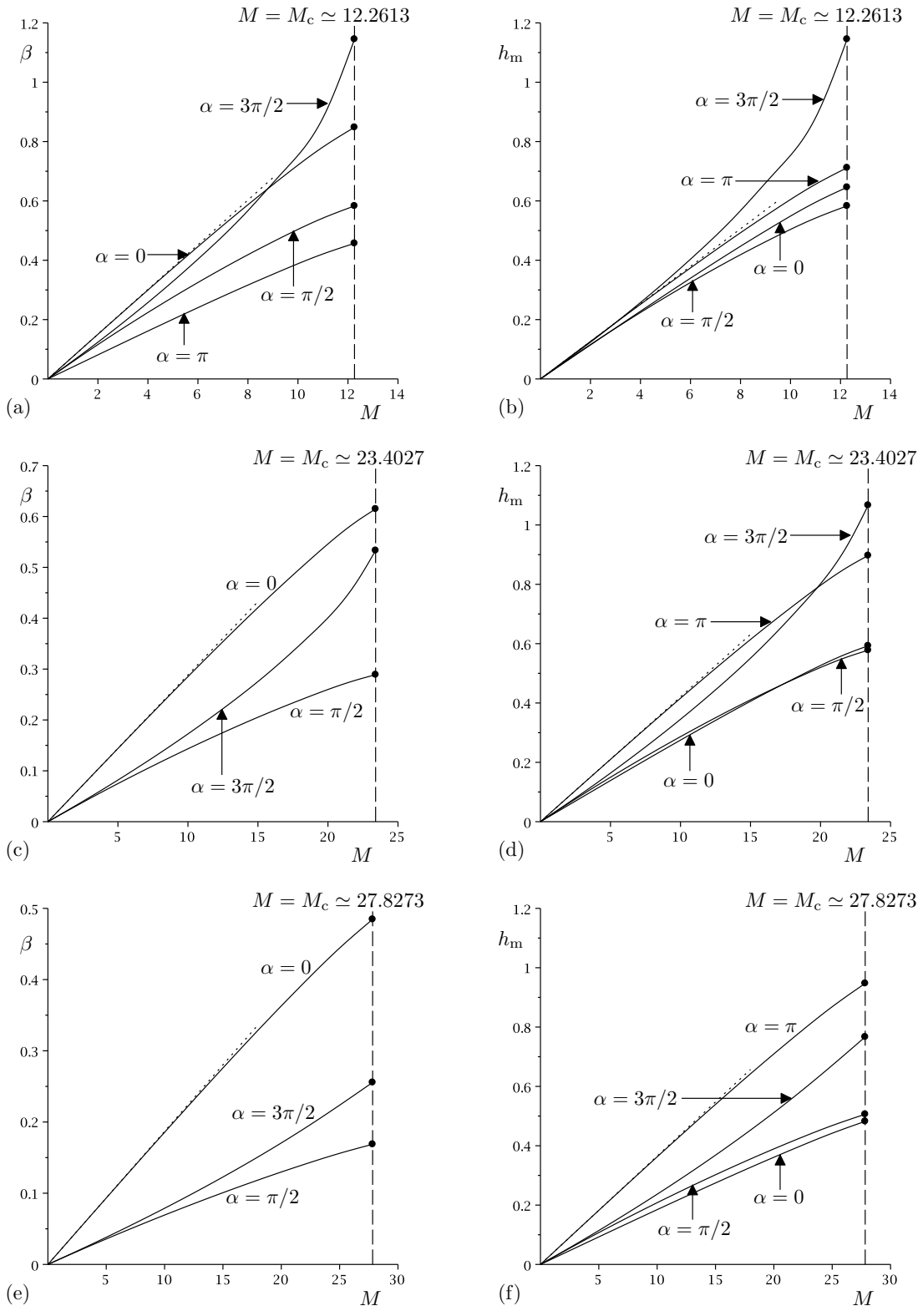

Figure 5.11: Plots of (a,c,e) the contact angle β and (b,d,f) the maximum thickness h_m as functions of the mass M when $\tau = 1$ and (a,b) $\bar{a} = 2\,(< \pi)$, (c,d) $\bar{a} = 4\,(\pi < \bar{a} < 5^{1/4}\pi)$ and (e,f) $\bar{a} = 6\,(> 5^{1/4}\pi)$, at $\alpha = 0, \pi/2, \pi, 3\pi/2$. The dotted lines show the asymptotic results in the limit of small mass, $M \to 0^+$, given by (5.16) at $\alpha = 0$ for (a,c,e), given by (4.7) in Chapter 4 with β given by (5.16) at $\alpha = \pi$ for (b), and given by (5.17) at $\alpha = \pi$ for (d,f). For clarity, the asymptotic solution for $M \to 0^+$ is shown for one value of α only in each plot and, also for clarity, the vertical ranges for plots of β in parts (a,c,e) differ from each other; however, the vertical ranges for plots of h_m in parts (b,d,f) are the same.

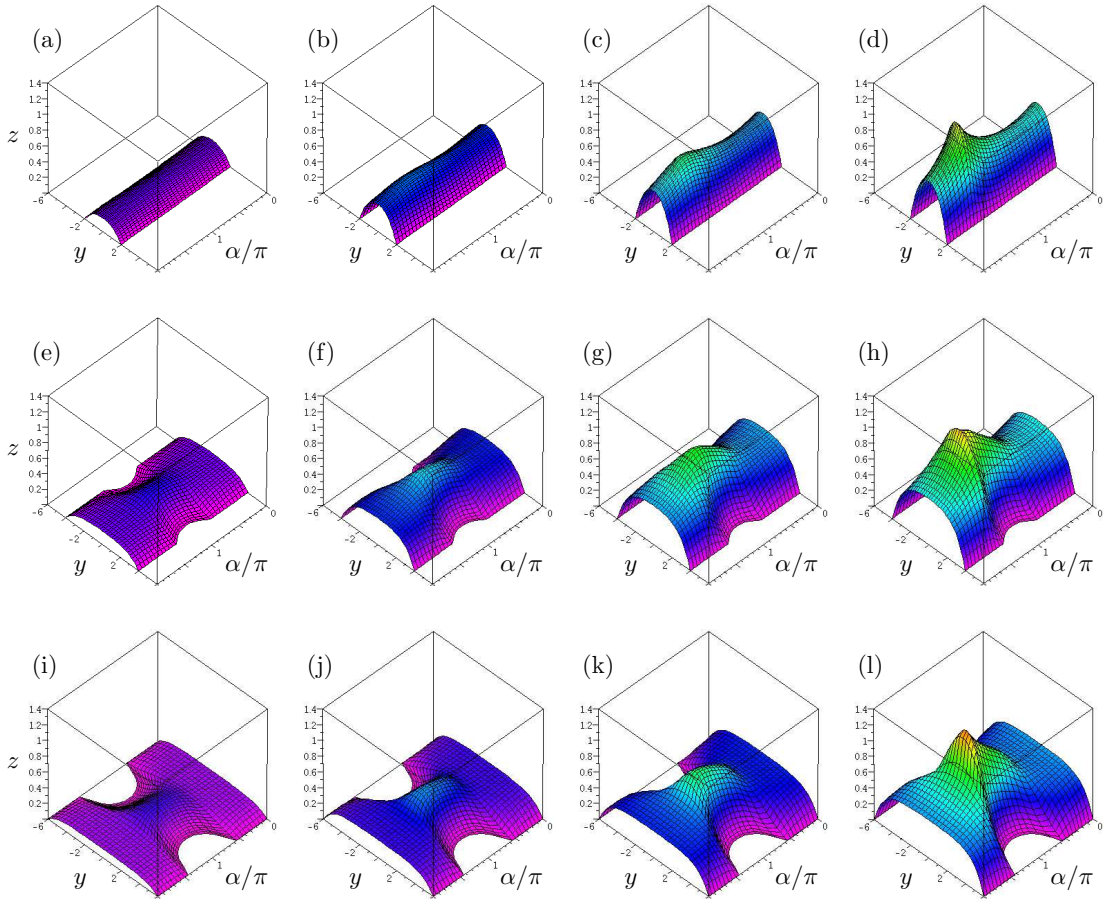

Figure 5.12: Three-dimensional plots of the ring profile h as a function of y and α/π when $\tau = 1$ for: (a) $M = \pi$, (b) $M = 2\pi$, (c) $M = 3\pi$ and (d) $M = M_{\rm c} \simeq 12.2613$ when $\bar{a} = 2\,(< \pi)$, (e) $M = 2\pi$, (f) $M = 4\pi$, (g) $M = 6\pi$ and (h) $M = M_{\rm c} \simeq 23.4027$ when $\bar{a} = 4\,(\pi < \bar{a} < 5^{1/4}\pi)$, and (i) $M = 2\pi$, (j) $M = 4\pi$, (k) $M = 6\pi$ and (l) $M = M_{\rm c} \simeq 27.8273$ when $\bar{a} = 6\,(> 5^{1/4}\pi)$.

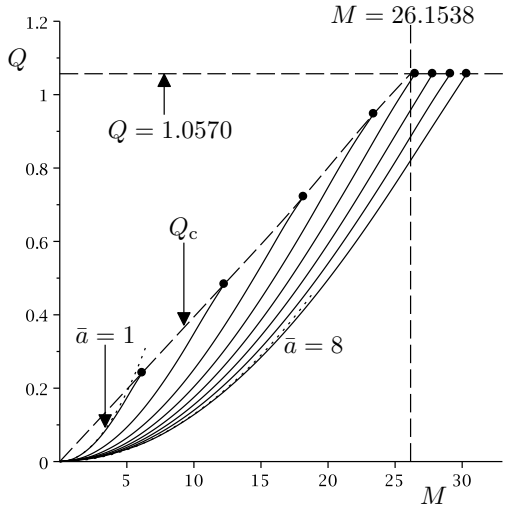

Figure 5.13: The flux Q plotted as a function of the mass M when $\tau = 1$ for $\bar{a} = 1, 2, ..., 8$. The critical flux Q_c is shown with a dashed curve, and the values $Q = Q_c \simeq 1.0570$ and $M = M_c \simeq 26.1538$ when $\bar{a} = 5^{1/4}\pi \simeq 4.6978$ are shown with horizontal and vertical dashed lines, respectively. The dotted curves show the asymptotic results in the limit of small mass, $M \to 0^+$, given by (5.15), when $\bar{a} = 1$ and $\bar{a} = 8$.

shape of the ring varies with both $\bar{a}$ and M. In the limit of a very wide ring, $\bar{a} \to \infty$, the contact lines are de-pinned on the entire lower half of the cylinder (i.e. $\alpha_{\text{depin}} \to \pi/2^+$ and $\alpha_{\text{repin}} \to 3\pi/2^-$) so that the ring profile on the lower half of the cylinder is independent of $\bar{a}$, and is given by (5.3b). Figures 5.9, 5.11 and 5.12 show that β is an increasing function of M for $0 \leq \alpha < \alpha_{\text{depin}}$ and $\alpha_{\text{repin}} < \alpha < 2\pi$, and that h_{m} is an increasing function of M for all α $(0 \leq \alpha < 2\pi)$.

Figure 5.13 shows Q plotted as a function of M for a range of values of $\bar{a}$ when $\tau = 1$, together with the critical flux Q_c, shown as a dashed curve. The critical flux remains constant at $Q_c \simeq 1.0570$ for $\bar{a} \geq 5^{1/4}\pi$, as given by (5.7); however, the critical mass M_c continues to increase as $\bar{a}$ is increased beyond this value.

5.3.1 The Limit of Small Mass ($M \to 0^+$)

In the limit of small mass, $M \to 0^+$, the flux becomes small according to

$$Q \sim \frac{3\tau M^2}{32C^2} \to 0^+, \tag{5.15}$$

the contact angle becomes small according to

$$\beta \sim \frac{\sqrt{3}m^{3/2}M}{4C\sqrt{g(m\bar{a})}} \to 0^+, \tag{5.16}$$

and the maximum thickness becomes small according to (4.7) in Chapter 4 with β given by (5.16) in the pinned interval, and according to

$$h_{\mathrm{m}} \sim \frac{\sqrt{m}M}{2C\sqrt{\pi}} \to 0^+, \tag{5.17}$$

in the de-pinned interval, where $C = C(\bar{a})$ is given by

$$C = \sqrt{3}\int_0^{\frac{\pi}{2}} \frac{m\bar{a}\coth m\bar{a} - 1}{\sqrt{mg(m\bar{a})}}\,\mathrm{d}\alpha + \sqrt{3}\int_{\frac{\pi}{2}}^{\alpha_{\mathrm{depin}}} \frac{1 - m\bar{a}\cot m\bar{a}}{\sqrt{mg(m\bar{a})}}\,\mathrm{d}\alpha + \sqrt{\pi}\int_{\alpha_{\mathrm{depin}}}^{\pi} \frac{1}{\sqrt{m}}\,\mathrm{d}\alpha. \tag{5.18}$$

There is no full-ring solution in the limit of large mass, $M \to \infty$, since full-ring solutions exist only for $M \leq M_{\mathrm{c}}$. The asymptotic results for Q given by (5.15) are included as dotted curves in Figure 5.13 for $\bar{a} = 1$ and $\bar{a} = 8$ (the asymptotic results for other values of $\bar{a}$ being omitted for clarity). The asymptotic result for β given by (5.16) is included as a dotted curve in Figures 5.9(a), 5.9(c) and 5.9(e) on the curves for the two smallest values of M displayed in each case (namely, 0.5π and π, π and 2π, and π and 2π, respectively), and in Figures 5.11(a), 5.11(c) and 5.11(e) on the curve $\alpha = 0$ (the asymptotic results for $\alpha = \pi/2, \pi, 3\pi/2$ being omitted for clarity). The asymptotic result for h_{m} given by (4.7) in Chapter 4 with β given by (5.16) in the pinned interval, and given by (5.17) in the de-pinned interval, is included as a dotted curve in Figures 5.9(b), 5.9(d) and 5.9(f) on the curves for the two smallest values of M displayed in each case (namely, 0.5π and π, π and 2π, and π and 2π, respectively), and in Figures 5.11(b), 5.11(d) and 5.11(f) on the curve $\alpha = \pi$ (the asymptotic results for $\alpha = 0, \pi/2, 3\pi/2$ being omitted for clarity). Figure 5.14 shows three-dimensional plots of the asymptotic solution for the ring profile h when $\bar{a} = 6$ and $\tau = 1$ for various values of M, and correspond to the exact solutions shown in Figures 5.12(i)–(l). In particular, Figure 5.14

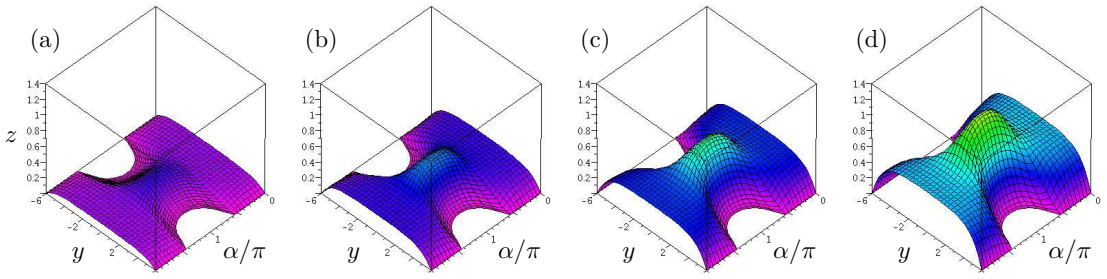

Figure 5.14: Three-dimensional plots of the asymptotic solutions for the ring profile h in the limit of small mass, $M \to 0^+$, as a function of y and α/π when $\bar{a} = 6$ and $\tau = 1$ for (a) $M = 2\pi$, (b) $M = 4\pi$, (c) $M = 6\pi$ and (d) $M = M_c \simeq 27.8273$. These asymptotic solutions correspond to the exact solutions shown in Figures 5.12(i)–(l).

shows that the asymptotic solution for h provides a good approximation to the exact solution for most values of $M \leq M_c$; however, comparing Figures 5.12(l) and 5.14(d) shows that, as expected, this approximation is poorest in comparison with the exact solution in the case $M = M_c$, where the asymptotic solution predicts that h_m in the de-pinned interval is smaller than in the exact solution. For brevity, we do not display plots for other values of $\bar{a}$ in Figure 5.14.

5.4 Backflow

In this Section we will show that, while the direction of the velocity u is mostly in the same direction as that of the surface shear stress τ and of the flux Q (i.e. $u > 0$), there is a region of $\bar{a}$–M parameter space in which backflow (that is, flow in the direction opposite to the surface shear stress τ) can occur. Further, backflow may occur only on the left-hand side of the cylinder, that is, the side in which the shear stress opposes gravity. Figure 5.15 shows the two types of flow pattern that are possible for the present three-dimensional ring flow, namely (in the terminology of Wilson and Duffy [108]) type I, in which $u > 0$ everywhere, and type IV, in which $u < 0$ in a region adjacent to the substrate near the centre of the ring. Regions with $u > 0$ are shaded and regions with $u < 0$ (that is,

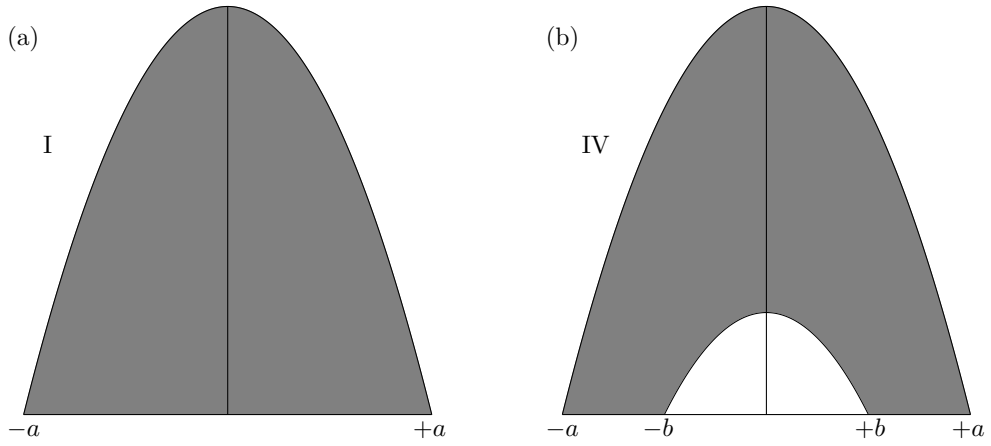

Figure 5.15: Sketches of the two possible types of cross-sectional flow pattern for a full ring of fluid, denoted (in the terminology of Wilson and Duffy [108]) as type I and IV. Regions with $u > 0$ are shaded and regions with $u < 0$ (that is, regions of backflow) are unshaded. Note that the profiles are parabolic only for $\alpha = \pi/2$ and $\alpha = 3\pi/2$ but that the flow patterns are qualitatively the same for all values of α.

regions of backflow) are unshaded. From (4.3) in Chapter 4, other than at the substrate $z = 0$, the azimuthal velocity may be zero (i.e. $u = 0$) only on the three-dimensional surface defined by

$$z = 2\left(h + \frac{\tau}{\sin\alpha}\right) \tag{5.19}$$

in $0 < z \leq h$. Given that $\tau > 0$, it is immediately apparent that (5.19) may have solutions satisfying $z \leq h$ only for $\pi < \alpha < 2\pi$ (i.e. on the left-hand side of the cylinder). The surface (5.19) intersects the substrate $z = 0$ when $h = -\tau/\sin\alpha$, which, from (4.6) in Chapter 4 or (5.3b) when the contact lines are pinned or depinned, respectively, means that it may intersect the substrate only in the curves

$y = \pm b(\alpha)$ defined by

$$b(\alpha) = \begin{cases} \dfrac{1}{m}\cos^{-1}\left[-\dfrac{2\tau}{h_{\mathrm{m}}\sin\alpha} - 1\right] & \text{for} \quad \pi < \alpha \leq \alpha_{\mathrm{repin}}, \\ \dfrac{1}{m}\cos^{-1}\left[\cos m\bar{a} - \dfrac{\tau m \sin m\bar{a}}{\beta \sin\alpha}\right] & \text{for} \quad \alpha_{\mathrm{repin}} < \alpha < \dfrac{3\pi}{2}, \\ \sqrt{\bar{a}^2 - \dfrac{2\tau\bar{a}}{\beta}} & \text{for} \quad \alpha = \dfrac{3\pi}{2}, \\ \dfrac{1}{m}\cosh^{-1}\left[\cosh m\bar{a} + \dfrac{\tau m \sinh m\bar{a}}{\beta \sin\alpha}\right] & \text{for} \quad \dfrac{3\pi}{2} < \alpha < 2\pi, \end{cases} \tag{5.20}$$

which provides an explicit expression for the "footprint" of the region of backflow on the cylinder (i.e. in the α–y plane). The endpoints in the α direction of the region of backflow given by (5.20) occur at $y = b = 0$, so that at these endpoints we have $h_{\mathrm{m}} = -\tau/\sin\alpha$, and therefore β is given by (4.7) in Chapter 4 as

$$\beta = \begin{cases} 0 & \text{for} \quad \pi < \alpha \leq \alpha_{\mathrm{repin}}, \\ -\dfrac{\tau m}{\sin\alpha}\cot\left(\dfrac{m\bar{a}}{2}\right) & \text{for} \quad \alpha_{\mathrm{repin}} < \alpha < \dfrac{3\pi}{2}, \\ \dfrac{2\tau}{\bar{a}} & \text{for} \quad \alpha = \dfrac{3\pi}{2}, \\ -\dfrac{\tau m}{\sin\alpha}\coth\left(\dfrac{m\bar{a}}{2}\right) & \text{for} \quad \dfrac{3\pi}{2} < \alpha < 2\pi. \end{cases} \tag{5.21}$$

We may substitute $h_{\mathrm{m}} = -\tau/\sin\alpha$ into (5.3c) when the contact lines are de-pinned (i.e. for $\pi < \alpha \leq \alpha_{\mathrm{repin}}$), or substitute (5.21) into (5.2) when the contact lines are pinned (i.e. for $\alpha_{\mathrm{repin}} < \alpha < 2\pi$), to give an equation that determines the values of α at the endpoints of the region of backflow in terms of Q, namely

$$Q = \begin{cases} \dfrac{\pi\tau^3}{6m\sin^2\alpha} & \text{for} \quad \pi < \alpha \leq \alpha_{\mathrm{repin}}, \\ \dfrac{\tau^3}{18m\sin^2\alpha}\cot^2\left(\dfrac{m\bar{a}}{2}\right)\left[9g(m\bar{a}) - 2\cot\left(\dfrac{m\bar{a}}{2}\right)f(m\bar{a})\right] & \text{for} \quad \alpha_{\mathrm{repin}} < \alpha < \dfrac{3\pi}{2}, \\ \dfrac{8\tau^3\bar{a}}{35} & \text{for} \quad \alpha = \dfrac{3\pi}{2}, \\ \dfrac{\tau^3}{18m\sin^2\alpha}\coth^2\left(\dfrac{m\bar{a}}{2}\right)\left[9g(m\bar{a}) - 2\coth\left(\dfrac{m\bar{a}}{2}\right)f(m\bar{a})\right] & \text{for} \quad \dfrac{3\pi}{2} < \alpha < 2\pi. \end{cases} \tag{5.22}$$

Figure 5.16 shows plots of Q given by (5.22) as a function of α/π when $\tau = 1$ for different values of $\bar{a}$. In particular, Figure 5.16 shows that Q is a positive, monotonically decreasing function from $\alpha = \pi$ to $\alpha = \alpha_{\min}$, where $\alpha_{\min} = \alpha_{\min}(\bar{a})$, and is a positive, monotonically increasing function from $\alpha = \alpha_{\min}$ to $\alpha = 2\pi$. At $\alpha = \alpha_{\min}$, the flux takes its minimum value $Q = Q_{\min}$, where $0 < Q_{\min} < Q_{\rm c}$ for any $\bar{a}$ (and there is a corresponding minimum mass denoted by $M = M_{\min}$ satisfying $0 < M_{\min} < M_{\rm c}$), and therefore (5.22) has two solutions $\alpha = \alpha_1$ and $\alpha = \alpha_2$ (with $\pi < \alpha_1 < \alpha_{\min} < \alpha_2 < \alpha_{\max}$, where $\alpha_{\max} = 2\pi - \sin^{-1}(18/7\sqrt{7}) \simeq 4.9500$) when $Q > Q_{\min}$, one solution $\alpha = \alpha_1 = \alpha_2 = \alpha_{\min}$ when $Q = Q_{\min}$, and no solutions when $Q < Q_{\min}$. When $Q > Q_{\rm c}$ there is, of course, no full-ring solution, when $Q < Q_{\min}$ there is a full-ring solution with no backflow, and when $Q_{\min} \leq Q \leq Q_{\rm c}$ there is a full-ring solution with a small region of backflow adjacent to the substrate between $\alpha = \alpha_1$ and $\alpha = \alpha_2$. The largest interval of backflow in the α direction for a given $\bar{a}$ occurs in the case of a critical full ring (i.e. when $Q = Q_{\rm c}$); we denote the endpoints of the region of backflow in this case by $\alpha = \alpha_{1{\rm c}}$ and $\alpha = \alpha_{2{\rm c}}$. Figure 5.16 also shows that for different values of $\bar{a}$ the region of backflow may occur entirely in the pinned interval $\alpha_{\rm repin} < \alpha < 2\pi$ (shown in parts (a) and (b)), partly in each of the pinned and de-pinned intervals (shown in part (c)), or entirely in the de-pinned interval $\pi < \alpha < \alpha_{\rm repin}$ (shown in part (d)). Figure 5.17(a) shows the difference between the critical flux and the minimum flux below which backflow is not possible, $Q_{\rm c} - Q_{\min}$, and Figure 5.17(b) shows the difference between the critical mass and the minimum mass below which backflow is not possible, $M_{\rm c} - M_{\min}$, plotted as functions of $\bar{a}$ when $\tau = 1$, which, in conjunction with Figures 5.4(d) and 5.4(e), show the regions of the $\bar{a}$–Q and $\bar{a}$–M parameter planes in which backflow occurs. In particular, Figure 5.17 shows that backflow occurs only when Q and M are relatively close to the critical values $Q_{\rm c}$ and $M_{\rm c}$, respectively, and so we restrict our attention in the rest of this Section to backflow

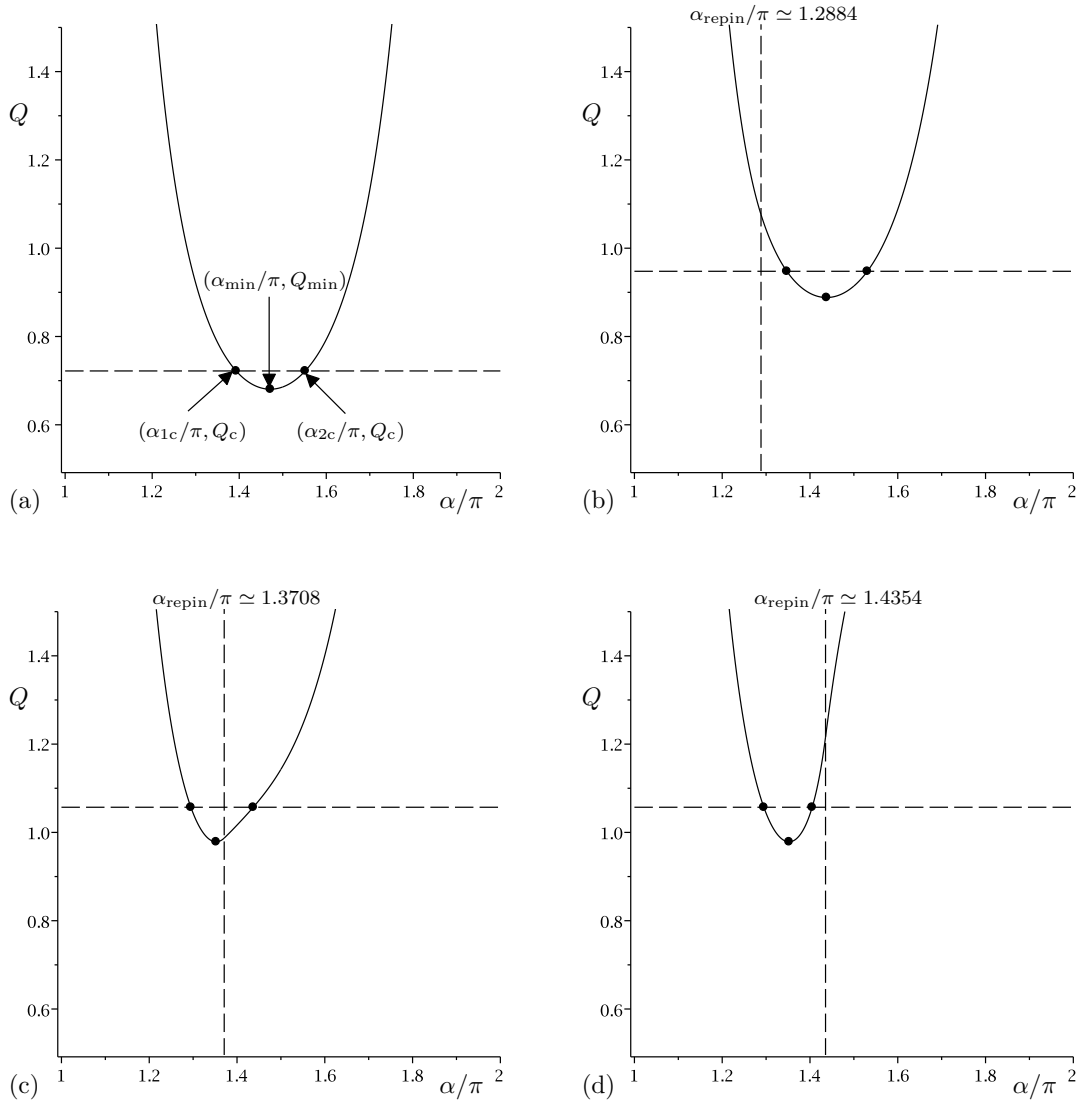

Figure 5.16: Plots of Q given by (5.22) as a function of α/π when $\tau = 1$ showing the endpoints of any region of backflow for (a) $\bar{a} = 3$, (b) $\bar{a} = 4$, (c) $\bar{a} = 5$, and (d) $\bar{a} = 7$. The horizontal dashed lines indicate the values $Q_{\rm c}$ and the vertical dashed lines indicate the values $\alpha_{\rm repin}/\pi$.

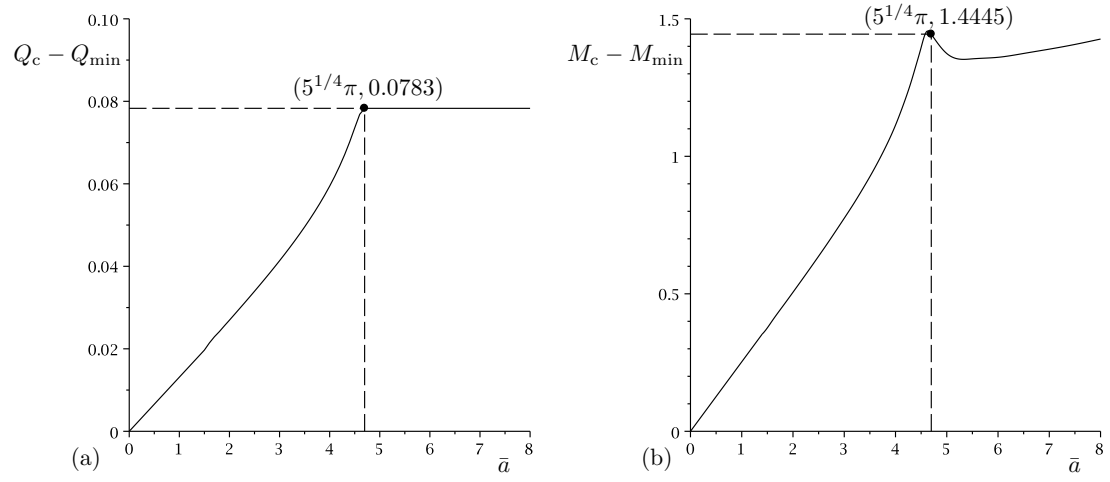

Figure 5.17: The differences between (a) the critical flux and the minimum flux below which backflow is not possible, $Q_c - Q_{min}$, and (b) the critical mass and the minimum mass below which backflow is not possible, $M_c - M_{min}$, plotted as functions of $\bar{a}$ when $\tau = 1$.

in the critical solution.

Figure 5.18(a) shows the scaled endpoints of the region of backflow in the critical case, α_{1c}/π and α_{2c}/π, plotted as functions of $\bar{a}$, together with the scaled position of the corner in the critical solution, $\hat{\alpha}_c/\pi$, and, in particular, shows that the corner always lies between the endpoints. In the limit of a very narrow ring, $\bar{a} \to 0^+$, the endpoints are equal distance from the station $\alpha/\pi = 3/2$, one on the lower half, namely $\alpha_{1c}/\pi \to 1 + \sin^{-1}(18/7\sqrt{7})/\pi^- \simeq 1.4244^-$ as $\bar{a} \to 0^+$, and one on the upper half, namely $\alpha_{2c}/\pi \to 2 - \sin^{-1}(18/7\sqrt{7})/\pi^- \simeq 1.5756^-$ as $\bar{a} \to 0^+$. Both α_{1c} and α_{2c} are monotonically decreasing functions of $\bar{a}$ from $\bar{a} = 0$ to $\bar{a} = 5^{1/4}\pi \simeq 4.6978$ and $\bar{a} \simeq 5.7937$, respectively. When $\bar{a} \geq 5^{1/4}\pi$ the lower endpoint remains constant at $\alpha_{1c}/\pi \simeq 1.2949$, and when $\bar{a} > 5.7937$ the upper endpoint remains constant at $\alpha_{2c}/\pi \simeq 1.4050$.

Figure 5.18(b) shows the footprint of the region of backflow in the α/π–y plane (i.e. the curves $y = \pm b(\alpha)$ given by (5.20)) in the critical case for a range of values of $\bar{a}$. Figure 5.18(b) also shows the curves $y = \pm\hat{b}_c$, where $\hat{b}_c = b_c(\hat{\alpha}_c)$, on which the region of backflow has maximum width. In particular, Figure 5.18(b) shows

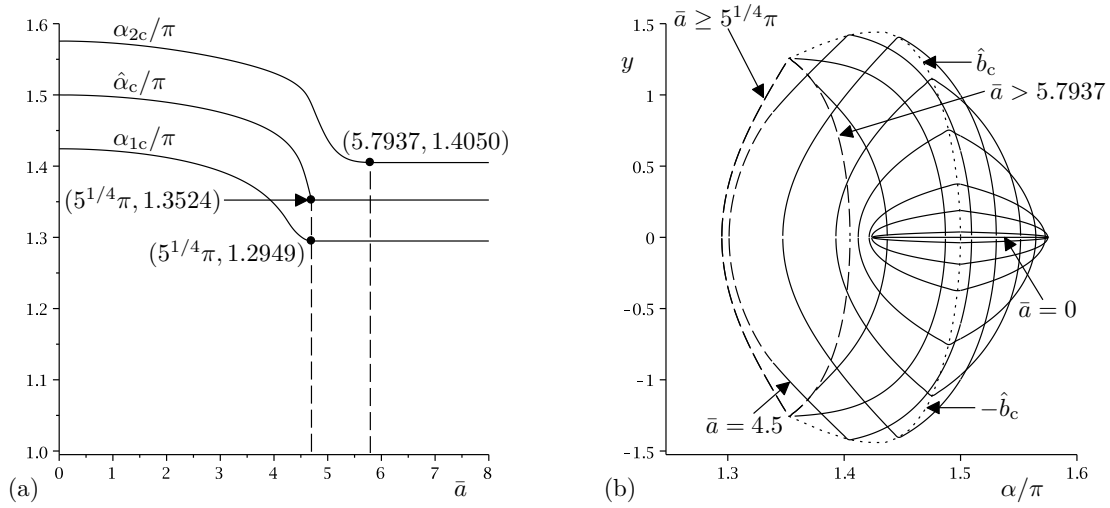

Figure 5.18: (a) The scaled endpoints of the region of backflow in the critical case, α_{1c}/π and α_{2c}/π, plotted as functions of $\bar{a}$ when $\tau = 1$ together with the scaled position of the corner in the critical solution, $\hat{\alpha}_c/\pi$. (b) The footprint of the region of backflow in the α/π–y plane (i.e. the curves $y = \pm b$ given by (5.20)) in the critical case when $\tau = 1$ for $\bar{a} = 0, 0.1, 0.5, 1, 2, 3, 4, 4.5, 5^{1/4}\pi \simeq 4.6978, 5$ and for $\bar{a} > 5.7937$, together with the dotted curves $y = \pm\hat{b}_c$, where $\hat{b}_c = b_c(\hat{\alpha}_c)$, on which the region of backflow has maximum width. The solid curves indicate regions of backflow where the contact lines are pinned (i.e. $a = \bar{a}$ and $\beta_c = \beta_c(\alpha)\,(> 0)$) and the dashed curves indicate regions where the contact lines are de-pinned (i.e. $\beta_c = \bar{\beta}_c = 0$ and $a = \pi/m$).

that in the limit of a very narrow ring, $\bar{a} \to 0^+$, the region of backflow also becomes narrow but approaches a constant width in the α/π direction, eventually becoming a line of length 0.1512 from $\alpha/\pi \simeq 1.4244$ to $\alpha/\pi \simeq 1.5756$ when $\bar{a} = 0$ (for which there is, of course, no full-ring solution). When $\bar{a} \geq 5^{1/4}\pi$ the "lower" part of the region of backflow occupying $\alpha_{1c} \leq \alpha \leq \hat{\alpha}_c$ is constant, and when $\bar{a} \geq 5.7937$ the "upper" part of the region of backflow occupying $\hat{\alpha}_c \leq \alpha \leq \alpha_{2c}$ is also constant. When $\bar{a} < 5^{1/4}\pi$ the entire region of backflow occurs in the pinned interval lines, when $5^{1/4}\pi < \bar{a} < 5.7937$ the region of backflow occurs partly in each of the pinned and de-pinned intervals, and when $\bar{a} > 5.7937$ the entire constant region of backflow occurs in the de-pinned interval.

5.5 Conclusions

In this Chapter we considered the steady flow of a three-dimensional thin, slowly varying ring of fluid with (when not de-pinned with zero contact angle but variable width) constant width but variable contact angle on either the outside or the inside of a large stationary horizontal cylinder subject to a uniform azimuthal surface shear stress. In particular, we studied full-ring solutions corresponding to a ring of continuous, finite and non-zero thickness that extends all the way round the cylinder, and found that the presence of shear is required for such solutions to exist. Analogously to the related problem of a full ring with constant non-zero contact angle but variable width (i.e. de-pinned contact lines) on a rotating horizontal cylinder in the absence of shear, studied by Leslie, Wilson and Duffy [48], in the present problem there is a critical solution corresponding to a maximum mass of fluid, $M = M_c$, above which no full-ring solution exists for a given shear stress τ.

In Section 5.1 we showed that a narrow ring of constant semi-width $\bar{a} < \pi$

can flow all the way round the cylinder with pinned contact lines but that for a wide ring with $\bar{a} > \pi$, de-pinning of the contact lines is unavoidable for a full-ring solution to exist. We assumed that the contact lines de-pin at some station $\alpha = \alpha_{\rm depin}$ and subsequently re-pin at some station $\alpha = \alpha_{\rm repin}$ on the lower half of the cylinder, corresponding to the locations at which the contact angle β is zero, and that between these two points the ring flows with zero contact angle $\beta = \bar{\beta} = 0$ but variable semi-width $a = \pi/m$, according to the solution for a perfectly wetting fluid given by (5.3).

In Section 5.2 we described the behaviour of the critical ring solution with $M = M_{\rm c}$ and, in particular, we showed that the critical ring profile, $h_{\rm c}$, has a corner in the free surface and further, this corner always occurs on the lower half of the cylinder on the side in which the shear stress opposes gravity. For a ring of semi-width $\bar{a} < 5^{1/4}\pi \simeq 4.6978$ the corner occurs in the pinned interval, but for $\bar{a} > 5^{1/4}\pi$ the corner occurs in the de-pinned interval. The critical flux $Q_{\rm c}$ is an increasing function of $\bar{a}$ for $\bar{a} < 5^{1/4}\pi$ but constant for $\bar{a} > 5^{1/4}\pi$ (i.e. independent of $\bar{a}$), whereas the critical mass $M_{\rm c}$ is an increasing function of $\bar{a}$ for all $\bar{a}$. In the pinned interval, the critical contact angle $\beta_{\rm c}$ and the critical maximum thickness $h_{\rm mc}$ are decreasing functions of $\bar{a}$, but in the de-pinned interval $\beta_{\rm c} = 0$ and $h_{\rm mc}$ is independent of $\bar{a}$. For a very narrow ring, $\bar{a} \to 0^+$, $\beta_{\rm c}$ becomes large but $h_{\rm mc}$ remains finite, while the location of the corner $\hat{\alpha}_{\rm c}$ approaches the middle of the cylinder. Three-dimensional plots of $h_{\rm c}$ are shown in Figure 5.7 for various values of $\bar{a}$.

In Section 5.3 we described the behaviour of the sub-critical ring solution when $M < M_{\rm c}$ in the three cases $\bar{a} < \pi$, $\pi < \bar{a} < 5^{1/4}\pi$ and $\bar{a} > 5^{1/4}\pi$. The contact angle β in the pinned interval is an increasing function of the mass M, while the maximum thickness $h_{\rm m}$ is an increasing function of the mass M everywhere on the cylinder. In the limit of small mass, $M \to 0^+$, the contact angle in the pinned

interval becomes small (while, of course, the contact angle in the de-pinned interval is zero), and the volume flux Q also becomes small.

In Section 5.4 we showed that there is a region in the $\bar{a}$–M parameter plane (specifically, when the mass is close to its critical value $M_{\rm c}$) in which backflow (that is, flow in the direction opposite to the surface shear stress) occurs, in a region adjacent to the substrate, and on the side of the cylinder in which the shear stress opposes gravity. As $\bar{a}$ increases from zero, this region of backflow moves downwards from the middle of the cylinder into the lower half of the cylinder and is constant for $\bar{a} \geq 5^{1/4}\pi$.

Chapter 6

Conclusions and Future Work

6.1 Conclusions

In this thesis we considered a number of different problems involving ridges (or two-dimensional droplets), rivulets and rings of fluid in the presence of various external airflows.

In Chapter 2 we studied the strongly-coupled interaction between a ridge on a planar substrate inclined to the horizontal and a spatially varying external pressure gradient arising from an external flow of air directed parallel to the substrate. We found that relatively "large" ridges of width comparable to the capillary length can be supported in a steady state only when the substrate is nearly horizontal, whereas relatively "small" ridges of width much less than the capillary length can be supported in a steady state for all values of substrate inclination (including a vertical substrate).

We focused mainly on a "large" sessile ridge and studied its quasi-static evolution as the airflow is gradually strengthened. When the contact lines are pinned (i.e. the ridge is of constant width), the ridge thickness becomes thinner near its edges, that is, smaller contact angles, and thicker near its centre as the airflow is

strengthened. This is because the pressure due to the external airflow near the edges (centre) of the ridge is slightly greater (less) than the ambient value far from the ridge, and so the free surface tends to be pushed down (pulled up) here. There is a maximum airflow strength, corresponding to the contact angle at the upslope contact line reaching its minimum physically realisable value of zero, beyond which no steady ridge profile exists. In reality, a contact line will de-pin when the contact angle reaches the receding angle, and it was found that the upslope contact angle always reaches this value before the downslope one does. Hence we studied the case when the ridge is de-pinned at its upslope contact line, and found that it becomes narrower and deeper as the strength of the external airflow is increased. In this case, we assumed that the upslope contact angle remains constant at the receding angle as the airflow is strengthened, and found that the downslope contact angle also remains constant, and so remains pinned.

We also studied the quasi-static evolution of the ridge as the substrate is gradually tilted. When the contact lines are pinned, the ridge becomes skewed downslope with smaller (larger) upslope (downslope) contact angle, and larger maximum thickness. In this case it is possible for either the downslope or the upslope contact line to de-pin first. When only the downslope contact line de-pins the ridge becomes wider and shallower, and there is a maximum value of the inclination of the substrate beyond which no steady solutions exist; however, when only the upslope contact line de-pins the ridge becomes narrower and deeper. In the general case in which both contact lines de-pin, irrespective of which contact line de-pins first there is a single value of the inclination of the substrate at which the other contact line subsequently de-pins, and beyond which no steady solutions exist.

In Chapters 3, 4 and 5 we studied the steady, locally unidirectional flow in the azimuthal direction of a rivulet or a ring on a large stationary horizontal cylinder and, in particular, in Chapters 4 and 5 we studied the effects of a prescribed (rather

than coupled, as in Chapter 2) uniform azimuthal surface shear stress due to an external airflow.

In Chapter 3 we considered a gravity-driven rivulet with prescribed volume flux as it flows from the top to the bottom of the cylinder in both the case of constant width but variable contact angle (i.e. pinned contact lines) and constant non-zero contact angle but variable width (i.e. de-pinned contact lines). We found that while a rivulet with de-pinned contact lines can flow all the way from the top to the bottom of the cylinder, a rivulet with pinned contact lines may do likewise only when it is sufficiently "narrow"; however, when it is sufficiently "wide", the contact angle reaches its minimum physically realisable value of zero at some location on the lower half of the cylinder. We then discussed a possible scenario in which the contact lines de-pin at this location, and the rivulet flows to the bottom of the cylinder with zero contact angle and slowly decreasing width.

For a rivulet with constant non-zero contact angle, we found that if the contact lines pin (which may occur on either the upper or the lower half of the cylinder) at a sufficiently narrow (wide) width then they will subsequently de-pin with non-zero (zero) contact angle on the lower half of the cylinder, and the rivulet will flow to the bottom of the cylinder with constant non-zero (zero) contact angle but slowly increasing (decreasing) width.

For a rivulet with constant width, we found that if it is sufficiently narrow the contact lines may de-pin on either the upper or lower half of the cylinder, and then re-pin on the lower half; however, a sufficiently wide rivulet will de-pin on the upper half of the cylinder and remain de-pinned all the way to the bottom. In addition, we found that the mass of a rivulet with constant width is an increasing function of the width.

In Chapter 4 we considered a rivulet with prescribed volume flux as it flows from the top to the bottom of a large horizontal cylinder subject to a prescribed

uniform azimuthal surface shear stress that acts in opposition to gravity. Unlike in the case of no surface shear in Chapter 3, we found that a rivulet with de-pinned contact lines cannot flow all the way from the top to the bottom of the cylinder when shear is present; rather, the width becomes infinite at some station on the upper half of the cylinder. We then discussed the possible scenario of an infinitely wide two-dimensional film of uniform thickness on the upper part of the cylinder that breaks into a single rivulet with prescribed flux that flows to the bottom with de-pinned contact lines.

As in the case of no surface shear discussed in Chapter 3, when shear is present a rivulet with pinned contact lines can flow all the way from the top to the bottom of the cylinder only when it is sufficiently narrow, and the contact angle of a sufficiently wide rivulet will reach its minimum physically realisable value of zero at some station on the lower half of the cylinder; in fact, this station is found to be independent of the value of the surface shear stress.

In Chapter 5 we studied a ring of fluid with pinned contact lines on a horizontal cylinder subject to a prescribed uniform azimuthal surface shear stress. In particular, we found that, analogously to the flow of a rivulet on one side of a cylinder studied in Chapters 3 and 4, while a sufficiently narrow ring can flow all the way round the cylinder (a "full ring") with pinned contact lines, the contact lines of a sufficiently wide ring de-pin with zero contact angle on the lower half of one side of the cylinder and then subsequently re-pin on the lower half of the opposite side of the cylinder for a full ring to exist.

For a prescribed surface shear stress, there is a maximum mass of fluid that can be supported against gravity for a full ring to exist. Alternatively, for a prescribed mass of fluid, there is a minimum surface shear stress required for a full ring to exist; however, we focused only on the case of prescribed shear. In the critical case of maximum mass, there is a corner in the free surface of the ring which

occurs on the side of the cylinder in which the shear opposes gravity. For a very narrow ring, the corner is located close to the middle of the cylinder, and moves downwards towards the bottom of the cylinder as the width is increased. The corner in a sufficiently narrow ring occurs in the interval where the contact lines are pinned (referred to as "the pinned interval"), while it occurs in the interval where the contact lines are de-pinned (referred to as "the de-pinned interval"), for a sufficiently wide ring, and the ring becomes deeper at all stations on the cylinder as the width is increased in the critical case.

In the sub-critical case in which the mass is less than its maximum value, the contact angle increases everywhere in the pinned interval, while the maximum thickness increases at all stations on the cylinder, as the mass increases. We also found that backflow may occur in a region adjacent to the substrate on the side of the cylinder in which the shear stress opposes gravity when the mass is close to its maximum value. This region is close to the middle of the cylinder in the pinned interval for a narrow ring, moves downwards as the width increases until the region is completely in the de-pinned interval, after which the region is constant as the width is further increased.

6.2 Future Work

There are many directions in which aspects of the work presented in this thesis could be extended.

In Chapter 2 we studied a ridge that is subject to an external pressure gradient arising from an external airflow. We assumed that the airflow was inviscid and so the obvious extension to this work would be to remove this simplifying assumption and include the effects of a prescribed shear stress arising from the external airflow at the air-fluid interface. Another natural extension would be to consider a three-

dimensional droplet that interacts with an external airflow. One motivation for this work was to aid understanding of the phenomenon of so-called rain-wind–induced vibrations (RWIV) mentioned in Section 1.1 and, while the interaction between the pressure gradient arising from the airflow and the fluid is thought to be significant, the shear stress arising from the airflow also plays an important role. With this application in mind, extending the present work to consider a ridge on a curved (rather than a planar) substrate would provide a more realistic model for flow on a cable.

Given that the cables are typically inclined to the horizontal in RWIV, there is usually a gravity-driven flow in the longitudinal direction, and so a gravity-driven rivulet flowing down an inclined substrate that interacts with the pressure gradient arising from an external airflow in the direction transverse to that of the flow could be considered. In such a situation, if the effects of surface tension are also included then a similar analysis to that in Chapter 2 yields the dimensionless governing equation for the free surface $h = h(y)$ of the rivulet (analogous to equation (2.10) in Chapter 2 for a ridge), namely

$$h''' - h' \cos\alpha + \Lambda \frac{\mathrm{d}}{\mathrm{d}y} \fint_{-a}^{a} \frac{h'(\xi)}{y - \xi} \, \mathrm{d}\xi = 0, \tag{6.1}$$

where a is the semi-width of the rivulet, α is the angle of inclination of the substrate to the horizontal and Λ is a measure of the strength of the external airflow, again given by equation (2.11) in Chapter 2. This must be solved subject to the contact line conditions $h(\pm a) = 0$, $h(\pm a) = \mp\beta \, (\geq 0)$, where β is the contact angle, and the condition of prescribed volume flux $Q = \bar{Q}$, where

$$Q = \frac{\sin\alpha}{3} \int_{-a}^{a} h^3 \, \mathrm{d}y. \tag{6.2}$$

In the special case of no external airflow, $\Lambda = 0$, the free surface profile h_0 and volume flux Q are given by equations (3.1) and (3.3) in Chapter 3, respectively, with $a = a_0$ and $\beta = \beta_0$. In the limit of a weak airflow, $\Lambda \to 0^+$, we pose the

expansions $h = h_0+\Lambda h_1+O(\Lambda^2)$, $a = a_0+\Lambda a_1+O(\Lambda^2)$ and $\beta = \beta_0+\Lambda\beta_1+O(\Lambda^2)$. In the special case of a vertical substrate (i.e. at $\alpha = \pi/2$) the equation and boundary conditions for h_1 are

$$h_1''' = \frac{\beta_0}{a_0}\frac{\mathrm{d}}{\mathrm{d}y}\int_{-a_0}^{a_0}\frac{\xi}{y-\xi}\,\mathrm{d}\xi, \tag{6.3}$$

$$h_1(a_0) = a_1\beta_0, \quad h_1'(0) = 0, \quad h_1'(a_0) = \frac{a_1\beta_0}{a_0} - \beta_1, \tag{6.4}$$

and whose solution is given by

$$\begin{aligned} h_1(y) = {} & \frac{\beta_0}{6a_0}\left[(a_0-y)^3\ln(a_0-y) + (a_0+y)^3\ln(a_0+y)\right] \\ & - \frac{\beta_0}{2}\left[(a_0-y)^2\ln(a_0-y) + (a_0+y)^2\ln(a_0+y)\right] \\ & + \frac{2a_0^2\beta_0}{3}\ln(2a_0) + \frac{1}{6a_0^2}\left(3a_0\beta_1 - 3a_1\beta_0 - a_0^2\beta_0\right)\left(a_0^2-y^2\right) + a_1\beta_0. \end{aligned} \tag{6.5}$$

In practice, either the contact angle or the width may be constant as Λ varies. In the case of constant contact angle $\beta = \beta_0$ we obtain $a_1 = -293a_0^2/720$ and in the case of constant semi-width $a = a_0$ we obtain $\beta_1 = -293\beta_0 a_0/540$, showing that, as in the case of a ridge in Chapter 2, increasing the strength of the external airflow has the effect of decreasing the width or decreasing the contact angle. We use the solution for a rivulet in the limit of a weak airflow, $\Lambda \to 0^+$, to plot examples of free surface profiles for (a) constant contact angle $\beta = \beta_0$ and (b) constant semi-width $a = a_0$, for various values of Λ when $\alpha = \pi/2$, shown in Figure 6.1. Specifically, Figure 6.1 shows that the maximum thickness increases as Λ is increased from zero for both the case $\beta = \beta_0$ and the case $a = a_0$. A complete description of the behaviour of the rivulet for all values of Λ and for different values of substrate inclination would be a useful extension to the present work.

In Chapters 3, 4 and 5 we considered steady rivulet flow on a large stationary horizontal cylinder. This could be extended to consider flow on non-cylindrical substrates. In particular, in Chapter 3 we considered gravity-driven rivulets with pinned contact lines that de-pin at both zero and non-zero contact angles. In

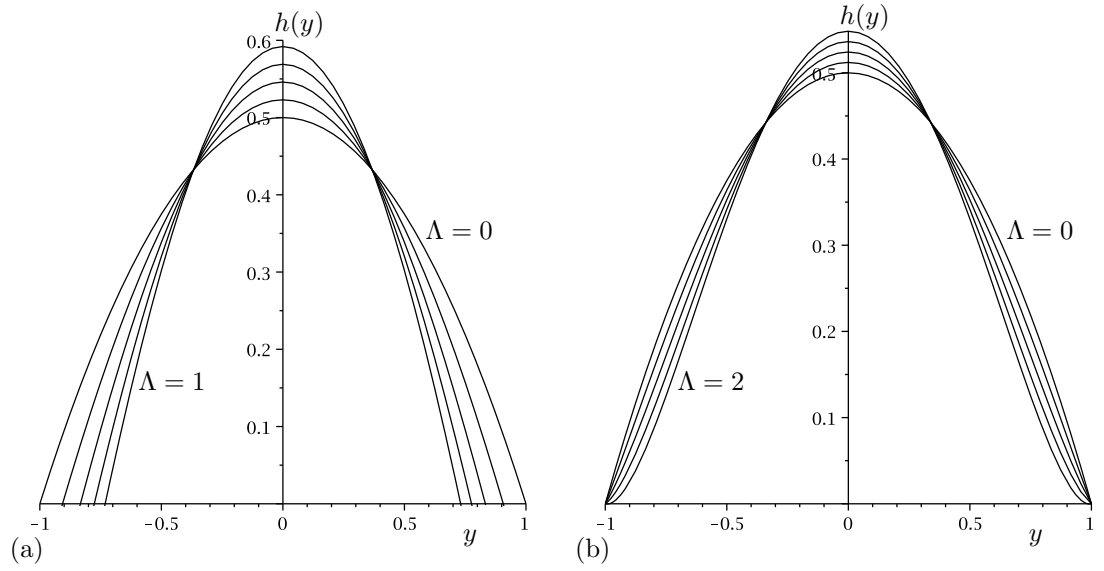

Figure 6.1: First-order-accurate cross-sectional profiles of a rivulet subject to an external airflow in the limit of a weak airflow, $\Lambda \to 0^+$, $h(y) = h_0(y) + \Lambda h_1(y)$ when $\Lambda = 0$, 0.5, 1, 1.5, 2 at $\alpha = \pi/2$, and (a) $a = a_0 + \Lambda a_1$, $a_1 = -293a_0^2/720$, $\beta = \beta_0 = 1$ and (b) $\beta = \beta_0 + \Lambda\beta_1$, $\beta_1 = -293\beta_0 a_0/540$, $a = a_0 = 1$.

Chapters 4 and 5 we extended this work to include an azimuthal surface shear stress, but only for a zero de-pinning contact angle, and so an obvious extension would be to consider a non-zero de-pinning (and re-pinning in the case of a full ring) contact angle (i.e. $\beta = \bar{\beta} > 0$). The behaviour of a wide ring with pinned contact lines, $\bar{a} > \pi$, and a non-zero de-pinning and re-pinning contact angle, $\bar{\beta} > 0$, is illustrated in Figure 6.2, which shows plots of the contact angle β, the semi-width a, and the maximum thickness h_m as functions of the scaled angle α/π for a range of values of $M \leq M_\mathrm{c} \simeq 23.2019$, together with a three-dimensional plot of the critical ring profile h_c, all when $\tau = 1$, $\bar{a} = 4\,(> \pi)$ and $\bar{\beta} = 0.2$. A complete description of this problem would be of interest. In Chapters 3 and 4 we considered both the case of constant contact angle and of constant width; however, in Chapter 5 we considered only the case of constant width and so the problem of a ring with constant contact angle subject to an azimuthal shear stress is a possible extension. Unlike for a full ring with constant width $a = \bar{a}$ described

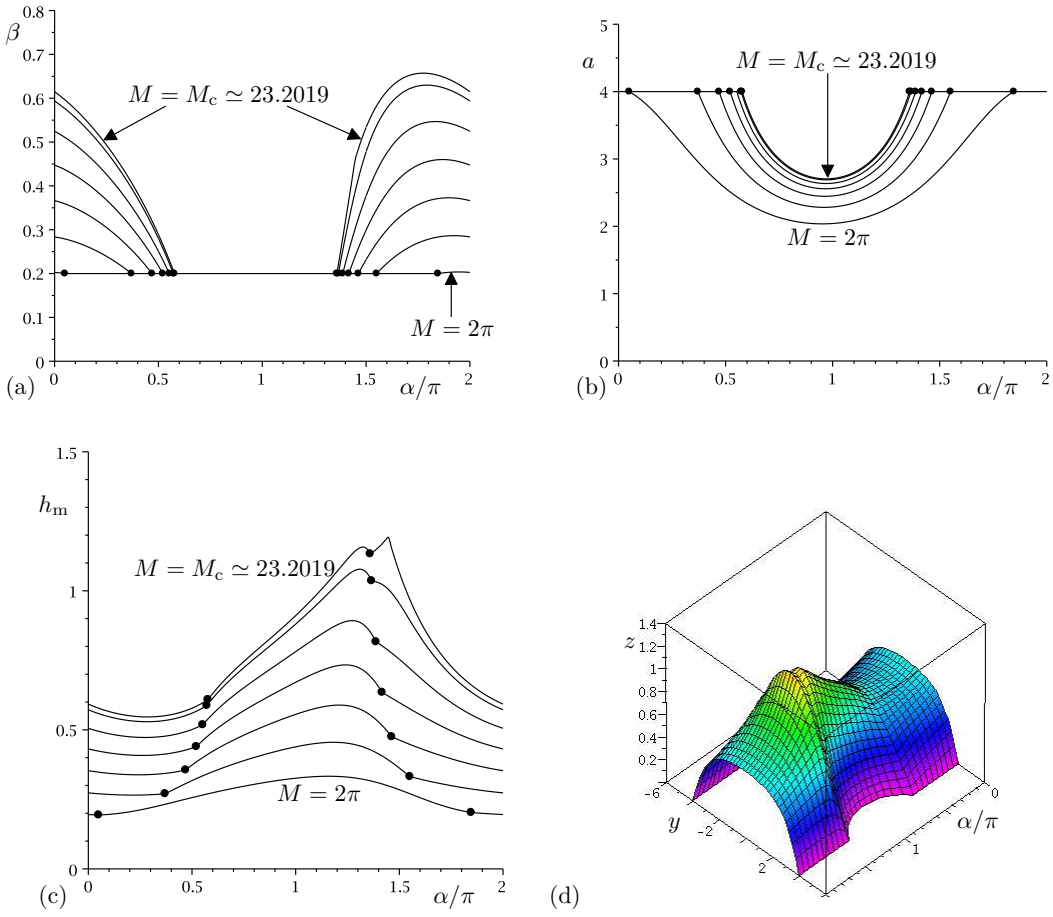

Figure 6.2: A ring with constant semi-width $a = \bar{a} > \pi$ on a horizontal cylinder subject to an azimuthal shear stress τ, whose contact lines de-pin and re-pin at a non-zero contact angle $\beta = \bar{\beta} > 0$; specifically, plots of (a) the contact angle β, (b) the semi-width a and (c) the maximum thickness $h_{\rm m}$ as functions of the scaled angle α/π for $M = 2\pi, 3\pi, ..., 7\pi, M_{\rm c} \simeq 23.2019$, and (d) a three-dimensional plot of the critical ring profile $h_{\rm c}$ as a function of y and α/π, all when $\tau = 1$, $\bar{a} = 4\,(> \pi)$ and $\bar{\beta} = 0.2$. The dots in parts (a)–(c) indicate the values $\alpha_{\rm depin}/\pi$ and $\alpha_{\rm repin}/\pi$.

in Chapter 5, we find that the azimuthal surface shear stress τ cannot be scaled out of the problem in the case of a full ring with constant non-zero contact angle $\beta = \bar{\beta} > 0$. The behaviour of a full ring in the critical case for $\beta = \bar{\beta} > 0$ is illustrated in Figure 6.3, which shows plots of the critical semi-width a_{c} and the critical maximum thickness h_{mc} as functions of the scaled angle α/π, together with three-dimensional plots of the critical ring profile h_{c}, all for a range of values of the shear stress τ when $M = M_{\mathrm{c}}$ and $\bar{\beta} = 1$. A complete description of this problem would be of interest. It would also be useful to consider the case when both the contact angle and the width vary as the rivulet flows round the cylinder.

The present work on a ring could be combined with the work of Leslie, Wilson and Duffy [48] to describe a ring on a rotating horizontal cylinder subject to an azimuthal surface shear stress, thus extending the work by Villegas-Diaz, Power and Riley [103, 104] on two-dimensional film flow to three dimensions. We could also extend the work on rivulets on cylinders to include the pressure gradient that arises from an external airflow, a uniform transverse shear stress as considered by Sullivan et al. [90] in the case of a rivulet on a vertical substrate, or even a non-uniform shear stress as considered by Saber and El-Genk [80] for a two-dimensional film. In Chapter 4 we considered a film that breaks into a single rivulet as it flows round a cylinder, but it would also be useful to consider a film that breaks into more than one rivulet. This is of relevance to falling-film flow found in evaporators and condensers as discussed in Subsection 1.4.3; the inclusion of non-isothermal effects (as studied by, for example, Leslie, Wilson and Duffy [47]) together with an external airflow would be useful with this application in mind.

In addition, other extensions to all of the work in this thesis that would be of interest would be to include inertial terms in the analysis which may be important for some applications, to consider unsteady solutions, to consider the stability of steady flows, and also to carry out experimental investigations to validate the

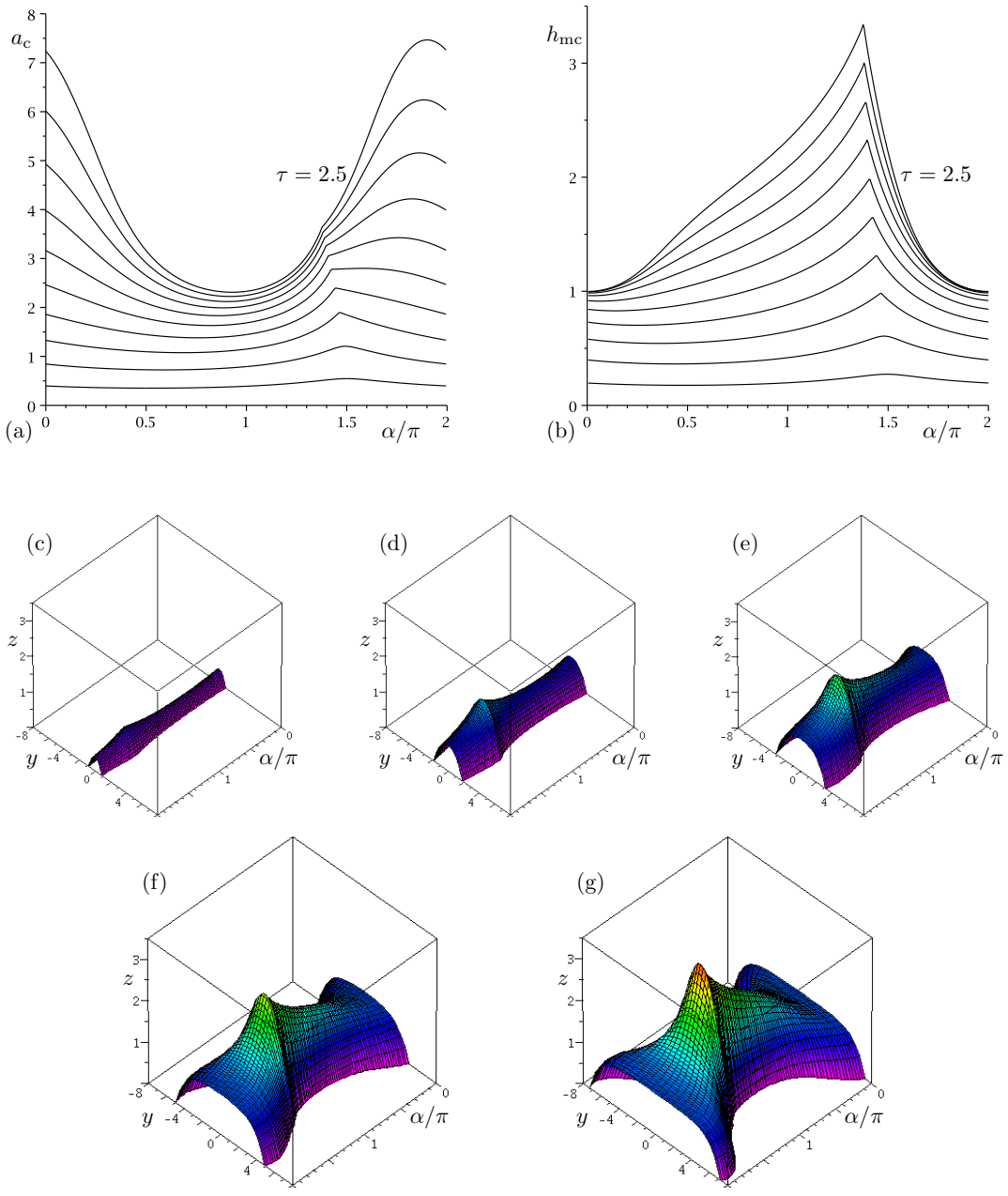

Figure 6.3: A ring with constant non-zero contact angle $\beta = \bar{\beta} > 0$ on a horizontal cylinder subject to an azimuthal shear stress τ and, in particular, in the critical case of maximum mass; specifically, plots of (a) the critical semi-width a_c and (b) the critical maximum thickness h_{mc} as functions of the scaled angle α/π for $\tau = 0.25, 0.5, ...2.5$, and (c)–(g) three-dimensional plots of the critical ring profile h_c as functions of y and α/π for (c) $\tau = 0.5$, (d) $\tau = 1$, (e) $\tau = 1.5$, (f) $\tau = 2$, (g) $\tau = 2.5$, all when $M = M_c$ and $\beta = \bar{\beta} = 1$.

analysis.

In Chapter 1 we described how thin-film flow in the presence of an external airflow continues to attract much theoretical and experimental research because of the occurrence of such flows in both nature and industry. I believe that this thesis provides a useful addition to the substantial body of work already available in this area; however, there are, of course, many open problems that remain to be considered.

Appendix A

Numerical Method used in Chapter 2

In this Appendix we outline the numerical method used to solve (2.10) subject to (2.9) in Chapter 2. We first map the ridge from the interval $x \in [0, L]$ onto the interval $x \in [0, 1]$, which is then divided into n equally spaced subintervals $[x_i, x_{i+1}]$, where $x_i = i/n$, $0 \leq i \leq n-1$. We adopt a method similar to that used by Tseluiko et al. [97] and use central differences to approximate $h'''(x)$, $h'(x)$ and the derivative of the integral term; the integral itself is approximated as half the sum of the integrals in each double subinterval $[\xi_{j-1}, \xi_{j+1}]$ for $1 \leq j \leq n-1$. Hence the term

$$\frac{\mathrm{d}}{\mathrm{d}x}\int_0^1 \frac{h'(\xi)}{x-\xi}\,\mathrm{d}\xi \tag{A.1}$$

is discretised and approximated by

$$
\begin{aligned}
& n\left(\fint_0^1 \frac{h'(\xi)}{x_{i+\frac{1}{2}}-\xi}\,\mathrm{d}\xi - \fint_0^1 \frac{h'(\xi)}{x_{i-\frac{1}{2}}-\xi}\,\mathrm{d}\xi\right) \\
= \;& \frac{n^2}{4}\sum_{j=1}^{n-1}(h_{j+1}-h_{j-1})\left(\int_{\xi_{j-1}}^{\xi_{j+1}} \frac{\mathrm{d}\xi}{x_{i+\frac{1}{2}}-\xi} - \int_{\xi_{j-1}}^{\xi_{j+1}} \frac{\mathrm{d}\xi}{x_{i-\frac{1}{2}}-\xi}\right) \\
+ \;& \frac{n^2 h_1}{2}\left(\int_{\xi_0}^{\xi_1} \frac{\mathrm{d}\xi}{x_{i+\frac{1}{2}}-\xi} - \int_{\xi_0}^{\xi_1} \frac{\mathrm{d}\xi}{x_{i-\frac{1}{2}}-\xi}\right) \\
- \;& \frac{n^2 h_{n-1}}{2}\left(\int_{\xi_{n-1}}^{\xi_n} \frac{\mathrm{d}\xi}{x_{i+\frac{1}{2}}-\xi} - \int_{\xi_{n-1}}^{\xi_n} \frac{\mathrm{d}\xi}{x_{i-\frac{1}{2}}-\xi}\right) \\
= \;& \frac{n^2}{4}\sum_{j=1}^{n-1}(h_{j+1}-h_{j-1})\ln\left|\frac{(2i-2j+3)\,(2i-2j-3)}{(2i-2j-1)\,(2i-2j+1)}\right| \\
+ \;& \frac{n^2 h_1}{2}\ln\left|\frac{(2i-3)\,(2i+1)}{(2i-1)^2}\right| \\
+ \;& \frac{n^2 h_{n-1}}{2}\ln\left|\frac{(2i-2n-1)\,(2i-2n+3)}{(2i-2n+1)^2}\right|,
\end{aligned}
\tag{A.2}
$$

where

$$
\delta x = x_{i+1}-x_i, \quad n=\frac{1}{\delta x}, \quad x_{i\pm\frac{1}{2}}=\frac{i\pm\frac{1}{2}}{n}, \quad \xi_{j\pm1}=\frac{j\pm1}{n}, \quad h_j=h(\xi_j), \tag{A.3}
$$

and $h_0 = h_n = 0$ from the boundary conditions. Then, rather than specifying the volume condition directly, we specify either θ_1 or θ_2 to give an expression for either h_1 or h_{n-1}, respectively. This yields a system of $(n-2)\times(n-2)$ linear equations for the ridge profile h_i at each node x_i, which is solved using the mathematical software package MAPLE. This is done iteratively, specifically the value of the specified angle is altered until the volume condition (2.9) is satisfied to within a prescribed tolerance (typically 10^{-6}). The numerical results show good agreement when checked against the transverse force balance (2.16) and the asymptotic results derived in Chapter 2.

Appendix B

Further Asymptotics in the Case of a Critical Ring

In this Appendix we describe the behaviour of the critical full ring at the stations shown in Figure 5.6 in Chapter 5 in the limits of a very narrow ring, $\bar{a} \to 0^+$, and a very wide ring, $\bar{a} \to \infty$.

At the top of the cylinder $\alpha = 0$ the contact angle becomes large and the maximum thickness remains finite according to

$$\beta_{\rm c} \sim \frac{7\tau}{3\sqrt{3}\bar{a}} \to \infty \quad \text{and} \quad h_{\rm mc} \to \frac{7\tau^-}{6\sqrt{3}} \simeq 0.6736\tau^- \tag{B.1}$$

as $\bar{a} \to 0^+$, and the ring becomes slender according to

$$\beta_{\rm c} \sim \frac{3\tau}{5^{3/8}}\sqrt{\frac{\pi}{8\bar{a}}} \to 0^+ \quad \text{and} \quad h_{\rm mc} \sim \beta_{\rm c} \to 0^+ \tag{B.2}$$

as $\bar{a} \to \infty$. At $\alpha = \pi/2$ the contact angle becomes large and the maximum thickness remains finite according to

$$\beta_{\rm c} \sim \frac{7\tau}{6\bar{a}} \to \infty \quad \text{and} \quad h_{\rm mc} \to \frac{7\tau}{12} \simeq 0.5833\tau \tag{B.3}$$

as $\bar{a} \to 0^+$, and the ring becomes slender according to

$$\beta_{\rm c} \sim \frac{3\tau}{5^{3/8}4}\sqrt{\frac{15\pi}{\bar{a}^3}} \to 0^+ \quad \text{and} \quad h_{\rm mc} \sim \frac{3\tau}{5^{3/8}8}\sqrt{\frac{15\pi}{\bar{a}}} \to 0^+ \tag{B.4}$$

as $\bar{a} \to \infty$. At the bottom of the cylinder $\alpha = \pi$ the contact angle becomes large and the maximum thickness remains finite according to

$$\beta_{\rm c} \sim \frac{7\tau}{3\sqrt{3}\bar{a}} \to \infty \quad \text{and} \quad h_{\rm mc} \to \frac{7\tau^+}{6\sqrt{3}} \simeq 0.6736\tau^+ \tag{B.5}$$

as $\bar{a} \to 0^+$, and the contact angle is identically zero, $\beta_{\rm c} \equiv 0$, and the maximum thickness remains finite according to

$$h_{\rm mc} = \frac{\sqrt{3}\tau}{5^{3/8}} \simeq 0.9472\tau \tag{B.6}$$

when $\bar{a} \geq 5^{1/4}\pi$. At $\alpha = 3\pi/2$ the the contact angle becomes large and the maximum thickness remains finite according to

$$\beta_{\rm c} \sim \frac{7\tau}{3\bar{a}} \to \infty \quad \text{and} \quad h_{\rm mc} \to \frac{7\tau^-}{6} \simeq 1.1667\tau^- \tag{B.7}$$

as $\bar{a} \to 0^+$, and the ring becomes slender according to (B.4) as $\bar{a} \to \infty$.

Bibliography

[1] D. J. Acheson. *Elementary Fluid Dynamics*. Oxford University Press, 1990.

[2] S. V. Alekseenko, A. V. Bobylev, V. V. Guzanov, D. M. Markovich, and S. M. Kharlamov. Regular waves on vertical falling rivulets at different wetting contact angles. *Thermophys. Aeromech.*, 17:345–357, 2010.

[3] S. V. Alekseenko, P. I. Geshev, and P. A. Kuibin. Free-boundary fluid flow on an inclined cylinder. *Physics Doklady*, 42:269–272, 1997.

[4] R. F. Allen and C. M. Biggin. Longitudinal flow of a lenticular liquid filament down an inclined plane. *Phys. Fluids*, 17:287–291, 1974.

[5] E. S. Benilov. On the stability of shallow rivulets. *J. Fluid Mech.*, 636:455–474, 2009.

[6] M. Bentwich, D. Glasser, J. Kern, and D. Williams. Analysis of rectlinear rivulet flow. *A. I. Ch. E. J.*, 22:772–779, 1976.

[7] B. Birnir, K. Mertens, V. Putkaradze, and P. Vorobieff. Meandering fluid streams in the presence of flow-rate fluctuations. *Phys. Rev. Lett.*, 101:114501, 2008.

[8] B. Birnir, K. Mertens, V. Putkaradze, and P. Vorobieff. Morphology of a stream flowing down an inclined plane. Part 2. Meandering. *J. Fluid Mech.*, 607:401–411, 2008.

[9] T. D. Blake and K. J. Ruschak. *Wetting: Static and dynamic contact lines, Chapter 3 in "Liquid Film Coating", Eds S. F. Kistler and P. M. Schweizer.* Chapman and Hall, 1997.

[10] P.-J. Chen, Y.-T. Tsai, T.-J. Liu, and P.-Y. Wu. Low volume fraction rimming flow in a rotating horizontal cylinder. *Phys. Fluids*, 19:128107, 2007.

[11] R. Chicharro, A. Vazquez, and R. Manasseh. Characterization of patterns in rimming flow. *Exp. Therm. Fluid Sci.*, 35:1184–1192, 2011.

[12] F.-C. Chou and P.-Y. Wu. Effect of air shear on film planarization during spin coating. *J. Electrochem. Soc.*, 147:699–705, 2000.

[13] S. Couvreur and A. Daerr. The role of wetting heterogeneities in the meandering instability of a partial wetting rivulet. *EPL*, 99:24004, 2012.

[14] R. V. Craster and O. K. Matar. Dynamics and stability of thin liquid films. *Rev. Mod. Phys.*, 81:1131–1198, 2009.

[15] J. A. Cuminato, A. D. Fitt, and S. McKee. A review of linear and nonlinear Cauchy singular integral and integro-differential equations arising in mechanics. *J. Int. Eqns Appl.*, 19:163–207, 2007.

[16] J. A. Cuminato, A. D. Fitt, M. J. S. Mphaka, and A. Nagamine. A singular integro-differential equation model for dryout in LMFBR boiler tubes. *IMA J. Appl. Math.*, 75:269–290, 2010.

[17] J. Deans and S. Kucuka. The formation of banded condensate films in weak ammonia-water mixtures. *J. Heat Transf.*, 133:010505, 2011.

[18] P. Dimitrakopoulos. Deformation of a droplet adhering to a solid surface in shear flow: onset of interfacial sliding. *J. Fluid Mech.*, 580:451–466, 2007.

[19] P. Dimitrakopoulos and J. J. L. Higdon. Displacement of fluid droplets from solid surfaces in low-Reynolds-number shear flows. *J. Fluid Mech.*, 336:351–378, 1997.

[20] P. Dimitrakopoulos and J. J. L. Higdon. On the displacement of three-dimensional fluid droplets from solid surfaces in low-Reynolds-number shear flows. *J. Fluid Mech.*, 377:189–222, 1998.

[21] H. Ding, M. N. H. Gilani, and P. D. M. Spelt. Sliding, pinch-off and detachment of a droplet on a wall in shear flow. *J. Fluid Mech.*, 644:217–244, 2010.

[22] H. Ding and P. D. M. Spelt. Onset of motion of a three-dimensional droplet on a wall in shear flow at moderate Reynolds numbers. *J. Fluid Mech.*, 599:341–362, 2008.

[23] B. R. Duffy and H. K. Moffatt. Flow of a viscous trickle on a slowly varying incline. *Chem. Eng. J.*, 60:141–146, 1995.

[24] B. R. Duffy and S. K. Wilson. A rivulet of perfectly wetting fluid with temperatue-dependent viscosity draining down a uniformly heated or cooled slowly varying substrate. *Phys. Fluids*, 15:3236–3239, 2003.

[25] P. A. Durbin. Free-streamline analysis of deformation and dislodging by wind force of drops on a surface. *Phys. Fluids*, 31:43–48, 1988.

[26] P. A. Durbin. On the wind force needed to dislodge a drop adhered to a surface. *J. Fluid Mech.*, 196:205–222, 1988.

[27] M. S. El-Genk and H. H. Saber. Minimum thickness of a flowing down liquid film on a vertical surface. *Int. J. Heat Mass Tran.*, 44:2809–2825, 2001.

[28] M. H. Eres, L. W. Schwartz, and R. V. Roy. Fingering phenomena for driven coating films. *Phys. Fluids*, 12:1278–1295, 2000.

[29] P. L. Evans, L. W. Schwartz, and R. V. Roy. Steady and unsteady solutions for coating flow on a rotating horizontal cylinder: Two-dimensional theoretical and numerical modeling. *Phys. Fluids*, 16:2742–2756, 2004.

[30] P. L. Evans, L. W. Schwartz, and R. V. Roy. Three-dimensional solutions for coating flow on a rotating horizontal cylinder: Theory and experiment. *Phys. Fluids*, 17:072102, 2005.

[31] J. Fan, M. C. T. Wilson, and N. Kapur. Displacement of liquid droplets on a surface by shearing air flow. *J. Colloid Interface Sci.*, 356:286–292, 2011.

[32] Y. Fujita and M. Tsutsui. Experimental investigation of falling film evaporation on horizontal tubes. *Heat Transf. Jpn Res.*, 27:609–618, 1998.

[33] D. E. Hartley and W. Murgatroyd. Criteria for the break-up of thin liquid layers flowing isothermally over solid surfaces. *Int. J. Heat Mass Tran.*, 7:1003–1015, 1964.

[34] L. M. Hocking and M. J. Miksis. Stability of a ridge of fluid. *J. Fluid Mech.*, 247:157–177, 1993.

[35] D. Holland, B. R. Duffy, and S. K. Wilson. Thermocapillary effects on a thin viscous rivulet draining steadily down a uniformly heated or cooled slowly varying substrate. *J. Fluid Mech.*, 441:195–221, 2001.

[36] A. E. Hosoi and L. Mahadevan. Axial instability of a free-surface front in a partially filled horizontal rotating cylinder. *Phys. Fluids*, 11:97–106, 1999.

[37] R. Hunt. The numerical solution of parabolic free boundary problems arising from thin film flows. *J. Comp. Phys.*, 84:377–402, 1989.

[38] R. Hunt. The numerical solution of the thin film flow surrounding a horizontal cylinder resulting from a vertical cylindrical jet. *Int. J. Num. Meth. Fl.*, 14:539–556, 1992.

[39] B. Jin and A. Acrivos. Rimming flows with an axially varying viscosity. *Phys. Fluids*, 16:633–640, 2004.

[40] M. F. G. Johnson, R. A. Schluter, M. J. Miksis, and S. G. Bankhoff. Experimental study of rivulet formation on an inclined plate by fluorescent imaging. *J. Fluid Mech.*, 394:339–354, 1999.

[41] R. E. Johnson. Steady-state coating flows inside a rotating horizontal cylinder. *J. Fluid Mech.*, 190:321–342, 1988.

[42] A. C. King and E. O. Tuck. Thin liquid layers supported by steady air-flow surface traction. *J. Fluid Mech.*, 251:709–718, 1993.

[43] A. C. King, E. O. Tuck, and J.-M. Vanden-Broeck. Air-blown waves on thin viscous sheets. *Phys. Fluids A*, 5:973–978, 1993.

[44] J. J. Kriegsmann, M. J. Miksis, and J.-M. Vanden-Broeck. Pressure driven disturbances on a thin viscous film. *Phys. Fluids*, 10:1249–1255, 1998.

[45] P. A. Kuibin. An asymptotic description of the rivulet flow along an inclined cylinder. *Russ. J. Engng. Thermophys.*, 6:33–45, 1996.

[46] C. Lemaitre, E. de Langre, and P. Hémon. Rainwater rivulets running on a stay cable subject to wind. *Euro. J. Mech. B/Fluids*, 29:251–258, 2010.

[47] G. A. Leslie, S. K. Wilson, and B. R. Duffy. Non-isothermal flow of a thin film of fluid with temperature-dependent viscosity on a stationary horizontal cylinder. *Phys. Fluids*, 23:062101, 2011.

[48] G. A. Leslie, S. K. Wilson, and B. R. Duffy. Three-dimensional coating and rimming flow: a ring of fluid on a rotating horizontal cylinder. *J. Fluid Mech.*, 716:51–82, 2013.

[49] X. Li and C. Pozrikidis. Shear flow over a liquid drop adhering to a solid surface. *J. Fluid Mech.*, 307:167–190, 1996.

[50] P. G. López, M. J. Miksis, and S. G. Bankoff. Inertial effects on contact line instability in the coating of a dry inclined plate. *Phys. Fluids*, 9:2177–2183, 1997.

[51] S. Luo, H. Li, W. Fei, and Y. Wang. Effect of counter current gas phase on liquid film. *Front. Chem. Eng. China*, 3:135–137, 2009.

[52] S. Luo, H. Li, W. Fei, and Y. Wang. Liquid film characteristics on surface of structured packing. *Chinese J. Chem. Eng.*, 17:47–52, 2009.

[53] I. S. McKinley and S. K. Wilson. The linear stability of a ridge of fluid subject to a jet of air. *Phys. Fluids*, 13:872–883, 2001.

[54] I. S. McKinley and S. K. Wilson. The linear stability of a drop of fluid during spin coating or subject to a jet of air. *Phys. Fluids*, 14:133–142, 2002.

[55] I. S. McKinley, S. K. Wilson, and B. R. Duffy. Spin coating and air-jet blowing of thin viscous drops. *Phys. Fluids*, 11:30–47, 1999.

[56] F. Melo and S. Douady. From solitary waves to static patterns via spatiotemporal intermittency. *Phys. Rev. Let.*, 71:3283–3286, 1993.

[57] K. Mertens, V. Putkaradze, and P. Vorobieff. Morphology of a stream flowing down an inclined plane. Part 1. Braiding. *J. Fluid Mech.*, 531:49–58, 2005.

[58] J. Mikielewicz and J. R. Moszynski. Minimum thickness of a liquid film flowing vertically down a solid surface. *Int. J. Heat Mass Tran.*, 19:771–776, 1976.

[59] J. Mitrovic. Flow structures of a liquid film falling on horizontal tubes. *Chem. Eng. Technol.*, 28:684–694, 2005.

[60] H. K. Moffatt. Behaviour of a viscous film on the outer surface of a rotating cylinder. *J. Méc.*, 16:651–673, 1977.

[61] T. G. Myers. Thin films with high surface tension. *SIAM Rev.*, 40:441–462, 1998.

[62] T. G. Myers and J. P. F. Charpin. A mathematical model for atmospheric ice accretion and water flow on a cold surface. *Int. J. Heat Mass Transf.*, 47:5483–5500, 2004.

[63] T. G. Myers, H. X. Liang, and B. Wetton. The stability and flow of a rivulet driven by interfacial shear and gravity. *Int. J. Nonlinear Mech.*, 39:1239–1249, 2004.

[64] A. Daerr N. Le Grand-Piteira and L. Limat. Meandering rivulets on a plane: A simple balance between inertia and capillarity. *Phys. Rev. Lett.*, 96:254503, 2006.

[65] T. Nakagwa. Rivulet meanders on a smooth hydrophobic surface. *Int. J. Multiphas. Flow*, 18:455–463, 1992.

[66] T. Nakagwa and J. C. Scott. Stream meanders on a smooth hydrophobic surface. *J. Fluid Mech.*, 149:89–99, 1984.

[67] C. J. Noakes, J. R. King, and D. S. Riley. On three-dimensional stability of a uniform, rigidly rotating film on a rotating cylinder. *Q. J. Mech. Appl. Math.*, 58:229–256, 2005.

[68] W. Nusselt. Die oberflachenkondensation des wasserdampfes. *Z. Vereines deutscher Ingenieure*, 60:541–546, 1916.

[69] W. Nusselt. Die oberflachenkondensation des wasserdampfes. *Z. Vereines deutscher Ingenieure*, 60:569–575, 1916.

[70] S. B. G. O'Brien and L. W. Schwartz. Theory and modeling of thin film flows. *Encyclopedia of Surface and Colloid Science (A. F. Hubbard, Ed.)*, pages 5283–5297, Marcel Dekker, New York 2002.

[71] A. Oron, S. H. Davis, and S. G. Bankoff. Long-scale evolution of thin liquid films. *Rev. Mod. Phys.*, 69:931–980, 1997.

[72] J. P. Pascal and S. J. D. D'Alessio. Instability of power-law fluid flows down an incline subjected to wind stress. *Appl. Math. Model.*, 31:1229–1248, 2007.

[73] C. Paterson, S. K. Wilson, and B. R. Duffy. Pinning, de-pinning and re-pinning of a slowly varying rivulet. *Euro. J. Mech. B/Fluids*, 41:94–108, 2013.

[74] C. A. Perazzo and J. Gratton. Navier-Stokes solutions for parallel flow in rivulets on an inclined plane. *J. Fluid Mech.*, 507:367–379, 2004.

[75] K. Pougatch and I. Frigaard. Thin film flow on the inside surface of a horizontally rotating cylinder: Steady state solutions and their stability. *Phys. Fluids*, 23:022102, 2011.

[76] V. V. Pukhnachev. Motion of a liquid film on the surface of a rotating cylinder in a gravitational field. *J. Appl. Mech. Tech. Phys.*, 18:344–351, 1977.

[77] G. Ribatski and A. M. Jacobi. Falling-film evaporation on horizontal tubes – a critical review. *Int. J. Refrig*, 28:635–653, 2005.

[78] A. C. Robertson, I. J. Taylor, S. K. Wilson, B. R. Duffy, and J. M. Sullivan. Numerical simulation of rivulet evolution on a horizontal cable subject to an external aerodynamic field. *J. Fluids Struct.*, 26:50–73, 2010.

[79] B. Ruan, A. M. Jacobi, and L. Li. Effects of a countercurrent gas flow on falling-film mode transitions between horizontal tubes. *Exp. Therm. Fluid Sci.*, 33:1216–1225, 2009.

[80] H. H. Saber and M. S. El-Genk. On the breakup of a thin liquid film subject to interfacial shear. *J. Fluid Mech.*, 500:113–133, 2004.

[81] A. D. Schleizer and R. T. Bonnecaze. Displacement of a two-dimensional immiscible droplet adhering to a wall in shear and pressure-driven flows. *J. Fluid Mech.*, 383:29–54, 1999.

[82] P. Schmuki and M. Laso. On the stability of rivulet flow. *J. Fluid Mech.*, 215:125–143, 1990.

[83] L. W. Schwartz and R. V. Roy. Theoretical and numerical results for spin coating of viscous liquids. *Phys. Fluids*, 16:569–584, 2005.

[84] G. K. Seevaratnam, H. Ding, O. Michel, J. Y. Y. Heng, and O. K. Matar. Laminar flow deformation of a droplet adhering to a wall in a channel. *Chem. Eng. Sci.*, 65:4523–4534, 2010.

[85] G. Seiden and P. J. Thomas. Complexity, segregation, and pattern formation in rotating-drum flows. *Rev. Mod. Phys.*, 83:1323–1365, 2011.

[86] N. H. Shuaib, H. Power, S. Hibberd, and K. Simmons. A numerical study of wave structures developed on the free surface of a film flowing on inclined planes and subjected to surface shear. *Int. J. Numer. Meth. Engng*, 68:755–789, 2006.

[87] P. D. M. Spelt. Shear flow past two-dimensional droplets pinned or moving on an adhering channel wall at moderate Reynolds numbers: a numerical study. *J. Fluid Mech.*, 561:439–463, 2006.

[88] K. Sugiyama and M. Sbragaglia. Linear shear flow past a hemispherical droplet adhering to a solid surface. *J. Eng. Math.*, 62:35–50, 2008.

[89] J. M. Sullivan. *Thin-film flows subject to an external shear stress.* PhD thesis, University of Strathclyde, 2008.

[90] J. M. Sullivan, C. Paterson, S. K. Wilson, and B. R. Duffy. A thin rivulet or ridge subject to a uniform transverse shear stress at its free surface due to an external airflow. *Phys. Fluids*, 24:082109, 2012.

[91] J. M. Sullivan, S. K. Wilson, and B. R. Duffy. A thin rivulet of perfectly wetting fluid subject to a longitudinal surface shear stress. *Q. J. Mech. Appl. Math.*, 61:25–61, 2008.

[92] A. J. Tanasijczuk, C. A. Perazzo, and J. Gratton. Navier–Stokes solutions for steady parallel-sided pendent rivulets. *Euro. J. Mech. B/Fluids*, 29:465–471, 2010.

[93] S. T. Thoroddsen and L. Mahadevan. Experimental study of coating flows in a partially-filled horizontally rotating cylinder. *Exp. Fluids*, 23:1–13, 1997.

[94] M. Tirumkudulu and A. Acrivos. Coating flows with a rotating horizontal cylinder: Lubrication analysis, numerical computations, and experimental measurements. *Phys. Fluids*, 13:14–19, 2001.

[95] M. Tirumkudulu, A. Tripathi, and A. Acrivos. Particle segregation in monodisperse sheared suspensions. *Phys. Fluids*, 11:507–509, 1999.

[96] G. D. Towell and L. B. Rothfeld. Hydrodynamics of rivulet flow. *A. I. Ch. E. J.*, 12:972–980, 1966.

[97] D. Tseluiko, M. G. Blyth, D. T. Papageorgiou, and J.-M. Vanden-Broeck. Electrified viscous thin film flow over topography. *J. Fluid Mech.*, 597:449–475, 2008.

[98] K. Ueno and M. Farzaneh. Linear stability analysis of ice growth under supercooled water film driven by a laminar airflow. *Phys. Fluids*, 23:042103, 2011.

[99] E. B. Dussan V. On the ability of drops to stick to surfaces of solids. Part 3. The influences of the motion of the surrounding fluid on dislodging drops. *J. Fluid Mech.*, 174:381–397, 1987.

[100] L. van Bokhoven, R. Badie, B. Brasjen, H. Gelderblom, A. Ghosh, A. Hirschberg, N. ten Kate, H. Kim, S. Kleijin, D. Lohse, C. Paterson, S. K. Wilson, and K. Winkels. Droplet removal with impinging planar micro jets. In *Physics with Industry*, pages 3–13. Badoux Drukkerij bv, 2010.

[101] M. Van Dyke. *Perturbation Methods in Fluid Mechanics*. Academic, 1964.

[102] J.-M. Vanden-Broeck and T. Miloh. The influence of a layer of mud on the train of waves generated by a moving pressure distribution. *J. Engng. Math.*, 30:387–400, 1996.

[103] M. Villegas-Díaz, H. Power, and D. S. Riley. On the stability of rimming flows to two-dimensional disturbances. *Fluid Dyn. Res.*, 33:141–172, 2003.

[104] M. Villegas-Díaz, H. Power, and D. S. Riley. Analytical and numerical studies of the stability of thin-film rimming flow subject to surface shear. *J. Fluid Mech.*, 541:317–344, 2005.

[105] S. K. Wilson and B. R. Duffy. On the gravity-driven draining of a rivulet of viscous fluid down a slowly varying substrate with variation transverse to the direction of flow. *Phys. Fluids*, 10:13–22, 1998.

[106] S. K. Wilson and B. R. Duffy. Strong temperature-dependent-viscosity effects on a rivulet draining down a uniformly heated or cooled slowly varying substrate. *Phys. Fluids*, 15:827–840, 2003.

[107] S. K. Wilson and B. R. Duffy. A rivulet of perfectly wetting fluid draining steadily down a slowly varying substrate. *IMA J. Appl. Math.*, 70:293–322, 2005.

[108] S. K. Wilson and B. R. Duffy. Unidirectional flow of a thin rivulet on a vertical substrate subject to a prescribed uniform shear stress at its free surface. *Phys. Fluids.*, 17:108105, 2005.

[109] S. K. Wilson and B. R. Duffy. When is it energetically favorable for a rivulet of perfectly wetting fluid to split? *Phys. Fluids.*, 17:078104, 2005.

[110] S. K. Wilson, B. R. Duffy, and R. Hunt. A slender rivulet of a power-law fluid driven by either gravity or a constant shear stress at the free surface. *Q. J. Mech. Appl. Math.*, 55:385–408, 2002.

[111] S. K. Wilson, B. R. Duffy, and A. B. Ross. On the gravity-driven draining of a rivulet of viscoplastic material down a slowly varying substrate. *Phys. Fluids*, 14:555–571, 2002.

[112] S. K. Wilson, R. Hunt, and B. R. Duffy. The rate of spreading in spin coating. *J. Fluid Mech.*, 413:65–88, 2000.

[113] S. K. Wilson, J. M. Sullivan, and B. R. Duffy. The energetics of the breakup of a sheet and of a rivulet on a vertical substrate in the presence of a uniform surface shear stress. *J. Fluid Mech.*, 674:281–306, 2011.

[114] S. Yon and S. Pozrikidis. Deformation of a liquid drop adhering to a plane wall: Significance of the drop viscosity and the effect of an insluble surfactant. *Phys. Fluids*, 11:1297–1308, 1999.

[115] H. Zhang, J. Yue, G. Chen, and Q. Yuan. Flow pattern and break-up of liquid film in single-channel falling film microreactors. *Chem. Engng. J.*, 163:126–132, 2010.

[116] J. Zhang, M. J. Miksis, and S. G. Bankoff. Nonlinear dynamics of a two-dimensional viscous drop under shear flow. *Phys. Fluids*, 18:072106, 2006.